

# **Examining lipid metabolism of colorectal adenomas and carcinomas using Rapid Evaporative Ionisation Mass Spectrometry (REIMS)**

**Sam Mason MBBS BSc MRCS FHEA**

Department of Surgery and Cancer, Imperial College London  
St Mary's Hospital, London, UK

2021

A thesis submitted to Imperial College London for the degree of Doctor of Philosophy

## **Supervisors**

**Mr James Kinross**

Department of Surgery and Cancer, Imperial College London

**Professor Zoltan Takats**

Department of Metabolism, Digestion and Reproduction, Imperial College London

**Professor Ara Darzi**

Department of Surgery and Cancer, Imperial College London

## Declaration

This thesis has been submitted to Imperial College London as part of a Doctor of Philosophy degree course. I hereby declare that I am the sole author of this thesis and the research represents my own, with any work conducted by co-authors, contributors or collaborators clearly described in the acknowledgements section.

Signed: Sam Mason

Date: 10/03/2021

The copyright of this thesis rests with the author. Unless otherwise indicated, its contents are licensed under a Creative Commons Attribution Non-Commercial 4.0 International Licence (CC BY-NC). Under this licence, you may copy and redistribute the material in any medium or format. You may also create and distribute modified versions of the work. This is on the condition that: you credit the author and do not use it, or any derivative works, for a commercial purpose. When reusing or sharing this work, ensure you make the licence terms clear to others by naming the licence and linking to the licence text. Where a work has been adapted, you should indicate that the work has been changed and describe those changes. Please seek permission from the copyright holder for uses of this work that are not included in this licence or permitted under UK Copyright Law.

## Funding and Conflicts of Interest

I am very grateful to the bodies responsible for directly or indirectly funding the work presented in this thesis:

1. Cancer Research UK PhD Fellowship, £256,000. '*Real time precision phenotyping of significant polyps and early colorectal cancers using rapid evaporative ionisation mass spectrometry (REIMS)*'. PI: Mr James Kinross, CIs: Professor Zoltan Takats, Professor Ara Darzi. Fellowship duration October 2017 – April 2021.
2. Infrastructure support for this thesis was provided by the NIHR Imperial Biomedical Research Centre

I have no conflicts of interest to declare.

# Abstract

## Background

There is an unmet need for real-time intraoperative colorectal tissue recognition, which would promote personalised oncologic decision making. Rapid Evaporative Ionization Mass Spectrometry (REIMS) analyses the composition of cellular lipids through the aerosol generated from electrosurgical instruments, providing a novel diagnostic platform and surgeon feedback.

## Thesis Hypothesis

Colorectal lipid metabolism and cellular lipid composition are associated with the phenotype of colorectal adenomas and carcinomas, which can be leveraged for tissue recognition *in vivo*.

## Methods

This thesis contains three work packages. First, a method for REIMS spectral quality control was developed based on a human dataset and analysis of a porcine model assessed the spectral impact of technical and environmental factors. Second, an *ex vivo* spectral reference database was constructed from analysis of human colorectal tissues, assessing the ability of REIMS for tissue recognition. Finally, REIMS was translated into the operating theatre, for proof-of-principle application of during transanal minimally invasive surgery (TAMIS).

## Results

Sensitivity analyses revealed seven minimum quality criteria for REIMS spectra to be included in all future statistical analyses, with quality also impacted by low diathermy power, coagulation mode and tissue contamination. Based on tissue of 161 patients, REIMS could differentiate colorectal normal, adenoma and cancer tissue with 91.1% accuracy, and disease from normal with 93.5% accuracy. REIMS could risk-stratify adenomas by predicting grade of dysplasia, however not histological features of poor prognosis in cancers. 61 pertinent lipid metabolites were structurally identified. REIMS was coupled to TAMIS in seven patients. Optimisation of the workflow

successfully increased signal intensity, with tissue recognition showing high accuracy *in vivo* and identification of a cancer-involved margin.

## Discussion

This thesis demonstrates that REIMS can be optimised and applied for accurate real-time colorectal tissue recognition based on cellular lipid composition. This can be translated *in vivo*, with promising results during first-in-man mass spectrometry-coupled TAMIS.

## Peer-Reviewed Publications and Presentations

The following are the peer-reviewed research outputs directly related to the content of this thesis until February 2021.

### Publications

1. **Mason SE**, Poynter L, Takats Z, Darzi A, Kinross JM. Optical Technologies for Endoscopic Real-Time Histologic Assessment of Colorectal Polyps: A Meta-Analysis. *American Journal of Gastroenterology*. 2019;114(8):1219-30.
2. **Mason SE**, Manoli E, Poynter L, Alexander J, Paizs P, Adebessin A, Goldin R, Darzi A, Takats Z, Kinross JM. Mass spectrometry transanal minimally invasive surgery (MS-TAMIS) to promote organ preservation in rectal cancer. *Surgical Endoscopy* 2020;34:3618-25

### International Oral Presentations

1. **Mason SE et al.** Mass spectrometry transanal minimally invasive surgery (MS-TAMIS) for organ preservation in rectal cancer. *Society of American Gastrointestinal and Endoscopic Surgeons*, Baltimore
2. **Mason SE et al.** Chemical endoscopy of mucosal lipids permits near real time identification of poor prognostic features in colorectal cancer. *European Association for Endoscopic Surgery congress*, London

### International Poster Presentations

1. **Mason SE et al.** Tumour lipid metabolism distinguishes mucinous and non-mucinous colorectal adenocarcinomas. *European Colorectal Congress*, St Gallen's
2. **Mason SE et al.** Prospective observational cohort study of rapid evaporative ionization mass spectrometry (REIMS) for near-real time diagnosis and stratification of colorectal cancer. *Digestive Diseases Week Congress*, Washington DC
3. **Mason SE et al.** Optical Technologies for Endoscopic Real-Time Histological Assessment of Colorectal Polyps; a Systematic Review and Meta-Analysis. *United European Gastroenterology Week*, Vienna

## Acknowledgements

Completion of this thesis would not have been possible without the input and support of a large group of people, to whom I am sincerely grateful.

First, I would like to thank my supervisor and mentor Mr James Kinross, who guided my path throughout this thesis and opened countless doors for both the progression of my work and my professional development. He was always available if ever I needed help, with an enthusiasm and eternal optimism that I certainly hope to carry forward with me. I am extremely appreciative of Professor Zoltan Takats, whose unimaginably broad biochemical and analytical knowledge never ceases to amaze me, and from whom I have learnt the value of a rigorous scientific approach, the importance of being data-driven and the power of deduction from first principles. And finally, to Professor Ara Darzi, whose honest feedback was always welcomed and whose ability to excel across so many disciplines has been an inspiration.

I have had the pleasure of working within a talented multi-disciplinary research team and certain members require specific recognition for their role in the success of the work. I am extremely appreciative to Efty Manoli, a friend, colleague and chemist who gave countless hours of his own time teaching me about analytical chemistry, helping me run experiments and showing the patience required to work with a clinician venturing into the scientific world. My predecessor Dr James Alexander was responsible for analysing colorectal tissues with REIMS prior to my start in October 2017 and samples in the colorectal biobank were also recruited by Mr Afeez Adebesein, Mr Liam Poynter, Ms Sarah Azadian and Mr Efty Manoli. I am grateful to Dr Lauren Ford, who I could always bounce ideas off of and deepen my understanding of mass spectrometry. The histopathology department have been unwavering in their support for this work and their expertise shown, including Professor Rob Goldin, Ms Martha Jamroziak and Ms Hiromi Kudo. I would also like to thank James McKenzie for his guidance on approaching big data and performing learning curve simulations.

I feel extremely fortunate for the cohort with whom I shared the 1092 office. I have made some lifelong friends and I am sure there will be many more bottles of wine, golf outings and ski trips to come.

I would like to thank the patients who altruistically volunteer to be involved in medical research, as without them, work such as this would be impossible. And to Cancer Research UK, whose belief in the project and funding has allowed me to complete this PhD fellowship.

I would like to dedicate this thesis to Sarah, for the love, understanding and patience shown over these past years. And to my parents, who have never doubted me and always encouraged me to fulfil my potential.

## Table of Contents

Declaration .....	2
Funding and Conflicts of Interest .....	2
Abstract .....	3
Background.....	3
Thesis Hypothesis .....	3
Methods .....	3
Results .....	3
Discussion .....	4
Peer-Reviewed Publications and Presentations .....	5
Publications .....	5
International Oral Presentations .....	5
International Poster Presentations.....	5
Acknowledgements .....	6
List of Figures.....	12
List of Tables .....	20
Abbreviations .....	22
Chapter 1 – Clinical Background and Introduction to Mass Spectrometry .....	24
1.1 Colorectal Cancer.....	24
1.1.1 Epidemiology .....	24
1.1.2 Investigation and Diagnosis .....	24
1.1.3 Pathology.....	25
1.1.4 Surgical and Endoscopic Management.....	27
1.1.5 Electrosurgery.....	28
1.2 Lipids and Cancer Metabolism.....	30
1.2.1 Common Lipid Structures .....	30
1.2.2 Normal Function and Metabolism of Lipids Within Cells .....	31
1.2.3 Dysregulation of Lipid Metabolism in Cancer .....	31
1.2.4 Lipid Abundance and Clinical Phenotype.....	34
1.3 Metabolomics.....	34
1.4 Mass Spectrometry.....	36
1.5 Rapid Evaporative Ionisation Mass Spectrometry.....	40
1.6 Tandem Mass Spectrometry and Metabolite Identification.....	41
1.7 REIMS Data Handling and Analysis .....	44
1.8 Statistical Principles and Techniques.....	45
1.8.1 Unsupervised Methods.....	46

1.8.2 Supervised Methods.....	47
1.8.3 Cross Validation and Diagnostic Accuracy.....	48
1.8.4 Tissue Recognition.....	49
1.8.5 Univariate Methods.....	50
1.9 Tissue Recognition using Mass Spectrometry.....	51
1.9.1 REIMS.....	51
1.9.2 Alternative Technologies for Intraoperative Use.....	54
1.9.3 Requirements for Future Technologies.....	54
Chapter 2 – Optical Technologies for Endoscopic Real-Time Histological Assessment of Colorectal Polyps: A Meta-Analysis.....	57
2.1 Introduction.....	57
2.2 Methods.....	58
2.2.1 Search Strategy.....	58
2.2.2 Criteria for Study Inclusion.....	58
2.2.3 Data Extraction and Analysis.....	59
2.3 Results.....	60
2.3.1 Digital Chromoendoscopy.....	61
2.3.2 Dye Chromoendoscopy.....	66
2.3.3 Fluorescence Analysis.....	69
2.3.4 Microscopic Imaging.....	69
2.3.5 Computer-aided Recognition.....	70
2.3.6 Chronologic Analysis.....	71
2.4 Discussion.....	71
2.5 Conclusion.....	76
Chapter 3 - Thesis Hypothesis, Rationale, Aims and Design.....	77
3.1 Hypothesis.....	77
3.2 Rationale.....	77
3.3 Thesis Aims.....	79
3.4 Thesis Design.....	79
Chapter 4 – Materials and Methods.....	81
4.1 Research oversight and governance.....	81
4.2 Ethical approval.....	81
4.3 Patient recruitment.....	81
4.4 Sample collection and storage.....	82
4.4.1 Tissue collection from surgical and endoscopic resections.....	82
4.4.2 Sample storage.....	82
4.5 REIMS tissue analysis.....	82

4.5.1	Technical specifications .....	82
4.5.2	Workflow for <i>ex vivo</i> tissue analysis .....	86
4.5.3	Workflow for <i>in vivo</i> tissue analysis.....	86
4.6	Histopathological validation .....	87
4.7	Statistical Analyses .....	88
4.7.1	Clinical data collection.....	88
4.7.2	<i>Ex vivo</i> REIMS data analysis .....	88
4.7.3	<i>In vivo</i> REIMS data analysis.....	90
4.7.4	<i>Non-spectral data analysis</i> .....	91
Chapter 5 – WP1:	REIMS spectral quality control .....	92
5.1	Introduction.....	92
5.2	Defining quality for REIMS spectra .....	93
5.2.1	Aim.....	93
5.2.2	Methods .....	93
5.2.3	Results .....	95
5.2.4	Discussion .....	108
5.3	Impact of Technical and Environmental Factors on REIMS Mass Spectra .....	113
5.3.1	Aim and Rationale .....	113
5.3.2	Methods .....	114
5.3.3	Results .....	117
5.3.4	Discussion .....	140
5.4	Chapter Conclusion.....	144
Chapter 6 – WP2:	Creation and analysis of an <i>ex vivo</i> colorectal REIMS spectral database .....	145
6.1	Chapter Aims, Objectives and Research Questions.....	145
6.2	Methods .....	146
6.2.1	Patient recruitment and sample collection .....	146
6.2.2	MS analysis and specifications.....	146
6.2.3	Statistical analyses.....	147
6.3	Results .....	147
6.3.1	Tissue recognition using REIMS .....	154
6.3.2	REIMS in risk stratification of colorectal cancers.....	162
6.3.3	REIMS in risk stratification of colorectal adenomas .....	170
6.3.4	Identification of lipid metabolites which differentiate colorectal tissue types .....	174
6.4	Discussion .....	191
6.4.1	Clinical impact of REIMS accuracy for tissue recognition and risk-stratification .....	191
6.4.2	Lipidomic features of colorectal carcinogenesis.....	194
6.4.3	Limitations .....	197

6.5 Chapter conclusion .....	206
Chapter 7 – WP3: <i>In vivo</i> application of REIMS during TAMIS.....	208
7.1 Chapter Rationale, Aims and Objectives .....	208
7.2 Methods .....	209
7.2.1 Patient recruitment .....	209
7.2.2 MS analysis and specifications.....	209
7.2.3 Statistical analyses.....	210
7.3 Results .....	210
7.3.1 LDA model for rectal tissue recognition .....	211
7.3.2 Optimising MS-TAMIS.....	212
7.3.3 Tissue recognition during MS-TAMIS.....	217
7.4 Discussion .....	218
7.4.1 Optimisation of REIMS for MS-TAMIS .....	219
7.4.2 Challenges translating REIMS technology <i>in vivo</i> .....	220
7.4.3 Clinical impact of MS-TAMIS.....	220
7.4.4 Limitations of histological validation .....	222
7.5 Chapter conclusion .....	223
Chapter 8 – Thesis conclusions and future work.....	224
8.1 Conclusions.....	224
8.2 Future work .....	226
8.2.1 Validation of <i>ex vivo</i> findings .....	226
8.2.2 Identifying biological drivers of metabolic dysregulation.....	227
8.2.3 Technological development.....	228
8.2.4 Clinical applications in colorectal disease.....	229
Bibliography.....	231
Appendix.....	254
Appendix 1 – TNM version 7 classification for colorectal cancers .....	254
Appendix 2 – AJCC and Duke’s staging for colorectal cancers.....	255
Appendix 3 – search strategy for meta-analysis on real-time optical technologies for histological assessment of colorectal polyps.....	256
Appendix 4 – QUADAS-2 scores for digital chromoendoscopy studies .....	257
Appendix 5 – QUADAS-2 scores for dye chromoendoscopy studies .....	261
Appendix 6 – QUADAS-2 scores for fluorescence studies .....	262
Appendix 7 – QUADAS-2 scores for microscopic imaging studies.....	263
Appendix 8 – QUADAS-2 scores for computer-aided recognition studies.....	263
Appendix 9 – Permissions from publishers for the use of figures .....	264

## List of Figures

Figure 1.1 – The normal-adenoma-carcinoma progression with the timepoints of commonly accumulated genetic changes, which ultimately results in tumour cells invading through the muscularis mucosae (orange) as an invasive carcinoma. Adapted with permission from Walther *et al.*

Figure 1.2 – The structure of glycerophospholipids, with the positions shown where fatty acyl chains (**R<sub>1</sub>** and **R<sub>2</sub>**) and an amino alcohol (**X**) can be substituted to change the subtype and molecular species of the lipid. Example headgroup substitutions are given in the inset table.

Figure 1.3 – dysregulation of lipid metabolism in cancer cells, revealing how changes to SREBP transcription factors influences enzymes in the lipid biosynthesis pathway. Adapted with permission from Santos & Schulze.

Figure 1.4 – schematic of a monopolar electrosurgical device coupled to a REIMS source. This demonstrates how the surgical aerosol is generated from tissue heating and is transported to the REIMS interface via PTFE tubing, powered by a Venturi device. The aerosol is then directed through a transfer capillary against a 900°C collision surface, generating gas-phase ions. Ions are then directed using a StepWave before injection into the mass spectrometer. The dashed blue line represents the path of the aerosol and ions (before and after the collision surface respectively).

Figure 1.5 – representative MS/MS spectrum demonstrating typical negatively charged product ions seen from fragmentation of PG(16:0/18:1), with the molecular structure presented (inset). The most common sites of fragmentation are annotated (dashed lines), with the green lines producing loss of fatty acid as a ketene and blue lines producing neutral loss of fatty acid.

Figure 1.6 – a representative mass spectrum, where 150-1200 m/z is plotted against intensity. The m/z ranges in negative mode where fatty acid (red), glycerophospholipid (GPL; blue) and triglyceride (TG; green) metabolites are commonly found are highlighted.

Figure 1.7 – representative PCA of six variables demonstrating a variety of intra- and inter-group variation and clustering.

Figure 1.8 – a representative 2x2 confusion matrix, denoting how common metrics of diagnostic accuracy are calculated.

Figure 2.1 – PRISMA flowchart of for the identification, screening, eligibility and inclusion of studies. Reproduced with permission Mason *et al.*

Figure 2.2 – the summary ROC for the three digital chromoendoscopy technologies. This demonstrated that there is very little apparent difference in accuracy between them, with summary points which plot very closely. Reproduced with permission Mason *et al.*

Figure 2.3 – funnel plots of digital chromoendoscopy (**A**) and dye chromoendoscopy (**B**) studies, with a shaded area representing the location that published studies are under-represented. Reproduced with permission Mason *et al.*

Figure 2.4 – the negative predictive value of digital chromoendoscopy (**A**) and dye chromoendoscopy (**B**) plotted chronologically based on the year that each study was published. Reproduced with permission Mason *et al.*

Figure 3.1 – the structure of the thesis with the narrative questions addressed in each chapter.

Figure 4.1 – The Xevo G2-S qToF mass spectrometer (Waters Corporation, USA) used for all *ex vivo* and *in vivo* analyses (**A**). A close view of the Venturi system attached to the REIMS source is presented (**B**), with the path of surgical aerosol shown (dashed maroon line).

Figure 4.2 – the monopolar diathermy pencil handpiece used in *ex vivo* REIMS analysis. The main electrode tip applies the current to the tissue following activation of buttons by the operator's thumb. An aperture at the base of the tip aspirates the surgical aerosol through the body of the handpiece and into the PTFE tubing to the mass spectrometer.

Figure 4.3 – the monopolar electrocautery current generator (Covidien, Medtronic, UK), used for *ex vivo* REIMS analysis and *in vivo* during TAMIS.

Figure 4.4 – screenshot of the AMX Recognition software, with a visual alert given to the operator both as a colour warning and as a written prediction with percentage. The lower panel denotes the ion intensity over time and three distinct analyses can be demonstrated in this excerpt. The right-sided panel lists the classification predictions as they occur, with the scan number that they apply to.

Figure 5.1 – PCA (**A**) and LDA (**B**) plots for all analyses of colorectal tissue, with the confusion matrix following LOPO CV (**C**).

Figure 5.2 – Scatter plot demonstrating how the accuracy of REIMS in differentiating cancer, adenoma and normal mucosa differs based on the minimum composition of cancer or adenoma tissue in the sample.

Figure 5.3 – 3-dimensional PCA plot of all data (**A**), revealing a batch effect (red circle) and a PCA plot after removal of all samples run by the Dolores instrument from March-June 2015 (**B**).

Figure 5.4 – plot of spectra coloured by whether they were present in the Dolores instrument batch effect or not, where masses were increased in the lower mass ranges and increased in the upper mass ranges.

Figure 5.5 – cumulative count of spectra from carcinoma, adenoma and normal mucosa plotted as the signal:noise ratio increases from the lowest to highest value along the x axis.

Figure 5.6 – the cumulative misclassification rate (blue) when spectra are ordered along the x axis from low to high signal:noise ratio. An equal probability of misclassification across the signal:noise range is presented (orange dotted line).

Figure 5.7 – Excess misclassifications as spectra are ordered along the x axis from low to high signal:noise ratio for all samples (**A**), carcinoma (**B**), adenoma (**C**) and normal mucosa (**D**). Polynomial trend lines are presented (dotted). A positive gradient denotes a greater rate of REIMS misclassifying tissue subtypes than expected.

Figure 5.8 – The impact of high and low signal:noise on how tumour spectra misclassify.

Figure 5.9 – the impact of minimum signal:noise thresholds on the accuracy of REIMS in differentiating spectra from tumour, adenoma and normal mucosa.

Figure 5.10 – PCA plot of the 802 spectra labelled by tissue subtype (**A**), demonstrating a possible batch effect (red oval), with this batch effect again evident when labelling the analytical run in January 2018 (**B**). A loadings plot of a model differentiating the January 2018 batch and other analyses (**C**) demonstrates marked increase in the intensity of the bins between  $x_{n.75} - x_{n+1.25}$ , as seen on the raw spectra (**D**). Plotting a PCA once the bins between common lipid peaks are excluded removes the batch effect (**E**).

Figure 5.11 – PCA plot with the 60 (7.5%) spectra of lowest TIC labelled (**A**). An aggregate of spectra with high intensity (**B**) compared to those with lowest intensity (**C**).

Figure 5.12 – Accuracy of REIMS in differentiating carcinoma, adenoma and normal mucosa when spectra are excluded using different centile thresholds of TIC.

Figure 5.13 – spectrum of the background of an analytical run (**A**) demonstrating clusters of sodium formate at intervals of 67.99 (red arrows), which carry-over when analysing samples and can be seen alongside the lipid peaks (**B**).

Figure 5.14 – the environment used for analysis of porcine colorectum, with sensors to ensure no change in temperature or humidity throughout the analysis.

Figure 5.15 – Laparoscopic hook diathermy sampling device, annotated to show the point used for analysis on the heel and the PTFE aspiration tubing taped alongside the instrument.

Figure 5.16 – PCA plots of the 10 experiments conducted and the environmental or technical factor that was being assessed. Red circles denote outliers that were identified visually and removed from further analyses.

Figure 5.17 – PCA plot of PC1 against PC2 across the 10 experiments (**A**) and with the two outlying clusters of 10W power and coagulation diathermy removed (**B**). The tolerance ellipse represents the 95% boundary on the 2-dimensional scores plot as per Hotelling's  $T^2$  distribution

Figure 5.18 – PCA plot (**A**) and OPLS-DA plot with 2 X-Y and 1 orthogonal components (**B**) of the different power settings.

Figure 5.19 – aggregate spectra of the 150 most intense peaks across the four power settings used.

Figure 5.20 – normalised REIMS spectra over 120-1200 m/z range comparing cut (**A**) and coagulation (**B**) diathermy, with the spectra normalised over 600-900 m/z presented in the inset.

Figure 5.21 – loadings plot of the OPLS-DA model differentiating cut and coagulation mode diathermy using the 150 most intense peaks in 600-900 m/z range (**A**), with the PCA plot (**B**) and OPLS-DA plot using 1 X-Y and 1 orthogonal component (**C**).

Figure 5.22 – Spectra of the 150 peaks with highest intensity comparing 1m, 2.5m and 4m aspiration tube lengths.

Figure 5.23 – PCA plot (A) and OPLS-DA plot using 2 X-Y and 1 orthogonal component (B) comparing the different aspiration tube lengths.

Figure 5.24 – PCA (A) and OPLS-DA using 2 X-Y and 1 orthogonal component (B) plots of the spectra generated with and without tissue contamination. The loadings plot from the OPLS-DA model is shown (C).

Figure 5.25 - The spectra of the 150 most intense peaks comparing no contamination (A), blood on the mucosa (B) and saline on the mucosa (C).

Figure 6.1 – four validation sections following REIMS analysis annotated with the tissue types seen and the final classification given. Section A shows no abnormalities but considering there was no mucosa evident (and instead only muscle), it was deemed non-diagnostic and the spectra generated were excluded. Section B shows a villous adenomatous polyp, which is deemed to be 90% adenoma due to the small portion of muscle in the centre. Section C is heterogeneous with multiple different regions of tissue subtypes. Despite the diathermy burn not being in a tumour region directly, this was classified as 50% tumour. Section D is a mixed sample, which is diagnostic for cancer and is validated at 80% due to the 20% villous adenoma adjacent.

Figure 6.2 – the mean spectrum generated from the REIMS analysis of tumour, adenoma and normal tissue in negative mode over the 150-1000 m/z range. Notable peaks across lipid classes are annotated.

Figure 6.3 – the mean spectrum generated from the REIMS analysis of tumour, adenoma and normal tissue over the 600-1000 m/z range in negative mode, focusing on GPLs and TGs.

Figure 6.4 – PCA plot of the 1013 REIMS spectra across the 150-1000m/z range. PC1 accounted for 40.5% of the variation, PC2 for 15.2% and PC3 for 12.1%.

Figure 6.5 – loading plot for the variation seen along PC1 (A), PC2 (B) and PC3 (C) in the 150-1000m/z range.

Figure 6.6 – spectrum from an adenoma sample of patient JLA55 (A), demonstrating the contaminant peak at 367.264m/z, a spectrum from normal tissue of patient JLA222 (B), demonstrating a high relative abundance of FAs compared to GPLs; and a spectrum from tumour tissue of patient JLA210 (C), demonstrating a contaminant peak at 212.075m/z.

Figure 6.7 - the accuracy of REIMS on LOPO CV for the prediction of normal, adenoma and tumour colorectal tissue across the 150-1000 m/z range.

Figure 6.8 – PCA plot of the 1013 spectra generated from the *ex vivo* analysis of colorectal tissues over 600-1000m/z mass range. PC1, PC2 and PC3 are responsible for 43.3, 21.7 and 4.9% of the variation respectively.

Figure 6.9 – loading plot of PC1 (A) and PC2 (B) over the mass range 600-1000m/z.

Figure 6.10 – LDA plot of REIMS in the differentiation of normal, adenoma and tumour spectra over the 600-1000m/z range. The blue arrows represent spectra from the same tissue piece (JLA249) which appear to be positioned in an incorrect region of the plot.

Figure 6.11 – the accuracy of REIMS on LOPO CV for the prediction of normal, adenoma and tumour colorectal tissue; with the predictions for each spectrum collected (**A**) and for the overall tissue sample (**B**).

Figure 6.12 - the accuracy of REIMS on LOPO CV for the prediction of disease (adenoma or tumour) vs normal colorectal tissue; with the predictions for each spectrum collected (**A**) and for the overall tissue sample (**B**).

Figure 6.13 – an OPLS-DA plot with 1 orthogonal and 2 X-Y components (**A**) and a cross validated OPLS-DA plot (**B**) demonstrating the ability of REIMS to differentiate early (T1-2) and advanced (T3-4) CRC. The tolerance ellipse in **A** represents the 95% boundary on the 2-dimensional scores plot as per Hotelling's  $T^2$  distribution.

Figure 6.14 – a confusion matrix of REIMS on LOPO CV of an LDA model for the differentiation of early (T1/2) or advanced (T3/4) tumours based on the TNM criteria.

Figure 6.15 – an OPLS-DA plot with 1 orthogonal and 2 X-Y components (**A**) and a cross validated OPLS-DA plot (**B**) demonstrating the ability of REIMS to differentiate tumours with (N 1-2) and without (N 0) presence of nodal micrometastasis. The tolerance ellipse in **A** represents the 95% boundary on the 2-dimensional scores plot as per Hotelling's  $T^2$  distribution.

Figure 6.16 – a confusion matrix of REIMS on LOPO CV of an LDA model for the differentiation of tumours with (N 1/2) or without (N 0) nodal micrometastasis based on the TNM criteria.

Figure 6.17 – an OPLS-DA plot with 1 orthogonal and 2 X-Y components (**A**) and a cross validated OPLS-DA plot (**B**) demonstrating the ability of REIMS to differentiate early (AJCC I/II) or advanced (AJCC III/IV) tumours. The tolerance ellipse in **A** represents the 95% boundary on the 2-dimensional scores plot as per Hotelling's  $T^2$  distribution.

Figure 6.18 – a confusion matrix of REIMS on LOPO CV of an LDA model for the differentiation of early (AJCC I/II) or advanced (AJCC III/IV) tumours.

Figure 6.19 – an OPLS-DA plot with 1 orthogonal and 2 X-Y components, demonstrating an  $R^2X$  of 0.357 and  $Q^2$  of 0.285 (**A**) and a cross validated OPLS-DA plot (**B**) demonstrating the ability of REIMS to differentiate tumours with or without EMVI. The tolerance ellipse in **A** represents the 95% boundary on the 2-dimensional scores plot as per Hotelling's  $T^2$  distribution.

Figure 6.20 – a confusion matrix of REIMS on LOPO CV of an LDA model for the differentiation of tumours with and without EMVI.

Figure 6.21 – an OPLS-DA plot with 1 orthogonal and 2 X-Y components, demonstrating an  $R^2X$  of 0.356 and  $Q^2$  of 0.389 (**A**) and a cross validated OPLS-DA plot (**B**) demonstrating the ability of REIMS to differentiate tumours with or without LVI. The tolerance ellipse in **A** represents the 95% boundary on the 2-dimensional scores plot as per Hotelling's  $T^2$  distribution.

Figure 6.22 – a confusion matrix of REIMS on LOPO CV of an LDA model for the differentiation of tumours with and without LVI.

Figure 6.23 – an OPLS-DA plot with 1 orthogonal and 2 X-Y components, demonstrating an  $R^2X$  of 0.35 and  $Q^2$  of 0.354 (**A**) and a cross validated OPLS-DA plot (**B**) demonstrating the ability of REIMS to differentiate tumours with or without tumour budding. The tolerance ellipse in **A** represents the 95% boundary on the 2-dimensional scores plot as per Hotelling's  $T^2$  distribution.

Figure 6.24 – a confusion matrix of REIMS on LOPO CV of an LDA model for the differentiation of tumours with and without tumour budding.

Figure 6.25 – an OPLS-DA plot with 1 orthogonal and 2 X-Y components, demonstrating an  $R^2X$  of 0.347 and  $Q^2$  of 0.368 (**A**) and a cross validated OPLS-DA plot (**B**) demonstrating the ability of REIMS to differentiate tumours that produce mucin from those that do not. The tolerance ellipse in **A** represents the 95% boundary on the 2-dimensional scores plot as per Hotelling's  $T^2$  distribution.

Figure 6.26 – a confusion matrix of REIMS on LOPO CV of an LDA model for the differentiation of tumours that produce mucin from those that do not.

Figure 6.27 – photos of validation polyp validation sections showing low-grade (**A**) and high-grade (**B**) dysplasia.

Figure 6.28 – an OPLS-DA plot with 1 orthogonal and 2 X-Y components, demonstrating an  $R^2X$  of 0.473 and  $Q^2$  of 0.544 (**A**) and a cross validated OPLS-DA plot (**B**) demonstrating the ability of REIMS to differentiate adenomas with low-grade from high-grade dysplasia. The tolerance ellipse in **A** represents the 95% boundary on the 2-dimensional scores plot as per Hotelling's  $T^2$  distribution.

Figure 6.29 – confusion matrices of REIMS on LOPO CV of an LDA model for the prediction of adenomas that have HGD present in the validation section (**A**) or anywhere in the polyp on formal histopathology (**B**).

Figure 6.30 – an OPLS-DA plot with 1 orthogonal and 2 X-Y components, demonstrating an  $R^2X$  of 0.503 and  $Q^2$  of 0.333 (**A**) and a cross validated OPLS-DA plot (**B**) demonstrating the ability of REIMS to predict the highest grade of dysplasia within a sampled adenoma. The tolerance ellipse in **A** represents the 95% boundary on the 2-dimensional scores plot as per Hotelling's  $T^2$  distribution.

Figure 6.31 – an OPLS-DA plot with 1 orthogonal and 2 X-Y components, demonstrating an  $R^2X$  of 0.529 and  $Q^2$  of 0.513 (**A**) and a cross validated OPLS-DA plot (**B**) demonstrating the ability of REIMS to differentiate villous and tubular adenomas. The tolerance ellipse in **A** represents the 95% boundary on the 2-dimensional scores plot as per Hotelling's  $T^2$  distribution.

Figure 6.32 – confusion matrix of REIMS on LOPO CV of an LDA model for the differentiation of villous adenomas (VA) and tubular adenomas (TA).

Figure 6.33 – VIP score plots from OPLS-DA models of tumour vs normal (**A**), tumour vs adenoma (**B**) and adenoma vs normal (**C**). The bins are ordered by descending score on the x axis, with those highlighted in red selected for MS/MS.

Figure 6.34 – MS/MS spectrum of PE\_Cer(d18:1/16:0)-NH<sub>3</sub>-H in bin 642.45m/z, with structural annotations of the fragments (**A**) and the parent ion (**B**).

Figure 6.35 – MS/MS spectrum of PE(18:1/18:1)-NH<sub>3</sub>-H and PE(18:0/18:2)-NH<sub>3</sub>-H in bin 725.55m/z, with structural annotations of the fragments (**A**) and the parent ion (**B**).

Figure 6.36 – MS/MS spectrum of PCh(18:1/16:0)-CH<sub>3</sub> in bin 744.55m/z, with structural annotations of the fragments (**A**) and the parent ion (**B**).

Figure 6.37 – MS/MS spectrum of DG(20:3/18:2,O<sub>2</sub>)+Cl and DG(20:4/18:1,O<sub>2</sub>)+Cl in bin 709.45m/z, with annotations of the fragments (**A**) and the parent ion structure presented(**B**).

Figure 6.38 – box and whisker plots of the relative abundance of 9 metabolites across colorectal normal, adenoma and tumour tissue; with the exact mass and identity from MS/MS shown. The box reflects the 25-75<sup>th</sup> percentiles with a median line and the whiskers are 1.5 x interquartile range without extending beyond a datapoint. A jitter plot of the raw data is presented (grey).

Figure 6.39 – box and whisker plots of the total relative abundance of 7 lipid classes across normal, adenoma and tumour tissue. The box reflects the 25-75<sup>th</sup> percentiles with a median line and the whiskers are 1.5 x interquartile range without extending beyond a datapoint. A jitter plot of the raw data is presented (grey).

Figure 6.40 – heatmap of how the relative abundance of different lipid subtypes is associated with colorectal tissue type, with unsupervised clustering represented with a dendrogram.

Figure 6.41 – heatmap of how the relative abundance of PUFAs and MUFAs within GPLs is associated with colorectal tissue type (**A**) and visualised in a box as whiskers plot with jitter (**B** and **C** respectively).

Figure 6.42 – box and whisker plots of the total relative abundance of 7 lipid classes across normal, low-grade dysplastic adenomas, high-grade dysplastic adenomas and tumour tissue.

Figure 6.43 – heatmap of how the relative abundance of PUFAs and MUFAs within GPLs is associated with colorectal tissue type with adenomas separated into those with high- and low-grade dysplasia (**A**) and visualised in a box as whiskers plot with jitter (**B** and **C** respectively).

Figure 6.44 – boxplots of the relative abundance of free PUFAs (**A**) and MUFAs (**B**) across colorectal tissue types with adenomas separated into those with high- and low-grade dysplasia.

Figure 7.1 – PTFE tubing taped alongside the TAMIS dissection instrument to allow aerosol aspiration intraoperatively.

Figure 7.2 – OPLS-DA plot with 1 orthogonal and 2 X-Y components, demonstrating an R<sup>2</sup>X of 0.424 and Q<sup>2</sup> of 0.538 differentiating spectra from rectal normal, adenoma and tumour tissues (**A**) and a confusion matrix of the diagnostic accuracy on LOPO CV from an LDA model (**B**).

Figure 7.3 – representative spectra over the 150-1000m/z range for the analysis of normal mucosa ex vivo (A), in vivo prior to the optimisation of the analytical system (B) and in vivo collection following optimisation (C). All spectra have the same y axis values to allow comparison.

Figure 7.4 – still photographs from MS-TAMIS cases showing the impact of tubing position on the dissector – with a tubing that is prone to aspirate blood from the dissection (A), obscuring the view of the surgeon (B) and optimally positioned (C).

Figure 7.5 – The internal connector used to adjoin two lengths of PTFE tubing, reducing the internal diameter from 3mm to approximately 1.5mm

Figure 7.6 – the raw spectra collected *in vivo* during MS-TAMIS from rectal mucosa, submucosa and a mixture of the two. The ratio between the glycerophospholipids (blue box) and triglycerides (orange box) can be used to differentiate the layers. Reused from Mason *et al.*

Figure 7.7 – confusion matrix of ability of REIMS to differentiate rectal disease from normal mucosa during MS-TAMIS in patient JLA 623.

## List of Tables

Table 1.1 – Design and clinical application for the most commonly used monopolar electrosurgical devices in management of colorectal disease.

Table 1.2 – a selection of lipid species found to have differential abundance when comparing CRC and normal mucosa from patients.

Table 1.3 – Summary of four common techniques for mass analysis within a mass spectrometer.

Table 1.4 – selected study cohorts where REIMS has been used for human tissue recognition

Table 1.5 – mass spectrometric technologies other than REIMS which can be used to differentiate cancerous from normal tissues without sample preparation and with the potential to be applied *in vivo*.

Table 2.1 – Diagnostic accuracy of digital chromoendoscopy and its constituent technologies with subgroup analyses. 95% CIs are presented in brackets.

Table 2.2 – the diagnostic accuracy of dye chromoendoscopy in differentiating neoplastic and benign colorectal polyps.

Table 5.1 – characteristics of patients included in the dataset, with clinico-pathological and analytical features for spectra generated.

Table 5.2 – the 150 bins with the highest median intensity across all analyses and the molecular structure of the corresponding lipid metabolite. 160 metabolites could be identified, of which 50 were <sup>13</sup>C or <sup>37</sup>Cl isotopes.

Table 5.3 – the impact of technical sampling factors on spectral characteristics. ‘Signal’ is defined as the total intensity of the 50 highest peaks in 600-1000mz, ‘Noise’ is defined as the median intensity of peaks in 600-1000mz. *p* values were determined using a two tailed t-test with statistically significant findings in bold. The comparator group for each analysis was the base-case settings of 20W diathermy in cut mode, using a 2.5m aspiration tube and with no tissue contamination.

Table 5.4 – ANOVA results comparing the relative abundance of statistically significantly different metabolites using medium (2.5m) and long (4m) aspiration tube lengths. The fold change represents the degree of increase seen in the tube length with the highest intensity.

Table 5.5 – the 30 most statistically significant *m/z* values on ANOVA between the spectra of saline and with no contamination. The fold change represents the degree of increase seen in the group with the highest intensity.

Table 5.6 – the 26 *m/z* values which were significantly different on ANOVA between the spectra of blood-covered mucosa and that with no contamination. The fold change represents the degree of increase seen in the group with the highest intensity.

Table 6.1 – the number of spectra which did not meeting the minimum standards of quality and therefore would be eligible for exclusion from statistical modelling.

Table 6.2 – demographics of the 161 included patients with details of how samples were collected.

Table 6.3 – the pathology of the colorectal carcinomas included in the REIMS analysis. Some cases are reported as 'unknown' due to patients not having a radical resection allowing complete staging or due to historically incomplete metadata.

Table 6.4 – the pathology of the colorectal adenomas included in the REIMS analysis. Some cases are reported as 'unknown' due to multiple polyps being present and it not being clear which one was sampled or historically incomplete metadata.

Table 6.5 – The structural identity of 61 metabolites across 40 m/z bins determined by analysis of fragments during MS/MS in negative ion mode.

Table 6.6 – the VIP score, change in relative intensity, fold change and corrected *p* value of the 61 identified lipid metabolites when performing binary comparisons between colorectal tumour, adenoma and normal tissue.

Table 7.1 – the demographics, lesion characteristics and case outcome for the seven recruited patients scheduled to undergo TAMIS.

Table 7.2 – Technical factors for the representative spectra from analysis of normal mucosa ex vivo, the second MS-TAMIS case and the penultimate one.

## Abbreviations

AJCC	American Joint Committee on Cancer
AMX	Abstract Model Builder
ANOVA	Analysis of Variance
APC	Adenomatous Polyposis Coli
ASGE	American Society for Gastrointestinal Endoscopy
ATP	Adenosine Triphosphate
AUC	Area Under the Curve
BCSP	Bowel Cancer Screening Programme
CI	Confidence Interval
CIN	Chromosomal Instability
CLE	Confocal Laser Endomicroscopy
CMS	Consensus Molecular Subtype
CRC	Colorectal Cancer
CT	Computerised Tomography
CV	Cross Validation
DESI	Desorption Electrospray Ionisation
DG	Diglyceride
DNA	Deoxyribonucleic Acid
ELOVL	Elongation of Very Long Fatty Acids
EMR	Endoscopic Mucosal Resection
EMVI	Extramural Venous Invasion
ESD	Endoscopic Submucosal Dissection
ESI	Electrospray Ionisation
FA	Fatty Acid
FASN	Fatty Acid Synthase
FICE	Fuji Intelligent Chromo Endoscopy
GPL	Glycerophospholipid
HGD	High Grade Dysplasia
HNPCC	Hereditary Nonpolyposis Colorectal Cancer
IPA	Isopropyl Alcohol
LC	Liquid Chromatography
LDA	Linear Discriminant Analysis
LGD	Low Grade Dysplasia
LOPO	Leave-One-Patient-Out
LVI	Lymphovascular Invasion
m/z	Mass-to-charge ratio
MALDI	Matrix-Assisted Laser Desorption Ionisation
MS	Mass Spectrometry
MSI	Microsatellite Instability
MUFA	Monounsaturated Fatty Acid
NBI	Narrow Band Imaging
NMR	Nuclear Magnetic Resonance
NPV	Negative Predictive Value
OPLS-DA	Orthogonal Partial Least Squares Discriminant Analysis
PA	Phosphatidic acid
PC	Principal Component
PCA	Principal Components Analysis

PCh	Phosphatidylcholine
PE	Phosphatidylethanolamine
PG	Phosphatidylglycerol
PI	Phosphatidylinositol
PIVI	Preservation and Incorporation of Valuable endoscopic Innovations
PPV	Positive Predictive Value
PS	Phosphatidylserine
PTFE	Polytetrafluoroethylene
PUFA	Polyunsaturated Fatty Acid
REIMS	Rapid Evaporative Ionisation Mass Spectrometry
RNA	Ribonucleic Acid
ROC	Receiver Operating Characteristic
SOP	Standard Operating Procedure
TA	Tubular Adenoma
TAMIS	Transanal Minimally Invasive Surgery
TG	Triglyceride
TIC	Total Ion Current
ToF	Time of Flight
TVA	Tubulovillous Adenoma
VA	Villous Adenoma
VIP	Variable Importance of Projection
WP	Work Package

# Chapter 1 – Clinical Background and Introduction to Mass Spectrometry

## 1.1 Colorectal Cancer

### 1.1.1 Epidemiology

Colorectal cancer (CRC) is a heterogenous disease that disproportionately impacts economically developed countries such as the United Kingdom (UK)<sup>1</sup>. In recent years, the overall incidence of the disease in the UK has remained stable at around 640 cases per million people, however from an age standardised perspective, it is increasing; driven by a rise in CRC in patients less than 50 years of age<sup>1-3</sup>. Whilst annual mortality rate has fallen over the past 30 years and currently sits at 250 deaths per million people, CRC is still the 2<sup>nd</sup> most common cause of cancer death in the UK<sup>3,4</sup>.

Many risk factors and causative mechanisms have been described for the formation of CRC from a population to molecular level, however these are incomplete in describing the observed variation in the incidence of carcinogenesis. Familial CRC caused by single gene mutations account for approximately 10% of cancers, however, of those remaining, multiple attempts to develop risk models incorporating family history, lifestyle, environmental factors and single-nucleotide polymorphisms consistently show predictive accuracies in the region of 60-70%<sup>5-7</sup>. A cohort of lifestyle and environmental risk factors have repeatedly been shown to increase CRC risk in a dose-dependent fashion, including alcohol intake, red and processed meat consumption, low fibre intake, tobacco smoking and obesity<sup>8-10</sup>. Gender also has an impact, with men in the UK suffering with a 50% higher age-standardised incidence and 56% higher age-standardised mortality<sup>3</sup>.

### 1.1.2 Investigation and Diagnosis

Early detection of CRC is recognised to improve patient outcomes by allowing surgical intervention when the cancer is at a lower stage and as such, a variety of national programs are in place to identify those patients who are at increased risk. The bowel cancer screening program (BCSP), the integration of rapid assessment pathways between primary and secondary care, and surveillance

programs all work to this end with noted success, however as a consequence, there has been a marked increase in demand for colonoscopy<sup>11-15</sup>.

Colonoscopy is the gold-standard method for investigating the colorectum<sup>15</sup>. It allows magnified mucosal visualisation in high definition and once indeterminate lesions are detected, biopsies can be conducted. These are fixed in formalin, paraffin embedded, sectioned and stained with Haematoxylin and Eosin, with the diagnosis made upon microscopy by a certified histopathologist. Whilst imaging modalities such as virtual colonoscopy by computerised tomography (CT) have a high sensitivity for CRC, the diagnosis can only be formally made with confirmation on biopsy<sup>16</sup>.

### 1.1.3 Pathology

The normal-adenoma-carcinoma progression describes a process by which colorectal carcinogenesis occurs through sequential genetic and epigenetic alterations, which is responsible for both the initiation and progression of the majority of neoplastic lesions<sup>17</sup>. The initial event is a mutation in the DNA of an epithelial stem cell, which clonally expands to fill the entire crypt and then further expands through crypt fission<sup>18,19</sup>. This process results in the formation of an adenoma, defined histologically by the presence of dysplastic cells; which can be considered a pre-cancerous lesion<sup>17</sup>. As the mutational burden increases further (often over many years), the grade of dysplasia increases (from low to high) and eventually, cells invade through the muscularis mucosae into the submucosa as a carcinoma (Figure 1.1). The genetic hallmarks of this progression include the inactivation of tumour suppressor genes (such as APC and p53), activation of oncogenes (such as KRAS) and loss of heterozygosity for the long arm of chromosome 18; with some ongoing debate as to the order of mutations, which are required and how they correlate with morphology<sup>20-22</sup>. It is believed that this sequence is responsible for 70-80% of all CRCs, with the rest caused by de novo carcinogenesis<sup>23</sup>.

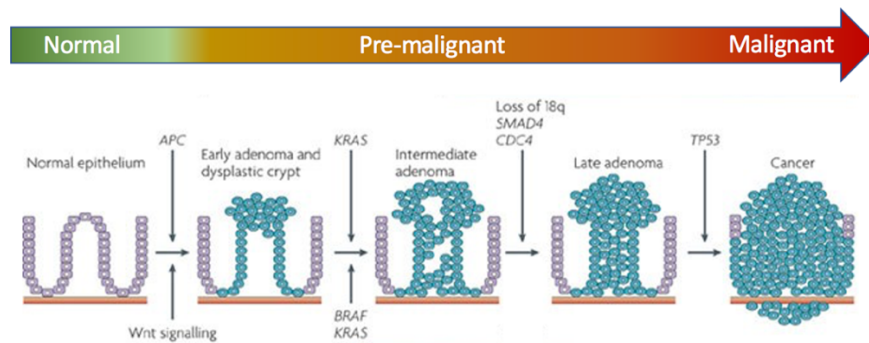


Figure 1.1 – The normal-adenoma-carcinoma progression with the timepoints of commonly accumulated genetic changes, which ultimately results in tumour cells invading through the muscularis mucosae (orange) as an invasive carcinoma. Adapted with permission from Walther *et al.*<sup>24</sup>

APC – adenomatous polyposis coli; CDC4 – cell division control protein 4.

Many histological subtypes of colorectal carcinoma are described, of which over 95% are adenocarcinoma, where they develop from the glandular columnar epithelium of the colorectum as described above<sup>25</sup>. The largest subgroup of adenocarcinomas are those that produce excess mucin, which when accounting for over 50% of the tumour volume, defines the presence of a ‘mucinous’ adenocarcinoma and when predominantly intracellular, defines the signet-ring phenotype<sup>26</sup>. This historical categorisation of CRC based on morphology has been augmented by the discovery that they can also be defined by molecular subtype, which can often directly correlate with clinical phenotype including treatment response. An example is chromosomal instability (CIN), which accounts for 85% of the adenoma-carcinoma transitions and is characterized by gains or losses of large portions of chromosomes and loss of heterozygosity of tumour-suppressor genes<sup>17</sup>. Microsatellite instability (MSI) is a further subtype, found in 20% of sporadic and almost all hereditary non-polyposis colorectal cancers (HNPCC); where there is impaired DNA mismatch repair causing increased mutation rate<sup>17</sup>. The consensus molecular subtype (CMS) of colorectal cancers is another classification system which integrates factors which are increasingly understood to impact tumour proliferation, such as the immune system and stroma<sup>27,28</sup>. This describes four subtypes (CMS1 – immune; CMS2 – canonical; CMS3 – metabolic; CMS4 – mesenchymal), which despite being defined transcriptomically, correlate closely with significant genomic, histological and clinical features (including cancer specific survival and response to radiotherapy)<sup>27-29</sup>. Adenomas are subtyped morphologically, by whether they present

tubular (similar to normal mucosa), villous (finger-like projections), serrated (saw-tooth like) or mixed features<sup>30</sup>.

The tumour, nodes and metastasis model (TNM), Dukes' criteria and the American Joint Committee on Cancer (AJCC) are clinico-pathological (or purely pathological in the case of Dukes) methods of staging CRCs by assigning scores to the anatomical location of the tumour cells (appendix 1-2)<sup>31-33</sup>. These correlate with clinical outcomes such as overall survival, with a worse prognosis associated with higher stages<sup>31,34</sup>; however concerns have been raised regarding their lack of biological basis, changing criteria over time and interobserver reproducibility<sup>35,36</sup>. In order to better correlate disease with relevant clinical outcomes, it is likely that the future of CRC staging will be an integration of morphological, genomic, transcriptomic and metabolic features.

#### 1.1.4 Surgical and Endoscopic Management

The approach to the management of colorectal polyps and cancers is significantly different. Colorectal polyps are found at 60% of colonoscopies (within a BCSP cohort), of which approximately 80% are adenomas<sup>37</sup>. Considering that adenomatous polyps may transform into carcinomas if left *in situ* for a sufficiently long time, removal via polypectomy has been demonstrated to reduce CRC mortality in the following 15 years by 53%<sup>22,38</sup>. This is commonly performed using a biopsy forceps for 1-3mm lesions, a 'cold' snare (where no diathermy is applied) or 'hot' snare using diathermy for lesions 4-9mm<sup>39</sup>. For larger polyps, endoscopic mucosal resection (EMR) can be performed, where the mucosa may be lifted from the muscularis using an injection, at which point a snare excises the lesion (using electrocautery)<sup>40</sup>. Whilst EMR is relatively simple and fast to perform, it suffers with an inability to remove large lesions in a single piece and it is believed that residual disease left after resection is responsible for the recurrence rate of 15-20%<sup>41</sup>. An alternative is endoscopic submucosal dissection (ESD), which dissects through the submucosal plane using diathermy to remove colorectal lesions en bloc; however this is technically challenging, time consuming and has a higher risk of perforation compared to EMR<sup>42</sup>. The role of real-time polyp diagnosis and tailored management strategies dependent on this are explored in more detail later in this thesis.

For the most part, curative strategies for colorectal cancer require resection of all cancer cells en bloc and is therefore most commonly achieved with surgical resection such as hemicolectomy. This can be augmented with oncologic therapies such as chemotherapy and/or radiotherapy, which can be administered pre-, intra- or post-operatively dependent on the disease stage or histological features of risk. As pre-operative staging with high resolution MRI for rectal cancer has improved, there is an increasing use of local excision rather than radical resection of the total mesocolon for early rectal cancers (radiologically T1 N0 M0)<sup>43,44</sup>. The capability for successful transanal local excision advanced significantly with the advent of transanal endoscopic microsurgery (TEMs), which uses a specially designed rigid endoscopic platform for access and resection<sup>45,46</sup>. Whilst TEMs is still used, transanal minimally invasive surgery (TAMIS) is a progression of the technique, where instead of using dedicated equipment, a hybrid approach is employed using similar instruments to those used in single incision laparoscopic surgery<sup>47</sup>. Local excision benefits from lower morbidity, mortality and length of hospital stay compared to radical resection, with a quality of life similar to healthy controls<sup>48,49</sup>; however, concerns have been raised regarding oncological outcomes. A database study from the USA has revealed a 5-year local recurrence rate of 12.5 *versus* 6.9% when local excision is compared to radical resection for stage I rectal cancers, with another study finding a reduced disease-specific survival<sup>50,51</sup>. The reasons for this have been hypothesized to be that local excision does not remove nodal micrometastasis (which is estimated to be 7-18% in T1 cancers) and that the R0 resection rate (cancer-free surgical margins) is lower than with resectional surgery<sup>44,51-54</sup>.

#### 1.1.5 Electrosurgery

Electrosurgery refers to the application of high frequency oscillating electric current to tissue in order to achieve a desired clinical effect, including haemostasis, tissue cutting and ablation<sup>55</sup>. Delivery of the current requires the formation of an electrical circuit, most commonly achieved using two electrodes (main and return). Monopolar diathermy integrates the main electrode into the surgical instrument, where the current passes through the patient to a broad pad used as the return electrode at a distant body site. Bipolar diathermy uses a surgical instrument containing both the main and return electrodes, for example forceps or scissors; with the current only passing through the tissue being manipulated. The nature of the electric current applied will influence the impact on tissues during electrosurgery, the most notable of which is the difference

between the modes of *cut* and *coagulation*. *Cut* uses continuous delivery of current with a sinusoidal waveform, creating significant heat to vaporise tissues, resulting in dissection. *Coagulation* mode uses a greater voltage however interrupts the delivery of current such that it is being applied for approximately 6% of the time, causing the formation of a coagulum due to the lower heat generation<sup>55</sup>. Furthermore, the magnitude of the power applied to the electro-surgical instrument (measured in watts) will relate to the degree of clinical effect.

Electrosurgical devices are indispensable tools used by clinicians for tissue manipulation and given the simple principles upon which they function, many different devices have been designed. Monopolar diathermy is the most ubiquitously applied electro-surgical technique in the management of patients with colorectal disease, with the handheld diathermy, TAMIS dissector and endoscopic snare being the three most commonly used devices (Table 1.1).

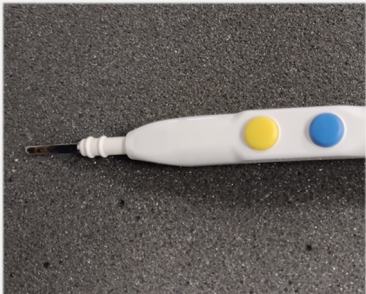
	Diathermy Pencil	TAMIS Dissector	Snare
Picture			
Description	Versatile handheld device with blade-style electrode most common	Laparoscopic instrument with a bent shaft of 5mm diameter and a pointed electrode tip	Retractable wire snare within a plastic sheath of 2-3mm diameter. The snare may be a single wire or braided, contain barbs and can open to varying shapes and sizes
Method of Use	Held like a pencil to apply current with the electrode tip. Finger switches to activate delivery of current in <i>cut</i> (yellow) or <i>coagulation</i> (blue) modes	Instrument passed transanally through a dedicated port with diathermy applied using a foot pedal	Passed down the working channel of an endoscope for snare deployment. Tissue is caught in the snare and diathermy applied during snare retraction. Activation is via a foot pedal
Clinical Indications	General purpose use in open surgery, including skin incision, tissue dissection and haemostasis	Used during TAMIS for dissection and haemostasis	Endoscopic mucosal resection (polypectomy)
Common Settings	25-30W	25-35W	15-25W

Table 1.1 – Design and clinical application for commonly used monopolar electro-surgical devices in management of colorectal disease.

## 1.2 Lipids and Cancer Metabolism

### 1.2.1 Common Lipid Structures

Lipids are organic biomolecules which are insoluble in water but can be dissolved in non-polar solvents such as ethanol and chloroform<sup>56</sup>. This broad group of molecules can be divided into eight categories based on the presence of ketoacyl and isoprene groups, of which three are the most biologically abundant and the focus of this thesis – fatty acids, glycerolipids and glycerophospholipids<sup>57</sup>.

Glycerolipids are characterized by a glycerol backbone of three carbon atoms, where groups can be esterified to the hydroxyl positions to create different complex lipids. Glycerophospholipids (GPLs) are where two hydroxyl groups are esterified by fatty acids ( $R_1$  and  $R_2$ ) and in the third position, a polar headgroup of an amino alcohol phosphate ester<sup>58</sup>. A large variety of alcohols can be substituted into the polar headgroup, which determines the subtype of GPL (examples given in figure 1.2). Furthermore, the fatty acids are commonly linear chains of between 12-22 carbons, with unsaturated versions having one or more C=C bonds (denoted as  $a:b$ , where  $a$  is the number of carbon atoms and  $b$  is the number of double bonds). Common glycerolipids without a phosphate ester linkage are the di- and tri- acylglycerols, containing two (DG) or three (TG) fatty acyl chains respectively.

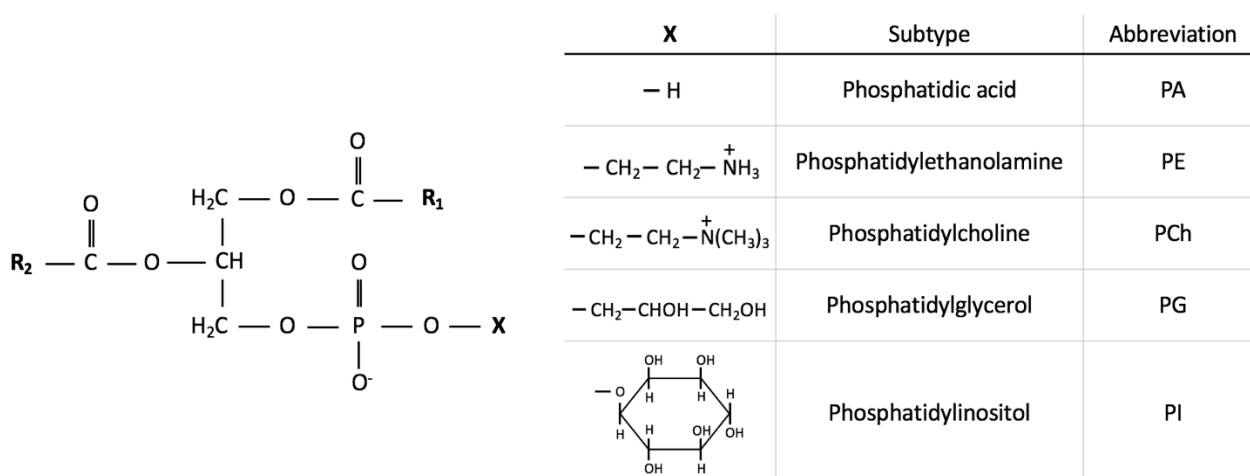


Figure 1.2 – The structure of glycerophospholipids, with the positions shown where fatty acyl chains ( $R_1$  and  $R_2$ ) and an amino alcohol ( $X$ ) can be substituted to change the subtype and molecular species of the lipid. Example headgroup substitutions are given in the inset table.

### 1.2.2 Normal Function and Metabolism of Lipids Within Cells

Lipids are abundant within mammalian cells, where they are responsible for a large variety of functions; most notably structure creation, signalling and energy provision<sup>59</sup>. 60% of cellular lipid mass is GPLs, which are largely located in bilayers to create the cellular membrane and intracytoplasmic organelles such as endoplasmic reticulum<sup>59</sup>. PCh, PS, PI and PE species are the most common GPLs in cell membranes, with a differential abundance between the inner and outer layer for both the GPL subtype as well as the saturation of FAs; due to the necessary interaction with cholesterol and membrane proteins to create structures such as signalling lipid rafts<sup>60,61</sup>. The role of lipids in energy creation is evident when examining their metabolism.

Lipids within the human body can be introduced through dietary intake or from *de novo* synthesis, which occurs mainly in the liver. *De novo* fatty acid biosynthesis is characterized by the creation of palmitic acid (16:0) through repeated condensations of acetyl groups from the TCA cycle by the fatty acid synthase enzyme (FASN). Chain lengths can be catabolized in the mitochondria or peroxisomes through a process called  $\beta$ -oxidation, where two carbon atoms are cleaved, producing acetyl-CoA which ultimately produces two ATP molecules following oxidative phosphorylation<sup>62</sup>. Considering the high number of carbon atoms in TGs that can undergo  $\beta$ -oxidation, they are a primary energy source for mammalian cells. Fatty acid chain elongation is again in multiples of two carbon atoms, where a four-step enzymatic process is initiated by a family of elongation of very long fatty acid (ELOVL) enzymes<sup>63</sup>. Desaturation (the creation of C=C bonds) can be performed by a family of enzymes named stearoyl-CoA desaturase (SCD)<sup>64</sup>.

### 1.2.3 Dysregulation of Lipid Metabolism in Cancer

A century ago, it was recognised that the metabolism of a tumour cell is vastly different to its normal counterparts. Otto Warburg was the first to describe how despite the presence of adequate oxygen, tumour cells preferably metabolise glucose using glycolysis rather than oxidative phosphorylation; despite this being less efficient<sup>65,66</sup>. As knowledge has progressed, transcriptional activation of oncogenes has been revealed to dramatically change the metabolism

of almost all biomolecules, including small metabolites, nucleotides, hormones, proteins, carbohydrates and lipids<sup>65</sup>.

When considering the key tenet of tumour cells – uncontrolled cellular growth and proliferation – it is possible to understand how regulatory changes to lipid metabolism may confer a selective advantage. Cell division is an energy intensive process which also requires *de novo* synthesis of fatty acids to be used in new lipid bilayers and as such, enzymes in the lipid biosynthesis pathway are commonly overexpressed<sup>67</sup>. This is driven by oncogenes such as p53 acting on the SREBP transcription factors, which impacts the expression of key enzymes such as FASN and SCD (figure 1.3)<sup>57,67,68</sup>. Furthermore, lipids are used by cancer cells for specific functions beyond energy generation and structural integrity. Examples include how FAs are used as ligands for nuclear receptors such as PPAR, PAs activate kinases used in intra-cellular signalling and sphingolipids impact the ability of cancer cells to migrate<sup>69-71</sup>. As such, lipid metabolic changes have been directly linked to differences in tumour cell proliferation, metastatic ability, avoidance of immune detection and resistance to apoptosis<sup>67,70,72-75</sup>.

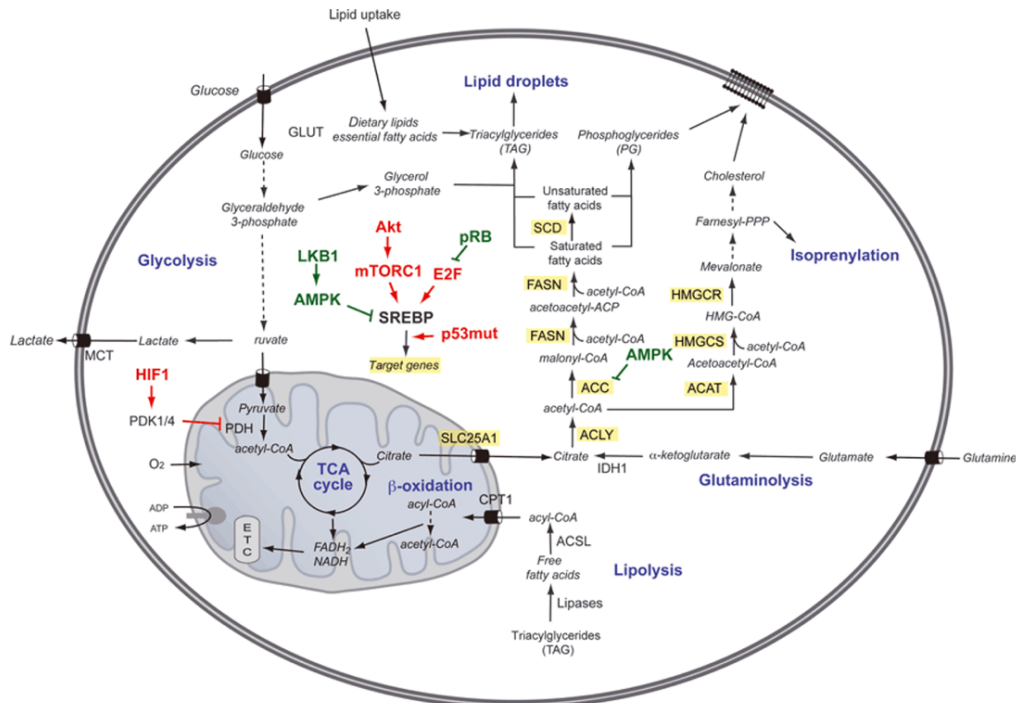


Figure 1.3 – Dysregulation of lipid metabolism in cancer cells, revealing how changes to SREBP transcription factors influences enzymes in the lipid biosynthesis pathway. Adapted with permission from Santos & Schulze<sup>67</sup>.

The dysregulation of lipid metabolism seen in carcinogenesis will inevitably impact the relative abundance of lipid species within cancer cells, even if the total lipid content may decrease<sup>76</sup>. Multiple studies have assessed this in CRC and whilst differences are commonly found when making comparisons to normal mucosa, the exact nature and extent of the differences varies between studies<sup>57</sup>. Table 1.2 details the differential abundance of certain lipid metabolites when comparing CRC to normal mucosa; demonstrating differences across lipid subtype and fatty acyl chain length.

Lipid Class	Structure	Relative Abundance in CRC	Study
Fatty Acids	14:0	Mixed findings	Mika <sup>77</sup> , Qiu <sup>78</sup> , Tian <sup>79</sup>
	16:0	Decreased	Mika <sup>77</sup> , Li <sup>80</sup>
	16:1	Mixed findings	Mika <sup>77</sup> , Zhang <sup>81</sup> , Qiu <sup>78</sup> , Tian <sup>79</sup>
	18:2	Mixed findings	Zhang <sup>81</sup> , Yang <sup>82</sup> , Mika <sup>76</sup>
	20:1	Increased	Guo <sup>83</sup> , Chen <sup>84</sup>
	20:5	Increased	Mika <sup>77</sup> , Yang <sup>82</sup>
Glycerophospholipids	PA(34:0)	Increased	Alexander <sup>85</sup>
	PA(34:2)	No change	Wang <sup>86</sup>
	PA(36:2)	Mixed findings	Wang <sup>86</sup> , Guo <sup>83</sup>
	PCh(32:1)	Increased	Kurabe <sup>87</sup> , Shen <sup>88</sup> , Wang <sup>86</sup>
	PCh(36:1)	Increased	Wang <sup>86</sup> , Guo <sup>83</sup>
	PG(38:4)	Decreased	Alexander <sup>85</sup>
	PE(36:1)	Increased	Wang <sup>86</sup>
	PE(36:2)	Increased	Wang <sup>86</sup>
Glycerolipids	PI(38:3)	Increased	Wang <sup>86</sup>
	TG(54:0)	Decreased	Alexander <sup>85</sup>
	Total TGs	Decreased	Mika <sup>76</sup>
Sphingolipids	DG(36:3)	Decreased	Alexander <sup>85</sup>
	SM(36:1:2)	Decreased	Wang <sup>86</sup>
	SM(40:1:2)	No change	Wang <sup>86</sup>
	Cer(34:1:2)	Increased	Wang <sup>86</sup>
	Cer(42:1:2)	No change	Wang <sup>86</sup>

Table 1.2 – a selection of lipid species found to have differential abundance when comparing CRC and normal mucosa from patients.

PA – phosphatidic acid; PCh – phosphatidylcholine; PG – phosphatidylglycerol; PE – phosphatidylethanolamine; PI – phosphatidylinositol; TG – triglyceride; DG – diglyceride; SM – sphingomyelin; Cer – ceramide.

#### 1.2.4 Lipid Abundance and Clinical Phenotype

Considering the composition of lipid molecules in a cell (coined the lipidome) is based on its underlying metabolic processes, this may be sufficiently unique that it could be characteristic of the cell type itself<sup>89</sup>. This link between cellular lipid composition and clinical phenotype is realised when considering that unique lipid signatures can be used to distinguish organ of origin and presence of different metabolic, degenerative and neoplastic diseases<sup>70,90,91</sup>. Therefore, a technique whereby the lipidome can be measured clinically may give data regarding the presence of neoplastic disease. In addition, there is the potential to inform on other clinically relevant features, such as whether the tumour is in the early or advanced stage<sup>80,81</sup> and whether DNA mismatch repair is deficient<sup>92</sup>.

#### 1.3 Metabolomics

Metabolomics is the comprehensive and quantitative study of all metabolites generated in a biological system, referred to as the metabolome<sup>93</sup>. This set of molecules can be considered the ultimate consequence and therefore a convergence point between all influences on the regulation of cellular metabolism, whether related to host biology or the environment<sup>94</sup>. These influences are often complex and dynamic systems themselves which can be intrinsically linked, including the host genome (DNA with its variants and mutations), the transcriptome (RNA transcripts of protein-coding and non-coding regions of DNA) the proteome (translation of RNA into polypeptides with consequent post-translational modifications into biologically active proteins), the microbiome (symbiotic and pathogenic organisms, of which just bacteria are of a similar number to human cells) and the chemical influence of the environment (such as toxins, diet and medications)<sup>93,95-98</sup>. Despite their interconnectivity, these systems are often analysed in isolation. This has yielded some success in increasing the understanding of human disease and the associated cellular processes, for example, transcriptomic studies of CRC have revealed how differential expression of genes promotes carcinogenesis, relates to disease stage and can impact recurrence and survival<sup>99-103</sup>. Genomic analyses have started to reveal the basis for the 35% of cancers believed to be caused by heritable genetic susceptibility, the cascade of cumulative DNA mutations required for carcinogenesis and describing how DNA stability impacts response to chemotherapeutics<sup>20,104,105</sup>. Attempts have been made to integrate several of these complex systems to develop a more

holistic understanding of biology and bridge the 'genotype-to-phenotype' gap, however this has been limited by incomplete understanding of each component and difficulties appreciating the impact of process variation on end function<sup>106,107</sup>.

Metabolites are the substrate of all metabolic processes such that they can be considered mechanistically linked to biochemical function and therefore, their relative abundance is intrinsic to cellular phenotype<sup>108</sup>. Metabolomics takes a systems biology approach, where large numbers of small metabolites in a relevant bio-sample (such as tissue, serum or urine) are measured and then statistically analysed to define the unique metabolic features associated with each phenotype. Differences in metabolite abundance can have many implications for human health and disease, where independent of whether they cause or are a consequence of the disease, they may be diagnostic (reveals presence of a pathology), predictive (forecasts response to treatment) or prognostic (insight into likely disease course). The profiling approach of metabolomics, where potentially thousands of diverse metabolites are measured to identify the few that are biologically relevant also benefits from the investigator not having to determine *a priori* which specific metabolites are of interest. As such, for pathologies where individual molecular biomarkers exist, metabolomics has been heralded as a promising discovery method<sup>109</sup>. In addition, for pathologies which share the same set of metabolites between groups with no novel biomarkers, metabolomics can assess how the fluctuations in their relative abundance correlate with disease phenotypes. By describing pathologies at such molecular resolution, researchers also have increasing ability to develop patient-specific diagnostics, monitoring and therapeutics; referred to as personalized medicine; which aims to optimise delivery of healthcare by reducing the impact of inter-patient variability<sup>110</sup>.

Untargeted metabolomics requires the totality of the metabolites within a sample to be analysed (even if their structure is unknown) however, no analytical platform currently exists which can achieve this<sup>110</sup>. Considering the total metabolome consists of molecules with a vast array of masses, chemical structures and physical properties; each technique developed to date demonstrates a bias towards certain sub-classes of metabolites based on its design, technical parameters and sample type used<sup>110,111</sup>. As a result, profiling metabolomic research often aims to be semi-targeted - the investigator decides the general sub-classes of metabolites that are of potential interest, before selecting one or more complementary analytical techniques (and their relevant technical parameters) which are best suited. Further considerations are that each

platform differs in the required sample size, method of sample preparation, cost, acquisition time, sensitivity and ease of metabolite identification<sup>112-114</sup>. In addition to Nuclear Magnetic Resonance (NMR) spectrometry, mass spectrometry (MS) has been at the forefront of metabolomic research<sup>115</sup>.

## 1.4 Mass Spectrometry

Mass spectrometry is a technique for metabolomic analysis which generates spectral data for molecules within a bio-sample in the form of a mass:charge ratio ( $m/z$ ) and a relative intensity<sup>116</sup>. The basic principle upon which this is achieved is by performing three processes in succession: ionisation, mass analysis and finally, detection.

First, metabolites within the analyte must be ionized to have a charge of integer value. Positive ions can be generated through protonisation (gain of  $H^+$ ), cationisation (gain of cations such as  $Na^+$  and  $NH_4^+$ ) or electron ejection. Negative ions can be generated through deprotonisation (loss of  $H^+$ ), decationisation (loss of cations such as  $CH_3^+$ ), anionisation (gain of anions such as  $Cl^-$  and  $HCOO^-$ ) or electron capture. Many ionisation techniques exist, with electrospray ionisation (ESI) and matrix-assisted laser desorption ionisation (MALDI) the most historically prominent. ESI passes a liquid analyte through a capillary tip subject to high voltages, creating an aerosol of charged droplets and after progressive evaporation of droplet solvent, the electric field strength reaches a critical point at which ions are ejected into the gas phase<sup>117</sup>. MALDI incorporates the analyte into a matrix of crystallised organic molecules, which are then excited by absorbing light from a laser, generating gas phase ions<sup>118</sup>. More recently, ambient ionisation techniques have been developed which do not require sample preparation and are therefore better designed for high-throughput or intraoperative use<sup>119</sup>. An example is desorption electrospray ionisation (DESI), which is a hybrid technique where a mist of charged solvent is pneumatically directed at a bio-sample, absorbing molecules of the analyte on impact and then releasing these as secondary ions in the gas phase<sup>120</sup>. Each ionisation technique and metabolite have unique physical and chemical properties, such that selection of an optimum technique requires consideration of metabolite patterns of ionisation, degree of analyte molecule fragmentation, charge number generation, optimal mass ranges, sensitivity and adaptability to MS<sup>121</sup>.

Once in the gas phase, ions are injected into the mass spectrometer where mass analysis can take place. Whilst many different approaches have been invented for this, they rely on the principle that ions move differently in magnetic or electric fields based on their  $m/z$  value. Four of the most common techniques for mass analysis are presented in Table 1.3. It has long been recognised that there is no single mass analysis technique which is superior for all uses<sup>122</sup>, however their strengths can be augmented and weaknesses limited through the use of hybrid technologies. One such hybrid uses a quadrupole immediately preceding a time-of-flight (TOF) analyser, known as a Q-TOF. Here, tandem MS can be conducted where the quadrupole is used for mass selection prior to fragmentation of the parent ion in a collision cell, with the fragments then entering the TOF for analysis across the whole mass range<sup>123</sup>. This complementary approach benefits from the high sensitivity of the quadrupole when selecting a single  $m/z$  and fast acquisition time with high mass accuracy using the TOF<sup>123</sup>.

Following mass analysis ions reach a detector, which registers the arrival of incident ions through their impact creating secondary electrons (which are then amplified) or by recording the current generated from the ion's moving electrical charge<sup>124</sup>. This allows formation of a mass spectrum, where the  $m/z$  ratios of detected ions can be plotted against the relative intensity, with the aim that this is closely representative of the relative intensity of the metabolites in the original bio-sample.

The vast potential number of molecules in a bio-sample undergoing analysis may create issues within the mass spectrometer. Ion suppression refers to biases in the ionisation efficiency due to other compounds that are present, whether they are part of the biological sample, additives (such as buffers) or contaminants (such as plasticisers from tubing)<sup>125</sup>. In addition, several distinct ions with similar  $m/z$  values arriving at the detector may cause peaks to overlap on the mass spectrum, causing a reduction in molecular specificity and ability to perform identification and quantification<sup>126,127</sup>. These errors can be addressed by performing a chromatography step prior to ionisation, as a method to separate complex matrices and reduce the number of species entering the mass spectrometer at each time point. One of the most popular techniques in metabolomic research is liquid chromatography (LC). In LC, a liquid bio-sample (or solution of extracted metabolites) travels through a column where the molecules separate based on an intrinsic physical or chemical property, such as polarity or hydrophobicity<sup>128,129</sup>. The compounds therefore elute into the mass spectrometer at different times and as a result, each ion detected will be

characterized by a retention time (time in the column until elution) and  $m/z$  ratio. This powerful technique can be used for complex samples containing a vast array of metabolite types (varying by biological class, polarity, volatility and mass), greatly reducing co-elution into the MS and its associated issues<sup>126</sup>. However, the addition of a chromatography step takes time (commonly 60 minutes) and requires significant sample preparation.

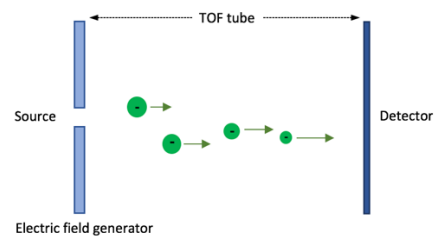
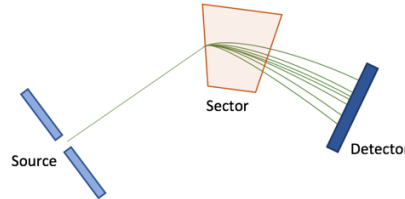
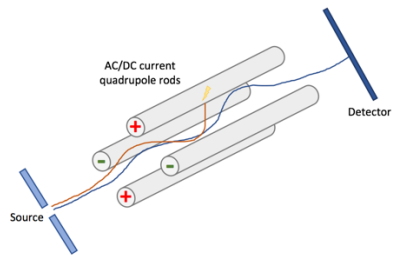
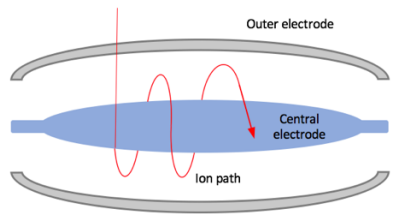
Design	Principle of Operation	Method for m/z Calculation	Diagram	Strengths	Weaknesses
<b>Time-of-Flight</b>	Ions are accelerated in a vacuum flight tube using an electric field of known strength, such that they all have the same kinetic energy. Given that kinetic energy is $\frac{1}{2}mv^2$ , lighter ions travel at a greater velocity than their heavier counterparts and reach the detector in a shorter time <sup>130</sup>	Travel time between ion source and detector		<ul style="list-style-type: none"> <li>- Large mass range</li> <li>- High mass resolution</li> <li>- Fast acquisition time</li> </ul>	<ul style="list-style-type: none"> <li>- Ion separation may be beneficial to avoid suppression at detector</li> <li>- High kinetic energies may cause fragmentation</li> </ul>
<b>Sector</b>	Static electric or magnetic fields are applied to differentially deflect the trajectory of ions according to their m/z ratio (lighter ions and those with higher charge will deflect to a greater extent than their heavier and less charged counterparts) <sup>131</sup>	Spatial differences between ions arriving at the detector		<ul style="list-style-type: none"> <li>- Very high reproducibility</li> <li>- High mass resolution and sensitivity</li> </ul>	<ul style="list-style-type: none"> <li>- Less well suited to pulsed ion sources</li> <li>- Larger and higher cost</li> </ul>
<b>Quadrupole</b>	Four parallel rods generate oscillating electric fields designed to stabilise or destabilise the spiral trajectory of ions based on their m/z ratio. Only ions with the selected m/z will pass through the quadrupole to the detector, with the others having unstable paths leading to collision with a rod and neutralisation <sup>123</sup>	Known relationship between electric fields and flight of ions with selected m/z		<ul style="list-style-type: none"> <li>- Low cost</li> <li>- 3 can be placed in series for tandem MS</li> </ul>	<ul style="list-style-type: none"> <li>- Low mass resolution</li> <li>- Low sensitivity when scanning large mass ranges</li> </ul>
<b>Orbitrap</b>	An electrostatic field is applied between a central spindle and a surrounding electrode, with ions 'trapped' in elliptical trajectories. Their axial oscillations are harmonic - it independent of all factors other than the m/z. Ions induce an image current on the outer electrode allowing mass analysis <sup>132</sup>	Fourier transformation of digitized image current		<ul style="list-style-type: none"> <li>- Small size</li> <li>- High mass resolution</li> <li>- Mass accuracy independent of dynamic range</li> <li>- Non-destructive ion detection</li> </ul>	<ul style="list-style-type: none"> <li>- Requires ultra-high vacuum</li> <li>- Higher mass resolutions require greater acquisition times</li> <li>- Spectra prone to artefacts</li> </ul>

Table 1.3 – Summary of four common techniques for mass analysis within a mass spectrometer.

*m* - ion mass; *v* - ion velocity

## 1.5 Rapid Evaporative Ionisation Mass Spectrometry

Rapid Evaporative Ionisation Mass Spectrometry (REIMS) is a technique first described in 2009, where aerosols containing biologically relevant molecules collide with a heated collision surface under ambient conditions, generating ions that can be injected directly into a mass spectrometer for analysis<sup>133,134</sup>. This approach benefits from not requiring sample storage or preparation, as it can be flexibly applied to continuously aspirate aerosols from a wide range of sources in real-time; most commonly electrosurgical devices, lasers and ultrasonic scalpels<sup>135</sup>. When coupled to a mass spectrometer designed for continuous ion injection (for example a TOF), it can create a rapid (and potentially high-throughput) platform for metabolite analysis and has been applied to tissue recognition, food safety, and microbiological detection<sup>136-138</sup>.

To date, REIMS has been most commonly paired with aerosols generated from electrosurgical dissection. The application of an electric current to tissue during electrosurgery causes Joule heating through dissipation with non-zero impedance, resulting in temperatures of 700-800°C, where intracellular water boils and cells explosively rupture<sup>133</sup>. This releases an aerosol of water droplets containing dissolved organic and inorganic components of the tissue, in addition to carbonized products from tissue burning<sup>139</sup>. This process also appears to create ions of tissue metabolites (both positive and negative), which can be within charged water droplets or as ionic clusters<sup>134,140</sup>. Surgical aerosols generated by electrosurgery are usually left to dissipate in the operating theatre or extracted using dedicated devices, however considering they contain biologically relevant molecules, could be used analyse the metabolome of the underlying tissue.

A schematic of the REIMS ion source coupled to an electrosurgical instrument can be seen in Figure 1.4. The surgical aerosol is delivered to the source via a sample inlet tube, with a Venturi pump used to generate a sufficient negative pressure for timely delivery. An organic solvent such as isopropanol may also be co-aspirated with the surgical aerosol through an orthogonal additional inlet, as this has been demonstrated to increase the signal intensity by a factor of 2<sup>141</sup>. This matrix is directed using a transfer capillary towards a ceramic coil heated to 900°C, which acts as the collision surface. Upon impact, the ion-containing water droplets and ionic clusters in the aerosol release singly molecular ions in the gas phase, with some neutral species also ionized at this stage<sup>141</sup>. A stepwave ion guide then separates charged ions from neutral compounds and contaminants (such as carbonized material) and directs the ions to the MS for mass analysis<sup>142</sup>.

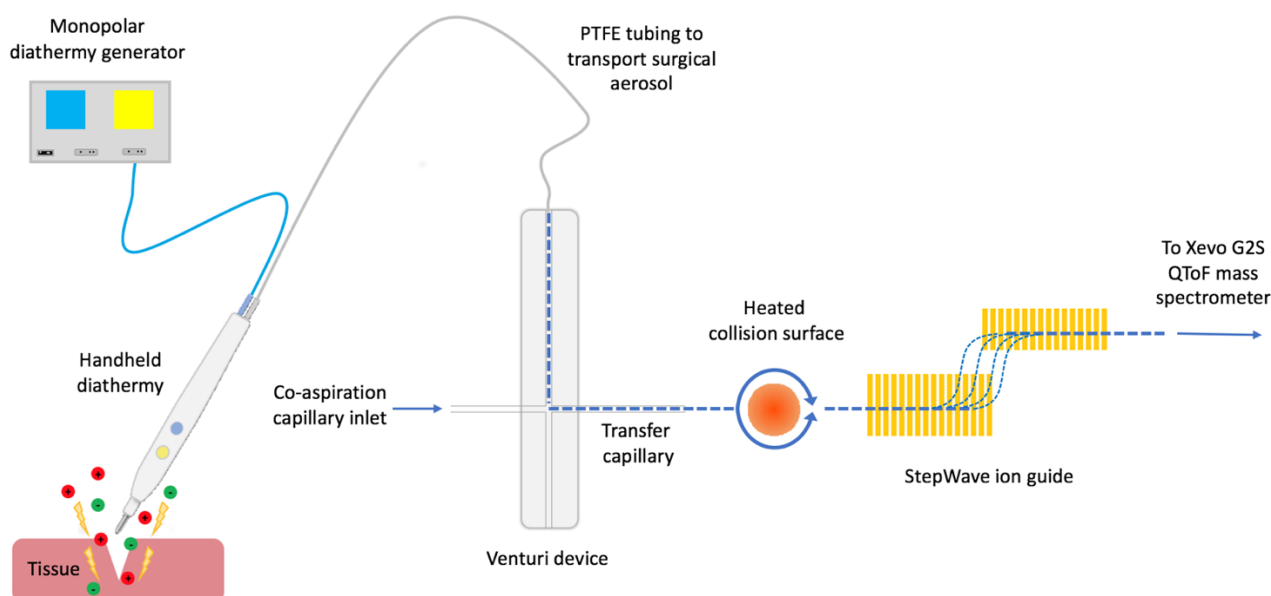


Figure 1.4 – schematic of a monopolar electrosurgical device coupled to a REIMS source. This demonstrates how the surgical aerosol is generated from tissue heating and is transported to the REIMS interface via PTFE tubing, powered by a Venturi device. The aerosol is then directed through a transfer capillary against a 900°C collision surface, generating gas-phase ions. Ions are then directed using a StepWave before injection into the mass spectrometer. The dashed blue line represents the path of the aerosol and ions (before and after the collision surface respectively).

Lipids have been demonstrated to be the most effective class of molecule for metabolomic analysis of tissues using REIMS. This is likely due to several factors including that they are the most abundant metabolite class, do not denature at the temperatures applied by the electrosurgical devices (unlike proteins for example), are often charged under physiological conditions, do not easily fragment (conserving them from tissue to spectrometer) and as previously described, their metabolism is markedly impacted by the tissue type and in conditions of interest such as cancer<sup>89,141</sup>.

## 1.6 Tandem Mass Spectrometry and Metabolite Identification

When a lipid ion is submitted to conditions where there is sufficient energy to disassociate bonds and fragment the molecule into product ions, the pattern and position of this fragmentation occurs in a predictable manner<sup>143</sup>. Considering this, and that complex lipids are relatively simply

categorised based on their functional headgroup and fatty acyl chains, this creates an opportunity to use ion fragmentation as a method of structural identification for molecules of interest.

This can be achieved by aligning two mass analysers, for example a single quadrupole which feeds into a TOF via a collision cell; hence the term 'tandem' MS (or MS/MS). First, it is necessary to identify in advance the  $m/z$  value of an ion that requires structural identification (referred to as the precursor or parent ion and is determined from statistical analyses). The quadrupole can then be used as a mass selector, where only ions of that  $m/z$  value coming from the source will be able to traverse the quadrupole. The parent ion will then enter the collision cell, where a technique will be used to cause fragmentation, commonly the bombardment with argon atoms (coined collision-induced dissociation). The resulting product ions are then injected into the TOF, where their  $m/z$  values are calculated.

A representative MS/MS spectrum can be seen in figure 1.5, which demonstrates the fragmentation of a parent ion with 747.52  $m/z$  in negative mode, in addition to the chemical structure with the likely points of bond disassociation. This typical pattern of fragmentation is often seen with many classes of glycerophospholipids and consists of fatty acid loss from the headgroup. As such, headgroup peaks can be very specific and characteristic of a lipid class, such as at 140.01 $m/z$  for ethanolamine phosphate ion, 245.04  $m/z$  for glycerophosphoglycerol ion or 168.04  $m/z$  for a demethylated phosphocholine. Fatty acyl loss will have a peak from the free ion (generally within the range 240-300  $m/z$ ), however neutral fatty acyl loss or loss as a ketene from the parent ion may also be seen. Therefore, identifying the likely structure of these fragments can assist in determining the identification of the parent metabolite.

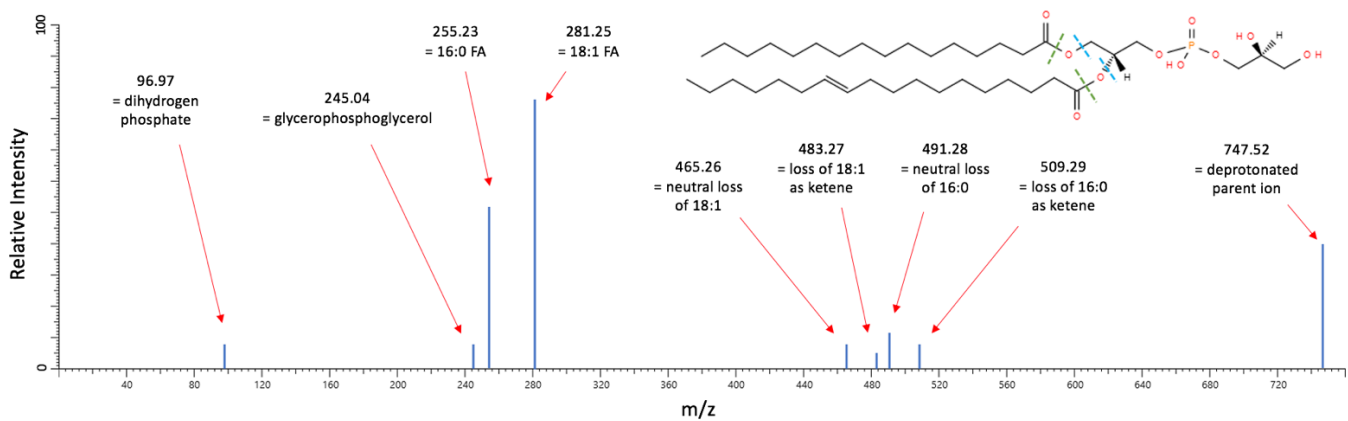


Figure 1.5 – representative MS/MS spectrum demonstrating typical negatively charged product ions seen from fragmentation of PG(16:0/18:1), with the molecular structure presented (inset). The most common sites of fragmentation are annotated (dashed lines), with the green lines producing loss of fatty acid as a ketene and blue lines producing neutral loss of fatty acid.

Four levels currently exist for metabolite identification<sup>144</sup>:

1. Identified metabolites - where two pieces of independent and orthogonal data (such as retention time and mass spectrum) have been directly compared to a chemical standard
2. Putatively annotated compounds - based on their physicochemical properties or spectral similarity with reference databases including METLIN<sup>145</sup> and LIPID MAPS<sup>146</sup>
3. Putatively characterized compound classes – as per level 2 but pertaining to a class of metabolite
4. Unknown compounds – whilst not identified these compounds can still be differentiated from others based on their spectrum

It is evident that MS/MS has a crucial role in reliable metabolite identification, however it may not always be able to provide level 1 identification even when chemical standards are used. MS/MS using a qToF from a REIMS source will not provide a retention time and therefore which fatty acyl chain is attached to the R<sub>1</sub> and R<sub>2</sub> positions (*sn*- isomerization), the location of double bonds within an acyl chain and *cis/trans* isomerisation at the double bonds cannot be reliably identified<sup>147,148</sup>. Additionally, chemical mixtures of precursor ions with sufficiently similar *m/z* values to traverse the quadrupole will hamper efforts to determine the parent ion for each distinct fragment.

## 1.7 REIMS Data Handling and Analysis

As REIMS does not have a chromatography step, the raw data for each analysis can be represented as a single mass spectrum in terms of  $m/z$  against intensity (figure 1.6). In order to create data most optimal for statistical analyses, where the impact of systematic errors and random noise are minimised, the raw data requires transformation through several pre-processing stages:

1. Background subtraction. Random signal from the instrument detector and background contaminants (for example from tubing) do not contain biological signal and therefore can be defined and subtracted from the spectrum
2. Lock-mass correction. The  $m/z$  values registered by the detector will undergo calibration prior to each analytical run, however this can be slightly different between days and there can also be mass drift in the hours following calibration. This can be addressed using a lock-mass standard of known  $m/z$  which is either in the bio-sample or is added during analysis, such that errors in the detected  $m/z$  can be measured and the whole spectrum corrected accordingly
3. Binning. This reduces the dimensionality of data by applying an intensity to equally spaced intervals ('bins') throughout the range of  $m/z$ , ideally having each metabolite falling solely within each bin. This process also helps mitigate for small mass drifts between analyses
4. Normalisation. There can be marked variation in the total ion current (TIC) between analyses, which may bias results if not corrected. This can be achieved through normalisation of each spectrum, such that metabolites are described using relative intensities

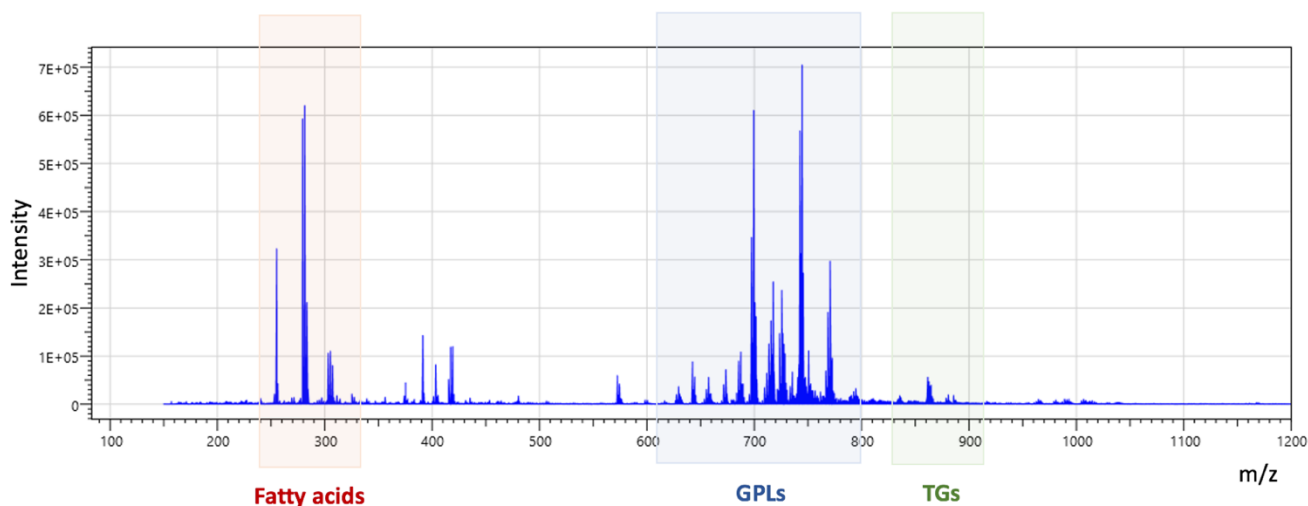


Figure 1.6 – a representative mass spectrum, where 150-1200 m/z is plotted against intensity. The m/z ranges in negative mode where fatty acid (red), glycerophospholipid (GPL; blue) and triglyceride (TG; green) metabolites are commonly found are highlighted.

## 1.8 Statistical Principles and Techniques

Untargeted metabolomics is used for the purposes of hypothesis generation, where the investigator is simultaneously exploring an array of known and unknown metabolic processes<sup>149</sup>. It often uses an approach termed ‘metabolic fingerprinting’. This refers to using a set of descriptive and predictive modelling techniques to compare the relative metabolic differences between normal and perturbed systems, where the perturbation can be any clinically relevant disease phenotype<sup>150,151</sup>. The statistical models can also be used to make predictions of sample classification and therefore these metabolic fingerprints can be used for diagnostics; where metrics such as diagnostic accuracy, sensitivity or specificity can be defined. In order to achieve this, spectra must be ‘annotated’ with high-quality and validated clinical metadata, such as patient demographics, disease severity according to established criteria, radiological images and histological diagnosis of the bio-sample.

The relative metabolic differences between disease states generated from this profiling approach can be used to infer a biological basis for the changes and as such, would generate a hypothesis for future hypothesis-driven targeted studies. This work will explore the techniques used for profiling and the methods of hypothesis generation.

### 1.8.1 Unsupervised Methods

Unsupervised statistical techniques manipulate and analyse metabolomic data without reference to the underlying class of the samples. This multivariate approach is used to provide an initial simplification of the data, allowing detection of general patterns such as variation by a biological or technical factor<sup>116</sup>.

Principal Components Analysis (PCA) is the most common method for unsupervised analysis, where the dimensionality of complex data is reduced to explore the variance across a dataset with minimal data loss, assisting in processes such as outlier detection and visualization<sup>152</sup>. This is achieved by creating a series of orthogonal linear vectors as functions of the metabolite intensities measured, which are designed to reflect the maximum variance between samples<sup>153</sup>. As additional vectors (or 'components') are added to the model, a greater proportion of the total variance will be addressed, and therefore a small number of principal components (PCs) may account for the large majority of a dataset's total variation.

Two or three PCs can be graphed against each other to generate a PCA loadings plot (in two or three dimensions respectively), as demonstrated in figure 1.7. In order to visualise the greatest variance, the PCs are graphed in succession starting with PC1. Given that PCA is unsupervised, it will only reveal clustering by group when the inter-group variance is greater than the intra-group variance and therefore lack of clustering does not imply insignificant inter-group variance (the biological signal the investigator will want to assess). Outliers can be identified visually or using a statistical test such as Hotelling's  $T^2$  to create a boundary outside of which outliers will fall<sup>154</sup>.

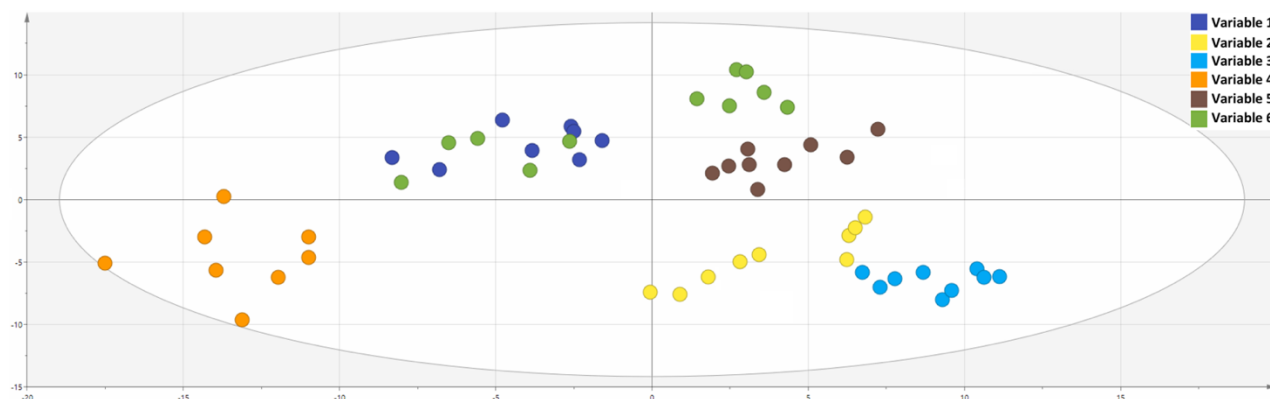


Figure 1.7 – representative PCA of six variables demonstrating a variety of intra- and inter-group variation and clustering.

### 1.8.2 Supervised Methods

Supervised statistical analyses identify the metabolic features which are most able to discriminate spectra based on the group or class of interest, whilst minimizing other sources of variation<sup>116</sup>. This can be used to create models able to predict the class of hitherto unknown spectra based on metabolite abundances and therefore can be applied to diagnostics and classification problems. Its strength lies in the fact that it can identify subtle relationships buried in large datasets whilst discounting other effects and correlations present (such as differences between study subjects unrelated to the disease of interest)<sup>155</sup>.

Partial Least Squares Discriminant Analysis (PLS-DA) is a regression-based technique to fit multivariate metabolic data to a categorical outcome, for example, the presence or absence of a disease. It involves creation of PLS components, which are subspace linear explanatory variables aiming to maximise the covariance between the independent and dependent variables<sup>156</sup>. These explain how the metabolic data maps to the outcome of interest through the subspace. One limitation of PLS-DA is that some features that are not correlated with the outcome may impact the model and to address this, an orthogonal component may be added (OPLS-DA)<sup>116</sup>. In OPLS-DA, the data variance is expressed as two values, one which directly contributes to the outcome and another which does not (and is assigned orthogonally); and similarly to PCA, these components can be graphed on a scores plot. The PLS-DA approach benefits from transparency regarding the relative importance of different metabolic features in the predictive ability of the model, through values such as the Variable Importance in Projection (VIP).

Linear Discriminant Analysis (LDA) has similarities with PCA in that it involves the creation of linear components however these are not orthogonal to each other and given that this is a supervised method, will maximise variance by group. It is a recognised limitation of LDA that the predictive ability is compromised if the variables significantly outnumber the observations (as is common with metabolomic data) and as such, it is often preceded by PCA as a method to reduce the number of input variables<sup>157</sup>. Metrics can be applied to LDA models to describe how well they fit the data, including  $R^2$  (the variation in the model explained by the variables, scaled from 0-1) and  $Q^2$  (an estimate of predictive ability using a cross validation technique and calculating the residual sum of squares, scaled from 0-1).

Once an LDA model has been plotted, unknown spectra can be classified by determining their location on the plot and calculating a distance to the centroid of each group cluster. This is weighted by the variance of the variables and known as the Mahalanobis distance, where the class is assigned where this is the shortest<sup>158</sup>. A consequence of this is the creation of a linear decision line (hence *linear* discriminant analysis), which separates the regions of the plot where each group will be assigned. The Mahalanobis distance can also be used for detection of outliers, where the mean distance and standard deviation for a group is calculated and then a threshold for maximum distance is defined as a multiple of the standard deviation from the mean<sup>159</sup>.

### 1.8.3 Cross Validation and Diagnostic Accuracy

Once a model has been created to predict a dependent variable such as through LDA, it is necessary to assess the model's accuracy. Ideally, this is achieved by determining a training dataset, upon which the model is trained and then a separate (ideally from a distinct patient cohort) validation dataset, to assess its predictive ability. Whilst this process mitigates against biases in the training dataset artificially increasing its perceived accuracy, it is also a powerful technique to assess for (and therefore take steps to avoid) over-fitting of the model. Over-fitting refers to when a model has over-utilised both the random noise and biological signal within a dataset, where relationships identified are not generalizable and therefore the goodness of fit (or  $R^2$ ) is inflated<sup>160</sup>. This is a particular concern with metabolomic datasets as they have high numbers of variables compared to observations, giving a relatively large amount of data with which models can over-fit. As additional components are added to model and it becomes over-fitted the  $Q^2$  will start to fall and as such, no additional increase in  $Q^2$  when a new component is added can be used as mark to avoid over-fitting<sup>161</sup>.

When a validation dataset is not available, internal cross validation (CV) can be conducted, where the single dataset can be partitioned into its own training and validation sets<sup>161</sup>. A common approach is to use  $k$ -fold CV, where the dataset is randomly divided into  $k$  approximately equal sections, where  $k-1$  are used to generate a model which is tested on the remaining portion; a process which is then repeated  $k$  times so each partition of the data has been used as the test set once. Metabolomic data often has several observations for each patient and therefore it is desirable to ensure that a single patient's data are not spread across the training and test sets, as

for example, similarities in spectra from the same patient could influence the model<sup>162</sup>. This can be achieved using leave-one-patient-out CV (LOPO CV), which is similar to  $k$ -fold however each data partition is that of each patient. This approach benefits from being more suitable to datasets where there is significantly less observations than variables, it reflects the real-world application of the models (as they will be exposed to each new patient in turn) and it is likely to have a reduced bias in estimating the model error compared to  $k$ -fold<sup>163</sup>.

During the test phase of CV, the predictive ability of the model is determined by describing the number of true positive, true negative, false positive and false negative predictions; which can then be formulated into a confusion matrix and used to calculate relevant metrics of diagnostic accuracy (figure 1.8). Furthermore, as the threshold for determining whether a test returns a positive or negative result can be changed, plotting sensitivity against 1-specificity for all thresholds reveals a receiver operating characteristic (ROC) curve, where the area under the curve can be used as an accuracy metric<sup>164</sup>.

		<b>True</b>		
		Positive	Negative	
<b>Predicted</b>	Positive	$a$	$b$	<b>Sensitivity</b> = $a/(a+c)$
	Negative	$c$	$d$	<b>Specificity</b> = $d/(d+b)$
				<b>Positive Predictive Value</b> = $a/(a+b)$
				<b>Negative Predictive Value</b> = $d/(d+c)$
				<b>Accuracy</b> = $(a+d)/total$
	$a$ = true positive		$c$ = false negative	
	$b$ = false positive		$d$ = true negative	

Figure 1.8 – a representative 2x2 confusion matrix, denoting how common metrics of diagnostic accuracy are calculated.

#### 1.8.4 Tissue Recognition

Following *ex vivo* data collection and formation of a high-quality spectral database with clinical annotation, models can be created to predict any characteristic associated with each spectrum, including the ability to recognise different tissue histological subtypes (for example, colorectal

normal, adenoma and carcinoma). The ability of a predictive model to classify a new spectrum is not computationally demanding and can be conducted in a fraction of a second. As a result, models can be loaded into a graphical interface and feedback can be given to a surgeon in real-time (2-3 seconds) during application of the energy device<sup>137</sup>. This provides the basis for translation of metabolomic technologies into clinical settings, where intraoperative decisions can be made based upon the histological subtype of the tissue encountered.

#### 1.8.5 Univariate Methods

In addition to feature extraction from predictive models using techniques such as the VIP score, differential relative abundance of metabolites between groups of interest can be determined using simple statistical processes. A t-test compares the means of a continuous variable in two independent parametric datasets and is able to give the probability that these are from the same overall distribution<sup>165</sup>. Analysis of variance (ANOVA) is able to compare more than two groups simultaneously (in a similar fashion to performing repeated t-tests) and will reveal if at least one group's mean is different; requiring further tests to determine where that difference is found.

Whether differences are deemed statistically significant or not are based on a threshold  $\alpha$ , which is the probability of rejecting the null hypothesis when it is in fact true. Historically for biomedical research, this is set at 0.05 (corresponding to a 95% chance of true effect), however, considering many thousands of metabolites may be compared in metabolomic datasets, multiple testing dramatically increases the probability of incorrectly rejecting the null hypothesis by chance (referred to as a type I error)<sup>160</sup>. This can be addressed by correcting the  $p$  value when performing multiple testing, using techniques such as the Bonferroni correction and Benjamini-Hochberg procedure. Debate exists as to which technique is optimal, with the Bonferroni correction generally considered more conservative<sup>153,160,166</sup>.

## 1.9 Tissue Recognition using Mass Spectrometry

### 1.9.1 REIMS

The initial validation work of REIMS studied a variety of animal tissues, primarily porcine and murine models; demonstrating that REIMS generates rich biological data, particularly in the lipid region. The large number of metabolites detected were analysed using supervised and unsupervised techniques, showing that cellular lipid composition was able to differentiate tissues by species, in addition to anatomical locations within species with high levels of accuracy<sup>133,134</sup>.

Studies which demonstrate the use of REIMS in recognition of human tissues are presented in table 1.4. The technology has been applied across multiple organ systems using a monopolar handpiece (referred to as the 'iKnife'), monopolar endoscopy snare and bipolar forceps. The majority of the focus has been the ability of REIMS in differentiating cancerous from pre-cancerous and normal tissues, with initial diagnostic accuracies showing promise. The approach has tended to be the creation of a validated spectral databases *ex vivo* and then generating diagnostic accuracy metrics using LOPO-CV or more robustly, a distinct validation cohort (whether *ex vivo* or *in vivo*). Both of these approaches showed that during the validation, REIMS appears to be consistent with its diagnostic accuracies. Colorectal tissue constitutes approximately 30% of the samples analysed to date, with its *in vivo* application (at open and endoscopic surgery) being limited largely to proof-of-concept studies. *Ex vivo*, REIMS of colorectal tissue has some degree of diagnostic accuracy, however, appears limited by false negatives for cancer in the range of 3-21%.

Many studies describe the lipid features that are responsible for differentiating pathological subtypes of tissue, which is most commonly achieved by cross-referencing the exact mass with known lipids; however, some studies did perform selected tandem MS. It is challenging to identify trends in how complex lipid metabolism changes with the development of cancer considering the range of organs analysed and the relative sparseness of metabolites identified. Certainly, there is no clear evidence of single biomarkers which can be used as simple diagnostic tools. One of the challenges in metabolite identification with the REIMS studies is that the ionisation method appears to commonly cause adducts and loss of small function groups, although this may be related somewhat to the class of lipid<sup>133,167</sup>. Adducts include chloride (Cl<sup>-</sup>, additional mass of 35Da,

seen in PChs and TGs) and function group loss including ammonia ( $\text{NH}_3$ , mass loss of 17Da seen particularly with PEs) and methyl ( $\text{CH}_3$ , mass loss of 15Da seen particularly with PChs).

Author	Year	Energy Device	Mass Analyser	Analysis Location	Patients (n)	Tissue Analysed	Pathological Subtypes	Accuracy for Tissue Recognition	Other Findings
Balog <sup>137</sup>	2013	Pencil monopolar diathermy and bipolar forceps	Quadrupole	<i>ex vivo</i>	302	Liver, lung, colon, stomach, breast, brain	Carcinoma, inflammatory, normal	70-98% accuracy for recognition of cancer, 0-8% false negative rate, 80-100% accuracy for normal	Able to differentiate some cancer subtypes
Balog <sup>137</sup>	2013	Pencil monopolar diathermy and bipolar forceps	Quadrupole	<i>in vivo</i>	81	Liver, lung, colon, stomach, breast, brain	Carcinoma, normal	98% sensitivity, 97% specificity for cancer tissue recognition	REIMS identified benign tissue in 9 cases where pre-operative biopsy implied cancer
Alexander <sup>85</sup>	2017	Handheld pencil monopolar diathermy	TOF	<i>ex vivo</i>	26	Colorectum	Carcinoma, adenoma, normal	94% accuracy distinguishing three tissue types, 79-92% NPV for cancer	Proof of concept for endoscopic collection. Ceramide and TGs differentiating groups. Some ability to distinguish cancers by histological features
Phelps <sup>168</sup>	2018	Handheld pencil monopolar diathermy	TOF	<i>ex vivo</i>	192	Fallopian tube, ovary, peritoneum	Carcinoma, normal	98% accuracy distinguishing four tissue types, 90% accuracy for borderline vs true ovarian cancer	Proof of concept for <i>in vivo</i> collection in 6 patients but no accuracy data.
Balog <sup>169</sup>	2015	Endoscopic snare, monopolar	TOF	<i>ex vivo</i>	25	Stomach, colorectum	Carcinoma, adenoma, normal	No accuracy given	Gastric: increased TGs and PIs in submucosa, plasmalogens depleted in cancer. Colorectum: heterogeneity in lipid metabolism within adenomas
Balog <sup>169</sup>	2015	Endoscopic snare, monopolar	TOF	<i>in vivo</i>	3	Colorectum	Adenoma, normal	2 colon polyps correctly identified as benign	Lipid metabolism differed along the normal colorectum. Polyps were
St John <sup>167</sup>	2017	Handheld pencil diathermy	TOF	<i>ex vivo</i>	113	Breast	Carcinoma, normal	Test set: 95% accuracy, 97% NPV for cancer	Slightly improved accuracy using <i>cut</i> rather than <i>coagulation</i> mode
St John <sup>167</sup>	2017	Handheld pencil monopolar diathermy	TOF	<i>ex vivo</i>	Unknown	Breast	Carcinoma, normal	Validation set: 96% accuracy, 95% NPV for cancer	-
St John <sup>167</sup>	2017	Handheld pencil monopolar diathermy	TOF	<i>in vivo</i>	6	Breast	Normal	No accuracy given	Proof of concept for <i>in vivo</i> sampling, showing high quality spectra with 0.7% outliers

Table 1.4 – selected study cohorts where REIMS has been used for human tissue recognition

TOF – time of flight; NPV – Negative Predictive Value; TG – triglyceride; PI – phosphatidylinositol

### 1.9.2 Alternative Technologies for Intraoperative Use

Beyond REIMS, a variety of ambient MS technologies have been invented and assessed for differentiation of tissue pathological subtypes both *ex* and *in vivo*<sup>170</sup>. The devices which have shown the most promise as a translatable MS technology for use on solid tissue intraoperatively, particularly with a focus on colorectal tissue recognition, are summarised in table 1.5. It is apparent that whilst these technologies have been applied to a variety of cancer types, they have been almost entirely *ex vivo*, with very little *in vivo* translation. Furthermore, the patient numbers are low (often less than 20), with almost no diagnostic accuracy presented and very little application to colorectal tissues. Lipids were the class of metabolites studied across all studies with glycerophospholipids of highest intensity. The lack of *in vivo* translation may be due to the design of some platforms and their lack of suitability for intraoperative use. An example would be DESI, which requires optimised sprayer geometry for metabolite ionisation and retrieval; and is therefore most prominently used for imaging when tissue sections can be cut<sup>171</sup>. Probe-based technologies which require placement on tissue to conduct analysis will interrupt the surgical process and increase operative time, the impact of which cannot be fully assessed from such pilot data. Conversely, those that contemporaneously analyse the products of surgical dissection (including REIMS), are by definition coupled to a destructive technology, where diagnostic application on normal tissue may cause additional damage.

### 1.9.3 Requirements for Future Technologies

Successful translation of MS technologies to support clinical decision making (such as the ‘resect and discard strategy’) places certain efficacy, logistic, safety, acceptability and economic demands on a platform. From the perspective of the clinical team, the greatest priority is patient safety, followed by the need for a platform which can seamlessly and reliably integrate into clinical pathways, to deliver clinically relevant information which will synergise with their expertise to generate improvements in patient outcome. The technology will therefore need to be proven to demonstrate a consistently high level of accuracy in clinical settings, analysing unprepared tissue rapidly and objectively, whilst being flexible to couple to devices and interfere as little as possible with the clinical process. The operator’s learning curve must be short, with a clear decision-making support structure to enable real-time decisions that improve patient care. Logistically, this needs

to be achieved using a platform which is not burdensome to set-up and operate, which requires little maintenance and does not cause significant delays to care. The use of machine learning algorithms to make decisions impacting delivery of care may cause concern for both patients and clinicians, where it raises both ethical and legal concerns. Finally, most healthcare systems globally have finite resources and the MS technology should therefore be able to make a compelling business case for its implementation.

Technology	Details of Operation	Colorectal Trial Use	Other Use	Key Findings	Limitations
Desorption electrospray ionisation (DESI) <sup>172</sup>	Pneumatic electrospraying of solvent onto tissues and collection of secondary droplets containing ionised metabolites. Endoscopic DESI probe with 4m transfer tube can be used	<i>Ex vivo</i> proof-of-concept in murine model	-	<ol style="list-style-type: none"> <li>1. Adequate transfer efficiency to sample lipids through colonoscope but low TICs</li> <li>2. High relative intensity of FA oligomers from intestine</li> </ol>	<ol style="list-style-type: none"> <li>1. Organic solvents are toxic and cannot be used <i>in vivo</i></li> <li>2. Optimised for sections on stable stage where sprayer mechanics can be controlled</li> </ol>
MasSpec Pen <sup>173,174</sup>	Handheld probe placed on tissue where 4-10µL water droplet used to extract metabolites from tissue surface before being retrieved. Total analysis time of 10s	-	Thyroid, breast, lung, ovary <i>ex vivo</i> , murine breast PDX <i>in vivo</i>	<ol style="list-style-type: none"> <li>1. Rich biological information with minimal tissue damage</li> <li>2. Overall accuracy differentiating cancer and normal of 96.3% after CV</li> </ol>	<ol style="list-style-type: none"> <li>1. Lipophobic solvent (water) generates low TICs when fat composition high</li> <li>2. Vacuum may cause aspiration of contaminants such as blood on tissue</li> </ol>
Laser desorption ionisation <sup>175</sup>	CO <sub>2</sub> and Nd:YAG surgical lasers cause explosive cell rupture through heating, releasing an aerosol containing ionised metabolites	<i>Ex vivo</i> carcinoma as liver metastasis	-	<ol style="list-style-type: none"> <li>1. Detects free FAs and GPLs</li> <li>2. Some differentiation of CRC from normal liver on PCA</li> </ol>	<ol style="list-style-type: none"> <li>1. Lasers are not commonly used in many surgical specialities</li> <li>2. Cost for infrastructure and laser equipment</li> </ol>
Probe electrospray ionisation <sup>176-179</sup>	Oscillating solid needle probe picks up bio-sample from tissue surface and then undergoes electrospray when retracted	<i>Ex vivo</i>	Renal cell carcinoma and HNSCC <i>ex vivo</i>	<ol style="list-style-type: none"> <li>1. Wide range of lipid metabolites identified</li> <li>2. Can differentiate CRC from normal on PCA and HNSCC from normal using LDA</li> </ol>	<ol style="list-style-type: none"> <li>1. Only 40pL of fluid bio-sample can be analysed each minute, causing generally low TICs</li> <li>2. More suited to liquid bio-samples</li> </ol>
SpiderMass <sup>180,181</sup>	Nd:YAG laser in infrared region used to excite vibrations in O-H bond in tissue water, with the water acting as an endogenous matrix	-	Ovarian <i>ex vivo</i> , canine <i>in vivo</i>	<ol style="list-style-type: none"> <li>1. Lipid metabolites detected across large m/z range</li> <li>2. Up to 500µm tissue depth analysed with little damage</li> </ol>	<ol style="list-style-type: none"> <li>1. 30s acquisition time</li> <li>2. Platform has limited degrees of freedom</li> <li>3. Very little diagnostic accuracy data</li> </ol>
CUSA with Sonic Spray <sup>182</sup>	Ultrasound waves transmitted by water jet cause mechanical tissue disintegration and nebulisation of metabolites where they can be ionised	-	<i>Ex vivo</i> liver, breast and brain	<ol style="list-style-type: none"> <li>1. Negative ion mode produced greater variety of lipid metabolites</li> <li>2. Normal liver from metastasis differentiated on PCA</li> </ol>	<ol style="list-style-type: none"> <li>1. Tissue debris may block tubing or inlet capillary</li> <li>2. Full spectral information requires at least 500µg tissue</li> </ol>

Table 1.5 – mass spectrometric technologies other than REIMS which can be used to differentiate cancerous from normal tissues without sample preparation and with the potential to be applied *in vivo*.

TIC – total ion current; FA – fatty acid; PDX – patient-derived xenograph; CV – cross validation; HNSCC – head and neck squamous cell carcinoma; PCA – principal components analysis; LDA – linear discriminant analysis; CUSA – Cavitron ultrasonic surgical aspirator

## Chapter 2 – Optical Technologies for Endoscopic Real-Time Histological Assessment of Colorectal Polyps: A Meta-Analysis

### 2.1 Introduction

Polyps of the colorectum that may be encountered during colonoscopy can confer a wide variety of clinical risk to the patient depending on the histological subtype. The current gold standard approach for polyp assessment is histopathological analysis following EMR, however, this takes greater than one week to report and as a consequence; clinical management pathways must be applied *post hoc* (largely through determining surveillance intervals).

There is a need for real-time (intra-procedure) technologies to be applied endoscopically in order to accurately determine polyp histological subtype *in vivo* and allow personalized decision-making for necessary interventions. This has the potential to confer several benefits. First, 43% of resected polyps are benign and therefore an unnecessary EMR exposes the patient to additional risks such as perforation and bleeding (at 1.4% and 3.5% respectively)<sup>183,184</sup>. An effective “diagnose and leave” strategy, particularly for benign hyperplastic polyps of the recto-sigmoid, would be successful in mitigating these risks<sup>185</sup>. Second, 1% of encountered colorectal polyps have become malignant, where it may be more appropriate to perform enhanced staging (using imaging) or surgical oncological resection<sup>183</sup>. Finally, real-time tissue recognition would allow implementation of the “resect and discard” strategy (low-risk adenomas can be discarded without pathological analysis), resulting in cost savings which have been estimated at \$1bn annually<sup>185,186</sup>.

The focus of this thesis will be the use of REIMS for real-time assessment of colorectal tissues (including polyps), however, it is therefore necessary to explore the existing and competing technologies which can be applied endoscopically. This is most commonly performed with the augmentation or manipulation of optical data, where clinicians make predictions of histological subtype based on a doctored image; however, concerns have been raised about the accuracy and safety of such approaches<sup>187</sup>. Previous work is limited by allowing *post hoc* diagnosis from images or videos, methodological incorporation of heterogeneity, preselecting a limited number of technologies and poorly presented accuracy data<sup>185,188,189</sup>.

The aim of this systematic review and meta-analysis was to determine the diagnostic accuracy of endoscopic optical technologies for the real-time histological assessment of colorectal polyps.

## 2.2 Methods

This meta-analysis was conducted in accordance with the preferred reporting items for systematic reviews and meta-analyses of diagnostic test accuracy (PRISMA-DTA)<sup>190</sup>.

### 2.2.1 Search Strategy

A combination of electronic database search, bibliography appraisal and broad internet searching was conducted to identify peer-reviewed manuscripts to be considered for inclusion. Medline (1946 – present), EMBASE (1947 – present) and the Cochrane database were searched on the 1<sup>st</sup> March 2018, using a comprehensive search strategy including the following terms and Boolean operators: ((exp Intestine, Large/ OR colon\* OR rect\*) AND (adenoma\* OR polyp\*) OR exp Colonic Polyps/) AND (exp Colonoscopy/ OR Endoscop\*) AND (Real adj time OR in adj vivo OR spectroscop\*OR narrow adj band OR optical) AND (diagnos\* OR classif\*), with a full strategy presented in appendix 3. Additional studies were captured by hand-searching the bibliographies of relevant studies and a Google Scholar search using selected key words.

### 2.2.2 Criteria for Study Inclusion

Manuscripts identified in the search were appraised independently by two reviewers (SM and LP), with the application of pre-defined inclusion and exclusion criteria. Studies were suitable for inclusion if they had prospectively compared the real-time diagnostic accuracy of an endoscopically deployed optical technology against histopathological analysis for colorectal polyps in a human population. The following outcomes were of interest: presence of adenoma, differentiation of low- and high-grade dysplasia in conventional adenomas, determination of adenoma subtype, or presence of invasive carcinoma. Histopathological analysis must have consisted of microscopy following H&E staining of sections and application of internationally

recognised diagnostic criteria, such as the Vienna criteria<sup>191</sup>. Studies were excluded if they presented data from less than 10 patients, predictions were made *post hoc* from videos or photographs, or patients had hereditary polyposis syndromes or inflammatory bowel disease. If multiple technologies had been used in conjunction, these studies were excluded as it was not possible to determine the accuracy of each individual technology. Data presented must have been primary, fully peer-reviewed (conference proceedings were not accepted) and diagnostic accuracy must have been presented to allow the reconstruction of a 2x2 confusion matrix.

### 2.2.3 Data Extraction and Analysis

The same two reviewers independently extracted the raw data from all included manuscripts as absolute values of the 2x2 diagnostic contingency table, defining adenocarcinoma and adenoma as 'positive' and benign tissues as 'negative'. If only a sensitivity was presented without a prevalence, authors were contacted by email to provide the necessary data. Other datapoints collected were country, specifications of technology used, endoscopist experience (defined as having undergone training or having previously used the technology on greater than 50 cases), separate analyses for diminutive (< 5mm) polyps and subgroups of predictions made with high confidence. Each included study underwent quality assessment using the QUADAS-2 score<sup>192</sup>.

If a technology had been assessed in at least three studies for the same outcome, Bayesian bivariate meta-analysis was performed using Laplace approximation in the meta4diag package<sup>193</sup> of RStudio v1.1.442 (with the rest undergoing narrative review). Diagnostic accuracy was assessed using the metrics sensitivity, specificity and the area under the ROC curve; with publication bias assessed using funnel plots.  $\alpha$  was set at 0.05 with 95% confidence intervals (CI) presented. Selected subgroup analyses were conducted based on the following clinically relevant factors: polyp size, prediction confidence, endoscopist experience, technical specifications of the technology and location of polyp. Chronological assessment of diagnostic accuracy was conducted by plotting the pooled estimate of NPV for each year.

## 2.3 Results

A total of 4,084 studies were identified from the search, of which 284 required full manuscript review (figure 2.1). The manuscript could not be sourced for three studies either through the British Library or directly contacting the authors and therefore had to be excluded. This generated 102 studies which were deemed suitable for inclusion in the meta-analysis, covering 129 patient cohorts and the assessment of 33,123 polyps.

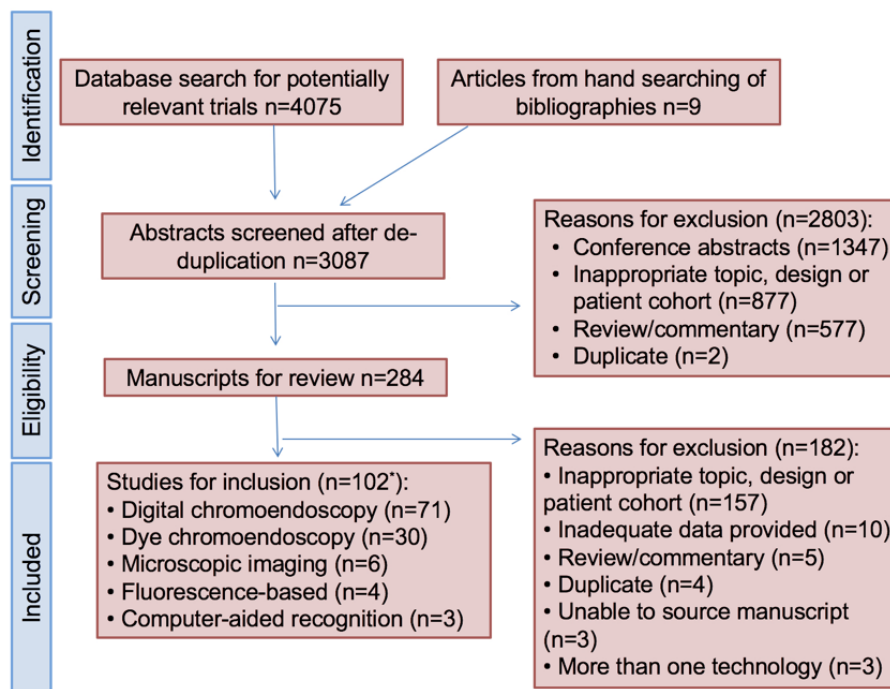


Figure 2.1 – PRISMA flowchart for the identification, screening, eligibility and inclusion of studies. Reproduced with permission Mason *et al.*<sup>194</sup>

\*Some manuscripts presented multiple patient cohorts, each assessing a different optical technology.

The vast majority of studies were carried out in developed countries (89%), the most two common of which were Japan and the USA. China was the most represented developing country, accounting for 6% of studies. The indication for performing the colonoscopy was often unclear, however when stated, it was most commonly for bowel cancer screening or surveillance following polypectomy. The nine distinct optical technologies that were included could be classified into five categories: digital chromoendoscopy, dye chromoendoscopy, fluorescence analysis, microscopic imaging and computer-aided recognition.

### 2.3.1 Digital Chromoendoscopy

Digital chromoendoscopy refers to the preselection of light wavelengths that are to be shown on the output screen, in order to enhance specific features of the mucosal surface. This was applied to 23,099 polyps in 84 patient cohorts across 71 trials, using three technologies – narrow band imaging (NBI; Olympus Medical Systems), Fuji Intelligent Chromo Endoscopy (FICE; Fujinon) and i-SCAN (PENTAX Medical).

NBI is designed to create a greater contrast between blood vessels and the mucosa, and performs this by only emitting light with the absorption spectrum of haemoglobin (blue 415nm and green 540nm)<sup>195</sup>. This technology underwent meta-analysis in 48 studies, where it assessed 17,568 polyps<sup>196-243</sup>. This assessment was most commonly performed by the endoscopist comparing the surface 'pit' patterns or the microvasculature to published criteria (from Kudo, Sano or NICE), which have been independently correlated to histological diagnosis<sup>241,244,245</sup>. Whilst the vast majority of studies defined neoplasia as only conventional adenomas or adenocarcinoma, 23 included a low prevalence of serrated adenomas and polyps at 2.8%. In all but one case<sup>225</sup>, the presence of dysplasia in these lesions was sufficient that it would be categorised into the neoplastic group. Five studies assessing 497 polyps could not be included in the meta-analysis as they only assessed serrated lesions, grades of dysplasia in conventional adenomas or the differentiation of adenocarcinoma from adenoma<sup>246-250</sup>. FICE and i-SCAN are technologies which emit and collect white light and then use spectral estimation to select the wavelengths of choice to output. This is used to enhance mucosal surface structure, tone and contrast; with the endoscopist again comparing the features to published standards in order to make the diagnosis<sup>251</sup>. The 12 studies included in the meta-analysis using FICE on 3,226 polyps<sup>197,232,252-261</sup> and the 9 studies using i-SCAN on 1,808 polyps<sup>204,262-269</sup> had an almost identical prevalence of serrated adenomas compared to the NBI cohort (2.1% across half of the studies), with a serrated polyp without dysplasia defined as benign in one study<sup>267</sup>.

Table 2.1 presents the diagnostic accuracy of digital chromoendoscopy and its constituent technologies across all polyps and for subgroup analyses. It demonstrates a moderate diagnostic ability, with an AUC of 0.885 and a sensitivity which is outperforming specificity (implying that false positives are a greater issue than false negatives). The subgroup analyses reveal that there is no statistically significant improvement in diagnostic accuracy when only high confidence

predictions are used, endoscopists are of high experience, high magnification is used, the output screen is in high definition or only diminutive polyps were included. A further set of subgroup analyses were conducted where experienced endoscopists made high confidence predictions of diminutive polyps, demonstrating an NPV of 86.8% (80.9-91.6% CI). When limited to left-sided polyps, the NPV increased to 92.7% (88.3-96.1% CI) and when only for recto-sigmoid polyps, it was 93.8% (90.9-96.4% CI). Whilst very clinically relevant, it was found that relatively few studies presented data on this final cohort, such that it was limited to only 2,149 polyps across 10 studies. When comparing the constituent digital chromoendoscopy technologies, there was no apparent difference in their diagnostic accuracies (figure 2.2).

**NBI**

	Studies (n)	Polyps (n)	Sensitivity (%)	Specificity (%)	AUC	PPV (%)	NPV (%)
All Polyps	48	17 568	93.1 (90.9-94.9)	82.1 (79.1-85.0)	0.909 (0.858-0.903)	90.5 (88.5-92.3)	86.5 (82.9-89.8)
Diminutive Polyps	22	8 299	92.4 (89.2-95.0)	83.9 (79.3-88.1)	0.921 (0.832-0.957)	89.0 (86.5-91.5)	88.5 (84.2-92.2)
High Confidence	17	8 055	94.7 (92.4-96.6)	82.0 (76.3-87.2)	0.898 (0.783-0.964)	90.0 (87.1-92.7)	90.2 (85.7-93.9)
Experienced Endoscopist	34	14 205	91.9 (89.0-94.3)	78.7 (75.6-81.8)	0.913 (0.870-0.944)	88.4 (86.2-90.4)	84.7 (80.6-88.4)
High Magnification	27	8 186	95.8 (93.9-97.4)	85.8 (81.3-89.8)	0.910 (0.783-0.967)	92.9 (90.0-95.2)	91.5 (87.6-94.8)
High Definition	39	14 254	93.2 (91.1-95.1)	81.9 (78.6-85.1)	0.909 (0.872-952)	89.5 (87.5-91.4)	87.9 (84.3-91.0)

**FICE**

	Studies (n)	Polyps (n)	Sensitivity (%)	Specificity (%)	AUC	PPV (%)	NPV (%)
All Polyps	11*	3 226	90.2 (86.8-93.2)	86.0 (79.2-91.4)	0.853 (0.413-0.946)	92.9 (89.8-95.4)	81.1 (75.6-85.9)
Diminutive Polyps	6	1 257	85.0 (78.9-90.3)	84.6 (79.4-88.8)	0.915 (0.674-0.934)	89.5 (85.6-93.1)	77.8 (72.0-83.0)
High Confidence	0	-	-	-	-	-	-
Experienced Endoscopist	7	2 236	88.5 (83.4-92.5)	88.5 (81.9-93.6)	0.631 (0.246-0.802)	93.9 (89.6-96.9)	79.3 (72.8-84.9)
High Magnification	6	2 096	91.1 (88.2-93.6)	90.3 (83.4-95.3)	0.821 (0.109-0.959)	94.7 (90.5-97.7)	84.5 (79.2-88.7)
High Definition	10	2 919	90.3 (86.3-93.6)	85.0 (77.1-91.1)	0.875 (0.468-0.954)	92.3 (89.1-94.9)	81.5 (75.0-86.9)

**iSCAN**

	Studies (n)	Polyps (n)	Sensitivity (%)	Specificity (%)	AUC	PPV (%)	NPV (%)
All Polyps	9	1 808	91.3 (85.5-95.5)	88.7 (82.3-93.9)	0.536 (0.376-0.850)	92.4 (87.3-96.2)	87.3 (77.8-94.1)
Diminutive Polyps	3	419	96.4 (91.7-99.0)	89.9 (80.2-96.1)	0.886 (0.176-0.991)	92.0 (84.3-96.8)	95.4 (89.3-98.7)
High Confidence	1	-	-	-	-	-	-
Experienced Endoscopist	7	1 551	89.4 (81.8-94.9)	88.0 (79.3-94.6)	0.568 (0.293-0.858)	91.2 (84.3-96.1)	85.8 (74.3-93.9)
High Magnification	0	-	-	-	-	-	-
High Definition	9	1 808	91.3 (85.5-95.5)	88.7 (82.3-93.9)	0.536 (0.384-0.855)	92.4 (87.3-96.2)	87.3 (77.8-94.1)

<b>All Digital Chromoendoscopy</b>	Studies (n)	Polyps (n)	Sensitivity (%)	Specificity (%)	AUC	PPV (%)	NPV (%)
All Polyps	65*	22 602	92.2 (90.6-93.9)	84.0 (81.5-86.3)	0.885 (0.825-0.926)	91.3 (89.7-92.7)	85.7 (82.9-88.4)
Diminutive Polyps	29	9 969	91.7 (89.1-94.0)	84.6 (81.3-87.7)	0.908 (0.839-0.948)	89.3 (87.5-91.2)	87.7 (84.2-90.8)
High Confidence	18	8 156	94.9 (92.7-96.8)	82.9 (77.3-87.9)	0.890 (0.765-0.962)	90.2 (87.5-92.8)	90.8 (86.6-94.4)
Experienced Endoscopist	44	17 992	91.1 (88.7-93.1)	82.0 (79.2-84.7)	0.888 (0.833-0.927)	89.9 (88.0-91.6)	84.0 (80.7-87.0)
High Magnification	33	10 282	94.8 (93.1-96.3)	87.0 (83.3-90.3)	0.892 (0.750-0.958)	93.4 (91.2-95.3)	89.6 (86.3-92.6)
High Definition	54	18 981	92.5 (90.7-94.0)	83.8 (81.1-86.3)	0.880 (0.836-0.936)	90.5 (89.0-92.0)	86.8 (83.9-89.4)

Table 2.1 – Diagnostic accuracy of digital chromoendoscopy and its constituent technologies with subgroup analyses. 95% CIs are presented in brackets. Reproduced with permission Mason *et al.*<sup>194</sup>

AUC – area under curve; PPV – positive predictive value; NPV – negative predictive value.

\*One author presented duplicated results of a diminutive polyp subgroup in a later study, such that the total number of studies in this meta-analysis are one greater than the number in the ‘all polyps’ analysis.

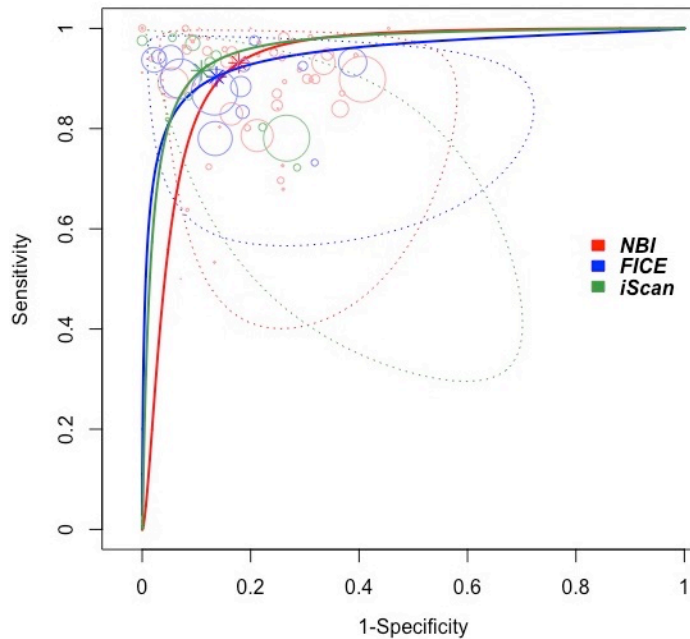


Figure 2.2 – the summary ROC curve for the three digital chromoendoscopy technologies. This demonstrated that there is little apparent difference in accuracy between them, with summary points which plot closely. Reproduced with permission from Mason *et al.*<sup>194</sup> Asterisk – summary point; circles – each study; dashed line – 95% prediction region.

A funnel plot was constructed for all digital chromoendoscopy studies within the meta-analysis, which revealed a marked paucity of studies with a low diagnostic odds ratio and high standard deviation (Figure 2.3.A). This lack of ‘small negative’ studies represents a high likelihood of there being a publication bias which acts to over-estimate the diagnostic accuracy of this technology. The quality of the included studies was high, with 57% of studies scoring full marks on the QUADAS-2 (appendix 4). The greatest potential sources of bias were the methods of patient selection and the application of the index test. It was unclear in 24% of the patient cohorts if consecutive patients were eligible for the study and therefore, the exact method by which they were selected. The most prevalent risk of bias associated with the index test was that the experience of the endoscopist using digital chromoendoscopy was unclear and therefore they may have still been on their learning curve. Additionally, blinding was compromised in some cohorts by the endoscopist potentially knowing that a patient had an adenoma prior to the procedure or having just used a different technology to assess the polyp. 6% of patient cohorts had unusually high incidences of adenomas or serrated lesions (89% in one study)<sup>208</sup> and therefore this limits the validity of the findings when comparing to a routine clinical scenario. Despite these potential

sources of bias, performing the same analysis only with studies that scored 100% on the QUADAS-2 did not impact the diagnostic accuracy.

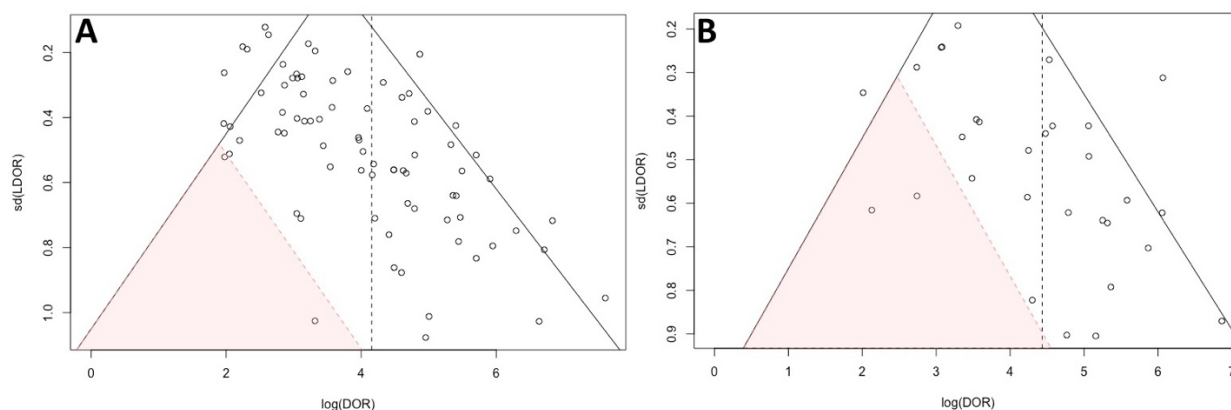


Figure 2.3 – funnel plots of digital chromoendoscopy (A) and dye chromoendoscopy (B) studies, with a shaded area representing the location that published studies are under-represented.

Reproduced with permission from Mason *et al.*<sup>194</sup>

DOR – diagnostic odds ratio.

### 2.3.2 Dye Chromoendoscopy

Dye chromoendoscopy is a method whereby a dye solution is sprayed down the working channel of an endoscope onto the mucosa, most commonly used for detection of dysplasia in inflammatory bowel disease, however, it can also be used for polyp characterisation<sup>270</sup>. A total of 30 studies assessed the technology across 32 patient cohorts on 8,336 colorectal polyps, of which 29 were suitable for meta-analysis<sup>205,208,252-256,258,261,271-290</sup>. All but two studies applied the Indigo Carmine dye, which lies on the mucosal surface without being absorbed to enhance its morphology; at which point the Kudo criteria were used to make a prediction of histological subtype<sup>244</sup>. The included studies were designed to assess the technology in differentiating neoplastic from benign polyps, where the neoplastic group largely consisted of conventional adenomas, with a small number of adenocarcinomas and serrated adenomas (1.5% prevalence in seven studies). The diagnostic accuracy is presented in table 2.2, with marked similarities with the ability of digital chromoendoscopy and with no significant difference between the two. Again, the accuracy is moderate, with an AUC of 0.866 and a sensitivity higher than the specificity. Whilst no subgroup analysis showed a statistically significant change in accuracy, there was a trend towards lower accuracy when only diminutive polyps were analysed (AUC 0.866 to 0.756). In all analyses the estimated NPV was below 90%. The single study that could not be included in the meta-

analysis used crystal violet dye to predict the presence of adenocarcinoma in adenomatous polyps, with a sensitivity and specificity of 82.9% and 67.7% respectively<sup>246</sup>.

The issues found with publication bias and risk of systematic bias in digital chromoendoscopy studies are again apparent when assessing those using dye chromoendoscopy. The funnel plot for the dye chromoendoscopy strongly implies the presence of a publication bias which is over-estimating the diagnostic accuracy (figure 2.3.B). The QUADAS-2 scores (appendix 5) were often displaying potential biases from an unclear patient selection process (and whether consecutive patients were eligible, evident in 35%), unclear endoscopist training (39%) and a lack of blinding where another diagnostic technology was used just prior to the dye instillation (16%). A subgroup analysis of the 29% of patient cohorts with 100% QUADAS-2 score did not significantly change the diagnostic accuracy.

## Dye Chromoendoscopy

	Studies (n)	Polyps (n)	Sensitivity (%)	Specificity (%)	AUC	PPV (%)	NPV (%)
All Polyps	28*	8 267	92.7 (90.1-94.9)	86.6 (82.9-89.9)	0.866 (0.778-0.948)	91.7 (88.6-94.3)	88.0 (84.0-91.5)
Diminutive Polyps	9	1 903	87.2 (78.3-93.6)	85.1 (77.4-91.0)	0.756 (0.598-0.937)	85.3 (77.9-91.0)	86.8 (75.9-94.1)
High Confidence	1	-	-	-	-	-	-
Experienced Endoscopist	13	2 931	94.7 (91.1-97.2)	88.2 (83.9-91.9)	0.881 (0.811-0.974)	93.5 (89.3-96.5)	89.7 (84.9-93.7)
High Magnification	21	6 318	93.5 (90.1-96.1)	88.4 (84.1-92.1)	0.865 (0.771-0.961)	93.1 (89.4-95.9)	89.1 (83.9-93.3)
High Definition	16	3 440	90.3 (85.8-93.9)	85.6 (80.2-90.0)	0.861 (0.693-0.947)	86.6 (81.5-90.8)	89.2 (83.2-93.7)

Table 2.2 – the diagnostic accuracy of dye chromoendoscopy in differentiating neoplastic and benign colorectal polyps. Reproduced with permission from Mason *et al.*<sup>194</sup>

\*One author presented duplicated results of a diminutive polyp subgroup in a later study, such that the total number of studies in this meta-analysis are 29 but only 28 are included in the ‘all polyps’ analysis.

### 2.3.3 Fluorescence Analysis

Colorectal tissues can be analysed using fluorescence technology in two primary ways. The first is termed autofluorescence, where endogenous molecules within the tissue have the property of being a fluorophore (such as flavins and aromatic acids), and can undergo excitation in order to release characteristic emissions<sup>291</sup>. This was used in three studies on 525 colorectal polyps, where light at 390-470nm and 540-560nm was used to excite tissues and generate images that were a mixture of green (benign) or magenta (neoplastic)<sup>196,202,292</sup>. The green:magenta ratio could be calculated or subjective assessment could be used to make a prediction of the histological subtype, which had a sensitivity, specificity, PPV and NPV of 94.4% (84.0-99.1% CI), 50.9% (13.2-88.8% CI), 72.7% (31.8-95.9%) and 85.6% (68.6-96.6% CI) respectively. There was insufficient data to conduct any subgroup analyses, however QUADAS-2 quality scoring was conducted; which revealed a high risk of bias in two studies. This was caused by the endoscopist using NBI immediately prior to the fluoroscopic assessment and therefore blinding may have been impacted (appendix 6).

The second fluoroscopic principle that can be applied is where an exogenous photosensitiser is administered. This accumulates in the tissue of interest and then when a specific wavelength of light is used for excitation, the tissue can be indirectly visualised<sup>291</sup>. This technology was used in one study to predict the presence of adenocarcinoma in 33 adenomatous polyps using a fluorescein-labelled antibody to carcinoembryonic antigen, demonstrating low diagnostic accuracy with a NPV of 45%<sup>293</sup>.

### 2.3.4 Microscopic Imaging

Microscopic imaging technologies display colorectal tissues on a cellular level in real-time, with two techniques identified in this review. Confocal laser endomicroscopy (CLE) can give a x1000 magnification of the colorectal mucosa with a resolution of 1µm, at which point classification systems can be applied to assess thickening of the epithelial layer (indicative of dysplasia)<sup>294-296</sup>. This was the most commonly used microscopic imaging technique, where four studies used it to assess 519 colorectal polyps<sup>295,297-299</sup>. When differentiating neoplastic from benign polyps, CLE demonstrated a sensitivity, specificity, PPV and NPV of 93.6% (85.3-98.3% CI), 92.5% (81.8-98.1%

CI), 92.8% (83.5-98.1% CI) and 93.1% (82.5-98.5% CI) respectively. This level of accuracy was not significantly higher than the chromoendoscopy approaches however, there was a trend in this direction. Funnel plotting demonstrated evidence of a publication bias and QUADAS-2 showed an unclear risk of bias from unknown endoscopist experience and unclear patient sampling (appendix 7).

The second microscopic imaging technique was endocytoscopy, which uses nuclear dyes (such as methylene blue and toluidine) to perform imaging on a supra- and sub-cellular level, allowing visualisation of glandular structure and cellular atypia<sup>300</sup>. The images produced are similar to H&E stained sections and can therefore be interpreted using similar diagnostic criteria<sup>301</sup>. This was conducted in two studies on 149 polyps and therefore was not suitable for meta-analysis<sup>302,303</sup>. This early data on small cohorts appears to show high levels of diagnostic accuracy in differentiating neoplastic from benign polyps (greater than 90%), with one study showing non-inferiority to traditional biopsy<sup>303</sup>.

### 2.3.5 Computer-aided Recognition

The use of computer algorithms to make histological predictions based on optical inputs from the endoscope were assessed by three studies, where it was applied to differentiate adenomatous and benign polyps. The wavSTAT4 probe (Spectra Science, USA) was used in two studies on 344 polyps, which emits 337nm light to cause laser-induced fluorescence; where the emissions are analysed with a proprietary algorithm to determine if the lesion is “suspect” or “non-suspect”<sup>304,305</sup>. One study trained machine learning algorithms on 2,247 clinically annotated images of neoplastic features on NBI, before applying it in real-time on 118 polyps<sup>306</sup>. These three studies underwent meta-analysis showing a sensitivity, specificity, PPV and NPV of 88.9% (74.2-96.7% CI), 80.4% (52.6-95.7% CI), 76.9% (38.8-96.5% CI) and 88.7% (67.3-98.1% CI) respectively. There was evidence of marked heterogeneity (for example, specificity ranged from 59-93% and PPV from 51-96%), however, there was a low risk of bias on QUADAS-2 (appendix 8).

### 2.3.6 Chronologic Analysis

In order to understand how the diagnostic accuracies of the optical technologies have been progressing over time, chronological meta-analyses were performed based on all studies published at each timepoint. NPV was chosen as the metric to plot given its importance as a threshold, where 90% must be exceeded to consider routine clinical implementation of a technology in certain clinical scenarios<sup>307</sup>. Given the similarity in constituent digital chromoendoscopy studies, they were pooled for this analysis. Figure 2.4 demonstrates that both digital and dye chromoendoscopy do not exceed the 90% NPV threshold, with the value having generally plateaued for over a decade. As the power of the meta-analyses increased with more studies (reflected by narrowing CIs), it appears to confirm that the true NPV of digital chromoendoscopy will remain below 90%. The NPV of dye chromoendoscopy appears likely to become statistically significantly below 90% in the coming years.

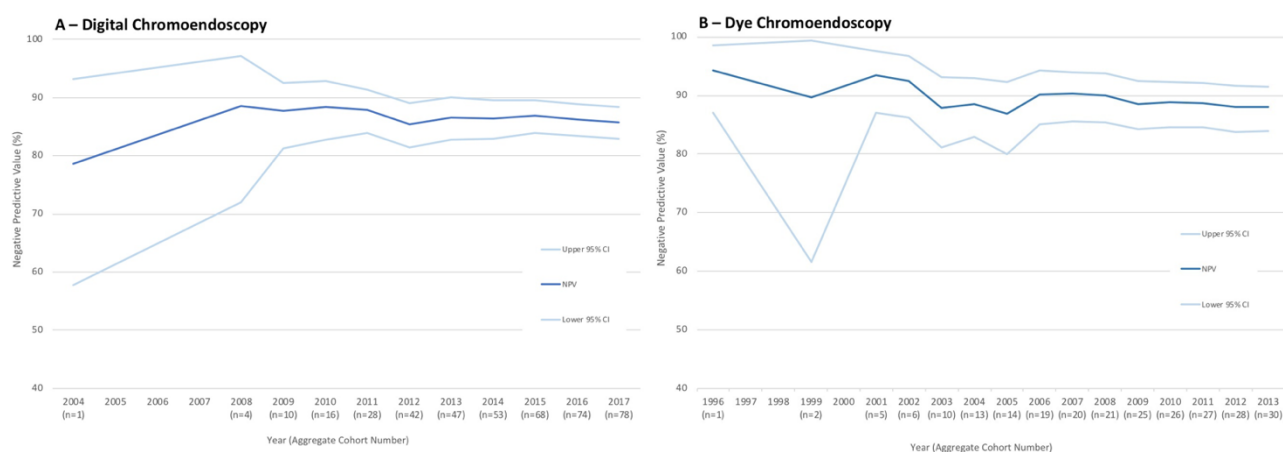


Figure 2.4 – the negative predictive value of digital chromoendoscopy (A) and dye chromoendoscopy (B) plotted chronologically based on the year that each study was published. Reproduced with permission from Mason *et al.*<sup>194</sup>  
CI – confidence interval; NPV – negative predictive value.

## 2.4 Discussion

This systematic review and meta-analysis assessed endoscopic optical technologies for the real-time prediction of histological subtype for colorectal polyps, chosen as an exemplar of technology being used for colorectal tissue recognition. The diagnostic accuracy of the nine included technologies in differentiating neoplastic from benign polyps was moderate and insufficient for

recommending routine clinical implementation. Furthermore, chronological analysis demonstrated that the accuracies have not been improving over the past decade and appear unlikely to meet clinical implementation thresholds in the coming years.

The ability to determine the histology of a colorectal polyp in real-time provides the endoscopist with an opportunity to make personalized management decisions during the procedure, to reduce risk exposure, improve clinical outcome, save time and reduce costs<sup>184-186</sup>. Historical studies could not confirm their hypothesis that white light reflected from the surface of a polyp contained sufficient information for accurate histological prediction, with data showing limited accuracies of 59-84%<sup>308</sup>. As this review demonstrates, this prompted the development of the several optical technologies, which use a combination of manipulation, wavelength selection, fluorescence techniques and computer analysis to increase prediction accuracy. The level of accuracy that a technology must achieve to be used routinely in clinical practice is contested, with recommendations from a variety of sources<sup>309</sup>. The American Society of Gastrointestinal Endoscopy (ASGE) has described the Preservation and Incorporation of Valuable endoscopic Innovation (PIVI) criteria. In brief, the first PIVI statement requires that diminutive polyps characterized with high confidence (in conjunction with histological assessment of those 6-9mm) should have a greater than 90% agreement in surveillance interval compared to histology<sup>185</sup>. The second statement requires the NPV for adenoma in diminutive recto-sigmoid polyps to be greater than 90%<sup>185</sup>. The large, multicentre DISCARD study appeared to prefer overall accuracy for small (<10mm) polyps<sup>308</sup> and the DISCARD-II trial determined the success of NBI for all small colorectal polyps aiming for a sensitivity of >95%<sup>236</sup>. It is beyond the scope of this thesis to debate the exact implementation threshold that should be applied and it is likely that there would be some debate between experts if a consensus was to be required for assessing tissue recognition technologies. An NPV for adenoma of greater than 90% was used in this thesis considering it is the most commonly applied in the literature, is used by the influential ASGE and focusses on minimising the most clinically impactful misclassification, the false negative.

Digital chromoendoscopy and its constituent technologies of NBI, FICE and i-SCAN were found to be the most commonly deployed in this review (68%), which is likely to be as a consequence of their ubiquity in endoscopy suites worldwide; where they are used throughout the gastrointestinal tract for lesion detection and optical biopsy<sup>310</sup>. It does not appear that there is any significant difference in the accuracy between the digital chromoendoscopy technologies, which is likely to

be as a result of their similar operating principles and diagnostic criteria employed. Whilst NBI was found to be the most commonly used, it is assumed this was due to greater availability of the technology with a more established evidence base, rather than a higher expected accuracy. This review highlighted that there is a single most important research question when it comes to the application of these technologies, which is whether they can accurately differentiate neoplastic (adenoma and adenocarcinoma) from benign (normal or hyperplastic) polyps. The estimated 92.2% sensitivity, 84.0% specificity and 85.7% NPV of digital chromoendoscopy shown in this review is similar to previous reviews, however, must be considered within the context of the significant publication bias that is likely to be present, acting to over-estimate this accuracy. Kobayashi *et al.* used the Begg test to assess for publication bias statistically (rather than simply graphically) where it was found to not be significant ( $p = 0.07$ ), however this was only in 10 NBI studies and was therefore likely underpowered<sup>311</sup>. Another perspective which implies a publication bias is that recently there have been higher quality, multicentre, well-powered studies using digital chromoendoscopy, which have been unable to match the accuracies demonstrated in earlier and lower-quality work<sup>203,236</sup>. When considering the PIVI II statement, digital chromoendoscopy of diminutive recto-sigmoid polyps appeared to demonstrate an NPV of over 90%, however this finding should be met with caution. Only a small subset of studies ( $n=8$ ) appraised this outcome, the total number of polyps was comparatively low, this was often a *post hoc* subgroup analysis and there was a clear inverse relationship between NPV and study size (the four largest studies contained the three lowest NPVs). It is unfortunate that high-quality implementation trials (such as DISCARD-II) did not assess the PIVI II statement in order to increase the power of this analysis. Considering these issues and the marked publication bias already described, using this finding to recommend routine clinical use is unlikely to be prudent. Future studies of this mature technology should be pre-registered, high-quality and multicentre; to ensure this publication bias is not perpetuated and 'real world' accuracies can be presented.

Dye chromoendoscopy is most commonly used to increase the detection rate of dysplasia within the context of inflammatory bowel disease, rather than for polyp characterisation in low-risk cohorts. Consequently, it was applied much less frequently than digital chromoendoscopy in this review. This may be due to the historical differences in indication but may also be accounted for by the increased time it takes to instil the dye (compared to an immediate button press for the digital alternative), the non-zero risk of anaphylaxis to the dye itself, dye interfering with interpretation of adjacent mucosa and its considerable learning curve<sup>255</sup>. However, it should be

noted that the lack of specialist equipment required (beyond a high magnification endoscope) may support its use in settings without the financial opportunity to have digital chromoendoscopy alternatives. The diagnostic accuracy of dye chromoendoscopy in differentiating neoplastic and non-neoplastic polyps was indistinguishable from digital chromoendoscopy, where it was considered moderate and insufficient to recommend routine clinical implementation. The heterogeneity in the method by which the dyes work may be such that one would have a greater diagnostic accuracy, however there was insufficient studies to be able to assess this. The publication bias seen in digital chromoendoscopy studies also appeared to be present here, once again raising a concern regarding headline diagnostic accuracy and reinforcing the need for pre-registered high-quality trials in the future.

Fluorescence and microscopic imaging technologies have been studied relatively rarely in comparison to chromoendoscopy, likely due to their younger age, the need for specialist equipment (such as dedicated probes) and the lack of evidence to support their clinical implementation. The limited number of polyps assessed was such that the power of the meta-analyses were low (showing wide CIs) and therefore comparisons between the technologies is problematic. Despite this, a few themes have emerged. Fluorescence technologies appear to suffer with a relatively high number of false positives (benign tissue predicted to be neoplastic). Microscopic imaging appears to have the most promising accuracy of all technologies exhibited, which may be explained by the fact that it is designed to visualise cellular and tissue structures directly; the same method by which the *gold standard* histology makes diagnoses.

Machine learning and artificial intelligence technologies are rapidly being developed and applied to a variety of healthcare problems, where they are able to find deep relationships in complex datasets; often vastly out forming human counterparts<sup>312</sup>. These techniques also benefit from theoretically increasing in accuracy as they are exposed to more data, they can be run in real-time on relatively inexpensive hardware and are not limited by the types of data input (as seen in this review, where it was applied to fluorescence and NBI images). When combined to an endocytoscope *in vivo*, real-time computer-aided recognition could differentiate neoplastic from benign polyps with an adenoma NPV of 96%<sup>313</sup>. Whilst these technologies have potential, caution should be taken when interpreting the headline diagnostic accuracies due to statistical models being prone to overfitting and lack of wider implementation studies in routine care settings.

This meta-analysis did not demonstrate that endoscopist experience is associated with higher accuracy levels, despite studies of training courses implying that this may be the case and findings in the DISCARD-II trial that BCSP endoscopists have test sensitivity of 83%, compared to 64% for those not in the BCSP<sup>188,236</sup>. This may be due to this meta-analysis using a different definition of experience and that this negative finding was a type II error. The fact that the diagnostic accuracy of technologies does not appear to change when only diminutive polyps are analysed implies that the difficulties of applying them to smaller surface areas is not clinically significant. Furthermore, the lack of improvement for high confidence predictions may be due to a bias from the endoscopist, who will have subconsciously assessed adenomatous risk during the initial WLE; and the post-test probability is not sufficiently increased to be identified statistically.

Studies on real-time polyp tissue recognition in endoscopy largely focus on differentiation of conventional adenomas from benign lesions, however approximately half of the cohorts included sessile serrated lesions with an incidence of 1-2%. These lesions do have a different appearance to conventional adenomas and therefore this may have impacted the diagnostic accuracy of the technologies (considering many of the classification criteria are validated for conventional adenomas)<sup>314</sup>. This impact is likely to be small and excluding them entirely is not likely to be a pragmatic approach, as they are commonly found in patients and therefore, they are a clinically relevant tissue type to predict.

The novel approach in this meta-analysis was the use of chronological meta-analyses, where NPV was plotted to determine how it has changed over time against the 90% threshold. The flat or falling NPV over the past decade is likely due to new large, multicentre studies; which have a greater power and the release of which counteracts some of the previous publication bias. Furthermore, the narrowing of the CIs over time is a reflection of overall analytical power increasing. Both of these factors raise a strong suspicion that digital and dye chromoendoscopy studies will not exceed the required 90% threshold in the coming years, implying that step-change innovation is required for it to be successful. Narrowing the clinical application of technologies, such as in the PIVI II statement where it is only focusing on diminutive recto-sigmoid polyps, limits the scale with which they can be employed clinically and makes recruitment for clinical trials more challenging. Whilst the quality of the studies included in this meta-analysis was generally good (according to the QUADAS-2), there were recurring issues with application of technologies immediately after one another on the same polyp, unclear selection of patients and a lack of

clarity whether endoscopists were still on their learning curves. This has an implication for future research, where methodological quality needs to be improved (for example, by randomising), whilst assessing pragmatically important outcomes such as the accuracy in 'real world' settings (rather than just academic hospitals).

This meta-analysis was designed to be comprehensive and to avoid many of the limitations shown in previous reviews, which include the preselection of a limited number of technologies, including predictions not made in real-time *in vivo* (such as from videos or photos), methodological incorporation of heterogeneity and presenting limited accuracy metrics<sup>185,188,189</sup>. Despite stringent inclusion criteria, there was still significant heterogeneity of diagnostic accuracies between studies, which may be related to uncontrollable factors such as underlying adenoma prevalence, colonoscopy indication or undefined confounders. The eventual scope of the work was relatively narrow at only nine technologies, however assessing those earlier in the development process (such as Ramen and elastic scattering spectroscopy) would not have adequately addressed the research question.

## 2.5 Conclusion

This systematic review and meta-analysis demonstrated that optical technologies are currently insufficiently accurate for routine clinical use in differentiating neoplastic from benign colorectal polyps *in vivo*. Furthermore, this accuracy has been flat or reducing over the past decade, indicating that incremental improvements in optical technologies are unlikely to reap sufficient accuracies in the coming years. Successful technologies for colorectal tissue recognition are likely to require step-change innovation, which may be through the development and validation of novel technologies which sample biological rather than optical data.

## Chapter 3 - Thesis Hypothesis, Rationale, Aims and Design

### 3.1 Hypothesis

The hypothesis of this thesis is that colorectal lipid metabolism and cellular lipid composition are associated with the phenotype of colorectal adenomas and carcinomas. This can be leveraged using REIMS for accurate real-time recognition of colorectal tissues *in vivo* and to give insight into the metabolic transitions along the normal-adenoma-carcinoma sequence.

### 3.2 Rationale

This thesis will apply REIMS to the problem of colorectal tissue recognition through metabolic phenotyping, the rationale for which can be described across 5 domains.

**1. Clinical need.** There are several clinical scenarios in colorectal surgery where there is an unmet need for accurate, real-time tissue recognition; which when effectively employed, would directly improve the quality, safety and associated costs of patient care. TAMIS for advanced rectal adenomas and early cancers is an exemplar case, where en bloc resection with no tumour-involved margins is paramount and correlated with improved oncologic outcome. Real-time tissue feedback for the surgeon during dissection would allow microscopic positive margins to be immediately recognised, dissection planes to be adapted and consequently; promotion of organ preservation through an increased R0 resection rate. This same principle applies endoscopically when performing an EMR to reduce the risk of polyp recurrence and transformation. Additionally, real-time tissue recognition would allow risk stratification and personalised management strategies for colorectal polyps, such as 'resect and discard' and 'diagnose and leave'. A solution to these clinical problems would be applicable on a vast scale considering both the volume of patients it would benefit and the ubiquity of the problems worldwide.

**2. Inadequacy of existing technologies.** Chapter 2 demonstrates that the most ubiquitous methods for real-time colorectal tissue recognition, optical technologies, are likely to remain

insufficiently accurate for routine clinical implementation in the coming years; despite extensive financial investment, research and staff training. This is reflected by its relatively low uptake by endoscopists, with them reporting that it is not sufficiently capable in its current form<sup>315</sup>.

Furthermore, only 50-60% of patients are happy for use of the 'resect and discard' and 'diagnose and leave' strategies given the diagnostic accuracies of current technologies<sup>316</sup>.

**3. Potential of REIMS for accurate tissue recognition.** REIMS pilot data has demonstrated high initial levels of accuracy for tissue recognition across a multitude of organs, including colorectal tissue. This is underpinned by strong biological plausibility, where the established metabolic changes of carcinogenesis are being directly sampled by the MS through differences in relative abundance of metabolites. Whilst the early data have shown promise, the true diagnostic accuracy of REIMS for colorectal tissues has yet to be established with a well-powered dataset and it has yet to be determined if this can be translated *in vivo*. There is potential for REIMS to supersede the diagnostic accuracies of its competitor technologies, which is likely to be necessary given that it is increasingly recognised that a 90% NPV implementation threshold is inadequately low from a patient safety and legal perspective<sup>309</sup>.

#### **4. Improvements over traditional histopathology.**

Tissue diagnosis using REIMS and its machine learning algorithms can be conducted in real-time unlike traditional histopathology, which can take up to 7 days to give results and therefore does not allow tailoring of management decision during the procedure. It also recognised to suffer with inter- and intra-observer variability, which can be mitigated with the objectivity and reproducibility that modern analytical techniques appear to offer<sup>317-319</sup>. Whilst the fixed costs of MS techniques such as REIMS are higher, the lower variable costs are such that it may be cheaper than histopathology if deployed at scale.

#### **5. Biological insight into the relationship between metabolism and tissue phenotype.**

Progression from relying simply on cancer morphology to the incorporation of biological features such as genotype has transformed the pan-specialty management of cancer. Considering the intimate relationship between metabolism and phenotype, sampling metabolic data is likely to give significant new insights from a research and clinical perspective into factors such as the drivers of carcinogenesis, determinants of clinical risk and optimal management strategies. Clinical

applications for integrated metabolomic data include diagnostics (such as risk stratification of early rectal cancers by predicting nodal micrometastasis), therapeutics (personalised use of anti-cancer agents based on metabolic risk and vulnerabilities) and prognostics (treatment response and optimisation of long-term surveillance programs).

### 3.3 Thesis Aims

The aims of this thesis are to:

1. Define the minimum quality of REIMS spectra which allows inclusion in tissue recognition models, with regards to technical, statistical and histological variables.
2. Determine the impact of environmental and technical factors on the quality and biological composition of REIMS spectra from colorectal mucosa.
3. Create a clinically and histologically validated *ex vivo* database of REIMS spectra from the analysis of colorectal tissues.
4. Use multivariate statistical techniques to determine the diagnostic accuracy of REIMS in differentiating colorectal carcinoma, adenoma and normal mucosa.
5. Assess the ability of REIMS to risk stratify colorectal cancers and adenomas.
6. Identify the molecular structure of lipid metabolites which are responsible for differentiating groups in statistical models.
7. Determine whether it is feasible for REIMS to be coupled to surgical instruments *in vivo* during TAMIS, to give real-time spectra of sufficient quality to undergo statistical analysis.

### 3.4 Thesis Design

The structure of this thesis is demonstrated in figure 3.1, where narrative questions have been used to explain both the journey of the thesis and the composition of each chapter. Chapters one and two have explored the clinical and scientific background of CRC, metabolomics and real-time tissue recognition, revealing unanswered research questions within the context of an unmet clinical need (as described in this chapter). The MS methodologies that will be employed across the experimental chapters share a common basis, which is described in detail in chapter four, to avoid unnecessary reproduction later. The three experimental chapters (five to seven) have been

designed to directly address the aims of this thesis, where I will present results, provide biological context, interpret their clinical and research impact, appraise the methodology used and identify unanswered questions that remain. The final chapter will conclude the thesis by providing a summary of the work, giving my opinion on progress in the field and giving recommendations for future research.

<b>Chapter 1</b>	<ul style="list-style-type: none"> <li>• What is the clinical problem?</li> <li>• What is the scientific basis of REIMS and how can it be leveraged?</li> </ul>
<b>Chapter 2</b>	<ul style="list-style-type: none"> <li>• What are the strengths and weaknesses of the technologies which compete with REIMS for real-time colorectal tissue recognition?</li> </ul>
<b>Chapter 3</b>	<ul style="list-style-type: none"> <li>• Why is this course of study being undertaken?</li> <li>• What does this thesis hope to accomplish?</li> </ul>
<b>Chapter 4</b>	<ul style="list-style-type: none"> <li>• What methods will be used to answer the research questions?</li> </ul>
<b>Chapter 5</b>	<ul style="list-style-type: none"> <li>• What defines a 'high quality' REIMS spectrum?</li> <li>• How does spectral quality impact diagnostic accuracy?</li> <li>• Which factors may impact the quality of REIMS spectra when translating it <i>in vivo</i>?</li> </ul>
<b>Chapter 6</b>	<ul style="list-style-type: none"> <li>• Can a validated database of REIMS spectra be created <i>ex vivo</i>?</li> <li>• What is the diagnostic accuracy of REIMS for colorectal tissue recognition?</li> <li>• Can REIMS be used to risk-stratify colorectal cancers and adenomas?</li> <li>• What is the molecular structure of statistically significant lipid metabolites?</li> </ul>
<b>Chapter 7</b>	<ul style="list-style-type: none"> <li>• Can REIMS be used <i>in vivo</i> during TAMIS to collect mass spectral data?</li> <li>• Can tissue recognition be performed during MS-TAMIS?</li> </ul>
<b>Chapter 8</b>	<ul style="list-style-type: none"> <li>• What are the conclusions and recommendations for future work?</li> </ul>

Figure 3.1 – the structure of the thesis with the narrative questions addressed in each chapter.

## Chapter 4 – Materials and Methods

### 4.1 Research oversight and governance

All research described in this thesis was conducted in accordance with the regulations and principles laid out in the International Conference on Harmonization Good Clinical Practice, the Data Protection Act, the UK Policy Framework for Health and Social Care Research and the recommendations for physicians involved in research on human subjects adopted by the 18th World Medical Assembly, Helsinki 1964 and later revisions. Oversight was provided by the frameworks of Imperial College London and the research department of any included NHS trust.

### 4.2 Ethical approval

Ethical approval for the studies contained in this thesis was achieved from two sources. *Ex vivo* collection of tissue was conducted as a sub-collection (JK\_17\_046) of the Imperial College Healthcare Tissue Bank, under the HTA license 12275 and REC: 17/WA/0161. *In vivo* data collection (and accompanied *ex vivo* sampling of tissue) was conducted under a dedicated ethical application (14/EE/0024), which was approved by both the London REC and Imperial College Joint Research Office.

### 4.3 Patient recruitment

Patients were considered eligible for inclusion if they were undergoing surgical or endoscopic resection of colorectal tissues at Imperial College NHS Trust or the Royal Marsden NHS Trust. Patients were identified pre-operatively through screening of MDT records and theatre lists, following which they were approached by a member of the research team. Written and informed consent following provision of a patient information sheet was necessary for inclusion in all cases, at which point a patient was assigned a study ID. Patients were excluded if they suffered with hereditary polyposis syndromes, inflammatory bowel disease or if the age was less than 18 years.

## 4.4 Sample collection and storage

### 4.4.1 Tissue collection from surgical and endoscopic resections

Tissue was collected from segmental surgical colorectal resections (such as hemicolectomies or anterior resections), local excision of rectal lesions (such as TAMIS) and endoscopic resections (such as EMR). In all cases, once resection had been complete, the fresh tissue was transported immediately to the histopathology department for *ex vivo* dissection by a histopathologist. In the case of radical resections, the specimen was opened longitudinally using Mayo scissors, avoiding non-peritonealised surfaces and the tumour mass. Macroscopically normal (at 10cm from the primary lesion), polyp or tumour tissues were dissected for research using a scalpel blade in pieces ranging from 5-500mg, in such a fashion as not to compromise the clinical diagnosis (such as by sampling the invasive margin). Following research sampling, specimens were submitted as usual for clinical pathological diagnosis.

### 4.4.2 Sample storage

Tissue samples were placed in sterile 2ml microcentrifuge tubes with a screw cap (Mircrowtube™, Simport Scientific, USA), labelled with tissue type, patient ID and if appropriate, location sampled. These were snap frozen in liquid nitrogen where possible, before being placed into a -80°C freezer for storage until analysis.

## 4.5 REIMS tissue analysis

### 4.5.1 Technical specifications

#### 4.5.1.1 MS Instrumentation

REIMS analysis was conducted on a Xevo G2-S qToF mass spectrometer (Waters Corporation, USA), which is a self-contained unit consisting of a wheel-mounted MS and computer screen; measuring approximately 69.2 x 162 x 101.8cm (W x H x D; figure 4.1.A).

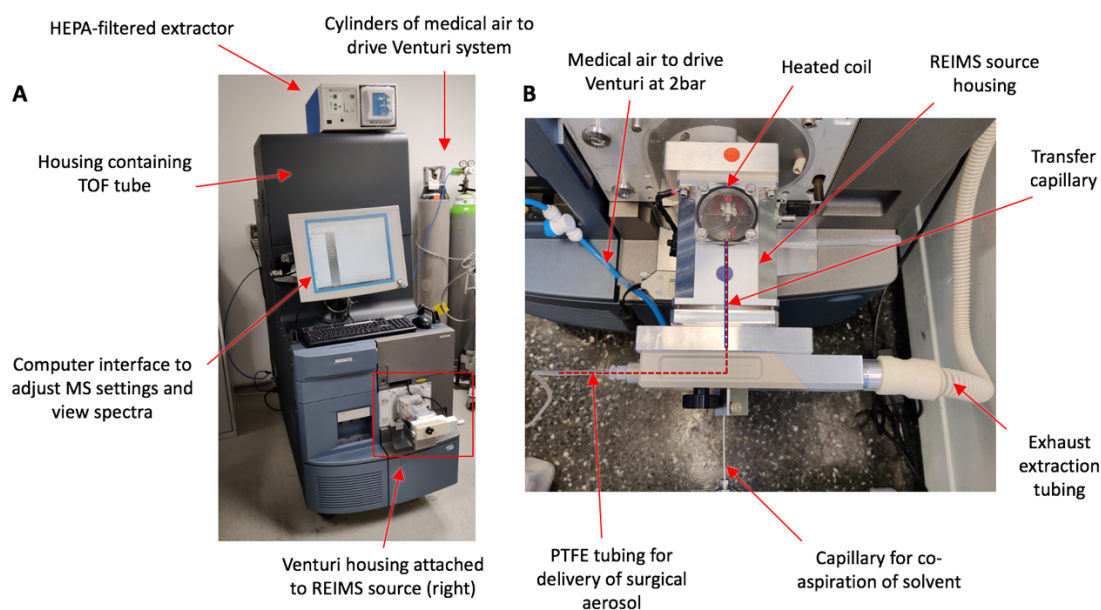


Figure 4.1 – The Xevo G2-S qToF mass spectrometer (Waters Corporation, USA) used for all *ex vivo* and *in vivo* analyses (A). A close view of the Venturi system attached to the REIMS source is presented (B), with the path of surgical aerosol shown (dashed maroon line).

For successful operation of the instrument, several infrastructure components were required. Medical-grade gases were either supplied from cylinders or the infrastructure of the space (for example, the plumbed medical air supply for anaesthetic machines in the operating theatre could be shared using a splitter). The power supply to the MS was the commonly found 240V outlet, with a surge-protector used. It was necessary that power was uninterrupted in the hours proceeding use to ensure the TOF vacuum pressure is pumped sufficiently low (maximum  $1.2 \times 10^{-6}$  mB) and to promote stability of the system electronics. The Venturi housing (shown in figure 4.1.B) contains the connections for tubing carrying surgical aerosol and the inlet for capillaries containing solvents for co-aspiration.

Calibration was performed using sodium formate, which forms clusters across the mass range with a  $m/z$  interval of approximately 68, with errors of <3ppm deemed acceptable. During MS acquisition, the device continuously acquired spectra across the 150-1200 $m/z$  mass range in negative ion mode, with a scan time of 1s. A solution of propan-2-ol (Sigma-Aldrich, UK) with

1ng/ $\mu$ l leucine enkephalin (Sigma-Aldrich, UK) was co-aspirated at a rate of 0.2ml/min, increasing the signal intensity whilst providing a lock mass reference standard. The collision surface of the REIMS source consisted of a Kanthal (an iron-chromium-aluminium) coil heated to 900°C.

During MS/MS analyses, data was acquired over a 50-1200m/z range, with co-aspiration of only propan-2-ol. An m/z value of interest (identified using statistical analyses) was inputted for selective passage through the quadrupole, with the m/z window tuned using a high mass (most commonly set to 18), a low mass slider (most commonly set to 14) and an ion energy of 0.5. The collision gas was either nitrogen or argon, with collision energies ranging from 30-60meV, aiming for an intensity of parent ion that is one third that of the highest fragment.

#### 4.5.1.2 Aerosol generation and delivery

Tissue was analysed using monopolar diathermy in the *cut* or *coagulation* modes at 20W power. *Ex vivo*, this was achieved using a generic handheld, finger-controlled diathermy pencil, with a short (approximately 1cm) flat blade acting as the main electrode (figure 4.2), with current generated by a commercially available electrosurgical unit (Covidien, Medtronic, UK; figure 4.3). *In vivo* application during TAMIS used the same electrosurgical generator but it was attached to a variety of pointed laparoscopic instruments and controlled by foot pedal.

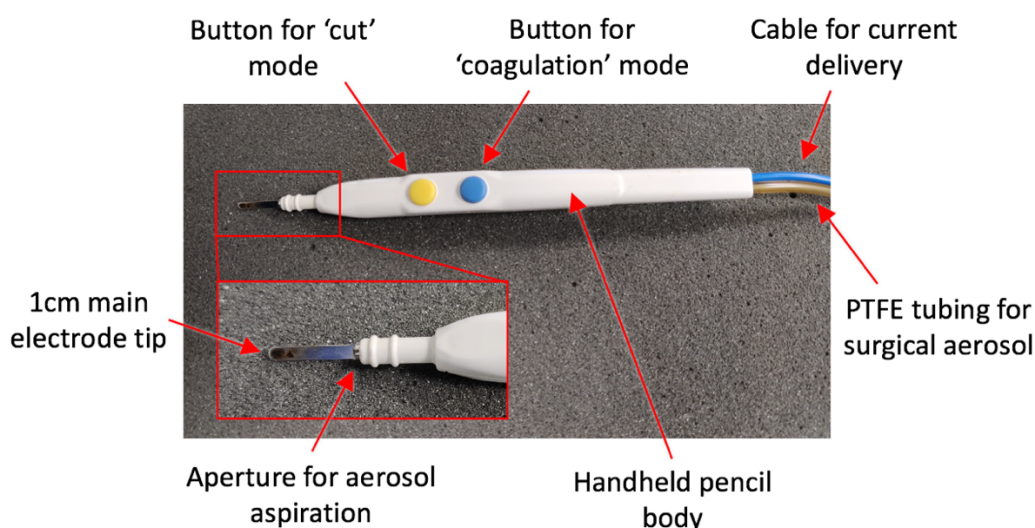


Figure 4.2 – the monopolar diathermy pencil handpiece used in *ex vivo* REIMS analysis. The main electrode tip applies the current to the tissue following activation of buttons by the operator's thumb. An aperture at the base of the tip aspirates the surgical aerosol through the body of the handpiece and into the PTFE tubing to the mass spectrometer.

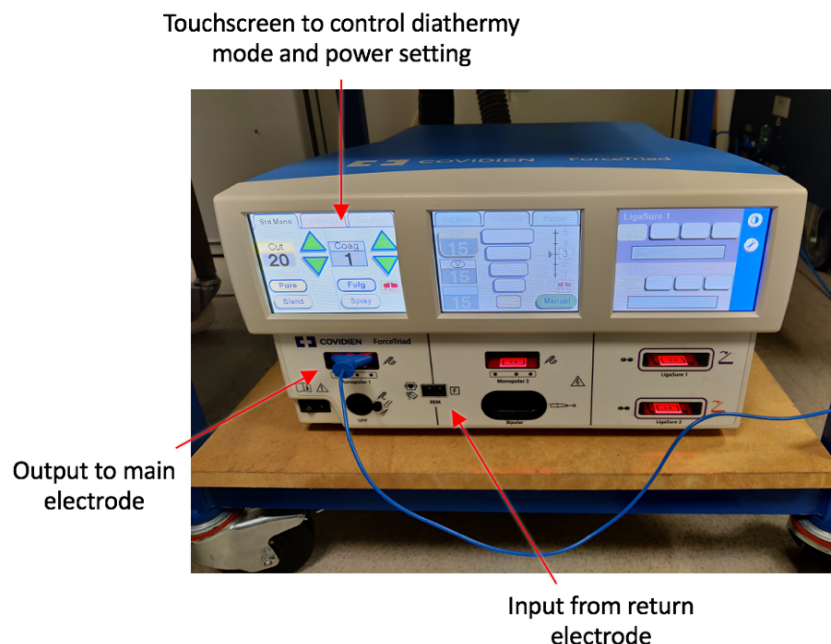


Figure 4.3 – the monopolar electrocautery current generator (Covidien, Medtronic, UK), used for *ex vivo* REIMS analysis and *in vivo* during TAMIS.

Tissue was also analysed *ex vivo* using a 10.6mm CO<sub>2</sub> laser (Omniguide Inc, USA), with a 1.46mm diameter flexible photonic bandgap fibre (Elevate Fibre, USA) inserting into a handpiece (BeamPath NEURO, OmniGuide Inc, USA). The laser was used with a power setting of 3W in superpulse mode, which equates to a peak power of 80W at a frequency of 330Hz, pulse on time of up to 100µs and pulse off time of 3.3ms. Pressurised helium gas (30psi) was used for fibre cooling. Experience applying the energy devices during *ex vivo* MS analysis was such that sufficient TICs could be generated from short applications, most commonly in the region of 1-2 s. Longer burns (2-5s) were used for MS/MS experiments, where a greater number of the parent ions was required to reduce noise.

The aerosol generated from an energy device was aspirated through a polytetrafluoroethylene (PTFE) tube with an internal diameter of 3mm, which was either integrated (in the case of the handheld pencil, as shown in figure 4.2), or taped alongside the TAMIS dissection instrument with the opening 1cm from the tip. The standard length of this tubing was 2.5m and would only be increased during *in vivo* sampling if deemed necessary, for example, to ensure adequate distance from the sterile field. In order to rapidly transport aerosol contents to the MS, a negative pressure was applied from an atmospheric Venturi interface (figure 4.1.B). This Venturi system is driven by

pressurised medical air at 2bar, applied orthogonally to the aerosol flow and towards the heated capillary inlet.

To protect the researchers from aerosols during *ex vivo* REIMS analyses, these were conducted in a hood equipped with a fume extractor (Wellar WFE 2ES) and the Venturi block was attached to a filtered extractor (RapidVac™, Covidien, Medtronic, UK; as shown in figure 4.1).

#### 4.5.2 Workflow for *ex vivo* tissue analysis

The workflow for *ex vivo* REIMS analysis is as follows:

1. Prepare instrument including calibration
2. Freshly thaw tissue sample to be analysed at room temperature
3. Cut tissue pieces for optimal analysis:
  - a. For larger samples - cut each piece to approximately 125mm<sup>3</sup>, allowing easier histological validation by reducing the risk of there being multiple tissue subtypes
  - b. For normal mucosa – remove the muscularis mucosae if possible to avoid solely muscle burns
4. Apply the energy instrument 1-3 times per tissue piece to perform the REIMS analysis. The burns are targeted at the luminal surface (and away from the cut edge). A dedicated raw spectral file is created for the analysis of each tissue piece
5. Tissue is placed in an embedding cassette with the burn placed face-down, labelled with the name of the raw spectral file
6. The cassette is placed in a 10% formalin solution and submitted to the histopathology department
7. Spectral files uploaded to research storage server
8. Instrument cleaning

#### 4.5.3 Workflow for *in vivo* tissue analysis

The workflow for *in vivo* REIMS analysis differs from the *ex vivo* approach as described below:

1. Transport mass spectrometer to the operating theatre the evening before to allow the TOF vacuum to pump down for at least 8 hours. The MS is to be positioned in a corner of the space to interfere as little as possible with the clinical procedure
2. On the morning of analysis, prepare the instrument and solvents, including calibration
3. Fix the PTFE aspiration tube alongside the TAMIS dissector using sterile adhesive sheets
4. Video record the instrument screen and the clinical environment using mounted GoPro™ cameras (GoPro, USA). The HD laparoscopic video output will be recorded directly through the stack system
5. Create a single raw spectral file for the whole case and continually collect REIMS data as the energy devices are being used clinically
6. The surgical specimen is to be transported to the pathology department where if necessary, the researcher will help orientate the specimen
7. Following the case, all videos and raw spectral files to be uploaded to research storage server
8. Instrument cleaning

#### 4.6 Histopathological validation

Histopathological validation of REIMS tissue samples was conducted to confirm the pathological subtype of the tissue analysed. Following REIMS analysis, the research tissue samples were placed in foam-lined embedding cassettes (Acetal Histosette™, Simport Scientific, USA), appropriately labelled using a printer (Sakura iDent™, Sakura, Netherlands) and fixed in solution of 10% neutral buffered formalin for at least 72 hours. Following fixation, samples were transported to the histopathology department for paraffin embedding following their standard protocols. In summary, this involved gradual dehydration with ethanol baths followed by impregnation of the tissue with molten paraffin wax attached to the original cassette. Once cooled, a 5µm section was cut on a microtome, floated out on a water bath at 45°C and then picked up into the centre of a labelled glass slide (SuperFrost Plus™, Thermo Scientific, USA). Once dry, haematoxylin and eosin (H&E) staining was conducted.

H&E sections were interpreted by a histopathology professor specializing in gastrointestinal disease (Professor Goldin), applying the same diagnostic criteria as are used clinically (such as the

revised Vienna Classification<sup>191</sup>). The following information was recorded: diagnosis, section percentage containing pathology of interest, pathological subtype of disease (such as adenoma type), grade of dysplasia (for adenomas only) and any other pertinent features (such as evidence of ischaemia or necrosis).

## 4.7 Statistical Analyses

### 4.7.1 Clinical data collection

Clinico-pathological data were collected from the electronic healthcare record for each included patient and stored in a pseudo-anonymised research database. This included patient demographics, co-morbidity status, operation date, lesion descriptors, pathological report of resected lesions and the use of neoadjuvant or adjuvant chemoradiotherapy. Clinical outcomes such as cancer recurrence and death were assessed by reviewing the health record and surveillance radiographic images.

### 4.7.2 *Ex vivo* REIMS data analysis

#### 4.7.2.1 *Data pre-processing*

Pre-processing of raw spectral data was conducted in Abstract Model Builder (AMX v1.0.2055, Waters Research Centre, Hungary), where burns within each data file could be automatically or manually selected, generating one mass spectrum per burn. These then underwent background subtraction, lock mass correction (to 554.2615m/z for [M-H]<sup>-</sup> leucine enkephalin ion in negative mode), normalisation and binning to 0.1.

#### 4.7.2.2 Univariate and multivariate statistical analysis

The multivariate statistical technique of PCA and LDA were conducted in AMX, where between 30 and 60 PCs were used (depending on the power of the dataset), applied over a selected m/z range. Analyses of the whole mass range were over 150-1200m/z and focused analyses for the complex lipids were conducted over 600-1000m/z. AMX could also be used to generate graphical outputs in addition to performing cross validation (CV), which was set at leave-one-patient-out (LOPO). Binned data that had undergone pre-processing could also be exported from AMX in the form of a CSV file, allowing further chemometric functions in other programs. Data was imported into SIMCA v15 (Umetrics, Sweden) to undergo multivariate statistical tests such as OPLS-DA, VIP scoring or plotting of S-curves. OPLS-DA models were built conservatively, where addition of new X-Y or orthogonal components would not cause a decrease in  $Q^2$  (and therefore should not suffer with over-fitting), with  $R^2$  used as the headline metric of goodness of fit. Univariate techniques such as ANOVA were conducted in RStudio v1.1.419 to determine differences in relative intensity between groups, with  $p$  value correction using the Bonferroni technique and a corrected  $p$  value of  $<0.05$  used to determine statistical significance. Signal:noise ratio (defined as the median intensity of the 20 most intense peaks divided by the median intensity of all peaks in 600-1000m/z) was calculated in Spectrum Quality Analyser (Waters Research Centre, Hungary).

#### 4.7.2.3 Metabolite identification

ANOVA, S-plots and VIP scores were used to highlight the m/z values which were responsible for differentiating groups of interest, which could then undergo MS/MS analyses. The exact mass of the parent ion was determined using MassLynx™ (v4.1, Waters Research Centre, Hungary), with visual spectral interrogation used to ensure this was a true peak (defined as at least three times the background intensity). Identification of metabolites or their fragments was conducted with the assistance of publicly available databases (METLIN<sup>145</sup> and LIPID MAPS<sup>146</sup>), published literature and calculation from first principles. The error accepted between the experimentally measured and theoretical mass of putatively identified molecules was 10ppm.

### 4.7.3 *In vivo* REIMS data analysis

Intraoperative tissue recognition could be performed using AMX Recognition (v1.0.1581, proprietary to Waters Research Centre, Hungary), which is built upon the LDA models generated from *ex vivo* analysis of colorectal tissues. As new MS data is presented, this program gives continual predictions of tissue subtype at 1s intervals whenever the TIC intensity exceeds a set threshold, with programmable outlier detection and lock-mass correction. The prediction of the recognition software is accompanied by a probability, calculated based on the Mahalanobis distance of the new spectra from the existing groups, such that a 50% probability represents equidistance from two groups. A threshold for this probability to allow predictions of disease (such as tumour or adenoma) can be applied, with 90% used in this thesis (representing a 50% further distance to the normal group than to the disease group, aiming to reduce false positives). The AMX software can be run in real-time on the computer of the MS and the prediction can be presented and continually updated in real-time to the surgeon via a graphical interface, as shown in figure 4.4.

To determine the *in vivo* accuracy of the recognition software, operative videos were co-registered with the raw spectral file and the histological report of the tissue sample, allowing clinical annotation of each burn with data such as tissue type being analysed, layer being dissected and presence of contamination. This produces a 2x2 contingency table from which diagnostic accuracy metrics could be calculated.



Figure 4.4 – screenshot of the AMX Recognition software, with a visual alert given to the operator both as a colour warning and as a written prediction with percentage. The lower panel denotes the ion intensity over time and three distinct analyses can be demonstrated in this excerpt. The right-sided panel lists the classification predictions as they occur, with the scan number that they apply to.

#### 4.7.4 Non-spectral data analysis

Non-spectral data underwent basic descriptive and analytical processes depending on the data type. Parametric data was described using mean and standard deviation (SD), whereas non-parametric data is presented as median and interquartile range. Continuous datasets were compared using Student's t-test or Kruskal-Wallis for parametric and non-parametric data respectively. Independent categorical variables were compared using the Pearson's chi-squared test ( $\chi^2$ ) unless >20% of the expected cell totals were less than five, in which case Fisher Exact test was used. Multivariate binary logistic regression was used to assess the effect of different dependent variables on an outcome. All of the above and their graphical outputs was conducted in RStudio v1.1.419 (using the *tidyverse* collection of packages<sup>320</sup>) or Excel (Microsoft Excel for Mac v16, Microsoft, USA).

## Chapter 5 – WP1: REIMS spectral quality control

### 5.1 Introduction

Mass spectrometers are complex and sensitive instruments where a large variety of factors can be responsible for variability in data quality, which has prompted the use of quality control procedures in techniques such as LC-MS<sup>321</sup>. These are applied during the sample analysis stage as well as during data processing and analysis, to mitigate against reproducibility and accuracy vulnerabilities of the instrument. Initial work using REIMS has focused on method development and proof-of-concept *in vivo* translation, however little work has been published on spectral quality control. This would be required to create a viable clinical diagnostic device by ensuring robust and reliable generation of high quality data<sup>322</sup>.

A significant challenge with REIMS data analysis is that no framework currently exists to appraise spectra for their quality and to define those with sufficiently high quality to allow inclusion in statistical analyses. Inclusion of poor-quality spectra with systematic biases would reduce the accuracy of the statistical models used for tissue recognition, increasing the probability of incorrect classifications that may adversely impact patient care. It is therefore necessary to systematically and objectively define these quality factors and create a REIMS data pipeline, where filtering can be used to select which spectra are included in creation of *ex vivo* databases and whether those collected *in vivo* are suitable for analysis. Once quality metrics have been defined for REIMS spectra and there is a better understanding of how these impact tissue recognition accuracies, it will then be possible to explore how other technical and environmental factors impact quality. This is of particular importance when considering translation of the technology into clinical settings, where the instrument operators have a much-reduced control in this dynamic and unpredictable environment.

This work plan will address spectral quality in two parts – first, by attempting to define minimum quality thresholds for REIMS spectra and second, assessing the impact of technical and environmental factors on REIMS spectral quality.

## 5.2 Defining quality for REIMS spectra

### 5.2.1 Aim

The aim of this study was to assess how technical, statistical and histological variables impact the accuracy of REIMS for colorectal tissue recognition, allowing minimum spectral quality standards to be defined.

### 5.2.2 Methods

An annotated dataset was constructed for this study in November 2018, containing all REIMS spectra from *ex vivo* analysis of colorectal tissue conducted by the research group to date.

#### *5.2.2.1 Patient recruitment and sample collection*

Patients who had undergone surgical or endoscopic colorectal resection from November 2014-August 2018 and had been recruited for colorectal tissue bio-banking were eligible for inclusion in this study (refer to chapter 4 for details). Patients with inflammatory bowel disease, hereditary polyposis syndromes or age less than 18 years were excluded.

#### *5.2.2.2 MS analysis and specifications*

Whole tissue samples were thawed immediately prior to MS analysis using either a handheld monopolar diathermy at 25W or a CO<sub>2</sub> laser in 'SuperPulse' mode at 3W. The surgical aerosol was aspirated into the Xevo G2-S qTOF mass spectrometer (Waters Corporation, USA) with the Venturi interface and co-aspiration of leu-enkephalin in isopropanol (20ng/ml concentration) at a flow rate of 0.2ml/min. The instrument used to analyse tissue was often determined pragmatically based on which MS was functioning at the laboratory site storing the batch of tissue for analysis. Dolores was primarily used during 2015 and a batch in August 2018, with the rest performed on

Christina. Spectra were collected in negative mode across the 150-1200 m/z range. Following analysis, samples underwent histological validation. All tissue samples and spectra generated prior to October 2017 were collected by Dr James Alexander, with me responsible for all data collection after this time. All processing, analysis and interpretation of all data was performed by me. Full details of the analytical methodology can be found in chapter 4.

### *5.2.2.3 Data Analysis*

Eight variables which have the potential to impact the quality of spectra and therefore the accuracy of REIMS in performing tissue recognition were chosen following discussion within the research group. These were:

1. Non-mucosal sampling
2. Percentage of histological section containing index tissue during validation
3. Presence of technical batch effects
4. Spectra signal:noise ratio
5. Background noise between lipid peaks
6. Total ion current
7. Presence of contaminants
8. Diathermy mode used

Raw spectral data were pre-processed in Abstract Model Builder (Waters Corporation), with binning at 0.1, normalization, lock-mass correction and background subtraction. Modelling was conducted using PCA and LDA (60 PC components) between 600-1000m/z, with LOPO CV used to determine model accuracy. For binary variables (such as the presence or absence of a contaminant) the accuracy of REIMS in differentiating carcinoma, adenoma and normal mucosa was compared between each condition. For continuous or ordinal data (such as TIC), sensitivity analyses were conducted. For each variable, several thresholds were chosen which when applied, would determine which spectra were to be excluded from analysis. The accuracy of REIMS for colorectal tissue recognition was then determined for each threshold, with comparisons made between them. The minimum quality requirement for spectra was defined as the point at which increasing a variable threshold caused no significant further increase in diagnostic accuracy.

### 5.2.3 Results

The dataset consisted of 1220 spectra generated from the tissue of 144 patients, with 589 spectra from normal mucosa, 443 from tumour and 188 from adenoma. Patient demographics in addition to clinico-pathological and analytical data for the spectra can be found in table 5.1.

When spectra of all quality are analysed, the PCA plot demonstrates a lack of clear clustering by tissue type, with an LDA plot demonstrating significant overlap between the cluster borders and notable spectra a large distance from the group centroid (figure 5.1). This results in an 81.2% accuracy for REIMS in the prediction of tissue subtype, with misclassifications demonstrated across all tissue subtypes and notably with 19% of tumour samples predicted to be normal.

		Factor	Number (%)
<b>Patient Demographics</b>	Gender	Male	79 (55)
		Female	65 (45)
	Mean Age		70.3
	Ethnicity	White	93 (65)
		Asian	18 (13)
		Black	9 (6)
Other		4 (3)	
Unknown		20 (16)	
		Factor	Number of Spectra (%)
<b>Samples</b>	Location	Right	505 (41)
		Left	238 (20)
		Rectum	422 (35)
		Unknown	55 (5)
	Tissue Subtype of Spectra	Tumour	443 (36)
		Normal	589 (48)
Adenoma		188 (15)	
		Year	
<b>Analysis</b>	Year	2014	42 (3)
		2015	786 (64)
		2016	56 (5)

	2017	68 (6)
	2018	268 (22)
Instrument	Dolores	191 (16)
	Christina	875 (72)
	Unknown	154 (13)

Table 5.1 – characteristics of patients included in the dataset, with clinico-pathological and analytical features for spectra generated.

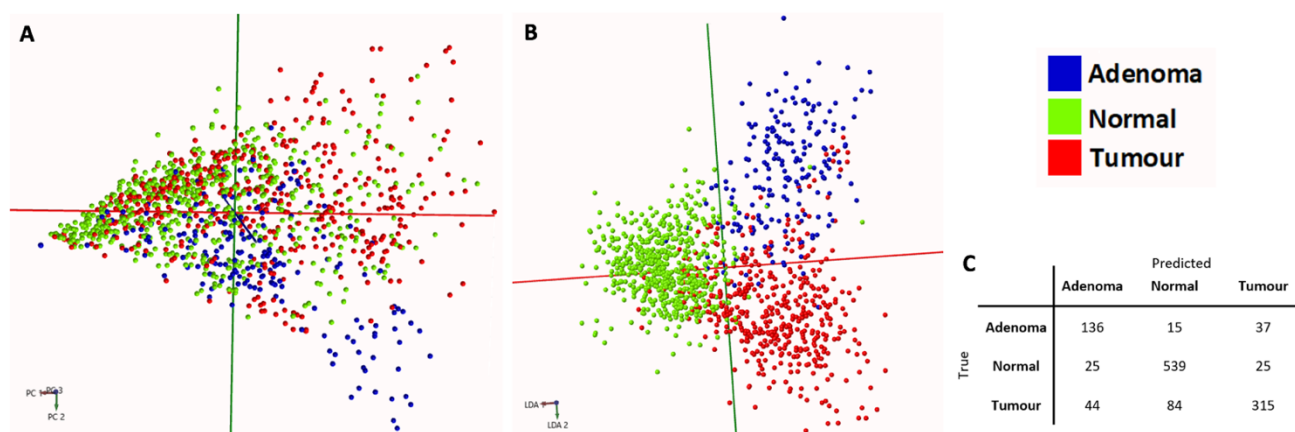


Figure 5.1 – PCA (A) and LDA (B) plots for all analyses of colorectal tissue, with the confusion matrix following LOPO CV (C).

### 5.2.3.1 Histological validation

Samples may be considered to fail histological validation following analysis with REIMS for a variety of reasons. The technology is designed to sample the colorectal mucosa and therefore if a research sample contained only muscularis or fat, then it was excluded from analysis ( $n = 93$ ). In addition, a greater intensity of TGs implies significant sampling of the submucosa and therefore if the maximum triglyceride intensity was greater than 50% of the maximum glycerophospholipid intensity, spectra were excluded ( $n = 35$ ). If the histological section was non-diagnostic, all spectra from this sample were excluded ( $n = 21$ ). These changes improved the accuracy of REIMS in differentiating carcinoma, adenoma and normal for the remaining 1071 spectra from 81.2 to 83.6%; and therefore, these exclusion criteria were applied forthwith.

When considering adenoma and carcinoma, it is also necessary to determine the minimum proportion of the validation section that needs to contain the tissue subtype in order to consider

validation successful. This is in consideration of the trade-off between diluting the metabolomic signal of tumour with an overwhelming proportion of normal tissue in the sample, against the need for REIMS to detect invasive margins where tumour cells may be in the minority. Sensitivity analyses were conducted for different threshold levels, where if the tumour or adenoma cells constituted less than the threshold level in the sample, all spectra from that analysis would be excluded (figure 5.2). This revealed that once 15% is reached, there is a relative plateau in diagnostic accuracy until 40%, where it increases to another plateau. In order to balance accuracy and sensitivity, a minimum of 15% of index tissue in the validation section was a requirement for the ongoing studies.

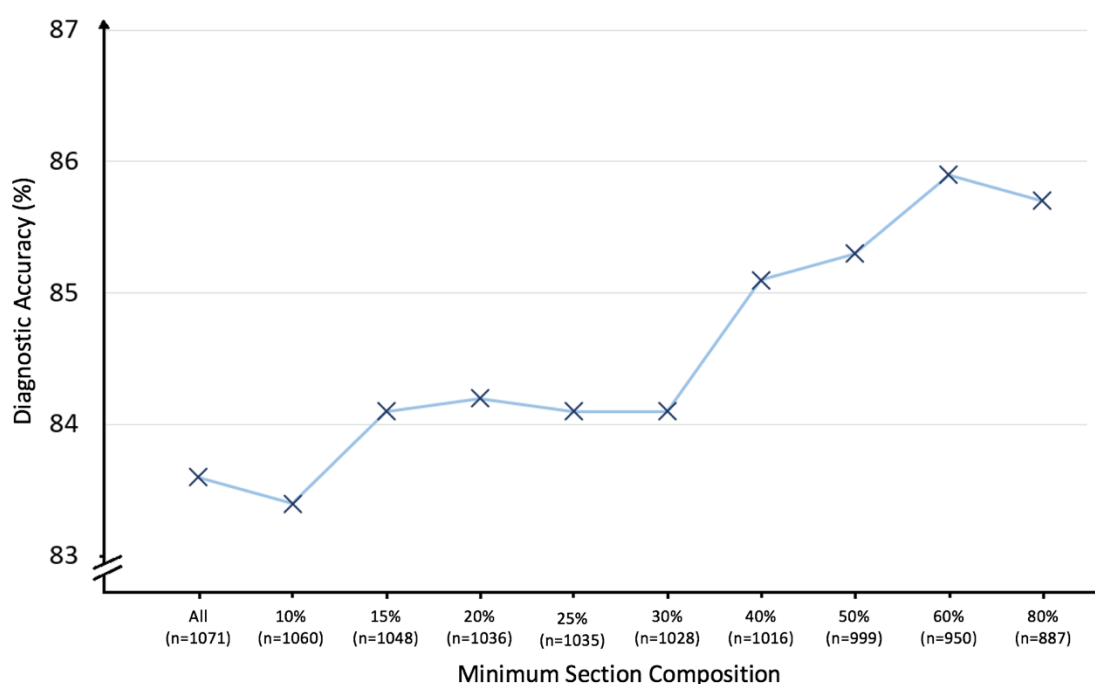


Figure 5.2 – Scatter plot demonstrating how the accuracy of REIMS in differentiating cancer, adenoma and normal mucosa differs based on the minimum composition of cancer or adenoma tissue in the sample.

### 5.2.3.2 Batch effect

When using 3-dimensional PCA plotting of all spectra, it is apparent that there is a batch effect of samples clustering distinctly to the majority along PC3, including all tissue types (figure 5.3.A). The cause of this was interrogated using multivariate binary logistic regression, where the analysis of deviance revealed that the use of the Dolores instrument had the greatest impact on the model,

with a high level of statistical significance ( $p = 2.2 \times 10^{-16}$ ). Deeper investigation revealed that the 109 spectra in the batch effect were all conducted on the Dolores instrument between March and June 2015. Plotting the spectra of the samples identified that the batch was caused by a mass shift, where peaks drifted up or down by a 0.1 width bin depending on their position in the mass range (figure 5.4). It was revealed on review of the instrument logs that the mass shift was caused by not calibrating the instrument prior to analysing samples. When the 109 spectra in the batch effect are removed, the cluster on the PCA resolves (figure 5.3.B). Furthermore, the accuracy of the LDA model increases from 83.5 to 85.7%, with improvements in classification accuracy across all tissue types. It was decided that spectra involved in a batch effect seen on PCA due to mass shift would be excluded from final modelling.

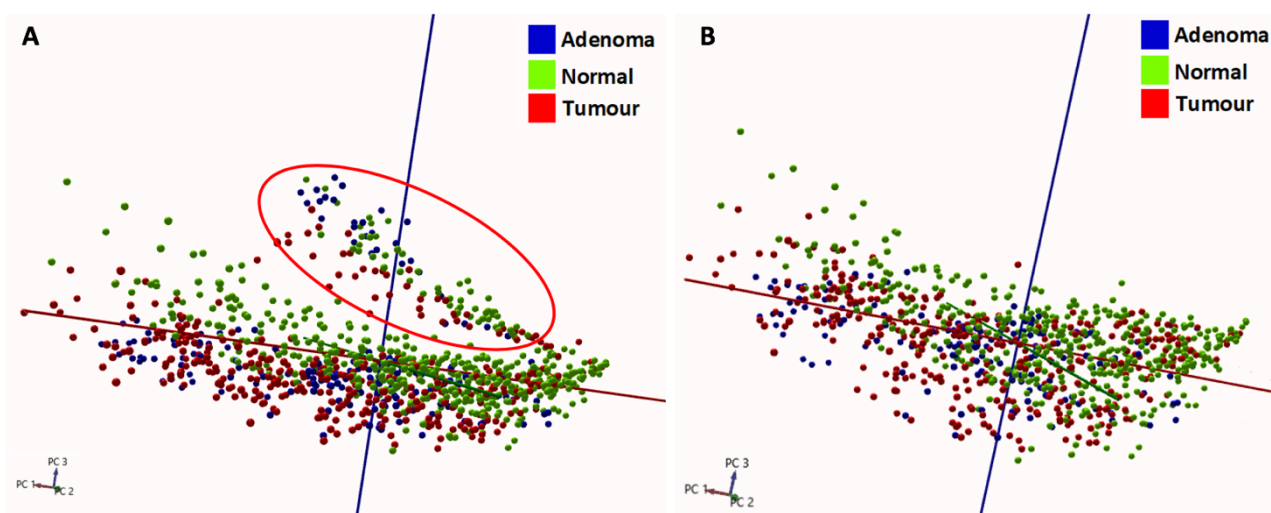


Figure 5.3 – 3-dimensional PCA plot of all data (A), revealing a batch effect (red circle) and a PCA plot after removal of all samples run by the Dolores instrument from March-June 2015 (B).

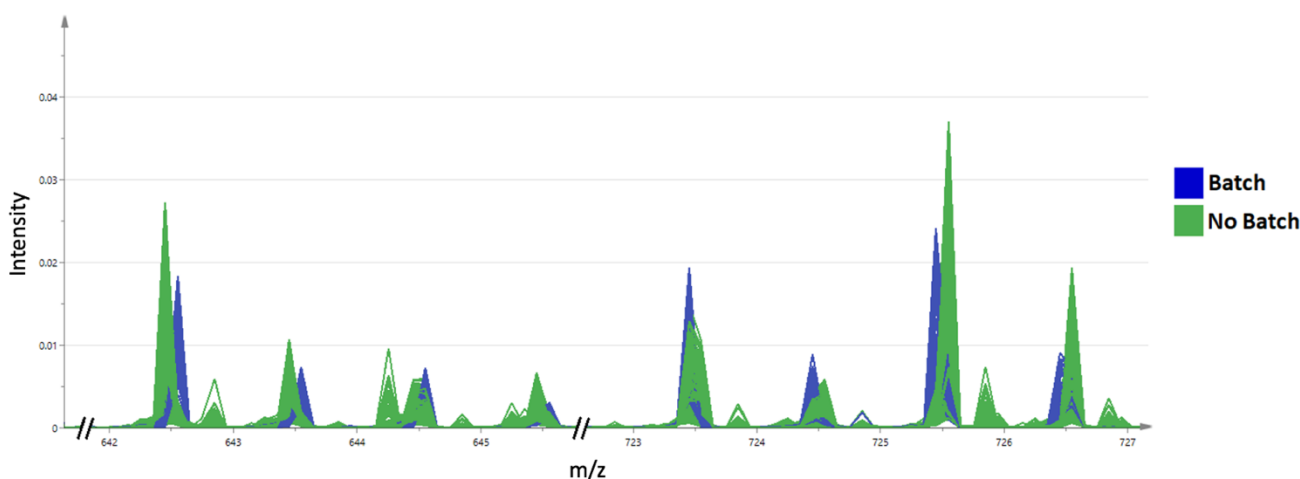


Figure 5.4 – plot of spectra coloured by whether they were present in the Dolores instrument batch effect or not, where masses were increased in the lower mass ranges and increased in the upper mass ranges.

### 5.2.3.3 Signal:noise ratio

Once spectra which had failed histological validation or which were involved in a batch effect had been excluded, the relationship between biological signal and random background noise was assessed for the 939 spectra remaining. This was achieved using the signal:noise ratio, based on the hypothesis that a higher value was more desirable as it indicated a greater relative sampling of biological and therefore metabolic data. The spectra demonstrated marked variation in signal:noise ratios, with a median of 3293, range of 101-49613 and a positive skew. Low signal:noise disproportionately impacted spectra from normal mucosa, with similarities between carcinoma and adenoma (figure 5.5). To understand how this impacts misclassification rate, spectra were ordered from low to high signal:noise and plotted against the cumulative count of REIMS misclassification, demonstrating that the lower signal:noise ratios appear to misclassify at a greater rate than their higher counterparts (figure 5.6).

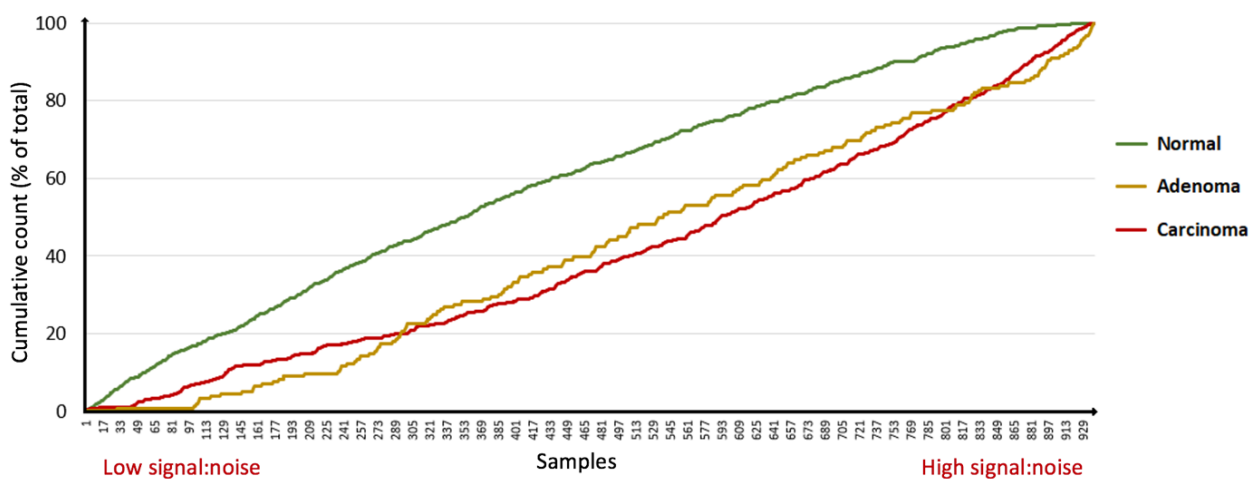


Figure 5.5 – cumulative count of spectra from carcinoma, adenoma and normal mucosa plotted as the signal:noise ratio increases from the lowest to highest value along the x axis.

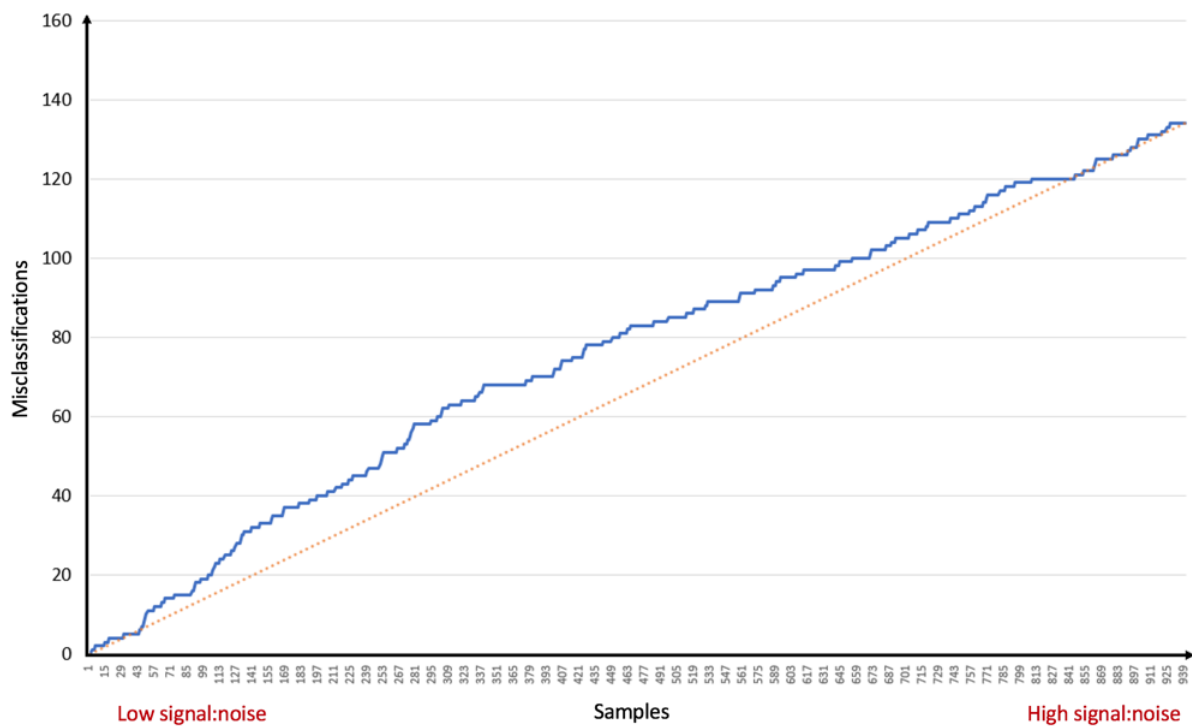


Figure 5.6 – the cumulative misclassification rate (blue) when spectra are ordered along the x axis from low to high signal:noise ratio. An equal probability of misclassification across the signal:noise range is presented (orange dotted line).

When plotting excess misclassifications for all tissue types (defined as observed - expected misclassification number and can be considered as the gap between the lines in figure 5.6), these appear to follow a pseudo-normal distribution, with an increase to a peak at approximately spectrum 330, corresponding to a signal:noise ratio of 2105 (figure 5.7.A). To assess whether this finding was specific to a particular tissue, this was also plotted for carcinoma, adenoma and normal mucosa. This demonstrates that low signal:noise spectra have the largest impact on misclassifications for tumour samples, with a rapid rise to a peak corresponding to a signal:noise ratio of 3000 (figure 5.7.B). Spectra from adenomas show a similar pattern however are impacted to a lesser degree, with a peak corresponding to a signal:noise of 2200 and a decreased gradient of downslope (reflecting a slower improvement in classification performance as spectral quality improves (figure 5.7.C)). Spectra from normal mucosa do not appear to have a clear relationship between misclassifications and signal:noise ratio, despite the earlier finding that they are over-represented in spectra with low signal:noise (figure 5.7.D).

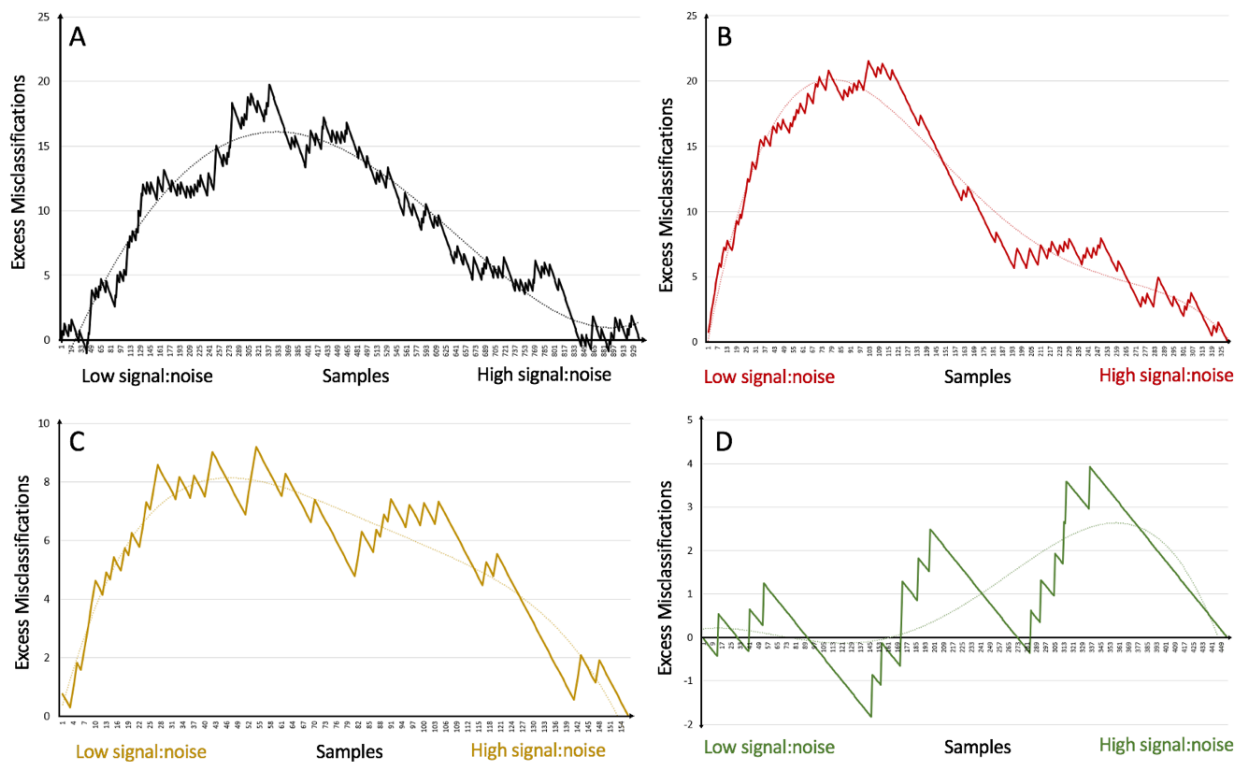


Figure 5.7 – Excess misclassifications as spectra are ordered along the x axis from low to high signal:noise ratio for all samples (A), carcinoma (B), adenoma (C) and normal mucosa (D). Polynomial trend lines are presented (dotted). A positive gradient denotes a greater rate of REIMS misclassifying tissue subtypes than expected.

Tumour spectra which misclassify have a background noise which is 64% higher than those that correctly classify ( $p < 0.001$ ), in addition to a signal that is 28% lower ( $p < 0.001$ ). A similar pattern is seen with adenoma spectra, however with spectra from normal mucosa, the signal and background noise are the same between those that classify correctly and those that do not ( $p = 0.45$  and  $0.65$  respectively). The signal:noise also had an impact on how tumour spectra misclassify, with a significantly higher rate of incorrect normal predictions when the signal:noise is low ( $p < 0.001$ ; figure 5.8).

	Tumour Misclassifications	
	Adenoma	Normal
High signal:noise	26	15
Low signal:noise	7	36

Figure 5.8 – The impact of high and low signal:noise on how tumour spectra misclassify.

A spectrum's signal:noise ratio has been shown to dramatically impact the risk of misclassification and therefore it is necessary to determine a minimum threshold for signal:noise, below which spectra will be excluded from statistical analyses. A sensitivity analysis with a range of thresholds is shown in figure 5.9, showing a marked increase in accuracy in differentiating tissue subtypes when a minimum signal:noise of 1000 is used, with no clear increase when using a higher threshold. For future analyses, this threshold will be applied.

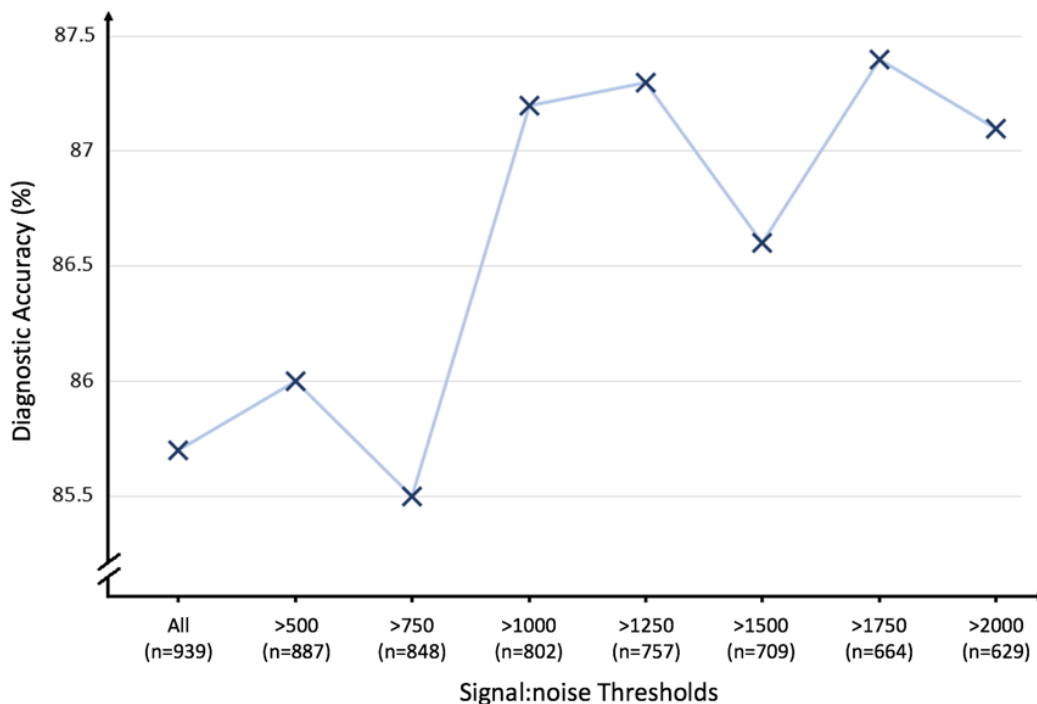


Figure 5.9 – the impact of minimum signal:noise thresholds on the accuracy of REIMS in differentiating spectra from tumour, adenoma and normal mucosa.

#### 5.2.3.4 Exclusion of bins with high background noise between lipid peaks

Following exclusion of spectra with a signal:noise of less than 1000, a PCA of the remaining 802 spectra demonstrates a possible batch effect (figure 5.10.A). Exploring the analysis date, it is apparent that this batch is largely due to a single analytical run in January 2018 (figure 5.10.B). The loadings plot reveals that this difference is being driven by bins where glycerophospholipids are less commonly seen in negative mode, such as between the  $m/z$  decimal places of  $x_{n.85} - x_{n+1.35}$  (figure 5.10.C). The cause for this is apparent when plotting the spectra, where it appears there is a markedly increased background noise across the bins between lipid peaks (figure 5.10.D). Excluding the bins that cover  $m/z$   $x_{n.80} - x_{n+1.40}$  for the whole mass range and  $x_{n.70} - x_{n.80}$  for the range 600-800 (to avoid excluding TGs found above this range), causes resolution of the batch effect on PCA (figure 5.10.E), however this process does not markedly improve diagnostic accuracy of REIMS, with a model accuracy changing from 87.2 to 87.4%. As such, the intensity of the background between lipid peaks was not used as a quality metric in future analyses.

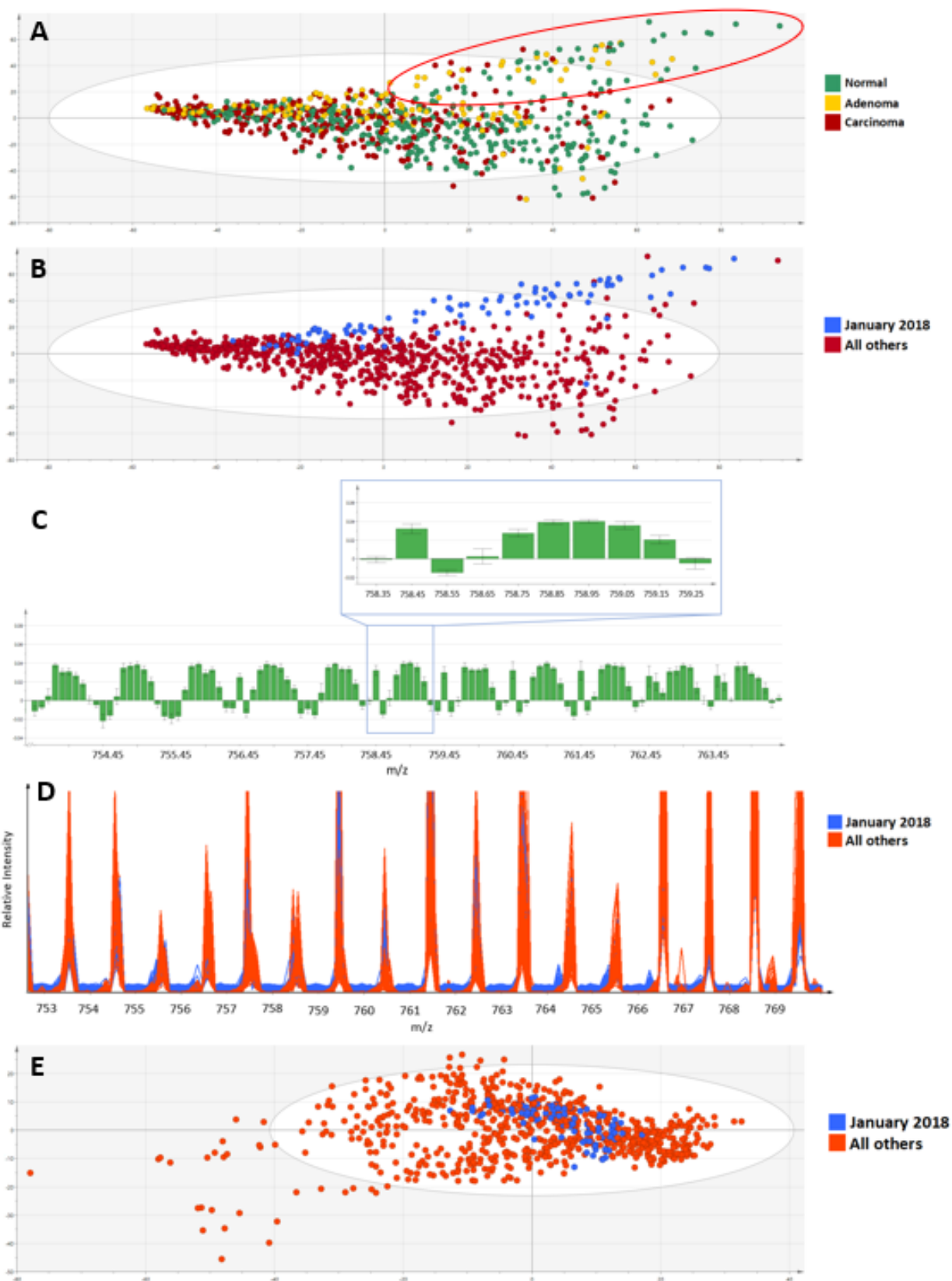


Figure 5.10 – PCA plot of the 802 spectra labelled by tissue subtype (A), demonstrating a possible batch effect (red oval), with this batch effect again evident when labelling the analytical run in January 2018 (B). A loadings plot of a model differentiating the January 2018 batch and other analyses (C) demonstrates marked increase in the intensity of the bins between  $x_{n-75}$  -  $x_{n+1.25}$ , as seen on the raw spectra (D). Plotting a PCA once the bins between common lipid peaks are excluded removes the batch effect (E).

### 5.2.3.5 Minimum TIC

Whilst the exclusion of bins between the common lipid peaks did not influence the diagnostic accuracy of REIMS, the updated PCA did reveal a new batch of outliers (figure 5.11.A), which when labelled, appeared to be due to low TIC. Despite subsequent normalization, this batch demonstrated reduced variation and intensity of biological data compared to spectra not in the batch (figure 5.11.B-C). The majority of samples analysed in this run were adenomas, however this was not a tissue-specific finding when the spectra were compared to adenomas analysed on other dates.

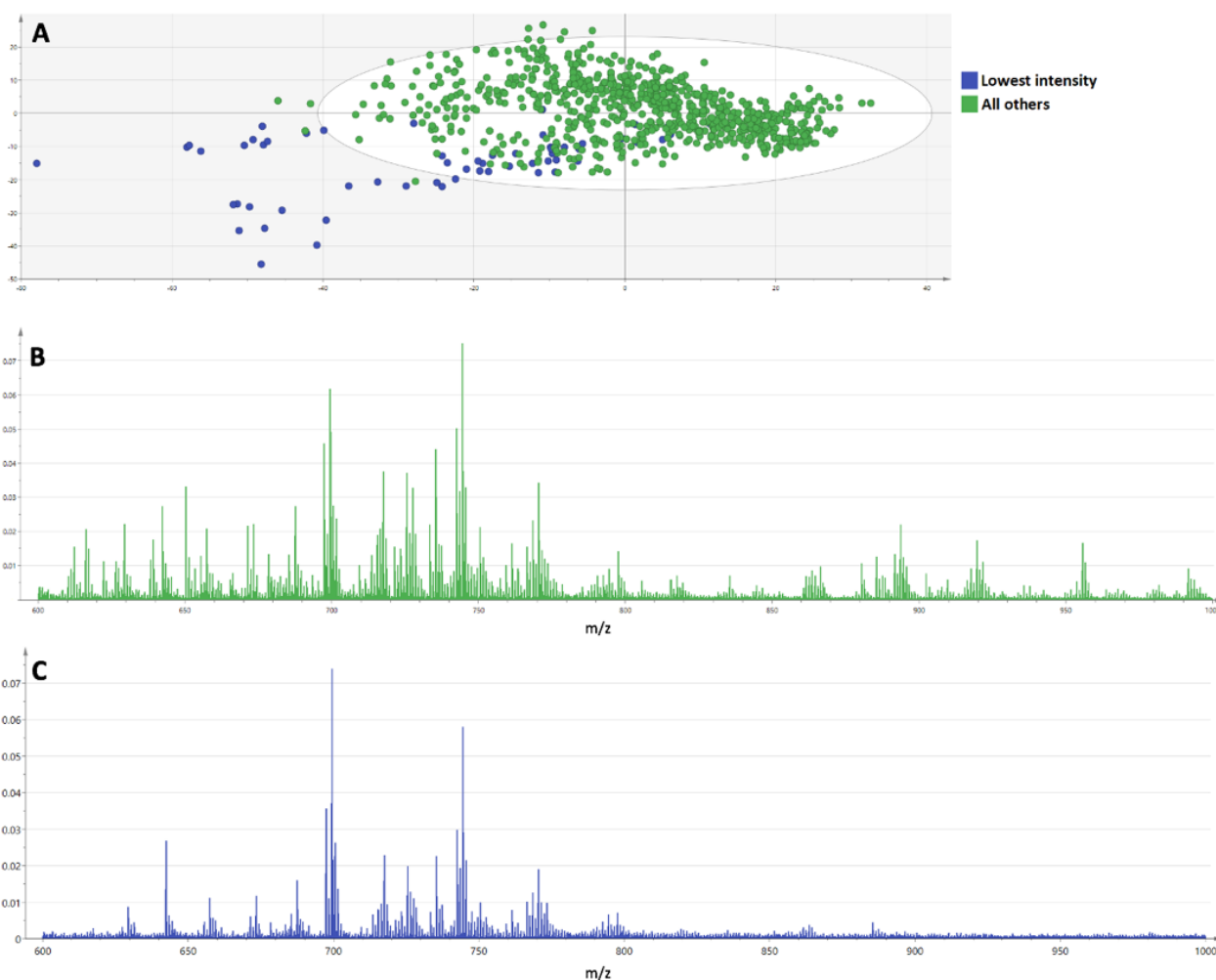


Figure 5.11 – PCA plot with the 60 (7.5%) spectra of lowest TIC labelled (A). An aggregate of spectra with high intensity (B) compared to those with lowest intensity (C).

A sensitivity analysis was conducted to assess for the impact of TIC on the accuracy of REIMS. Excluding the spectra with the lowest TIC in 5% increments did not appear to improve the diagnostic accuracy of REIMS significantly and therefore minimum TIC was not used as a quality metric (figure 5.12).

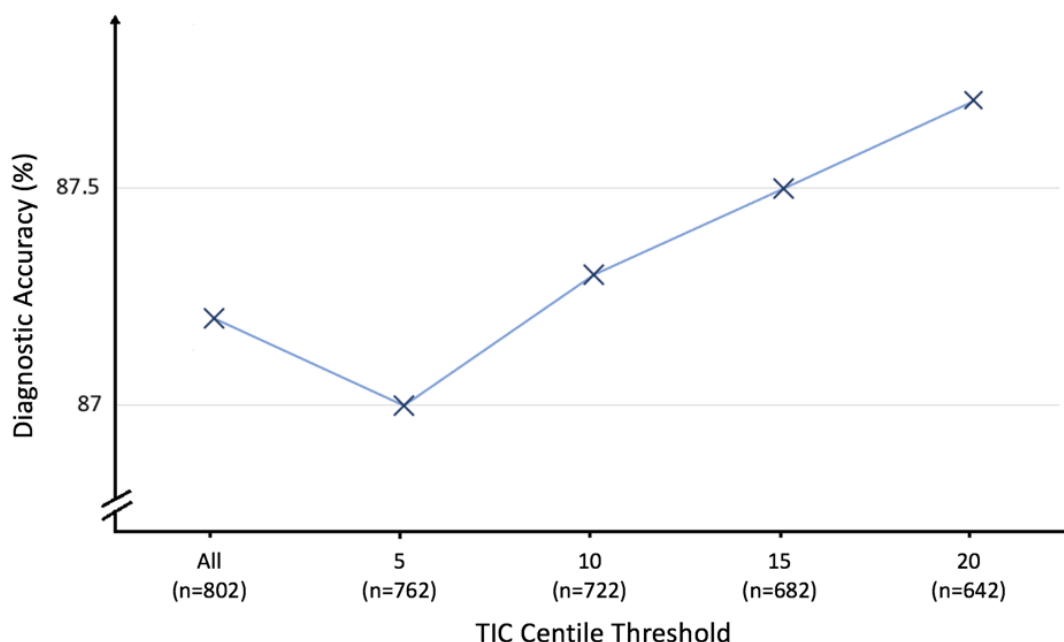


Figure 5.12 – Accuracy of REIMS in differentiating carcinoma, adenoma and normal mucosa when spectra are excluded using different centile thresholds of TIC.

#### 5.2.3.6 Presence of sodium formate contamination

On visual inspection of two spectra, there was a significant volume of sodium formate clusters present in the background of the spectra, most likely as a carry-over from the calibration step (figure 5.13.A). These peaks were still present after background subtraction (figure 5.13.B) contributing to them being outliers based on Hotelling's  $T^2$ . Furthermore, some of the sodium formate clusters were falling into the same bins as lipids, artificially increasing the relative intensity. An example is the cluster at 724.49 m/z, which joins the M+1  $^{13}\text{C}$  isotope of [PA(38:4)-H]<sup>-</sup> (exact mass 724.4998) in the bin covering 724.40 – 724.50 m/z. As a result, the presence of contaminants within the analytical mass range was considered sufficient for exclusion of spectra.

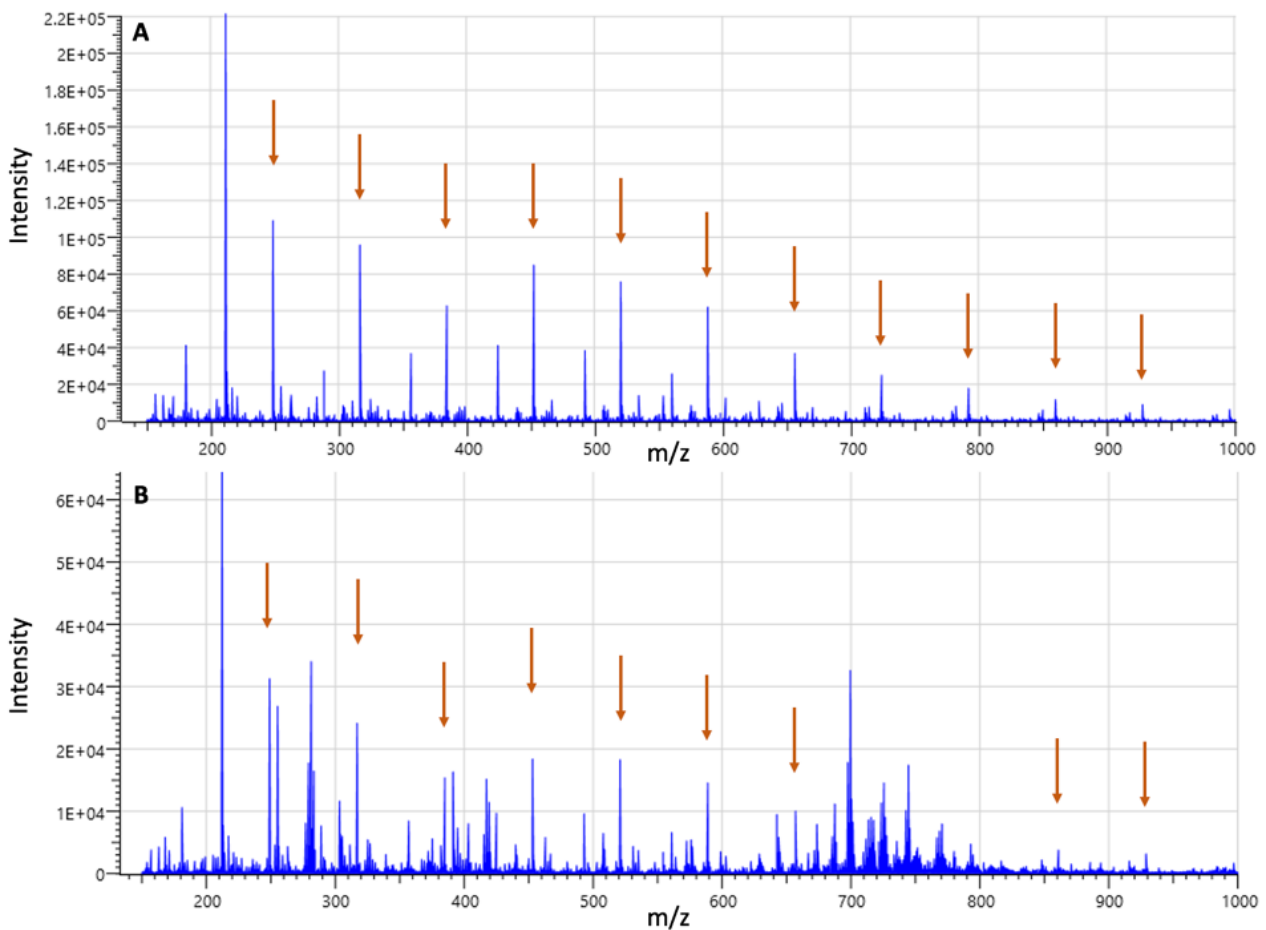


Figure 5.13 – spectrum of the background of an analytical run (**A**) demonstrating clusters of sodium formate at intervals of 67.99 (red arrows), which carry-over when analysing samples and can be seen alongside the lipid peaks (**B**).

### 5.2.3.7 Energy device used

Of the 800 remaining spectra, 4 were generated using the CO<sub>2</sub> laser, 13 were from monopolar diathermy in *coagulation* mode, with the rest using *cutting* mode diathermy. Significant differences between spectra generated by *coagulation* and *cutting* diathermy modes are seen (described in detail later in section 5.3.3.2) and the combined misclassification rate of the laser and coagulation mode spectra was 30%. Consequently, a model was created where only spectra generated using monopolar diathermy in *cutting* mode were included, however this did not increase the diagnostic accuracy of REIMS (86.7 vs 87.1%). Despite this not having a direct impact on diagnostic accuracy, the marked heterogeneity in spectral composition from using a different mode of energy delivery may be causing a systematic error that this methodology was unable to

detect and as such, it will still be required that spectra are analysed using *cutting* mode in order to be included in statistical analyses from here on.

#### 5.2.4 Discussion

This is the first attempt to systematically and robustly define minimum thresholds of quality for spectra generated by REIMS, in order to determine which are suitable for inclusion in statistical analyses. Whilst many different spectral characteristics were studied, it was determined that if spectra do not meet all the following seven requirements, they would be excluded from future analyses:

1. No significant sampling of non-mucosal tissue
2. Validation slide must be diagnostic
3.  $\geq 15\%$  of histological validation slide must include mucosa of the tissue of interest
4. No evidence of a technical batch effect from mass shift
5. Signal:noise ratio of  $\geq 1000$
6. No contamination with sodium formate
7. Monopolar diathermy must have been applied in *cutting* mode

Defining the 'quality' of REIMS spectra is a challenging process, where the impact of many factors required consideration and the optimal outcome against which they are measured was potentially unclear. The hypothesis of this thesis is that REIMS is able to differentiate tissue subtypes with high accuracy by sampling metabolites and this informed the decision for using diagnostic accuracy of models as the metric by which quality criteria can be compared. This approach benefited from being focused on the final goal of the technology (clinical diagnosis) whilst creating a simple metric which was easy to understand. Enforcement of the minimum quality standards for the spectra improves the diagnostic accuracy of REIMS in differentiating colorectal carcinoma, adenoma and normal mucosa from 81.2 to 86.7% in this preliminary dataset. Undergoing this process is vital to the development of the technology and understanding the biology of these tissue types. The inclusion of poor-quality spectra in statistical analyses increases the probability of making both type I and type II errors when performing tissue recognition or when exploring biological relationships. Whilst building models for tissue recognition, including spectra which are not truly representative of the annotated tissue type will move the group centroid in the

hyperplane and increase misclassification rate. Similarly, allowing such spectra to undergo recognition themselves will induce errors given that it is not a like-for-like comparison.

This approach to defining spectral quality has focused on experimental, study design and technical factors, which are often unique to REIMS considering the distinct differences between it and alternative MS techniques. These often take a differing approach by using quality control samples within the analytical run, do not suffer with the sampling and ionisation variability seen with REIMS and use techniques to reduce heterogeneity between bio-samples<sup>323,324</sup>. From an experimental perspective with REIMS, it is imperative to ensure that the tissue being analysed is in fact the pathological subtype that is expected. When sampling tissue for research, it may macroscopically appear to be a tumour, however after analysis by REIMS, the validation section may reveal the tissue not to be malignant. Similarly, normal tissue may be sampled from a surgical specimen which when dissected for REIMS analysis, may no longer have any mucosa and instead, only other bowel wall components such as muscularis. It is therefore necessary to exclude spectra impacted by this sampling issue, as they are not contributing to the aims of the project; which are to analyse the metabolic profiles of relevant tissue types as they may be encountered clinically. This was similar for the requirement for the maximal TG level not to exceed 50% of the maximal GPL level, which implies that an excess of the submucosa has been sampled. Mucosal analysis in a clinical setting should not include a large proportion of submucosa and considering the submucosa is often obliterated in tumours, including such spectra may bias the models; placing undue weight on TGs in the prediction of normal tissue. Choosing the appropriate level was challenging considering there is no prior literature to refer to and no method of deduction by first principles in order to determine a threshold. 50% was chosen by instinct, to strike a balance between the inevitable (and acceptable) partial sampling of submucosa and occasions when this dominated. Choosing a different threshold may have had an impact on the models created, however this was beyond the scope of this work. It may be possible to consider performing a sensitivity analysis of this in the future to determine an optimal threshold, if a sufficiently large dataset exists with a sufficient range of GPL and TG ratios.

Ideally, intraoperative REIMS would be able to detect the presence of a single tumour cell within an analysed region, even though this may represent a minute proportion of the bio-sample. This would be desirable considering microscopic extension of tumours can cause an 'involved' surgical margin and there are prognostic implications for the patient even if it is only a single cell causing

this involvement. The challenge with REIMS is that it is sampling the metabolic profile of the whole analysed region (approximately 1-5mg tissue), where the differential abundance of metabolites from a low number of tumour cells could be lost in the signal of the remaining normal tissue, causing a false negative prediction. This project identified that having a minimum 15% of the histological section containing tumour or adenoma decreases false negative predictions, whilst still having a large majority of normal tissue in the sample. Considering the development stage of the REIMS technology, the objectives of this project to document the unique metabolic profiles of different pathological subtypes and the need to reduce false negative predictions, a 15% minimum appears to be a fair balance. As the technology advances towards *in vivo* diagnostic use, it will be necessary to re-address this threshold and attempt to optimise the technology specifically to identify smaller proportions of tumour in samples.

When considering spectral quality from a technical perspective, batch effects were evident upon visual inspection of the PCA plots. This is a common problem in mass spectrometry, where these sensitive instruments can be affected by a range of factors to cause systematic variation in the dataset unrelated to the biological component. These factors can be the ambient atmosphere (humidity, temperature, pressure), vacuum pressure within the instrument, changes in ionisation efficiency, different sampling techniques and many more; including unknown factors<sup>325,326</sup>. The mass shift caused by the lack of calibration of the Dolores instrument between March and June 2015 were such that lipid peaks were shifting into adjacent bins, which could not be accounted for during supervised analysis and therefore, affected diagnostic accuracy. An alternative to excluding this cohort of 109 spectra would be to attempt to correct the masses by performing lock-mass correction on multiple peaks throughout the mass range, however, that functionality is not currently available on the AMX platform and requires metabolites at certain peaks to be identified in order to determine the exact mass. The strict adherence to calibration protocols following this period avoided any mass shift batches in the subsequent analyses and it is therefore anticipated that this will not be a recurring issue. It is unclear why the January 2018 analytical run had increased intensity in the background between lipid peaks despite background subtraction and normalisation, however given that supervised techniques were not impacted by this, it was not considered a metric of sufficiently poor quality that spectra should be excluded. Creating automated protocols for the recognition of future batches is troublesome considering the multitude of different factors which can cause batches on PCA, many of which will not impact diagnostic accuracy considering supervised techniques are used for model creation. One approach

to solving this is using the  $\delta$  statistic, which compares the variance of the first PC calculated by PCA and guided PCA; which is then compared between analytical runs<sup>327</sup>. Such statistical approaches could be augmented by analysing identical quality control samples at the start and end of each run, such as cancer cell lines, where the spectra generated can be compared to a historical dataset to identify possible technical batches<sup>328</sup>.

It is relatively straightforward to conceive how the ratio of biological signal to random background noise in a spectrum could impact its suitability for inclusion in statistical analyses and therefore be considered a marker of quality. If background noise is sufficiently high compared to the signal from metabolites, this is in direct opposition to the efforts of this thesis, which is to link complex metabolic signatures with tissue subtypes. A challenge arises when attempting to define signal:noise ratio for REIMS. Traditionally in mass spectrometry, it is described on a per-peak basis as the ratio of true signal amplitude to the standard deviation of the noise<sup>329</sup>, however this can be challenging to define for REIMS spectra as they present many hundreds of peaks simultaneously. This thesis used the median intensity of the top 20 most intense bins to define the signal, which corresponded to lipid peaks consistently seen in high relative abundance in colorectal tissues such as PE(18:1/16:0)-NH<sub>3</sub>-H in bin 699.45m/z. Noise was defined as the median of all bins and considering the number of bins was considerably larger than the number of metabolites present (particularly in the complex lipid region), this was deemed a suitable measure by not appearing to include true peaks in its calculation. Approaches similar to this have been applied previously with MS data, however it is beyond the scope of this thesis to explore how different definitions of signal-noise ratio impact classification accuracy<sup>330,331</sup>. A vast range of signal:noise was demonstrated across the spectra in this thesis (a factor of greater than 100), with potential causes for this remaining unclear. Co-aspiration of IPA is recognised to increase the signal by a factor of 2<sup>141</sup>, however this should have been running at the same flow rate throughout all analyses. It is possible this could reduce if the capillary geometry was suboptimal, however the impact of this should be relatively small. It does appear that the tissue type being analysed has a direct influence on the signal:noise, with normal tissue having a significantly higher median background noise and lower median signal than both tumour and adenoma spectra. Normal tissue was often sampled full thickness (unlike tumour and adenoma), which results in a significantly higher muscle component in the sample and REIMS analysis of this would be expected to cause an increase in noise and decrease in lipid signal (based on unpublished work from other members of the research group). This reflects the many potential causes of noise in analytical spectrometry data

(including electrical, biological and technical factors), with the relative impact of these requiring exploration in future work<sup>332,333</sup>. Inclusion of signal:noise as a marker of quality is justified by the clear finding of the inverse relationship between signal:noise and misclassification rate, notably for tumour and adenoma samples. Spectra with low signal:noise are also more likely to incorrectly classify spectra as normal rather than the other pathological state (false negative), which has a marked potential impact in the clinical setting. Tumour samples generated the spectra with the highest signal:noise, however it is unclear how factors such as necrosis, presence of mucin and non-viable cells would impact this metric. Additionally, it is beyond the scope of this work to determine if a different definition of signal:noise ratio would impact the threshold at which classification rate is most impacted.

These data did not appear to demonstrate a clear impact of energy mode on diagnostic accuracy of REIMS, despite this being a large source of heterogeneity and the finding that *coagulation* and *cut* diathermy profiles cluster very distinctly on PCA (detailed in section 5.3.3.2). Whilst *coagulation* mode and laser spectra misclassified at double the rate of rest of the dataset (30%), it was surprising to find that excluding them did not affect diagnostic accuracy. The reason for this is unclear and likely reflects the complexities of metabolomic data how small changes can impact the findings of multivariate modelling. Despite this, a decision was taken to still exclude spectra generated using a device other than *cut* diathermy mode as there is a strong suspicion that the negative impact of *coagulation* mode spectra on model accuracy cannot be fully appreciated in this limited preliminary dataset.

Whilst this project has been valuable in exploring quality of REIMS spectra, there are weaknesses in the approach used which must be understood. It has resulted in creation of stringent exclusion criteria and the loss of a significant portion of the dataset (447 spectra, 37%). This does raise concerns that the power of the statistical analyses may be impacted, such that nuances in the metabolic differences between groups may be under-recognised. Considering the diagnostic accuracy of REIMS increased when applying these quality metrics, this implies that the decreased number of observations are not impacting power. Furthermore, factors such as batch effects or failure in histological validation introduce systematic errors and it is desirable to remove or mitigate for these, even if there is some cost in terms of the model's theoretical power. The reproducibility and external validity of the findings in this project are unclear and may be impacted by a variety of factors. The dataset used contained all REIMS analyses until November 2018 and it

is unclear if some of the findings are unique to this data and may not hold true for an updated or externally collected dataset. It is possible that random variation in the data caused type I errors and therefore incorrect assumptions of the relationship between a variable and quality. This is challenging to explore using the single dataset and exacerbated given the outcomes do not provide an indication of error or uncertainty (such as confidence intervals). Conversely, the sensitivity analyses may not have been able to detect all variables which have an impact on quality. The dataset used was colorectal tissue and considering the marked variation in metabolic profiles and spectral characteristics between organs, it is likely to need repeating if a different body site is sampled. Whilst this project has started to define 'quality' in REIMS spectra, in most cases it has been unable to inform how analyses can be conducted differently in the future to improve the quality of data produced (with notable examples such as the need for immediate calibration prior to each analytical run to avoid mass shift batch effects). Improving quality of produced spectra is beyond the scope of this thesis, however, the definitions provided here can be used as proxy in future work.

## 5.3 Impact of Technical and Environmental Factors on REIMS Mass Spectra

### 5.3.1 Aim and Rationale

Collection of REIMS data *ex vivo* in the laboratory setting involves standardisation of technical parameters of the mass spectrometer and sampling device (such as aspiration tube length, power settings and diathermy mode), in addition to controlling many environmental factors (such as contamination on the tissue surface). This is performed in order to generate reproducible mass spectra of high enough quality that reliable results can be produced from statistical analyses. However, translating this technology *in vivo* involves taking it into a dynamic and unpredictable setting where it may not be possible to control or mitigate for many of these factors. For example, surgeons may choose to deploy diathermy differently in order to achieve a particular clinical goal, such as using coagulation instead of cut mode, changing the power settings and given the need to maintain a sterile field around the patient; a longer aspiration tube may be required to deliver the aerosol to the MS. Furthermore, the tissue being dissected may be contaminated by blood or mucus. The potential impact of such factors on spectra generated by REIMS is unknown, however

given this is a potential source of systematic error during *in vivo* translation (therefore impacting the ability of REIMS to accurately perform tissue recognition); it is necessary to explore this.

The aim of this experiment is to define the impact of technical and environmental factors on the quality and biological composition of spectra from colorectal mucosa collected by REIMS.

### 5.3.2 Methods

#### 5.3.2.1 Determination of Technical and Environmental Factors

Colorectal surgeons and mass spectrometry scientists within the research group were consulted to reach consensus on which technical and environmental factors should be studied. This decision was based on the likelihood that a factor could make a significant impact on the REIMS spectra, its clinical relevance and the ability to manipulate it experimentally in the laboratory. The variables to be studied were:

- Technical:
  - Diathermy power – 10W vs 20W vs 30W vs 40W
  - Diathermy mode – cut vs coagulation
  - Length of aspiration tube – 1m vs 2.5m vs 4m
- Environmental:
  - Presence of contamination on tissue – none vs saline vs blood

#### 5.3.2.2 Experimental Model

Apparatus was constructed in the laboratory consisting of a REIMS analytical space of approximately 4500cm<sup>3</sup>, in which technical and environmental conditions could be measured, modified and maintained (figure 5.14). Food grade porcine colorectum was procured (Fresh Tissue Supplies, UK) and stored at -80°C, before being freshly thawed just prior to analysis. A 12cm segment of distal colon (15-27cm from ano-rectal junction) was bisected longitudinally and

everted, leaving a rectangle of full-thickness colon approximately 12x7cm, which could be placed into the analytic environment.

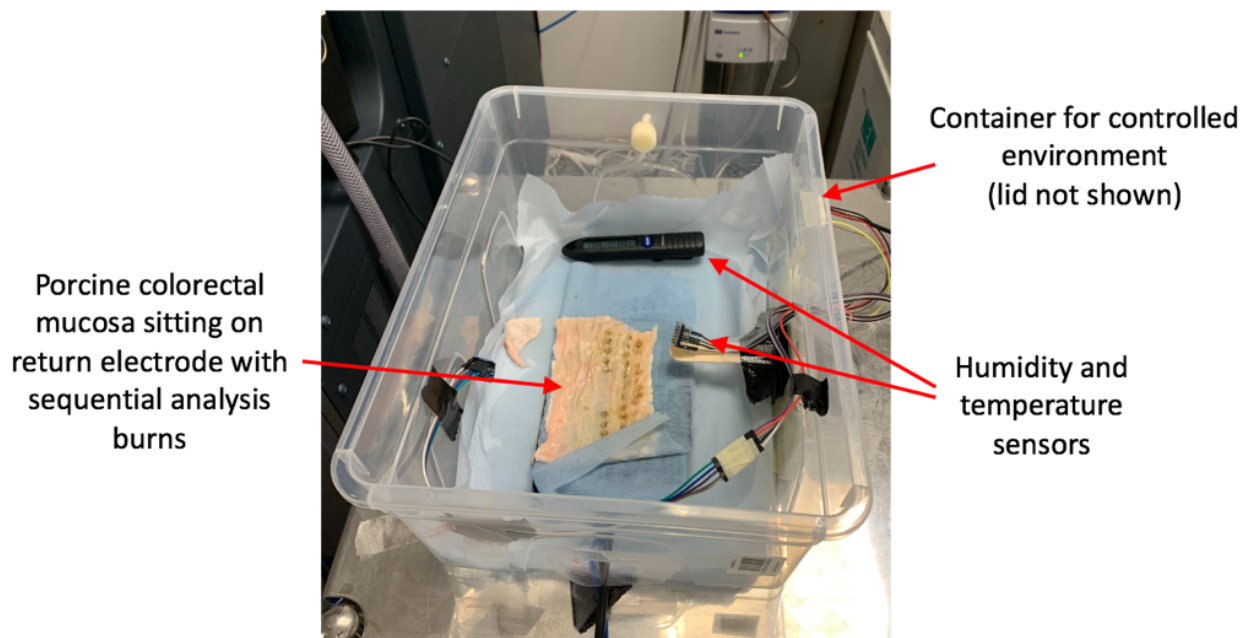


Figure 5.14 – the environment used for analysis of porcine colorectum, with sensors to ensure no change in temperature or humidity throughout the analysis.

### 5.3.2.3 Analytical Strategy

A series of experiments were designed to determine the impact of each variable on REIMS spectra. First, the standard operating procedure (SOP) conditions were applied, which used monopolar diathermy in cut mode at 20W, with a 2.5m aspiration tube, room temperature, room humidity and no tissue contamination (full details of analytical processes are presented in chapter 4). Analysis of the colonic mucosa was conducted using the heel of a laparoscopic hook diathermy alongside which a PTFE aspiration tube with 3mm internal diameter was taped, with the opening 1cm from the analytical site (figure 5.15). Diathermy current was applied to the colonic mucosa at 10 points for approximately 3 seconds, with the same operator throughout aiming for consistent sampling. The following experiments then changed one variable from the SOP before repeating the 10 burns, for example, increasing the power to 30W; such that direct comparisons could be

made between experiments to determine the impact of variables individually. Finally, the SOP conditions were applied for analysis again at the end as a quality control.

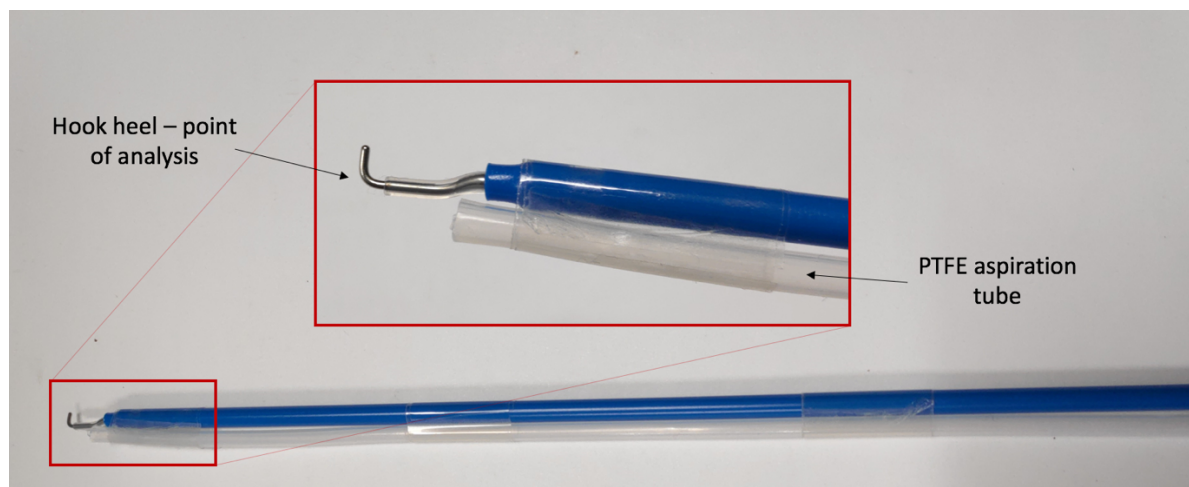


Figure 5.15 – Laparoscopic hook diathermy sampling device, annotated to show the point used for analysis on the heel and the PTFE aspiration tubing taped alongside the instrument.

#### 5.3.2.4 Control and Monitoring of Environmental Conditions

Atmospheric humidity and temperature within the analytical environment were monitored using two independent BME680 sensors (Adafruit Industries, USA), which were placed within 5cm of the tissue and gave updates on 1 second intervals. Tissue temperature was measured using a K-type insulated thermocouple (RS Components Ltd, UK) attached to a digital multimeter (Keithley 2110, Keithley, Tektronix Inc, USA). Porcine blood (Fresh Tissue Supplies, UK) and a 1.8% NaCl solution (Sigma-Aldrich, UK) were pipetted onto the mucosa as necessary.

#### 5.3.2.5 Mass Spectrometer Specifications

A Xevo G2-S qTOF mass spectrometer was used (Waters Corporation, USA) with a Venturi interface and co-aspiration of an internal standard of leucine-enkephalin in isopropanol (20ng/ml concentration) at a flow rate of 0.2ml/min. Spectra were collected in negative mode across the 150-1200 m/z range.

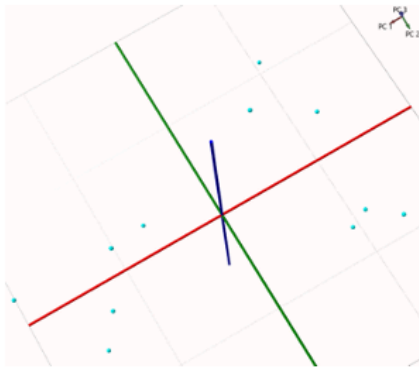
#### 5.3.2.6 Data Analysis

Raw data were pre-processed using lock mass correction, background subtraction and normalisation. Analysis was conducted over the 600-1000 m/z range using binning of 0.1 and one spectrum per burn. A PCA plot was performed for each experiment to identify and exclude outliers. Once outliers had been excluded, the 150 most intense bins were identified for further analysis. This was achieved by exporting non-normalised binned data, preserving only the 150 m/z values with the highest median intensity and then performing the normalisation step. Experiments were compared based on TIC, signal:noise ratio, PCA, OPLS-DA and univariate regression.

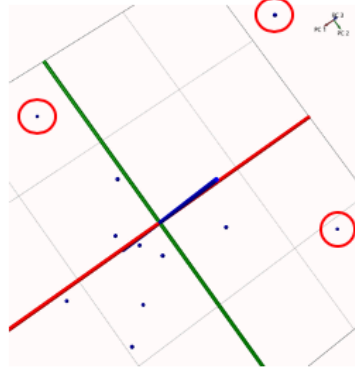
#### 5.3.3 Results

A total of 10 experiments were conducted to generate 106 REIMS spectra from porcine colonic mucosa whilst controlling six environmental and technical factors. PCA plotting for each experiment identified a total of 19 outliers, which were removed from further analyses (figure 5.16). The 150 bins with the highest median intensity are presented in table 5.2, with level 2 or 3 identification of 160 lipid metabolites achieved using either a search of a reference database using exact mass or MS/MS.

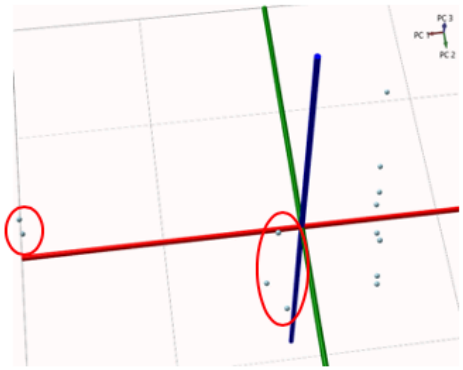
**Experiment 1 – normal conditions**



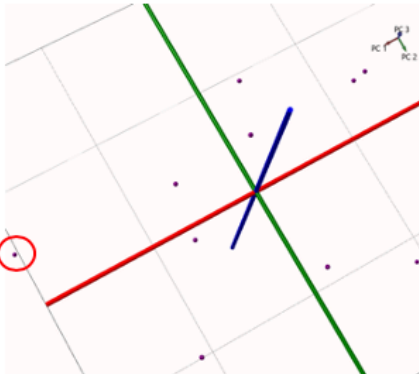
**Experiment 2 – long tubing**



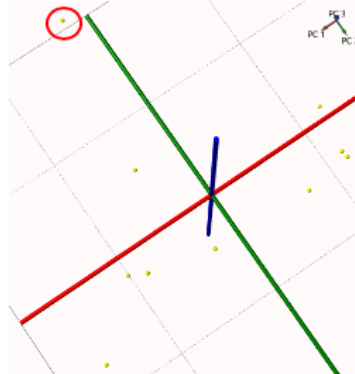
**Experiment 3 – 10W power**



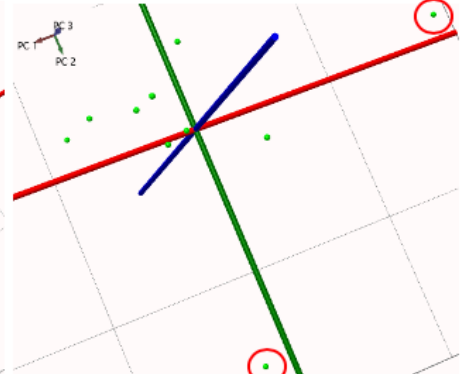
**Experiment 4 – 30W power**



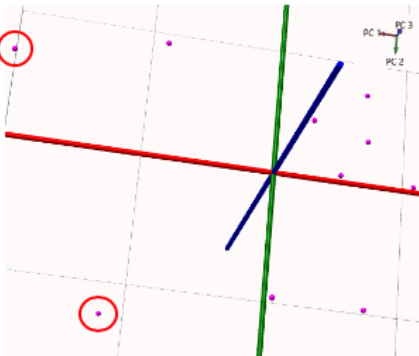
**Experiment 5 – 40W power**



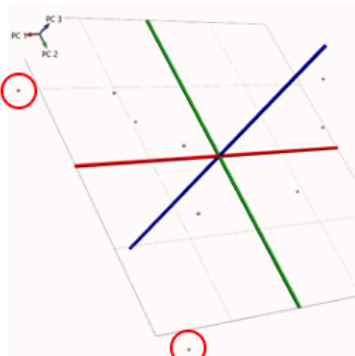
**Experiment 6 – coagulation diathermy**



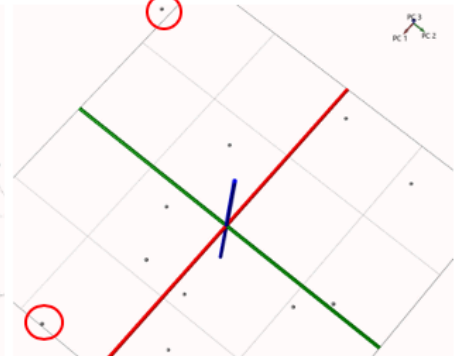
**Experiment 7 – saline**



**Experiment 8 – blood**



**Experiment 9 – short tubing**



**Experiment 10 – normal conditions 2**

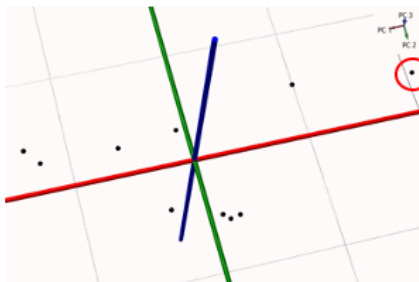


Figure 5.16 – PCA plots of the 10 experiments conducted and the environmental or technical factor that was being assessed. Red circles denote outliers that were identified visually and removed from further analyses.

Bin m/z	Exact m/z Observed	Molecular Identity	ID Level	Theoretical m/z	Error (ppm)
600.45	600.475	CerP(d34:0)-H <sub>2</sub> O-H	Putative	600.4757	-1.17
601.35	601.396	Background noise			
601.45	601.461	DG(32:1)+Cl	Putative	601.4604	0.83
602.45	602.463	<sup>13</sup> C isotope of DG(32:1)+Cl	Putative	602.4638	-1.33
603.45	603.478	DG(32:0)+Cl	Putative	603.4761	3.81
605.45	605.456	LPA(30:0)-H	Putative	605.4552	1.49
607.45	607.471	Unknown			
611.55	611.525	DG(34:0;O)-H	Putative	611.5256	-0.98
613.55	613.519	Background noise			
616.15	616.176	Unknown			
616.45	616.470	CerP(d18:1/16:0)-H	MS/MS	616.4711	-0.97
617.45	617.420	PA(30:1)-H	Putative	617.4188	1.94
618.15	618.172	Background noise			
620.25	620.237	Unknown			
629.45	629.490	DG(34:1)+Cl	Putative	629.4917	-2.70
630.45	630.487	PE(O-30:0)-H <sub>2</sub> O-H	Putative	630.4863	0.79
631.45	631.482	PE_Cer(d32:1)-H	Putative	631.4820	-0.32
633.45	633.485	LPA(32:0)-H	Putative	633.4865	-2.37
636.15	636.199	Unknown			
636.25	636.267	Same peak as m/z 636.15			
639.55	639.552	Unknown			
642.45	642.485	PE_Cer(d34:1)-NH <sub>3</sub> -H	MSMS	642.4860	-0.93
642.55	642.552	Same peak as m/z 642.45			
643.45	643.491	<sup>13</sup> C isotope of PE_Cer(d34:1)-NH <sub>3</sub> -H	Putative	643.4940	-4.66
643.55	643.552	Same peak as m/z 643.45			
644.45	644.503	Same peak as m/z 644.55			
644.55	644.503	PE_Cer(d34:0)-NH <sub>3</sub> -H	MSMS	644.5019	1.71
645.45	645.449	PA(32:1)-H	Putative	645.4501	-1.08
646.45	646.453	<sup>13</sup> C isotope of PA(32:1)-H	Putative	646.4529	-0.46
647.45	647.467	PA(32:0)-H	Putative	647.4657	2.01
656.55	656.574	Cer(40:1;O2)+Cl	Putative	656.5754	-2.13
657.45	657.485	PE(P-16:0/16:0)-NH <sub>3</sub> -H	MSMS	657.4859	-1.52
657.55	657.525	DG(36:1)+Cl	MSMS	657.5230	3.04
658.45	658.492	<sup>13</sup> C isotope of PE(P-16:0/16:0)-NH <sub>3</sub> -H	Putative	658.4892	4.25
658.55	658.525	<sup>13</sup> C isotope of DG(36:1)+Cl	Putative	658.5263	-1.52
659.15	659.182	Unknown			
659.45	659.182	Same peak as m/z 659.55			
659.55	659.505	PE(O-16:0/16:0)-NH <sub>3</sub> -H	MSMS	659.5021	4.40
659.55	659.505	PA(P-18:0/16:0)-H	MSMS	659.5021	4.40
659.55	659.505	PA(O-16:0/18:1)-H	MSMS	659.5021	4.40
659.55	659.505	PA(O-18:0/16:1)-H	MSMS	659.5021	4.40
660.45	660.505	Same peak as m/z 660.55			
660.55	660.505	<sup>13</sup> C isotope of PE(O-16:0/16:0)-NH <sub>3</sub> -H	MSMS	660.5054	-0.61
661.45	661.486	DG(34:1;O2)+Cl	Putative	661.4816	6.65
665.55	665.551	Unknown			
670.55	670.518	CerP(38:2)-H	Putative	670.5181	-0.15

671.45	671.465	PE(16:0/16:1)-NH <sub>3</sub> -H	Putative	671.4652	-0.30
671.45	671.465	PE(18:1/14:0)-NH <sub>3</sub> -H	Putative	671.4652	-0.30
671.55	671.515	SM(d32:2)-H	Putative	671.5133	2.53
672.45	672.500	PCh(P-16:1/14:0)-CH <sub>3</sub>	MSMS	672.4974	3.87
672.45	672.471	<sup>13</sup> C isotope of PE(16:1/16:0)-NH <sub>3</sub> -H	MSMS	672.4685	3.72
672.45	672.471	<sup>13</sup> C isotope of PE(18:1/14:0)-NH <sub>3</sub> -H	MSMS	672.4685	3.72
673.35		Background noise			
673.45	673.481	PA(18:1/16:0)-H	MSMS	673.4814	-0.15
673.55		Same peak as m/z 673.45			
674.45	674.487	<sup>13</sup> C isotope of PA(18:1/16:0)-H	Putative	674.4847	3.41
674.55		Same peak as m/z 674.45			
675.45	675.496	PA(34:0)-H	Putative	675.4970	-1.48
678.45	678.461	HexCer(32:5;O3)-H	Putative	678.4587	3.10
679.45	679.461	<sup>13</sup> C isotope of HexCer(32:5;O3)-H	Putative	679.4620	-1.47
680.45	680.465	CerP(38:5;O3)-H	Putative	680.4661	-1.62
682.55	682.588	Ceramide(d42:2)+Cl	Putative	682.5911	-4.10
683.55	683.594	<sup>13</sup> C isotope of Ceramide(d42:2)+Cl	Putative	683.5944	-0.59
684.55	684.594	Acer(44:4)-H or Cer(44:5)-H	Putative	684.5936	0.73
685.45		Same peak as m/z 685.55			
685.55	685.520	PE(P-18:0/16:0)-NH <sub>3</sub> -H	MSMS	685.5172	4.08
685.55	685.520	PE(O-16:0/18:1)-NH <sub>3</sub> -H	MSMS	685.5172	4.08
685.55	685.520	SM(d18:2/16:0)-CH <sub>3</sub>	MSMS	685.5290	-13.13
686.55	686.519	<sup>13</sup> C isotopes of above mixture	MSMS	686.521	-1.75
687.35	687.332	Unknown			
687.45		Same peak as m/z 687.55			
687.55	687.545	SM(d16:1/18:0)-CH <sub>3</sub>	MSMS	687.5447	0.44
687.55	687.545	SM(d16:0/18:1)-CH <sub>3</sub>	MSMS	687.5447	0.44
687.55	687.545	PE(O-18:0/16:0)-NH <sub>3</sub> -H	MSMS	687.5329	17.6
688.55	688.548	<sup>13</sup> C isotopes of above mixture	Putative	688.5474	0.87
689.55	689.550	x2 <sup>13</sup> C isotopes of above mixture	MSMS	689.5508	-1.16
690.55	690.552	X3 <sup>13</sup> C isotopes of above mixture	Putative		
691.45	691.493	PA(34:0;O)-H	Putative	691.4920	1.45
697.45	697.479	PA(18:2/18:1)-H	MSMS	697.4814	-3.58
697.45	697.479	PA(16:0/20:3)-H	MSMS	697.4814	-3.58
698.25		Background noise			
698.55	698.515	PE(P-34:2)-H	Putative	698.5130	2.86
699.45	699.496	PE(18:1/16:0)-NH <sub>3</sub> -H	MSMS	699.4965	-0.14
699.55		Same peak as m/z 699.45			
700.45		Same peak as m/z 700.45			
700.55	700.525	<sup>13</sup> C isotope of PE(18:1/16:0)-NH <sub>3</sub> -H	MSMS	700.4999	35.8
700.55	700.525	PE(P-18:0/16:1)-H	MSMS	700.5287	-5.28
700.55	700.525	PE(P-16:1/18:0)-H	MSMS	700.5287	-5.28
701.45		Same peak as m/z 701.55			
701.55	701.513	PA(18:1/18:0)-H	MSMS	701.5127	1.00
702.55	702.515	<sup>13</sup> C isotope of PA(18:1/18:0)-H	Putative	702.516	-0.71
703.55	703.530	PA(18:0/18:0)-H	MSMS	703.5283	2.42
703.55	703.530	SM(34:1;O3)-CH <sub>3</sub>	MSMS	703.5396	-13.65

704.55	704.547	ACer(42:4)-H or Cer(42:5)-H	Putative	704.5471	-0.71
707.45	707.486	Unknown			
709.45	709.4551	PA(34:1)+Cl	Putative	709.4581	-4.23
713.55	713.545	PE(P-18:0/18:0)-NH <sub>3</sub> -H	MSMS	713.5485	-4.91
713.55	713.545	PE(O-18:0/18:1)-NH <sub>3</sub> -H	MSMS	713.5485	-4.91
714.55	714.545	CerP(40:2;O3)-H	Putative	714.5443	0.98
715.55	715.582	SM(d20:0/16:1)-CH <sub>3</sub>	MSMS	715.5760	8.38
716.55	716.525	PE(16:0/18:1)-H	MSMS	716.5236	1.95
716.55	716.525	PE(16:1/18:0)-H	MSMS	716.5236	1.95
717.45		Same peak as m/z 717.55			
717.55	717.530	<sup>13</sup> C isotope of PE(16:0/18:1)-H	MSMS	717.5269	4.32
717.55	717.530	<sup>13</sup> C isotope of PCh(16:1/16:0)-CH <sub>3</sub>	MSMS	717.5269	4.32
718.55	718.538	PCh(16:0/16:0)-CH <sub>3</sub>	MSMS	718.5392	-0.97
718.55	718.538	PE(18:0/16:0)-H	MSMS	718.5392	-0.97
719.45	719.486	PG(16:1/16:0)-H	MSMS	719.4869	-1.81
719.55	719.540	<sup>13</sup> C isotope of PCh(16:0/16:0)-CH <sub>3</sub>	MSMS	719.5420	-2.78
719.55	719.540	<sup>13</sup> C isotope of PE(18:0/16:0)-H	MSMS	719.5420	-2.78
721.45	721.478	PE(20:4/16:0)-NH <sub>3</sub> -H	MSMS	721.4811	-4.30
722.55	722.512	PE(P-36:4)-H	Putative	722.5130	-1.38
723.45	723.496	PE(20:3/16:0)-NH <sub>3</sub> -H	MSMS	723.4970	-0.28
723.45	723.496	PA(20:4/18:0)-H	MSMS	723.4970	-0.28
725.55	725.512	PA(18:0/20:3)-H	MSMS	725.5127	-0.96
725.55	725.512	PA(18:1/20:2)-H	MSMS	725.5127	-0.96
725.55	725.512	PA(18:2/20:1)-H	MSMS	725.5127	-0.96
726.55	726.545	PE(P-18:1/18:1)-H	MSMS	726.5443	-0.28
726.55	726.545	PE(P-18:0/18:2)-H	MSMS	726.5443	-0.28
727.55	727.530	PA(18:2/20:0)-H	MSMS	727.5283	2.06
728.55	728.561	PE(P-18:0/18:1)-H	MSMS	728.5600	1.37
729.55	729.562	<sup>13</sup> C isotope of PE(P-18:0/18:1)-H	Putative	729.5628	-1.10
730.55	730.575	PE(O-18:0/18:1)-H	MSMS	730.5756	-0.82
730.55	730.575	PCh(P-18:0/16:0)-CH <sub>3</sub>	MSMS	730.5756	-0.82
730.55	730.575	PCh(P-16:0/18:0)-CH <sub>3</sub>	MSMS	730.5756	-0.82
731.55	731.579	<sup>13</sup> C isotope of above mixture	Putative	731.5784	1.09
732.55	732.580	x2 <sup>13</sup> C isotope of above mixture	Putative	732.5818	-2.46
733.55	733.515	PE(P-18:0/20:4)-NH <sub>3</sub> -H	MSMS	733.5172	-3.00
735.45	735.474	PA(36:2)+Cl	Putative	735.4737	-0.95
739.35	739.338	Unknown			
742.55	742.540	PE(18:1/18:1)-H	MSMS	742.5392	0.81
742.55	742.540	PE(18:2/18:0)-H	MSMS	742.5392	0.81
742.55	742.540	PCh(18:1/16:1)-CH <sub>3</sub>	MSMS	742.5392	0.81
742.55	742.540	PCh(18:2/16:0)-CH <sub>3</sub>	MSMS	742.5392	0.81
743.55	743.543	<sup>13</sup> C isotope of above mixture	Putative	743.5420	1.75
744.55	744.556	PE(18:1/18:0)-H	MSMS	744.5549	1.48
744.55	744.556	PCh(18:1/16:0)-CH <sub>3</sub>	MSMS	744.5549	1.48
744.55	744.556	PCh(18:0/16:1)-CH <sub>3</sub>	MSMS	744.5549	1.48
745.55	745.503	PG(18:2/16:0)-H	MSMS	745.5025	0.67
745.55	745.559	<sup>13</sup> C isotope of PE(18:1/18:0)-H	MSMS	745.5577	1.74

745.55	745.559	<sup>13</sup> C isotope of PCh(18:1/16:0)-CH <sub>3</sub>	MSMS	745.5577	1.74
746.55	746.559	x2 <sup>13</sup> C isotope of PE(18:1/18:0)-H	Putative	746.5610	-2.68
746.55	746.559	x2 <sup>13</sup> C isotope of PCh(18:1/16:0)-CH <sub>3</sub>	Putative	746.5610	-2.68
747.45		Same peak as m/z 747.55			
747.55	747.517	PG(18:1/16:0)-H	MSMS	747.5182	-2.01
748.55	748.520	<sup>13</sup> C isotope of PG(18:1/16:0)-H	MSMS	748.5210	-1.07
749.55	749.525	x2 <sup>13</sup> C isotope of PG(18:1/16:0)-H	MSMS	749.5243	0.93
750.55	750.541	PE(P-18:0/20:4)-H	MSMS	750.5443	-4.40
750.55	750.541	PE(P-16:0/22:4)-H	MSMS	750.5443	-4.40
751.55	751.545	<sup>13</sup> C isotopes of above mixture	Putative	751.5453	-0.40
752.55	752.550	Unknown			
754.65	754.611	PE_Cer(d42:1)-NH <sub>3</sub> -H	MSMS	754.6115	-0.66
757.55	757.552	DG(44:7)+Cl	Putative	757.5543	-2.51
766.55	766.537	PE(20:4/18:0)-H	MSMS	766.5392	-2.87
768.55	768.558	PE(20:3/18:0)-H	MSMS	768.5549	4.03
770.55	770.572	PE(18:1/20:1)-H	MSMS	770.5705	2.47
770.55	770.572	PE(18:2/20:0)-H	MSMS	770.5705	2.47
770.55	770.572	PE(22:2/16:0)-H	MSMS	770.5705	2.47
771.55	771.521	PG(18:2/18:1)-H	MSMS	771.5182	3.63
771.65	771.635	SM(40:1)-CH <sub>3</sub>	MSMS	771.639	-4.67
772.55	772.520	<sup>13</sup> C isotope of PG(18:2/18:1)-H	MSMS	772.5210	-1.29
772.55	772.585	PCh(18:1/18:0)-CH <sub>3</sub>	Putative	772.5862	-1.55
772.65		Same peak as m/z 772.55			
773.55	773.532	PG(18:1/18:1)-H	MSMS	773.5338	-1.94
773.55	773.532	PG(18:2/18:0)-H	MSMS	773.5338	-1.94
774.55	774.535	<sup>13</sup> C isotopes of above mixture	Putative	774.5366	-2.32
775.55	775.549	PG(18:1/18:0)-H	MSMS	775.5495	-0.64
776.55	776.553	<sup>13</sup> C isotope of PG(18:1/18:0)-H	MSMS	776.5523	0.90
778.55	778.574	PCh(P-16:0/22:4)-CH <sub>3</sub>	MSMS	778.5756	-2.06
788.55	788.544	PS(18:0/18:1)-H	MSMS	788.5447	-0.89
789.55	789.546	<sup>13</sup> C isotope of PS(18:0/18:1)-H	MSMS	789.5475	-2.03
794.55	794.570	PE(22:4/18:0)-H	MSMS	794.5705	-0.63
795.55	795.575	Unknown			
797.55	797.535	PG(20:3/18:1)-H	MSMS	797.5338	2.01
797.65	797.654	SM(42:2)-CH <sub>3</sub>	MSMS	797.6542	-0.25
798.65	798.652	<sup>13</sup> C isotope of SM(42:2)-CH <sub>3</sub>	MSMS	798.6570	-6.26
799.65	799.670	SM(42:1)-CH <sub>3</sub>	MSMS	799.6699	0.13
816.75	816.744	Acer(52:2;O3)-H	Putative	816.7451	-1.35
818.75	818.759	Acer(52:1;O3)-H	Putative	818.7607	-2.08
819.75	819.761	<sup>13</sup> C isotope of Acer(52:1;O3)-H	Putative	819.7640	-3.66
820.75	820.772	Acer(52:0;O3)-H	Putative	820.7764	-4.14
875.75	875.771	Unknown			
893.75	893.736	TG(18:1/18:1/16:0)+Cl	MSMS	893.7370	-1.12
894.75	894.738	<sup>13</sup> C isotope of TG(18:1/18:1/16:0)+Cl	Putative	894.7403	-2.57
895.75	895.751	TG(18:1/18:0/16:0)+Cl	MSMS	895.7527	-1.90
896.75	896.756	<sup>13</sup> C isotope of TG(18:1/18:0/16:0)+Cl	Putative	896.7560	0.00

897.75	897.751	<sup>37</sup> Cl isotope of TG(18:1/18:0/16:0)+Cl	Putative	897.7498	1.34
--------	---------	---	----------	----------	------

Table 5.2 – the 150 bins with the highest median intensity across all analyses and the molecular structure of the corresponding lipid metabolites. 160 metabolites could be identified, of which 50 were <sup>13</sup>C or <sup>37</sup>Cl isotopes.

CerP – ceramide-1-phosphate; DG – diacylglycerol; LPA – lysophosphatidic acid; PA – phosphatidic acid; PE – phosphatidylethanolamine; PE\_Cer – ceramide phosphatidylethanolamine; Cer - ceramide; HexCer – hexosylceramide; SM – sphingomyelin; PCh – phosphatidylcholine; PG – phosphatidylglycerol; PS – phosphatidylserine; Acer - acylceramide; TG - triacylglycerol.

The impact of the technical and environmental variables on REIMS spectra is presented in table 5.3, with the PCA plots revealing large sources of variation (figure 5.17). Some experiments form clusters distinct from the main bulk of analyses whilst having low intra-group variance and can be considered outliers using Hotelling's  $T^2$  distribution (10W power and coagulation; figure 5.17.A). When these are removed from the PCA (figure 5.17.B) a greater degree of variation between the remaining experiments is apparent, however clusters have marked overlapping borders such that this 2 component PCA model would be poorly predictive ( $Q^2 = 0.49$ ). The two experiments using the normal operating conditions (20W diathermy in cut mode, 2.5m aspiration tube and no tissue contamination) at the beginning and end of the analytical run show greater intra- rather than inter-group variation on PCA, implying that no significant batch effect developed throughout the analyses. Whilst these two groups will be presented separately in PCA plots, they will be combined for OPLS-DA to avoid attempts to discriminate between them.

Factor	Variable	Burns Included	Total Ion Count (x10 <sup>7</sup> )	<i>p</i> value	Mean Signal x10 <sup>6</sup> (range)	Mean Noise x10 <sup>3</sup> (range)	Mean Signal:Noise x10 <sup>3</sup> (range)	<i>p</i> value
<b>Power</b>	10W	8	0.6 (0.4-0.9)	<b>&lt;0.001</b>	0.7 (0.5-1.6)	0.5 (0.4-0.6)	1.4 (1.0-2.8)	<b>&lt;0.001</b>
	20W	20	4.3 (2.2-8.3)	-	9.0 (3.7-17.9)	2.5 (1.7-4.1)	3.4 (2.2-5.1)	-
	30W	9	6.5 (5.0-7.5)	<b>0.001</b>	13.2 (10.0-16.2)	4.1 (3.2-4.7)	4.1 (3.2-4.7)	0.81
	40W	9	4.1 (3.4-4.6)	0.76	7.6 (5.8-9.1)	2.7 (2.3-3.1)	2.7 (2.3-3.1)	0.18
<b>Diathermy Mode</b>	Cut	20	4.3 (2.2-8.3)	-	9.0 (3.7-17.9)	2.5 (1.7-4.1)	3.4 (2.2-5.1)	-
	Coagulation	8	3.5 (3.1-4.0)	0.26	2.4 (1.9-2.8)	3.0 (2.7-3.5)	0.8 (0.7-0.9)	<b>&lt;0.001</b>
<b>Tubing Length</b>	Short (1m)	9	4.5 (3.0-6.1)	0.75	9.6 (5.8-86)	2.6 (1.9-3.3)	3.7 (3.0-4.2)	0.49
	Medium (2.5m)	20	4.3 (2.2-8.3)	-	9.0 (3.7-17.9)	2.5 (1.7-4.1)	3.4 (2.2-5.1)	-
	Long (4m)	8	2.9 (1.5-4.1)	<b>0.04</b>	5.2 (2.5-7.7)	2.0 (1.2-2.5)	2.6 (2.21-3.2)	0.10
<b>Contamination</b>	None	20	4.3 (2.2-8.3)	-	9.0 (3.7-17.9)	2.5 (1.7-4.1)	3.4 (2.2-5.1)	-
	Blood	8	3.4 (2.3-4.4)	0.18	5.8 (4.2-7.6)	2.3 (1.7-2.9)	2.5 (2.0-3.2)	0.07
	Saline	8	2.8 (1.3-3.8)	<b>0.04</b>	4.5 (1.6-6.0)	2.1 (1.1-2.7)	2.1 (1.4-2.8)	<b>0.01</b>

Table 5.3 – the impact of technical sampling factors on spectral characteristics. ‘Signal’ is defined as the total intensity of the 20 highest peaks in 600-1000mz, with ‘noise’ defined as the median intensity of peaks in 600-1000m/z. *p* values were determined using a two tailed t-test with statistically significant findings in bold. The comparator group for each analysis was the base-case settings of 20W diathermy in cut mode, using a 2.5m aspiration tube and with no tissue contamination.

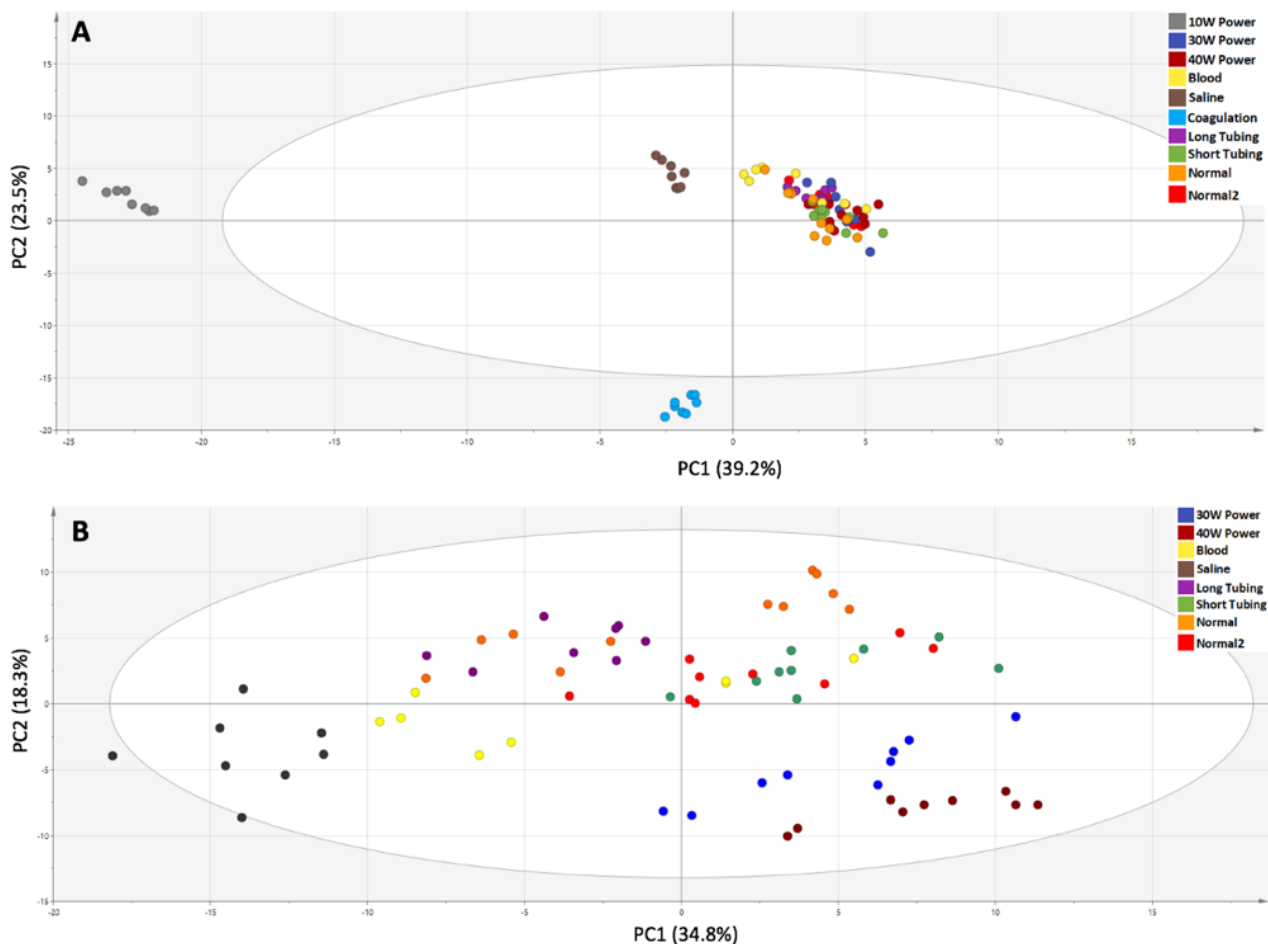


Figure 5.17 – PCA plot of PC1 against PC2 across the 10 experiments (A) and with the two outlying clusters of 10W power and coagulation diathermy removed (B). The tolerance ellipse represents the 95% boundary on the 2-dimensional scores plot as per Hotelling’s  $T^2$  distribution

Manipulating the diathermy power, diathermy mode, aspiration tube length and presence of contamination required experiments to be conducted with limited variation in ambient atmospheric conditions. It is evident that this was achieved, with room temperature varying from 19.9-21.5°C, relative humidity varying from 48.1-56.2% and tissue temperature from 18.4-20.9°C.

### 5.3.3.1 Power

Adjusting the power of diathermy appears to have a dramatic impact on the spectra generated by REIMS. Use of 10W appeared to have insufficient power to consistently increase the temperature of the mucosa and cause tissue ablation, which is reflected in the significantly reduced TIC and signal. As a consequence, 10W is an outlier on the PCA (figure 5.18.A). Plotting the spectra of the

top 150 most intense bins demonstrates that this sparse signal causes large peaks to appear upon normalisation (as the impact of random noise is amplified), which are unrelated to the true biological signal generated consistently by the other power settings (figure 5.19).

The PCA appears to differentiate the remaining 20W, 30W and 40W power settings along PC2, with relative cluster separation. Increasing the power from 20 to 30W significantly increased the TIC, however, this was not reflected in the signal:noise ratio as there was a marked increase in the background noise produced ( $2.5 \times 10^3$  to  $4.1 \times 10^3$ ). This trend did not continue when raising the power to 40W, where a TIC and signal:noise ratio similar to 20W was demonstrated ( $7.6 \times 10^6$  vs  $9.0 \times 10^6$  and  $2.7 \times 10^3$  vs  $3.4 \times 10^3$  respectively). This is likely due to the characteristics of the thermal ablation, where the highest power caused rapid localized tissue evaporation and loss, causing the mean burn duration to reduce 30% (7.0 vs 4.9s) and therefore a decreased total sampling of biological data. Furthermore, this setting generated a greater amount of carbon products on the device and tissue. An OPLS-DA model continued to clearly distinguish the 10W analysis (and to a lesser degree the 20W), however was unable to accurately differentiate between the two highest power settings (figure 5.18.B). As a result, the model had a moderate predictive ability ( $R^2X = 0.67$ ,  $Q^2 = 0.64$ ).

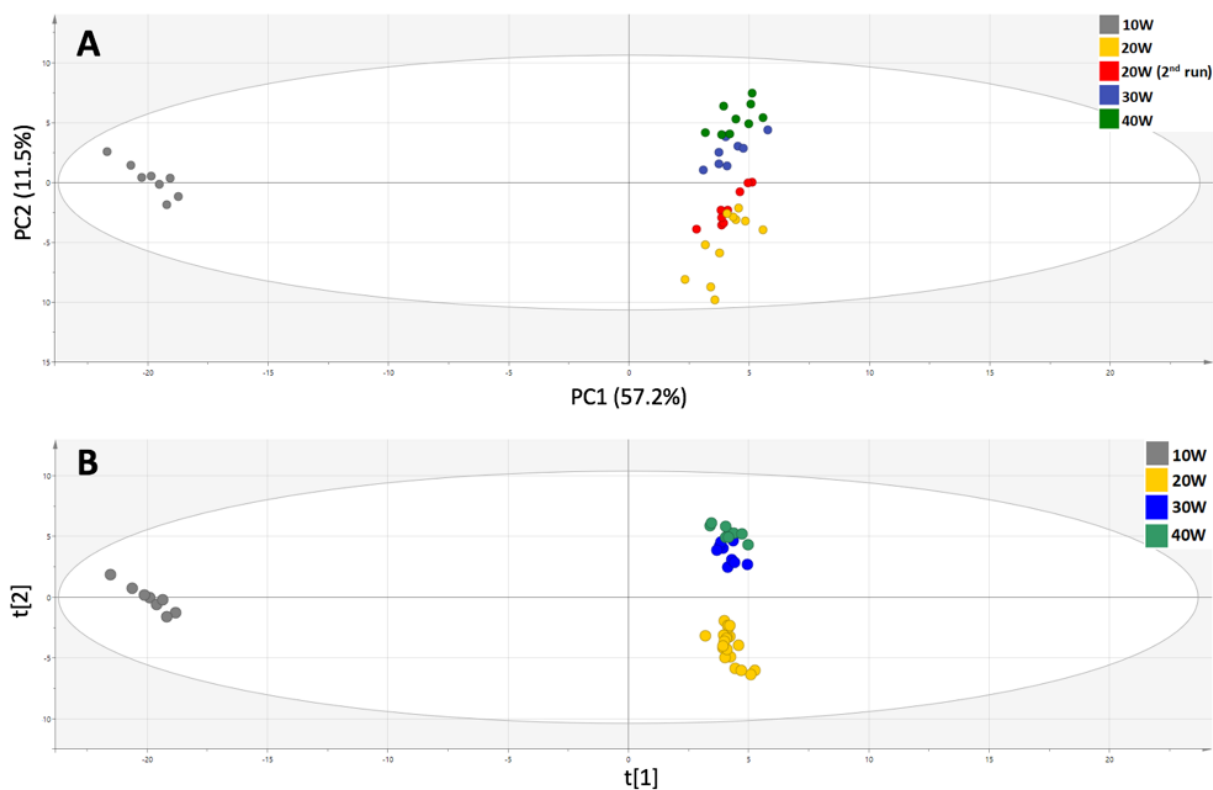


Figure 5.18 – PCA plot (A) and OPLS-DA plot with 2 X-Y and 1 orthogonal component (B) of the different power settings.

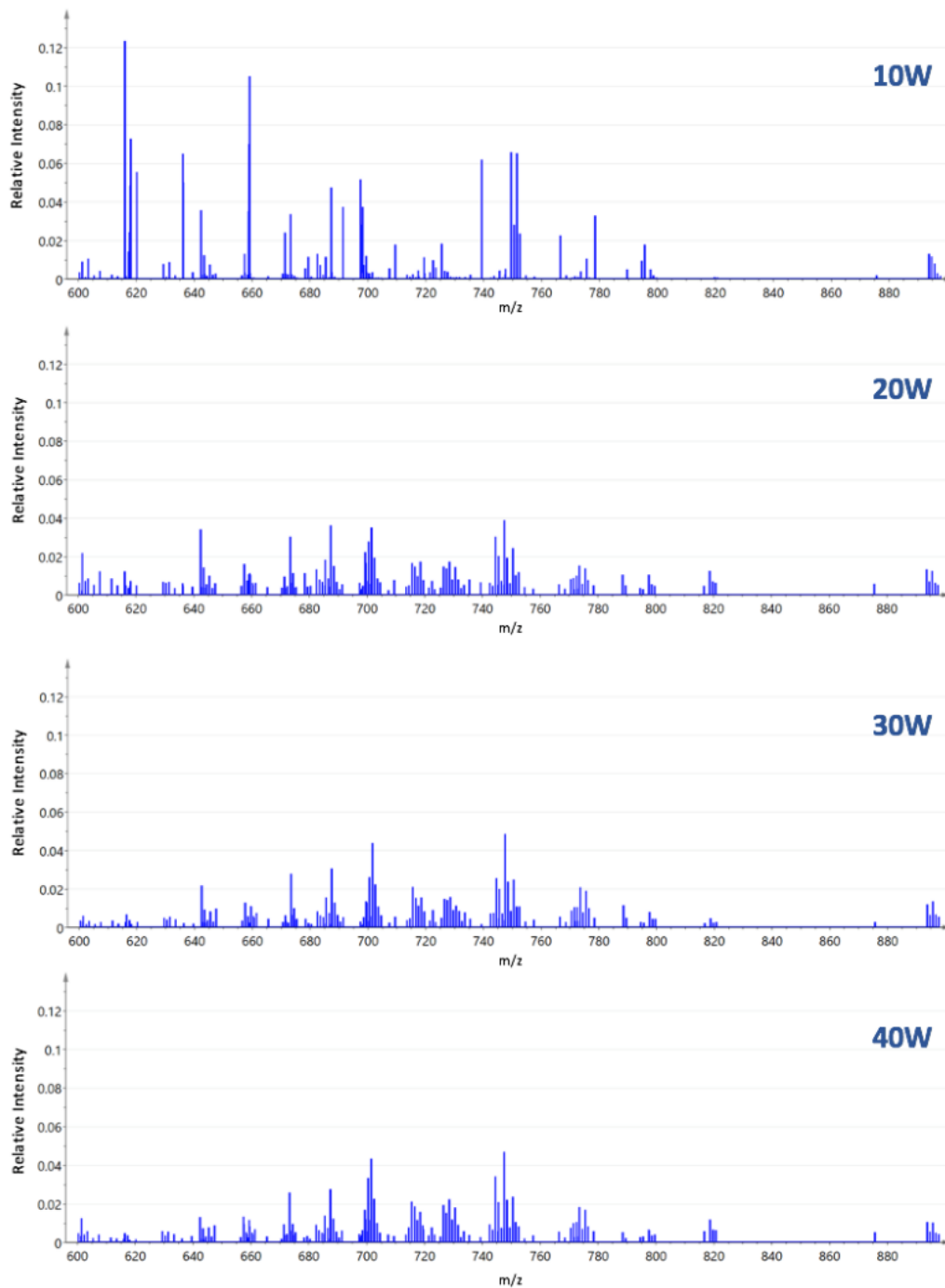


Figure 5.19 – aggregate spectra of the 150 most intense peaks across the four power settings used.

### 5.3.3.2 Diathermy Mode

Application of *coagulation* diathermy to the porcine mucosa causes markedly different spectra to be generated when compared to *cut* diathermy across the whole mass range (figure 5.20). These differences are characterized by a general reduction in the relative intensity of each peak, changes to which peaks have the highest intensity and a notable increase in total number of peaks

constituting background noise (particularly in the 150-450 m/z range). Cut diathermy generates a higher FA signal (250-350 m/z range) and GPL signal (600-800 m/z range), despite a similar TIC across the whole mass range. This signal difference caused a significant 76% reduction in signal:noise ratio in the 600-900 m/z range ( $p = <0.001$ ).

After normalising the 150 most intense bins in the 600-900 m/z range and plotting the spectra, there is a continued difference in the spectra between *cut* and *coagulation* diathermy (figure 5.20, inset). Some spectral regions show similarities, such as the GPLs between 742-753 m/z, which are largely consisting of ester linked PEs, PChs and PGs. However, the region 726-735 m/z show marked differences between diathermy modes, a region largely consisting of ether-linked PChs and PEs. There does not appear to be a difference of ionisation method as deprotonation dominates. In addition, *coagulation* mode generally seems to present a bias towards metabolites with a lower m/z, a finding which is corroborated by the loadings plot of the OPLS-DA model (figure 5.21.A). It is also apparent that less biological signal is being generated using *coagulation* diathermy even after normalisation, as the 10 metabolites with the highest relative abundance across all experiments are all statistically significantly less abundant in this group. The spectral differences are apparent in the PCA plot (figure 5.21.B), where there is clear clustering by mode and also in an OPLS-DA plot (figure 5.21.C), which has high predictive ability ( $R^2Y = 0.99$ ,  $Q^2 = 0.99$ ). ANOVA of the 150 most intense bins shows a statistically significant difference in 116 m/z values, with an almost equal split between an increase and decreased relative abundance.

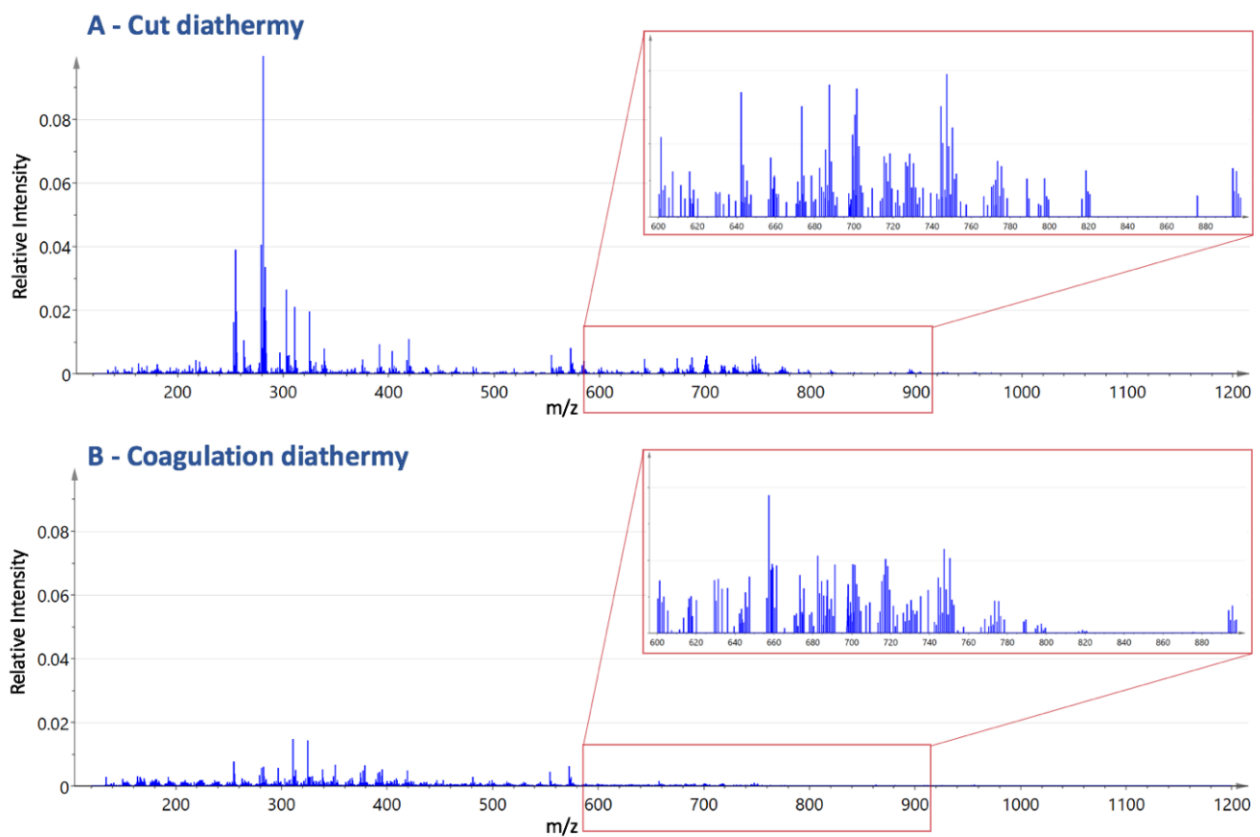


Figure 5.20 – normalised REIMS spectra over 120-1200 m/z range comparing cut (A) and coagulation (B) diathermy, with the spectra normalised over 600-900 m/z presented in the inset.

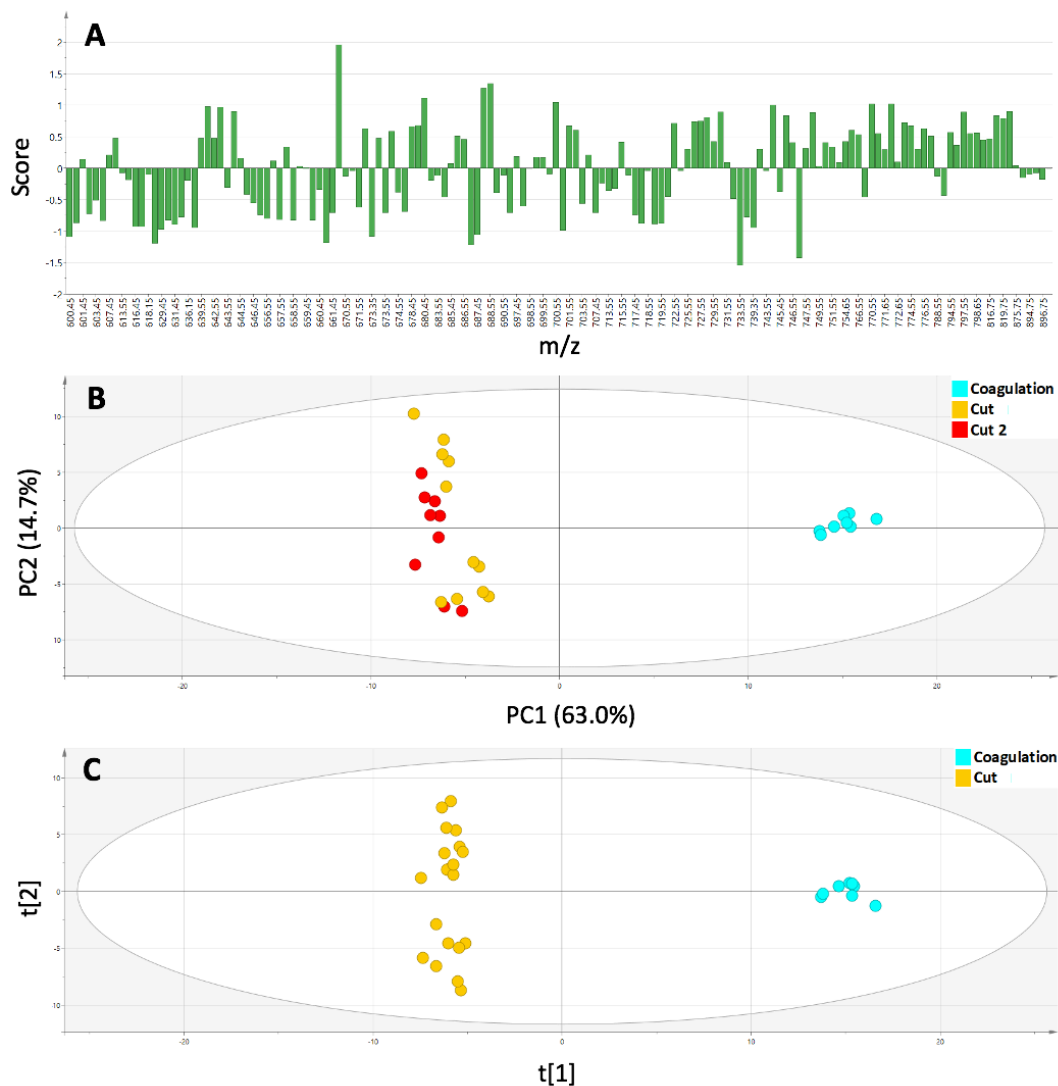


Figure 5.21 – loadings plot of the OPLS-DA model differentiating cut and coagulation mode diathermy using the 150 most intense peaks in 600-900 m/z range (A), with the PCA plot (B) and OPLS-DA plot using 1 X-Y and 1 orthogonal component (C).

### 5.3.3.3 Aspiration Tubing Length

The length of aspiration tube used in the experiments were chosen as they represent the shortest possible (1m), the standard operating procedure length (2.5m) and a longest that might be required clinically such as during laparoscopic surgery (4m). The different tubing lengths did not appear to make a difference visually to the operator during the analyses and the tubing flexibility was such that it did not interfere with instrument handling. Whilst the short (1m) and medium (2.5m) aspiration tube lengths generated very similar TICs and signal:noise ratios, there was a greater than 20% drop in TIC when increasing the tubing length to 4m ( $p = 0.04$ ). There was also a

concurrent drop in the background noise at 4m, such that there was no significant difference in signal:noise ratio between groups. Plotting the spectra of the 150 most intense bins shows great similarity between the biological signal transmitted using each tubing (figure 5.22).

Whilst the long and short tubing lengths appear to cluster separately on PCA (figure 5.23.A), spectra from the medium length tubing are interspersed and show no clear clustering. When an OPLS-DA model is plotted (figure 5.23.B), the similarities between the short and medium tubing are again revealed, with a large intra-group compared to inter-group variance; contributing to a low predictive ability of the model ( $R^2Y = 0.60$ ,  $Q^2 = 0.46$ ). ANOVA revealed only 12 m/z values that were statistically significantly different between long and medium tubing lengths, representing 17 distinct metabolites (of which five were  $^{13}C$  isotopes). There was no evidence of a clear relationship with differential lipid abundance and its subclass or adduct; however, the lower mass metabolites appeared to be of increased relative abundance in the shorter tubing length (table 5.4).

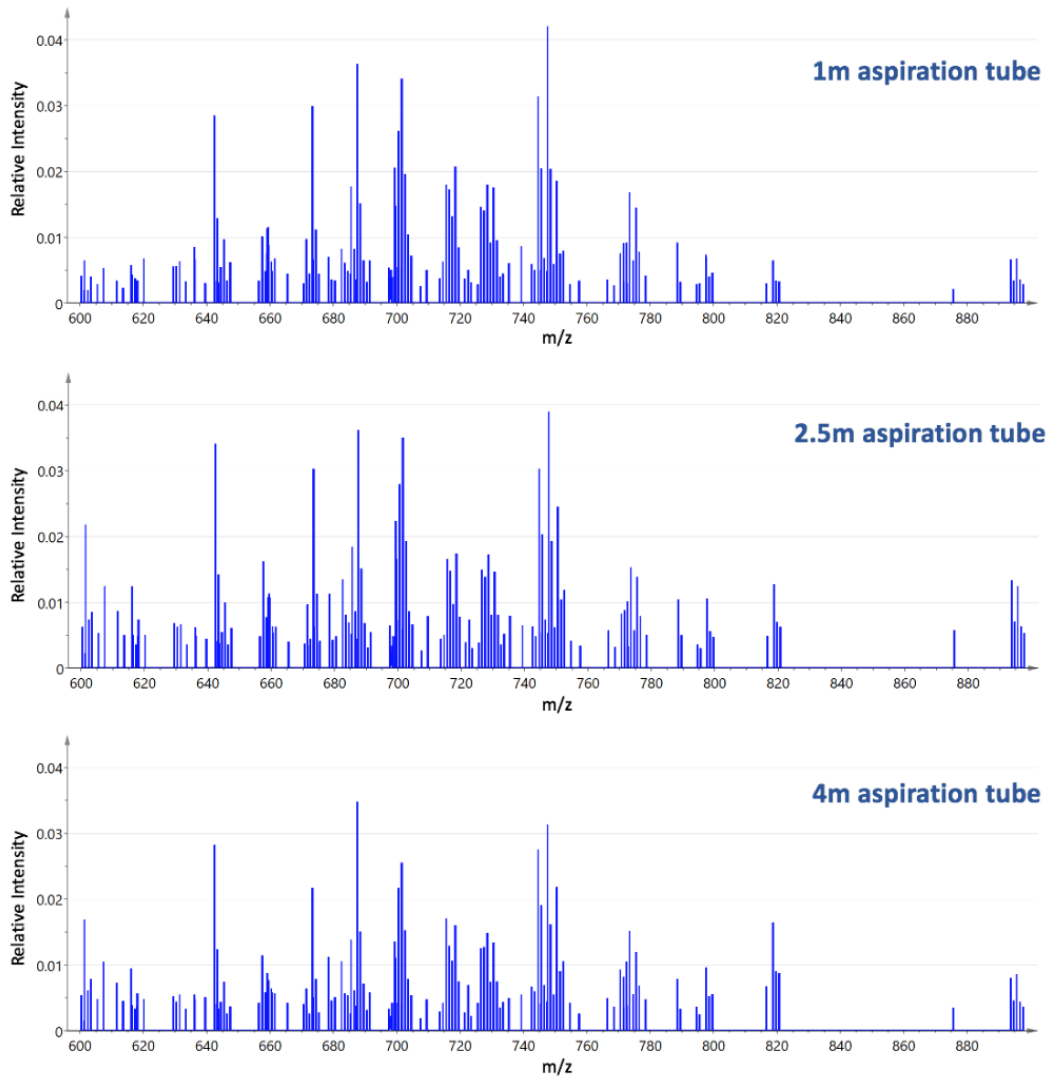


Figure 5.22 – Spectra of the 150 peaks with highest intensity comparing 1m, 2.5m and 4m aspiration tube lengths.

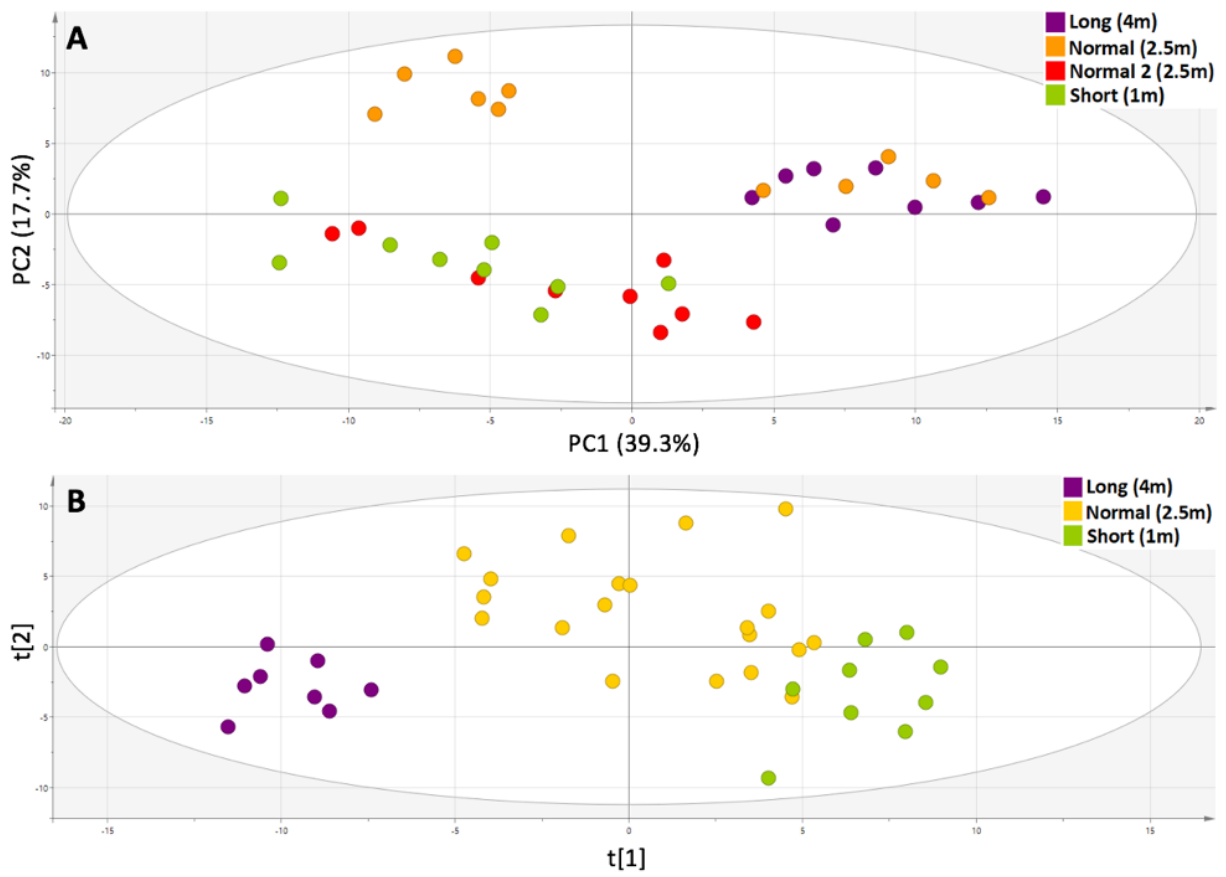


Figure 5.23 – PCA plot (A) and OPLS-DA plot using 2 X-Y and 1 orthogonal component (B) comparing the different aspiration tube lengths.

Bin	Metabolite	Highest Intensity Length	Fold Change	Corrected $p$ Value
630.45	PE(O-30:0)-H <sub>2</sub> O-H	2.5m	1.22	0.01
657.45	PE(P-16:0/16:0)-NH <sub>3</sub> -H	2.5m	1.29	0.02
672.45	PCh(P-16:1/14:0)-CH <sub>3</sub> <sup>13</sup> C isotope of PE(16:1/16:0)-NH <sub>3</sub> -H <sup>13</sup> C isotope of PE(18:1/14:0)-NH <sub>3</sub> -H	2.5m	1.60	0.03
673.45	PA(16:0/18:1)-H	2.5m	1.25	0.05
685.45	PE(O-16:0/18:1)-NH <sub>3</sub> -H PE(P-18:0/16:0)-NH <sub>3</sub> -H SM(d18:2/16:0)-CH <sub>3</sub>	2.5m	1.86	0.01
701.45	PA(18:1/18:0)-H	2.5m	1.23	0.03
719.45	PG(16:1/16:0)-H	2.5m	1.41	0.006
743.55	<sup>13</sup> C isotope of PE(36:2)-H <sup>13</sup> C isotope of PCh(34:2)-CH <sub>3</sub>	4m	1.30	<0.001
816.75	Acer(52:2;O3)-H	4m	1.43	0.02
818.75	Acer(52:1;O3)-H	4m	1.59	<0.001
819.75	<sup>13</sup> C isotope of Acer(52:1;O3)-H	4m	1.59	<0.001
820.75	Acer(52:0;O3)-H	4m	1.51	0.004

Table 5.4 – ANOVA results comparing the relative abundance of statistically significantly different metabolites using medium (2.5m) and long (4m) aspiration tube lengths. The fold change represents the degree of increase seen in the tube length with the highest intensity.

PE – phosphatidylethanolamine; PCh – phosphatidylcholine; PA – phosphatidic acid; SM – sphingomyelin; PG – phosphatidylglycerol; Acer – acylceramide.

#### 5.3.3.4 Presence of Contamination

The common contaminants blood and NaCl (as saline solution at 1.8%) were placed on the tissue at the point of dissection, which is similar to how it may be encountered clinically. It was observed during the analysis that having additional aqueous material on the tissue fractionally increased the time taken for tissue ablation to occur, however the burn duration in the MS was not increased compared to normal mucosal sampling. The presence of both contaminants appeared to have caused ion suppression, with the TIC falling by 21 and 54% respectively for blood and saline (Table 5.3).

The PCA plot reveals saline analyses clustering distinctly, however the presence of blood does not appear to cause additional variation from the analyses with no contamination (figure 5.24.A). An

OPLS-DA model (figure 5.24.B) is able to distinguish between each contaminant and normal tissue with a high degree of accuracy ( $R^2Y = 0.88$ ,  $Q^2 = 0.84$ ). When plotting the spectra of the 150 most intense bins (figure 5.25), it appears that the spectra have a generally similar biological signal, however the presence of saline causes a consistent increase in the relative abundance of certain metabolites, which in turn, impact the model loadings (figure 5.24.C). Table 5.5 lists the 30 bins with the most significantly different abundance with the addition of saline. When looking at the metabolites that ionize with a  $Cl^-$  adduct, they tend to increase in abundance with the addition of saline (the case with all TGs and one DG). Those metabolites ionizing through deprotonation or demethylation only increase in 9% of cases when saline is added. 26 bins representing 42 identified metabolites (including 15 isotopes) were found to be of significantly different relative abundance with the presence of blood, as shown in table 5.6. This demonstrates that 71% of bins with increased abundance contained a PE species (often in a mixture), in comparison to 29% of those that decreased in abundance.

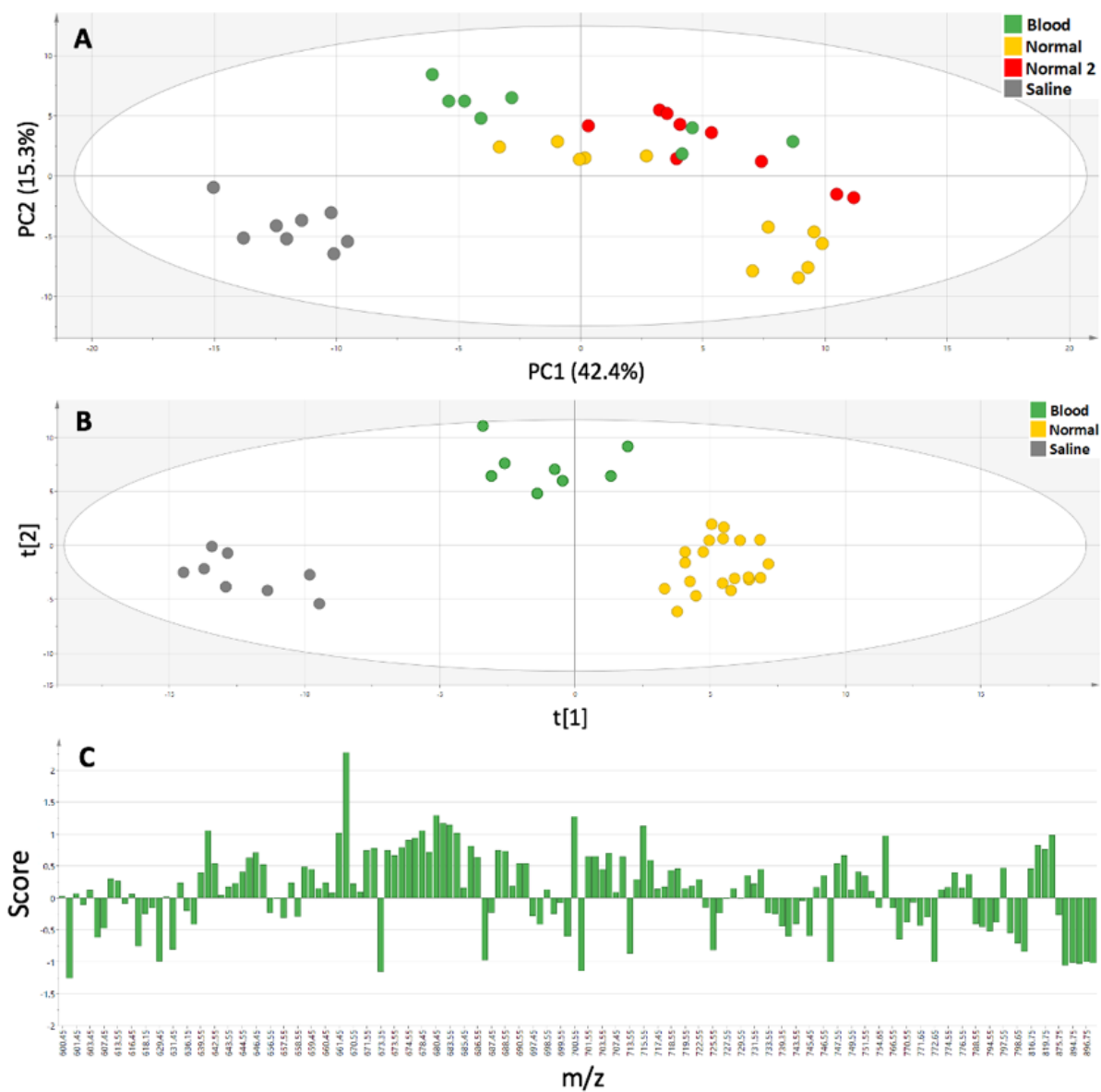


Figure 5.24 – PCA (A) and OPLS-DA using 2 X-Y and 1 orthogonal component (B) plots of the spectra generated with and without tissue contamination. The loadings plot from the OPLS-DA model is shown (C).

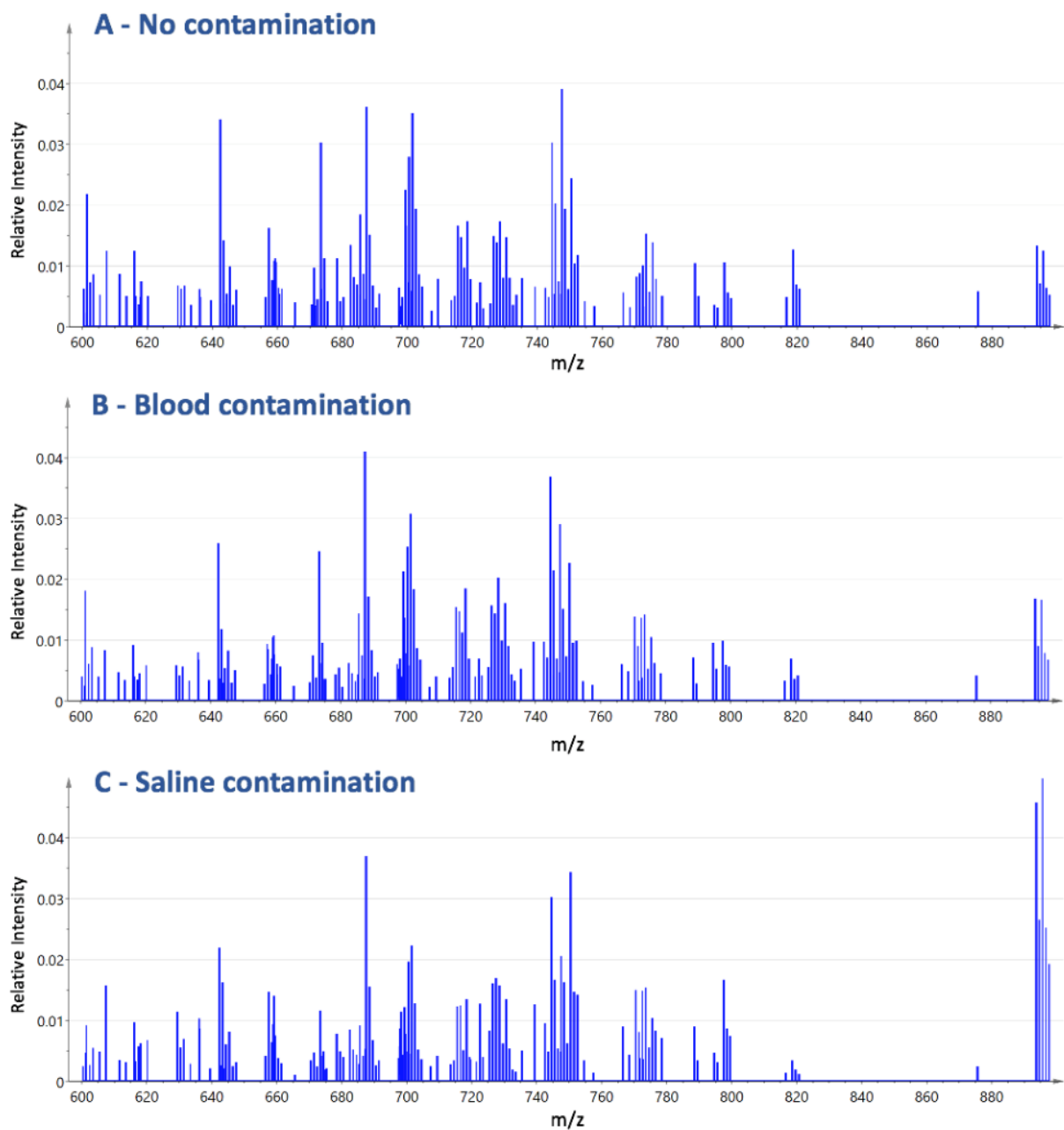


Figure 5.25 - The spectra of the 150 most intense peaks comparing no contamination (A), blood on the mucosa (B) and saline on the mucosa (C).

Bin m/z	Metabolite	Relative Abundance with Saline	Fold Change	Corrected p Value
600.45	CerP(d34:0)-H <sub>2</sub> O-H	Decreased	2.18	1.99E-06
601.35	Background noise	Increased	0.43	1.78E-09
629.45	DG(34:1)+Cl	Increased	0.53	1.72E-09
642.55	PE_Cer(34:1)-NH <sub>3</sub> -H	Decreased	1.66	1.53E-07
643.55	<sup>13</sup> C isotope of PE_Cer(34:1)-NH <sub>3</sub> -H	Decreased	1.73	3.14E-07
644.55	PE_Cer(34:0)-NH <sub>3</sub> -H	Decreased	1.83	1.67E-08
660.45	Same peak as m/z 660.55	Decreased	2.02	3.15E-10
660.55	<sup>13</sup> C isotope of PE(O-16:0/16:0)-NH <sub>3</sub> -H	Decreased	1.48	8.35E-07
661.45	DG(34:1;O2)+Cl	Decreased	2.33	1.57E-11
665.55	Unknown	Decreased	3.61	2.44E-07
673.45	PA(16:0/18:1)-H	Decreased	2.29	5.27E-10
674.45	<sup>13</sup> C isotope of PA(16:0/18:1)-H	Decreased	2.16	4.96E-09
674.55	Same peak as m/z 674.45	Decreased	1.92	2.34E-06
685.55	PE(O-16:0/18:1)-NH <sub>3</sub> -H PE(P-18:0/16:0)-NH <sub>3</sub> -H SM(d18:2/16:0)-CH <sub>3</sub>	Decreased	1.76	2.53E-06
686.55	<sup>13</sup> C isotope of above mixture	Decreased	1.86	7.83E-07
703.55	PA(18:0/18:0)-H SM(34:1;O3)-CH <sub>3</sub>	Decreased	1.60	3.00E-07
717.55	<sup>13</sup> C isotope of PE(18:1/16:0)-H <sup>13</sup> C isotope of PCh(16:1/16:0)-CH <sub>3</sub>	Decreased	2.10	1.45E-08
723.45	PE(20:3/16:0)-NH <sub>3</sub> -H PA(20:4/18:0)-H	Increased	0.62	2.86E-07
733.55	PE(P-18:0/20:4)-NH <sub>3</sub> -H	Decreased	3.04	6.63E-08
747.55	PG(18:1/16:0)-H	Decreased	1.78	7.12E-08
757.55	DG(44:7)+Cl	Decreased	2.25	3.30E-06
816.75	Acer(52:2;O3)-H	Decreased	4.78	3.34E-09
818.75	Acer(52:1;O3)-H	Decreased	4.77	6.16E-08
819.75	<sup>13</sup> C isotope of Acer(52:1;O3)-H	Decreased	4.47	1.86E-07
820.75	Acer(52:0;O3)-H	Decreased	6.20	4.00E-09
893.75	TG(18:1/18:1/16:0)+Cl	Increased	0.15	4.39E-13
894.75	<sup>13</sup> C isotope of TG(18:1/18:1/16:0)+Cl	Increased	0.14	4.86E-13
895.75	TG(18:1/18:0/16:0)+Cl	Increased	0.15	8.90E-13
896.75	<sup>13</sup> C isotope of TG(18:1/18:0/16:0)+Cl	Increased	0.15	6.11E-13
897.75	<sup>37</sup> Cl isotope of TG(18:1/18:0/16:0)+Cl	Increased	0.17	2.47E-12

Table 5.5 – the 30 most statistically significant m/z values on ANOVA between the spectra of saline and with no contamination. The fold change represents the degree of increase seen in the group with the highest intensity.

CerP – ceramide-1-phosphate; DG – diacylglycerol; PE\_Cer – ceramide phosphatidylethanolamine; PE – phosphatidylethanolamine; PA – phosphatidic acid; SM – sphingomyelin; PCh – phosphatidylcholine; PG – phosphatidylglycerol; Acer - acylceramide; TG - triacylglycerol.

Bin m/z	Metabolite	Relative Abundance with Blood	Fold Change	Corrected <i>p</i> Value
601.35	Background noise	Increased	0.68	0.003
630.45	PE(O-30:0)-H <sub>2</sub> O-H	Decreased	1.23	0.005
643.55	<sup>13</sup> C isotope of PE_Cer(34:1)-NH <sub>3</sub> -H	Decreased	1.36	0.001
660.55	<sup>13</sup> C isotope of PE(O-16:0/16:0)-NH <sub>3</sub> -H	Decreased	1.24	0.008
661.45	DG(34:1;O2)+Cl	Decreased	1.26	0.045
687.55	SM(d16:1/18:0)-CH <sub>3</sub> SM(d16:0/18:1)-CH <sub>3</sub> PE(O-18:0/16:0)-NH <sub>3</sub> -H	Increased	0.85	0.039
688.55	<sup>13</sup> C isotopes of above mixture	Increased	0.82	0.001
689.55	x2 <sup>13</sup> C isotope of above mixture	Increased	0.84	0.008
698.25	Background noise	Increased	0.45	1.6E-4
719.45	PG(16:1/16:0)-H	Decreased	1.40	0.007
723.45	PE(20:3/16:0)-NH <sub>3</sub> -H PA(20:4/18:0)-H	Increased	0.67	4.1E-4
733.55	PE(P-18:0/20:4)-NH <sub>3</sub> -H	Decreased	1.61	0.003
742.55	PE(18:1/18:1)-H PE(18:2/18:0)-H PCh(18:1/16:1)-CH <sub>3</sub> PCh(18:2/16:0)-CH <sub>3</sub>	Increased	0.70	8.1E-7
743.55	<sup>13</sup> C isotopes of above mixture	Increased	0.70	2.4E-5
744.55	PE(18:1/18:0)-H PCh(18:1/16:0)-CH <sub>3</sub> PCh(18:0/16:1)-CH <sub>3</sub>	Increased	0.77	7.4E-6
745.55	PG(18:2/16:0)-H <sup>13</sup> C isotope of PE(18:1/18:0)-H <sup>13</sup> C isotope of PCh(18:1/16:0)-CH <sub>3</sub>	Increased	0.87	0.008
747.55	PG(18:1/16:0)-H	Decreased	1.28	0.01
770.55	PE(18:1/20:1)-H PE(18:2/20:0)-H PE(22:2/16:0)-H	Increased	0.61	0.03
772.55	PCh(18:1/18:0)-CH <sub>3</sub> <sup>13</sup> C Isotope of PG(18:2/18:1)-H	Increased	0.76	0.009
772.65	Same peak as m/z 772.55	Increased	0.74	0.008
775.55	PG(18:1/18:0)-H	Decreased	1.21	0.04
794.55	PE(22:4/18:0)-H	Increased	0.47	7.8E-5
795.55	Unknown	Increased	0.65	1.9E-4
816.75	Acer(52:2;O3)-H	Decreased	1.48	0.02
818.75	Acer(52:1;O3)-H	Decreased	1.52	0.04
820.75	Acer(52:0;O3)-H	Decreased	1.56	0.02

Table 5.6 – the 26 m/z values which were significantly different on ANOVA between the spectra of blood-covered mucosa and that with no contamination. The fold change represents the degree of increase seen in the group with the highest intensity.

PE – phosphatidylethanolamine; PE\_Cer – ceramide phosphatidylethanolamine; DG – diacylglycerol; SM – sphingomyelin; PG – phosphatidylglycerol; PA – phosphatidic acid; PCh – phosphatidylcholine; Acer – acylceramide.

#### 5.3.4 Discussion

This project explored the impact of technical and environmental factors on the quality and composition of spectra generated by REIMS when coupled to monopolar diathermy in a porcine model. It revealed that some factors dramatically impact REIMS spectra, which raises concern for how this would influence the ability of REIMS to accurately perform intraoperative tissue recognition and may prompt recommendations to be made for intraoperative use.

When translating the REIMS technology into a clinical setting such as in the operating theatre, the nature of the procedure being undertaken will place requirements on the analytical platform for which there is little control. The variables studied in this project were chosen as there was reason to believe that they could impact REIMS spectra whilst being factors which could vary considerably between the laboratory setting and different *in vivo* scenarios. The analytical plan for this project was designed to generate the most representative spectra for each experimental condition, where spectra which were demonstrably outlying on PCA were removed; as these are, by definition, not characteristic of the rest of the group. This reduced the total number of analyses by 10-20% in some cases but was necessary to ensure experiment clusters had small intra-group variance, aiding discrimination between experiments using the inter-group variance. There was no apparent reason when conducting the analyses why some spectra would become outliers when plotted with PCA (they were macroscopically identical to the operator in a very controlled setting), with the possibility of it being a stochastic process. This is with the exception of the 10W power setting, where the power was insufficient to rapidly and reliably generate enough heat to cause explosive cell rupture; with this variability causing large differences when plotting a PCA. Whilst the possible impact of ambient humidity and temperature on REIMS spectra is unknown, these were diligently measured and maintained within tight bounds to ensure minimal impact on the findings. For pragmatic reasons these were set at standard room conditions (19.9-21.5°C temperature, 48.1-56.2% relative humidity), however it is recognised that during *in vivo* use, the temperature and humidity may be very different (for example, the colon lumen is likely to have a humidity approaching 100%); or may fluctuate throughout a procedure. Humidity has previously been demonstrated to impact the relative abundance of small anionic electrolytes within aerosols when analysed by TOF MS, likely due to the impact on droplet size<sup>334</sup>. Whether this impacts REIMS is an important consideration and will need to be the focus of future work. The efforts to generate representative spectra for each condition appears a success when noting that the two 'normal'

conditions, performed at the beginning and end of the analytical run, cluster on PCA with an inter-group variance that is less than the intra-group variance. This reassures that differences seen between the experiments are not as a function of time and therefore a possible technical batch effect (caused by factors such as mass drift or loss of TOF vacuum pressure).

It was decided to use the 150 most intense  $m/z$  bins across the dataset to build the PCA and OPLS-DA models, in order to identify group differences based on biologically relevant molecules and to exclude the impact of random background noise. It was also important to select a considered number of  $m/z$  values to be able to identify differences in abundance by lipid class and this was possible, where level 2 or 3 identification was achieved for 160 metabolites. Furthermore, considering only 5  $m/z$  values appeared to be of background peaks, the number of variables chosen appears suitable. It may be possible that some differences between experiments would have been evident when including peaks of lesser intensity, however, models built with a variation in the number of  $m/z$  values showed little difference between them.

When a clinician is deciding the diathermy power setting, it is standard practice to choose the lowest power that will efficiently achieve the surgical goal (usually concomitant dissection and coagulation), in order to avoid any unnecessary additional tissue damage due to thermal spread. This power may vary considerably depending on the clinical scenario and therefore guidelines are not prescriptive in which power setting to use and warn more of an inappropriately low rather than high power<sup>41</sup>. Whilst the inadequacy of 10W to reliably cause cell rupture has been discussed, relatively little difference was apparent between 20, 30 and 40W. It may be expected that increasing the power would cause a progressively greater TIC, however this was not apparent and instead, increased formation of carbonised products was witnessed over a shorter burn duration. This is consistent with previous findings, which also raise the concern that increased powers may also cause thermal degradation of lipids, such as loss of ammonia from PEs<sup>133</sup>. Considering the high-quality data generated using at least 20W power, the similarities between these power settings, and that intraoperative use of diathermy is typically at 20W or greater; variation in the power setting will not be considered a risk for successful translation of REIMS. The diathermy mode does, however, appear to cause dramatic differences in REIMS spectra; such that a large proportion of the biological information is lost when using *coagulation* rather than *cut* mode. In *coagulation* mode, the intermittent application of the current waveform is designed not to cause a thermal load sufficient for explosive cell rupture (as seen with *cut* mode) and instead, is

designed to dry cells and coagulate proteins to cause haemostasis<sup>335</sup>. Considering the majority of complex lipids are found in cell membrane bilayers<sup>336</sup>, which would require explosive rupture to be released in the aerosol; this explains why coagulation mode has a significantly decreased signal within 600-1000 m/z and a bias towards generating metabolites of a lower mass. A further consideration is the use of mixed or blended diathermy modes, where the waveform applied is somewhere on a continuum between pure *cut* and pure *coagulation*; designed to offer the benefits of both modes<sup>41</sup>. This is of particular clinical relevance for endoscopy, as the exact settings chosen can differ significantly between endoscopists<sup>337</sup>, which can be impacted by personal preference, local practice and the shape or size of the polyp being removed. The European Society of Gastrointestinal Endoscopy recommend the use of automated microprocessor-controlled blended diathermy, which will vary the electrocautery waveform administered during application; based on tissue response<sup>41</sup>. The impact of variation in blended diathermy modes on REIMS spectra is unclear and needs to be explored in future work. The loss of metabolic information when pure coagulation diathermy is used presents spectra as dramatic outliers on a PCA plot and therefore incorporating this source of heterogeneity (and systematic bias) when creating high quality *ex vivo* spectral databases counteracts the aims of this thesis.

It was necessary to assess whether the distance between the analytical site and mass spectrometer impacts REIMS spectra considering the variation in aspiration tube length that can occur during *in vivo* deployment. For example, during colonoscopy, the surgical aerosol must travel the length of the colonoscope (circa. 1.7m) and then across the room to the MS, which must be away from the bedside as to not interfere with direct patient care. The concern is that during transport, there may be loss of ionic clusters or metabolite-containing water droplets due to ion-ion interactions or impact with the tubing material<sup>338</sup>. Previous research has shown that free gas-phase ions are largely eradicated over long tubing distances, with a 6 fold drop over just the first 5cm, implying that these are not a significant component of the metabolites detected with REIMS<sup>339</sup>. This project demonstrated only a 35% TIC reduction between a 1 and 4m tube (similar to previous findings over 1 and 3m<sup>340</sup>), implying that the aerosol has a high degree of stability over this distance and that the majority of losses are likely to be between the point of formation and before the creation of a linear gas flow. The reduction in background noise when using long tubing was not as marked as when transporting ions in DESI<sup>340</sup>, most likely due to the collision surface used in REIMS and the additional background that this will create. However, the signal:noise ratio was preserved and therefore it is reassuring when longer tubing must be used *in vivo*. It is unclear

why there was a slight bias towards higher  $m/z$  metabolites within the 600-1000  $m/z$  range when the tubing length was increased, raising the possibility that a higher mass protects against transport losses.

Contamination of the mucosal surface during an interventional procedure is commonplace, with blood being a consequence of trauma (most often through tissue dissection) and NaCl (saline) solution being used as an irrigation fluid (to clear items such as tissue debris, blood and faecal residue). Both contaminants could be found at the point of dissection and the ion suppression that was evident was likely due to additional salts being carried into the MS within the polar water droplets. Furthermore, the chemical and biological constituents of saline and blood appear to impact REIMS spectra differently. The increase in metabolites with  $\text{Cl}^-$  adducts when NaCl solution was added to the tissue surface is likely due to the increased concentration of free  $\text{Cl}^-$  ions impacting the ionisation efficiency of those metabolite classes which are liable to ionize with this adduct, most notably TGs and DGs<sup>341</sup>. This is the first description of this phenomenon during REIMS, with it previously described during ESI using  $\text{Cl}^-$ ,  $\text{Li}^+$ ,  $\text{NH}_4^+$  and  $\text{Na}^+$ <sup>342-344</sup>. The concentration of NaCl solution was 1.8% in this project, which was deliberately chosen as double the isotonic solution used clinically in order to more clearly demonstrate the difference. Considering the difference in TG presence throughout the bowel wall (higher abundance in submucosa and pericolic fat, demonstrated in unpublished work by the research group), the presence of saline at the analytical surface may impact layer detection accuracy. The increase in relative abundance of PEs seen with the presence of blood may not represent a change in ionisation efficiency but instead an increase in PEs present at the point of analysis, as they are major constituents of the lipid bilayer of red blood cells and are free in plasma<sup>345,346</sup>. Blood is a complex mixture of many other biological materials (for example proteins and carbohydrates), electrolytes (of which the most abundant are  $\text{Cl}^-$ ,  $\text{Na}^+$ ,  $\text{HCO}_3^-$  and  $\text{Ca}^{2+}$ ) and environmental molecules such as medications; such that it is difficult to predict the response of REIMS spectra when variation in the constituents exist between patients. Considering the impact on REIMS spectra demonstrated by the presence of both blood and saline contaminants, it will be recommended that these are minimised during intraoperative use of the technology.

The greatest limitation of this work is that although the impact on REIMS spectra between these technical and environmental factors have been described using a controlled and repeatable method in a porcine model, the impact on diagnostic accuracy has not been assessed. Achieving

this would require the use of a large volume of tissue from a single patient, which contains a variety of pathologically homogenous pathologies that are sufficient in size for the greater than 100 required analyses. It is not possible to access such patient tissue (due to sampling limitations with the histopathology department) and any compromise would not allow the consistent and reproducible sampling methodology employed in this experiment. Another limitation is in understanding how the findings are to be applied for future experiments. For example, whilst recommendations have been made to exclude spectra generated using coagulation diathermy from the *ex vivo* reference spectral database (that is then used to build models for *in vivo* tissue recognition), if a clinician chooses to use coagulation diathermy during a case, it is unclear if that should be permitted to undergo tissue recognition. It is necessary to strike a balance between the accuracy of tissue recognition and being flexible to the requirements and variation that comes with clinical practice, which can be challenging when the experimental data to inform those decisions are limited.

#### 5.4 Chapter Conclusion

This chapter has explored the raw spectral data generated by REIMS analysis of colorectal tissues in an attempt to understand how spectral quality can be defined in addition to the impact of technical and environmental variables. For the most part, the experiments conducted have never been described in the literature, with many insights generated here which will directly inform the development and application of the technology moving forward. By taking a rigorous and systematic approach to the experiments, the findings allow data-driven decisions which will be applied later in this thesis to improve the quality, reproducibility and applicability of REIMS. Ultimately, application of these findings will be used to improve the accuracy of REIMS in tissue recognition with the final goal of that positively impacting patient care.

The next phase in developing this technology is the creation and curation of an *ex vivo*, high-quality, clinically annotated spectral reference database. Improvements in the sample and data analysis derived from this chapter will allow this to be achieved to the highest potential whilst managing identified systemic biases. This can then be used to determine the accuracy of REIMS in differentiating colorectal pathologies using lipid metabolites and appraise the biological processes underpinning this.

## Chapter 6 – WP2: Creation and analysis of an *ex vivo* colorectal REIMS spectral database

### 6.1 Chapter Aims, Objectives and Research Questions

The aim of this chapter is to create a high-quality, powerful, pathologically validated and clinically annotated spectral database of *ex vivo* REIMS analysis of colorectal tissues, upon which chemometric functions will be applied. This is necessary to understand how REIMS can be applied to clinically relevant problems such as tissue recognition and risk stratification, whilst having the potential to reveal the metabolic fingerprints associated with specific clinical phenotypes. It is also a fundamental requirement of the *in vivo* work presented in chapter 7, where this database will be used to power the machine learning algorithms for real-time tissue recognition.

This task can be distilled into three phases, which have the following objectives:

#### **1. Creation of a spectral database**

- a. To perform REIMS analysis of human colorectal tissues *ex vivo*
- b. To collect relevant experimental, clinical and pathological metadata to annotate each REIMS spectra
- c. To apply the minimum spectral quality requirements determined from chapter 5 and formulate a finalised database suitable for statistical analysis

#### **2. Application of chemometric functions**

- a. To build multivariate statistical models to assess REIMS' ability to differentiate clinically and pathologically relevant groups based on the cellular composition of lipid metabolites
- b. To use univariate and multivariate techniques to identify the m/z of lipid metabolites that are of different relative abundance between groups in multivariate models

#### **3. Identification of lipid metabolites**

- a. To perform REIMS MS/MS on colorectal normal, adenoma and carcinoma tissues to collect spectra detailing the fragmentation patterns of unknown metabolites
- b. To propose the molecular structure of lipid metabolites from their mass and fragmentation pattern

- c. To understand how the relative abundance of lipid metabolites differs between clinically and pathologically relevant groups

The completion of these objectives will allow the following research questions to be addressed:

1. What is the diagnostic accuracy of REIMS in performing colorectal tissue recognition? Can it differentiate between normal, adenoma and carcinoma; or between normal and diseased tissues?
2. Can REIMS risk-stratify colorectal adenomas and carcinomas by predicting the presence of histological features of poor prognosis?
3. What are the unique lipid metabolic fingerprints associated with clinical phenotypes?

## 6.2 Methods

Full details of the methodologies used in this chapter regarding patient recruitment, sample collection, MS analysis and statistical processes can be found in chapter 4; with specific features to this study stated below.

### 6.2.1 Patient recruitment and sample collection

Patients who had undergone surgical or endoscopic colorectal resection between November 2014 and November 2019 and had been recruited for colorectal tissue bio-banking were eligible for inclusion in this study. Patients with inflammatory bowel disease, hereditary polyposis syndromes, age less than 18 years or tissue samples of less than 5mg were excluded.

### 6.2.2 MS analysis and specifications

REIMS MS analysis was conducted *ex vivo* in 24 batches between January 2015 and November 2019, using a handheld monopolar diathermy pencil at 20-25W or a CO<sub>2</sub> laser in 'SuperPulse'

mode at 3W. The surgical aerosol was aspirated into the Xevo G2-S qTOF mass spectrometer with the Venturi interface and co-aspiration of leu-enkephalin in isopropanol (20ng/ml concentration) at a flow rate of 0.2ml/min. Spectra were collected in negative mode across the 150-1200 m/z range. All tissue samples and spectra generated prior to October 2017 were collected by Dr James Alexander, with me responsible for all data collection after this time. All processing, analysis and interpretation of all data was performed by me.

MS/MS was conducted in 5 batches between November 2017 and October 2020 using the methodology previously described (see section 4.5.1.1). Where possible, additional tissue samples were sourced from the biobank from patients whose tissue had previously been analysed with MS to build the models. m/z values were prioritised for MS/MS based on a combination of the log fold change in relative abundance, the degree to which differences were statistically significant and their contribution to the statistical model.

### 6.2.3 Statistical analyses

Raw spectral data were binned at 0.1 and underwent normalization, lock-mass correction and background subtraction. The minimum thresholds of spectral quality as defined in chapter 5 was applied, with poor-quality spectra excluded from further analyses. Modelling was conducted using PCA and LDA (up to 60 PC components) between 150-1000m/z, with LOPO CV used to determine the accuracy of REIMS in differentiating the groups of interest. This was achieved in AMX, where clinico-pathological data of choice could be used to assign a 'classification' to each spectra ahead of building the models. OPLS-DA models were also built in SIMCA to assess the robustness of classification accuracy by using a cross-validation plot and using accuracy metrics such as  $R^2$  and  $Q^2$ .

## 6.3 Results

1526 spectra were generated from the *ex vivo* REIMS analysis of colorectal tissue from 189 patients. The minimum spectral quality thresholds defined in chapter 5 were applied, with the impact on spectra shown in table 6.1. There was 554 instances of spectra failing a quality

threshold, however due to some spectra failing for more than one reason, a total of 513 were excluded. Figure 6.1 presents examples of validation sections annotated with the tissue types present and explanations of how they were classified.

Criteria for Exclusion	Total Number of Spectra Affected	Notes
Presence in batch effect	116	This covered the same batch of spectra described in section 5.2.3.2 where there was mass shift due to inadequate calibration of an instrument
Inadequate signal:noise	171	These spectra all had signal:noise ratios of <1000, with an average of 616 and range of 96-998
Sampling of non-mucosal tissue	160	This was largely consisting of spectra demonstrating high TG levels (and therefore excess sampling of the submucosa) in addition to validation sections where no mucosa was present (most often showing only muscle or fat)
Validation slide non-diagnostic	85	The validation slide showed evidence of mucosa being present in the sample, but the proportion of the section that was the adenoma or carcinoma was below 15%.
Energy device not monopolar diathermy	20	These consist of the use of coagulation diathermy (n=16) or a CO <sub>2</sub> laser (n=4)
Sodium formate contamination	2	Clusters of sodium formate were seen across the mass range of one sample, including in bins with known lipid metabolites

Table 6.1 – the number of spectra which did not meeting the minimum standards of quality and therefore would be eligible for exclusion from statistical modelling.

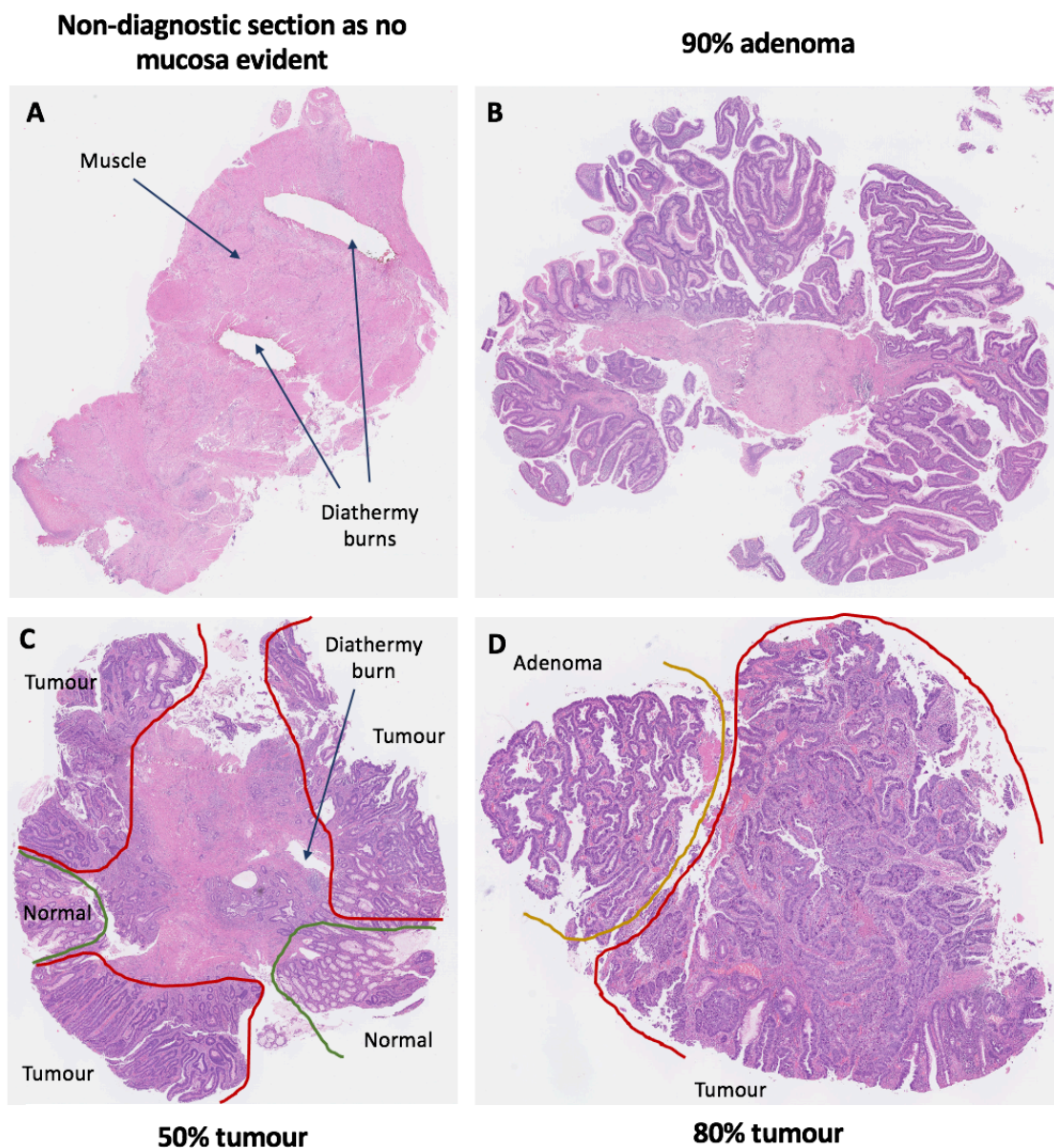


Figure 6.1 – four validation sections following REIMS analysis annotated with the tissue types seen and the final classification given. Section **A** shows no abnormalities but considering there was no mucosa evident (and instead only muscle), it was deemed non-diagnostic and the spectra generated were excluded. Section **B** shows a villous adenomatous polyp, which is deemed to be 90% adenoma due to the small portion of muscle in the centre. Section **C** is heterogeneous with multiple different regions of tissue subtypes. Despite the diathermy burn not being in a tumour region directly, this was classified as 50% tumour. Section **D** is a mixed sample, which is diagnostic for cancer and is validated at 80% due to the 20% villous adenoma adjacent.

After spectral quality control, data from 161 patients was suitable for inclusion in statistical modelling, generating a total of 1013 REIMS spectra from tumour (n=346), adenoma (n=247) and normal (n=420) colorectal tissues. The demographics of the included patients and sampling details are presented in table 6.2. REIMS analysis was conducted on 109 tissue samples from 79 distinct

tumours, 134 tissue samples from 56 polyps and 137 pieces of normal mucosa. Of the 56 polyps analysed by REIMS, 50 were validated as adenomas, 5 were carcinomas and one was a fibro-epithelial polyp (classified as normal for classification models). Of the 79 tumours sampled, 75 were histologically validated as carcinomas, 3 were adenomas and 1 only sampled normal tissue. The pathological metadata for the carcinomas and adenomas included in the study are presented in tables 6.3 and 6.4 respectively.

<b>Characteristic</b>		<b>Number (%)</b>
Mean age (range)		70 (34-91)
Gender (M:F)		88:73
Ethnicity	White	98 (61)
	Asian	18 (11)
	Black	14 (9)
	Other	12 (7)
	Unknown	19 (12)
Hospital of collection	St Mary's	139 (86)
	Royal Marsden	12 (7)
	Charing Cross	10 (6)
Collection method	Radical surgery	119 (74)
	Endoscopic	32 (20)
	Local excision	10 (6)
Location of sample	Right	62 (39)
	Left	36 (22)
	Rectum	57 (35)
	Unknown	6 (4)

Table 6.2 – demographics of the 161 included patients with details of how samples were collected.

Pathology of Carcinomas		Number (%)
Pathological subtype	Adenocarcinoma	61 (76)
	Mucin-producing adenocarcinoma	3 (4)
	Mucinous adenocarcinoma	14 (18)
	Unknown	2 (3)
Differentiation	Well	9 (11)
	Moderate	49 (61)
	Poor	17 (21)
	Unknown	5 (6)
Tumour budding	Yes	54 (68)
	No	21 (26)
	Unknown	5 (6)
Lymphovascular invasion	Yes	29 (36)
	No	46 (58)
	Unknown	5 (6)
Extramural venous invasion	Yes	28 (35)
	No	46 (58)
	Unknown	6 (8)
T stage	1	5 (6)
	2	15 (19)
	3	41 (51)
	4	15 (19)
	Unknown	4 (5)
N stage	0	49 (61)
	1	18 (23)
	2	8 (10)
	Unknown	5 (6)
M stage	0	72 (90)
	1	5 (6)
	Unknown	3 (4)
AJCC stage at diagnosis	I	18 (23)
	II	31 (39)
	III	22 (28)
	IV	5 (6)
	Unknown	4 (5)
Neoadjuvant oncologic therapy	Yes	5 (6)
	No	73 (91)
	Unknown	2 (3)
R0 resection	Yes	73 (91)
	No	2 (3)
	Unknown	5 (6)

Table 6.3 – the pathology of the colorectal carcinomas included in the REIMS analysis. Some cases are reported as ‘unknown’ due to patients not having a radical resection allowing complete staging or due to historically incomplete metadata.

Adenoma Pathology		Number (%)
Mean lesion size (range)		33mm (5-80mm)
Pathological subtype	Tubulovillous	20 (38)
	Villous	15 (28)
	Tubular	12 (23)
	Serrated	3 (6)
	Unknown	3 (6)
Grade of dysplasia	High	8 (15)
	Low	42 (79)
	Unknown	3 (6)

Table 6.4 – the pathology of the colorectal adenomas included in the REIMS analysis. Some cases are reported as ‘unknown’ due to multiple polyps being present and it not being clear which one was sampled or historically incomplete metadata.

Representative REIMS spectra from the analysis of tumour, adenoma and normal tissues across the whole mass range (150-1000m/z) are presented in figure 6.2. These demonstrate that REIMS is capable of detecting large quantities of metabolites across multiple lipid subclasses, including the fatty acids (FAs; 220-310m/z), glycerophospholipids (GPLs; 600-850m/z) and triglycerides (TGs; 850-950m/z). FAs appear to be the lipid subclass with the highest relative abundance across all tissue types, however it is not possible to determine from these data if they are free FAs in the tissue or are also a consequence of fragmentation of more complex lipids at the tissue interface or collision cell. The complex lipid region is presented in figure 6.3 over the 600-1000m/z range, demonstrating a large degree of similarity between tissue types. It appears that the differences are not due to novel metabolites in a specific tissue subtype (which would be represented by peaks which are present in one spectrum but completely absent in another), but differences in their relative intensity. Visual inspection reveals some regions where the relative intensities differ between tissue types, for example when comparing the peaks at 699.45m/z and 744.55m/z; however multivariate models will be required to start interrogating these differences in more detail.

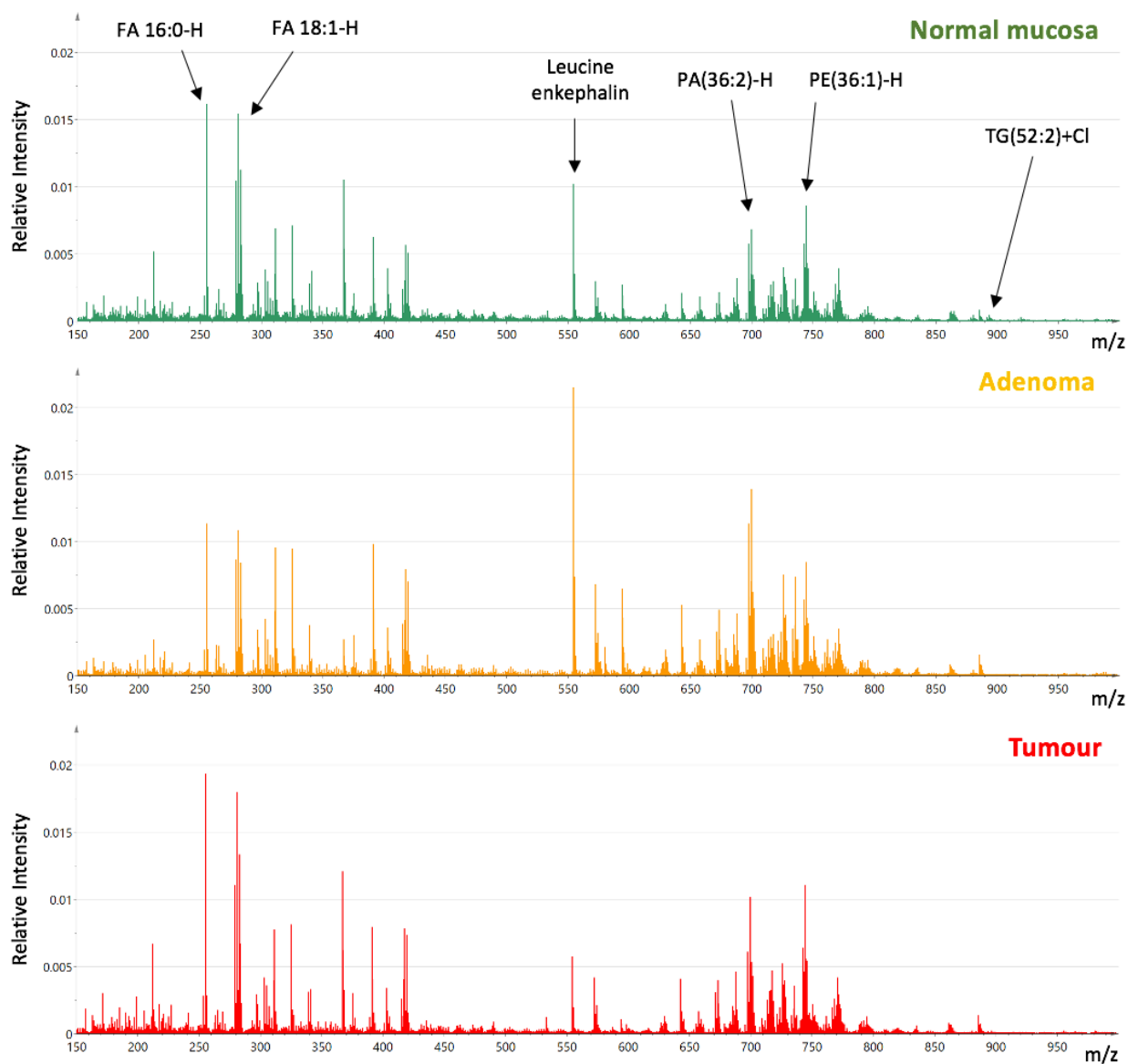


Figure 6.2 – the mean spectrum generated from the REIMS analysis of tumour, adenoma and normal tissue in negative mode over the 150-1000 m/z range. Notable peaks across lipid classes are annotated.

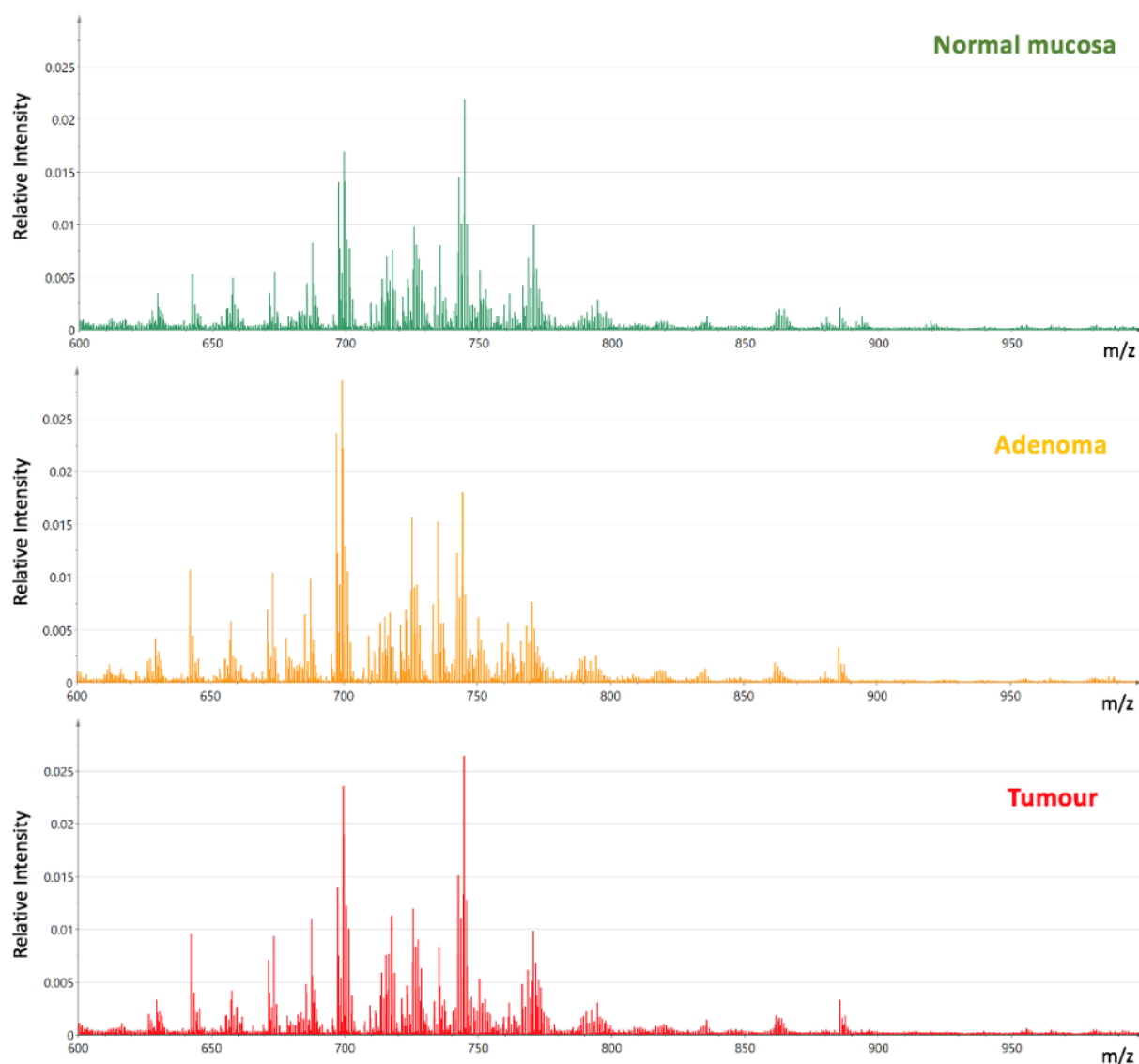


Figure 6.3 – the mean spectrum generated from the REIMS analysis of tumour, adenoma and normal tissue over the 600-1000 m/z range in negative mode, focusing on GPLs and TGs.

### 6.3.1 Tissue recognition using REIMS

#### 6.3.1.1 Tissue recognition using whole mass range 150-1000m/z

The PCA plot of the 1013 included REIMS spectra over the whole mass range of 150-1000m/z can be seen in figure 6.4, demonstrating marked batch effects. A loading plot (figure 6.5.A) revealed that the batch along PC1 was caused by a contaminant at 367.264m/z, which was present in all samples analysed between February and March 2015 (figure 6.6.A). The batch along PC2 was

largely driven by a much-increased relative intensity of FAs compared to the GPLs (figure 6.5.B), particularly 16:0, 18:0, 18:1 and 18:2; seen in a single analytical run of 8 samples from 4 patients in January 2016 (figure 6.6.B). Variation along PC3 was largely caused by a contaminant at 212.075m/z (figure 6.5.C), present in the spectra from a single analytical run in August 2018 (figure 6.6.C).

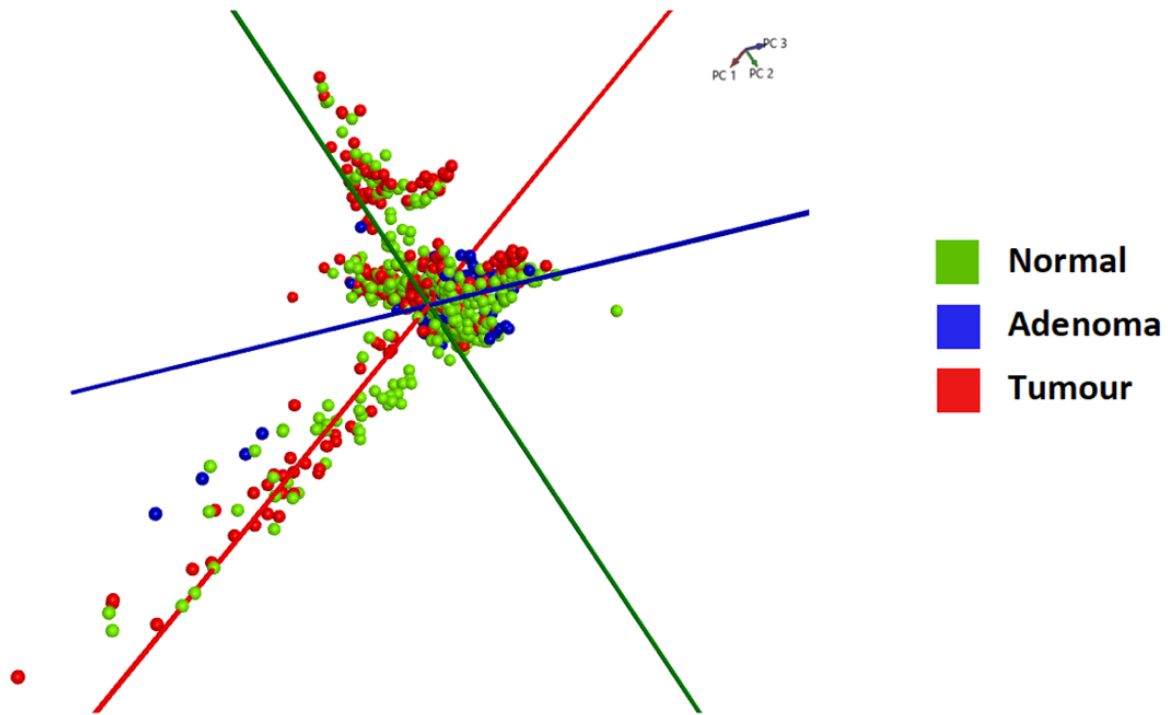


Figure 6.4 – PCA plot of the 1013 REIMS spectra across the 150-1000m/z range. PC1 accounted for 40.5% of the variation, PC2 for 15.2% and PC3 for 12.1%.

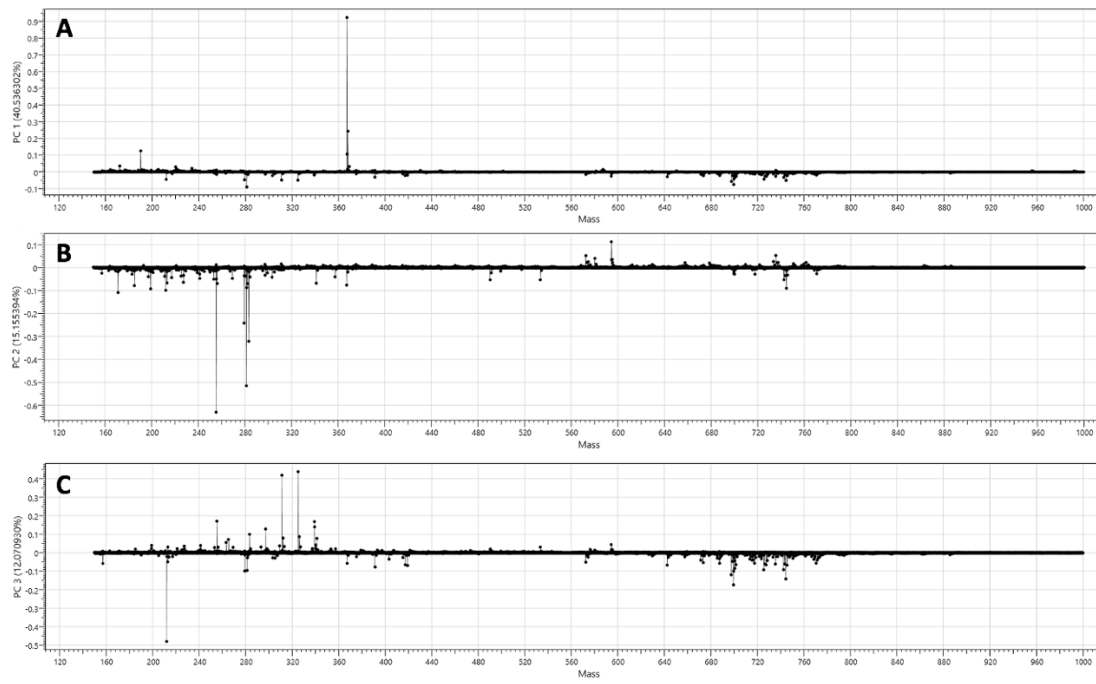


Figure 6.5 – loading plot for the variation seen along PC1 (A), PC2 (B) and PC3 (C) in the 150-1000m/z range.

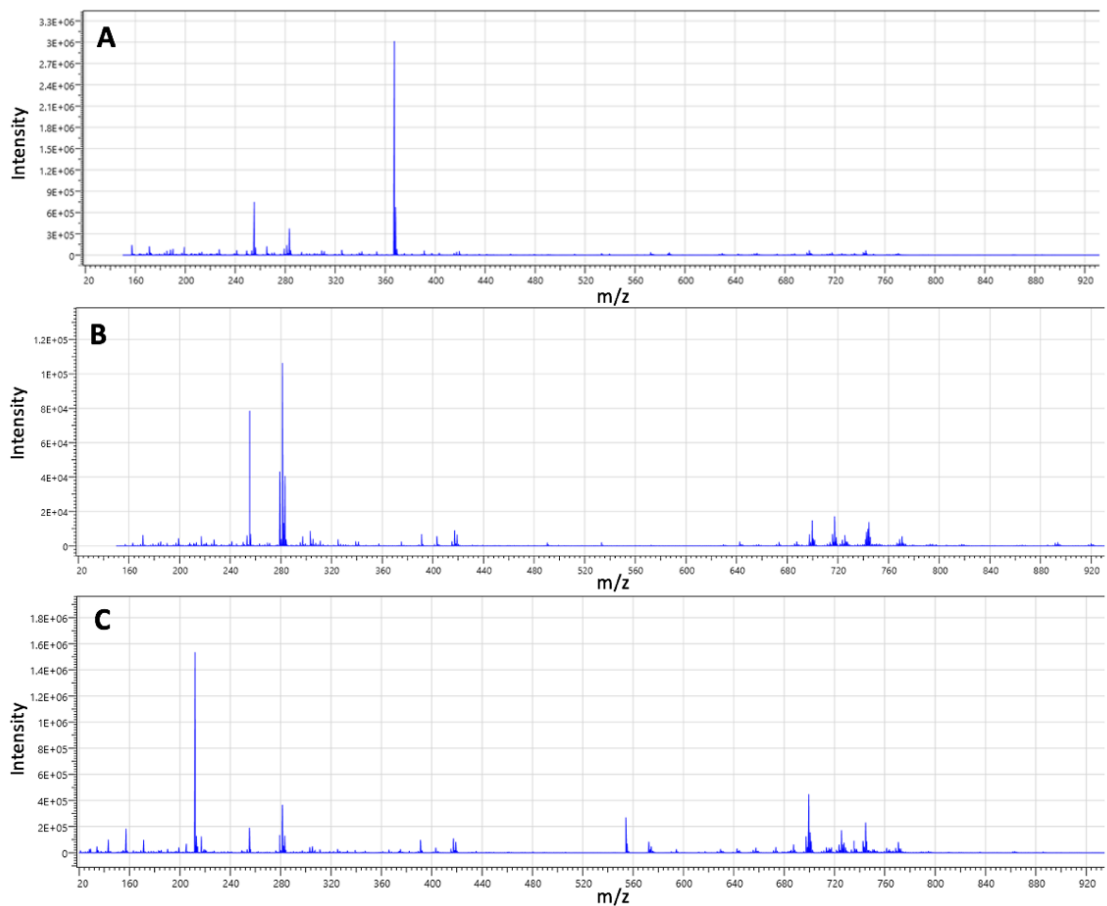


Figure 6.6 – spectrum from an adenoma sample of patient JLA055 (A), demonstrating the contaminant peak at 367.264m/z; a spectrum from normal tissue of patient JLA222 (B), demonstrating a high relative abundance of FAs compared to GPLs; and a spectrum from tumour tissue of patient JLA210 (C), demonstrating a contaminant peak at 212.075m/z.

An LDA model was constructed to assess ability of REIMS for tissue recognition over the mass range of 150-1000m/z, with LOPO CV demonstrating an accuracy of 84.6%, 80.3% sensitivity, 90.9% specificity, 82.0% PPV and 89.9% NPV for tumour (figure 6.7). There was no apparent pattern to the misclassifications and they did not appear to focus on the spectra included in the batches on PCA. Exclusion of the bins covering the described contaminants did not dramatically change the model accuracy, with an increase from 84.6 to 85.3%. The significant variation between spectra in the lower mass ranges appears to be largely driven by unpredictable and undefined contaminant peaks and therefore, not by an underlying biological process. This variability may be a cause of the moderate diagnostic ability of REIMS, where the supervised chemometric functions incorporates these features into the models despite them not being a biological source of variability. To combat this, models will be assessed which focus on the well-conserved complex lipid region of 600-1000m/z.

		Predicted Subtype For Each Spectrum		
		Normal	Adenoma	Tumour
True Subtype	Normal	367	14	39
	Adenoma	13	212	22
	Tumour	49	19	278

Figure 6.7 - the accuracy of REIMS on LOPO CV for the prediction of normal, adenoma and tumour colorectal tissue across the 150-1000 m/z range.

#### 6.3.1.2 Tissue recognition focused on complex lipid mass range 600-1000m/z

The PCA plot of the 1013 included REIMS spectra over the 600-1000m/z range can be seen in figure 6.8. It demonstrates that the greatest source of variability does not appear to be tissue type, considering the intra-group variance is markedly larger than the inter-group variance. This is reflected by the group clusters largely overlapping for tumour and normal tissue, however there is evidence of some degree of clustering separately for adenoma spectra. When the plot was labelled by experimental factors (such as MS instrument or date of analysis), clinical factors

(location of sample) or demographic data (such as patient sex and ethnicity), there was no evidence of a batch effect caused by these factors (data not shown). The loading plots for PC1 and PC2 can be seen in figure 6.9, demonstrating that the variability between spectra involves many different metabolites across the complex lipid range; with no evidence of single contaminants driving the models.

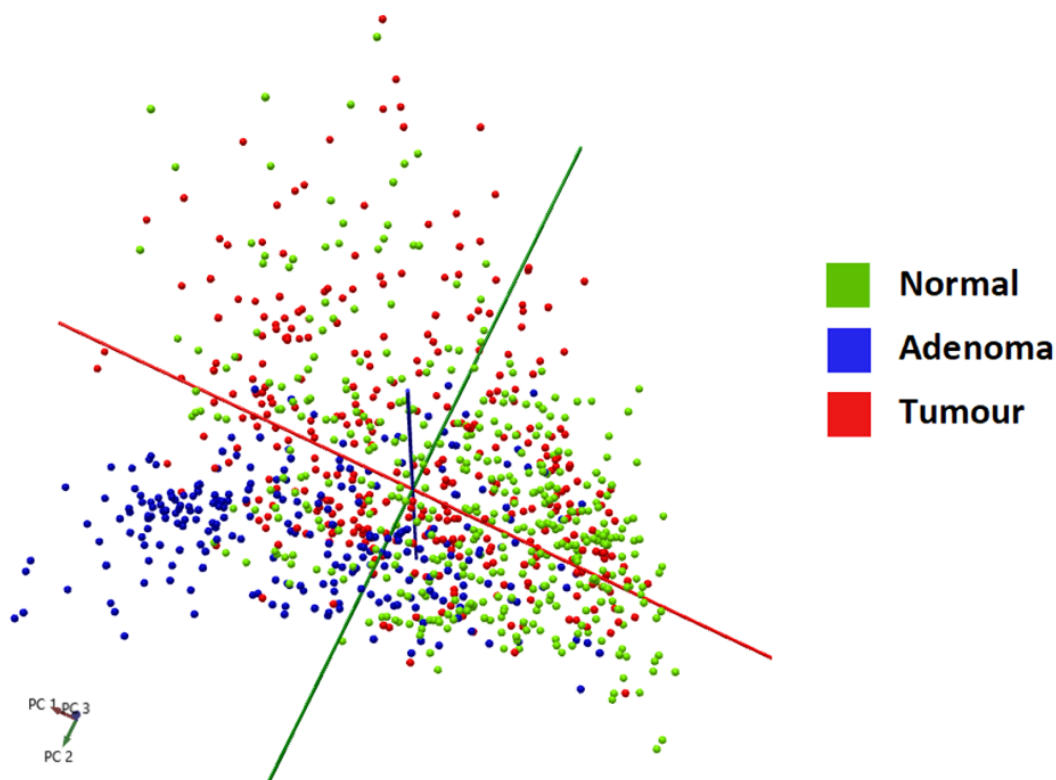


Figure 6.8 – PCA plot of the 1013 spectra generated from the *ex vivo* analysis of colorectal tissues over 600-1000m/z mass range. PC1, PC2 and PC3 are responsible for 43.3, 21.7 and 4.9% of the variation respectively.

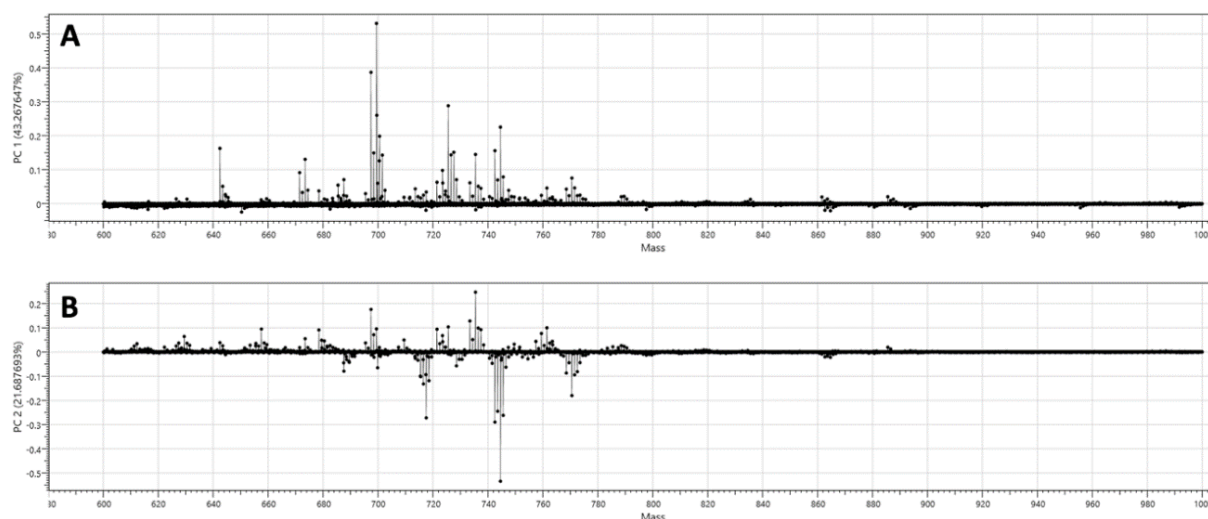


Figure 6.9 – loading plot of PC1 (A) and PC2 (B) over the mass range 600-1000m/z.

The ability of REIMS to differentiate normal, adenoma and carcinoma colorectal tissues was assessed by building an LDA model (figure 6.10). This model demonstrates clear clustering by tissue type, with a particularly small intra-group variance for normal spectra. The tumour and adenoma groups appear to have a small degree of overlap, reflecting the model's difficulty differentiating them completely based on the lipid metabolites. Across all three groups there are notable examples of spectra positioned in the centre of an incorrect cluster, many of which come from the same tissue sample (as shown by the arrows in figure 6.10).

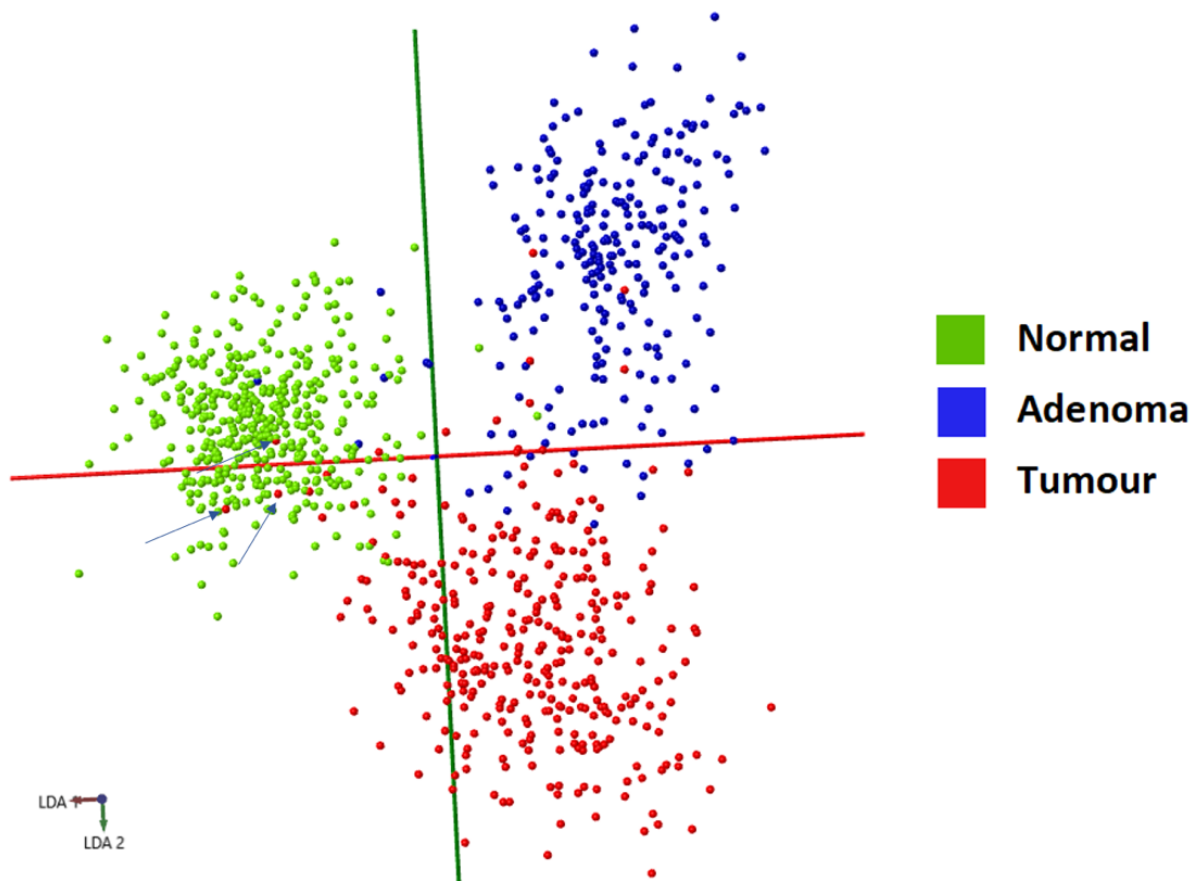


Figure 6.10 – LDA plot of REIMS in the differentiation of normal, adenoma and tumour spectra over the 600-1000m/z range. The blue arrows represent spectra from the same tissue piece (JLA249) which appear to be positioned in an incorrect region of the plot.

The results of LOPO CV can be seen in a confusion matrix in figure 6.11.A, demonstrating an overall accuracy for each spectrum of 91.1%, sensitivity of 86.4%, specificity of 95.4%, PPV of 90.7% and NPV of 93.1% for tumour. There were two primary sources of misclassifications. The first was adenomas being misclassified as tumours and the second was tumours being misclassified as normal or adenoma. Closer inspection revealed that false negatives for tumour were commonly when larger tissue pieces generated multiple REIMS spectra and a small percentage of those collected made incorrect predictions. To address this, accuracy metrics were defined based on the ability of REIMS to predict the subtype of the whole tissue piece using all collected spectra (rather than the accuracy for each spectrum individually). The subtype of the whole tissue sample could then be defined as that which is most frequently predicted by the individual spectra (with the most clinically significant taken in cases of a tie). For example, if seven spectra were generated from a tissue sample and six were predicted to be tumour with one

predicted to be normal; the overall tissue prediction would be of tumour. Using this definition, the ability of REIMS in tissue recognition improved, with an accuracy of 93.1%, sensitivity of 91.5%, specificity of 95.7%, PPV of 90.7% and NPV of 96.1% for tumour (figure 6.11.B). The potential causes of adenoma spectra misclassifying to tumour were explored and it was found that 78% (21 of 27) were adenoma samples with either high-grade dysplasia (HGD) or were sampled immediately adjacent to tumour cells (sampling aimed to collect macroscopic tumour however validation of the sections revealed only adenoma).

Technical factors of the 89 misclassifying spectra were compared to the spectra that classified correctly, with no difference in mean TIC ( $p = 0.31$  on ANOVA), however the signal:noise ratio was significantly higher in those that correctly classified (7242 vs 5803;  $p = 0.004$  on Kruskal Wallis test). Excluding the spectra with the lowest 5% of signal:noise (equivalent to a threshold of 1294) increases the overall model accuracy for each spectrum from 91.1 to 92.2%, and notably, decreases false negatives for tumour from 4.6 to 3.6%. No other association with misclassifications could be demonstrated when assessing factors such as date of analysis or MS instrument used.

Learning curve simulations were used to assess whether the dataset had sufficient power to differentiate carcinoma, adenoma and normal mucosa; or whether further tissue samples required analysis. This demonstrates that maximum classification accuracy was reached for all tissue subtypes with less than 140 spectra included in the modelling, markedly below the 247 included in the smallest group. In addition, it appears that no more than 50 variables (metabolite abundances selected with the smallest  $p$  values) were required to reach maximum accuracy.

<b>A</b>		<b>Predicted Subtype For Each Spectrum</b>			<b>B</b>		<b>Predicted Subtype For Each Tissue Sample</b>		
		Normal	Adenoma	Tumour			Normal	Adenoma	Tumour
<b>True Subtype</b>	Normal	410	6	4	<b>True Subtype</b>	Normal	135	3	-
	Adenoma	6	214	27		Adenoma	2	107	11
	Tumour	28	19	299		Tumour	5	5	107

Figure 6.11 – the accuracy of REIMS on LOPO CV for the prediction of normal, adenoma and tumour colorectal tissue; with the predictions for each spectrum collected (**A**) and for the overall tissue sample (**B**).

From a clinical perspective, both adenomas and carcinomas are lesions that require excision and therefore, may be considered as one group for the purposes of REIMS prediction. Models were created to assess the ability of REIMS in differentiating disease (tumour or adenoma) and normal colorectal tissue, with the accuracy for each spectrum of 93.5%, a sensitivity of 91.2%, specificity of 96.7%, PPV of 97.5% and NPV of 88.6% for disease (figure 6.12.A). This causes an overall increase in accuracy and specificity, however NPV suffers from the increased misclassifications of disease to normal tissue. When making predictions for each tissue sample analysed, the accuracy was 96.0%, sensitivity of 94.9%, specificity of 97.8%, PPV of 98.7% and NPV of 91.8% for disease (figure 6.12.B).

<b>A</b>		<b>Predicted Subtype For Each Spectrum</b>		<b>B</b>		<b>Predicted Subtype For Each Tissue Sample</b>	
		Normal	Disease			Normal	Disease
<b>True Subtype</b>	Normal	406	14	<b>True Subtype</b>	Normal	135	3
	Disease	52	541		Disease	12	225

Figure 6.12 - the accuracy of REIMS on LOPO CV for the prediction of disease (adenoma or tumour) vs normal colorectal tissue; with the predictions for each spectrum collected (**A**) and for the overall tissue sample (**B**).

One objective of this thesis is to translate REIMS *in vivo* to accurately perform colorectal tissue recognition. It is evident that REIMS has a much-increased diagnostic accuracy over the 600-1000m/z rather than 150-1000m/z range, with it focusing on the complex lipid region rather than additional smaller metabolites and regions prone to unpredictable contamination. For the reason of increased diagnostic accuracy, the 600-1000m/z range will be used for all further modelling in this thesis.

### 6.3.2 REIMS in risk stratification of colorectal cancers

The heterogeneity of CRC is such that there are a multitude of different factors which can influence the clinical pathway a patient will take, with research having focused on identifying

which features are associated with a poor outcome. These data are vital to support clinical decision-making, as it can determine the use of neoadjuvant or adjuvant oncologic therapies (such as chemo and radiotherapy), surgical strategy (radical vs local excision) and need for surveillance post-operatively.

Features associated with poor prognosis are traditionally defined based on morphological factors, such as how the location of tumour cells relates to organ structures, most likely due to the fact that this data is readily determined during the usual diagnostic process of microscopy. Considering the relationship between phenotype and metabolism, this section hypothesises that the mucosal metabolome can be used to stratify cancers based on established features of risk.

#### *6.3.2.1 Tumour stage*

An advanced tumour stage (as per the TNM criteria) reflects an increased degree of local tumour invasion through the bowel wall, with a T1 and T2 staged cancers having a 5 year survival of 87% compared to 41% for T3 and T4 cancers<sup>347</sup>. Figure 6.13.A demonstrates that an OPLS-DA model of REIMS spectra has a limited ability to differentiate early (T1-2) from advanced (T3-4) tumours, with a large overlap of the groups and multiple outliers present. This is reflected with an  $R^2X$  of 0.337 and  $Q^2$  of 0.231. A cross validated plot (figure 6.13.B) supports this finding, where the little separation between groups is mostly lost, with many spectra crossing the line of 0 on the x axis (reflecting uncertainty in their classification). LOPO CV reveals an overall model accuracy of 52.6%, with a sensitivity of 52.6%, specificity of 52.6%, PPV of 78.4% and NPV of 25.3% for advanced stage (figure 6.14). Whilst the greatest absolute value of misclassifications is when advanced tumours were being classified as early, this is a consequence of the prevalence difference between the groups and in fact, there is an identical proportion of early tumours misclassifying as advanced (reflected in the equal sensitivity and specificity).

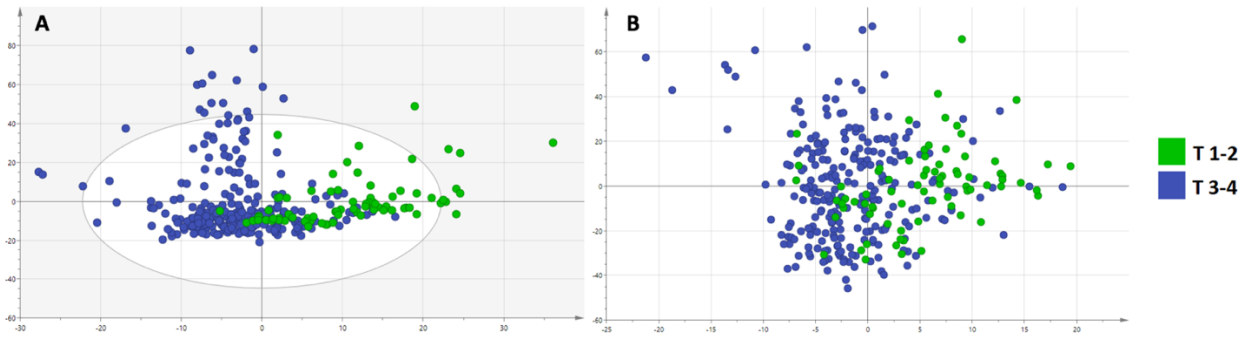


Figure 6.13 – an OPLS-DA plot with 1 orthogonal and 2 X-Y components (A) and a cross validated OPLS-DA plot (B) demonstrating the ability of REIMS to differentiate early (T1-2) and advance (T3-4) CRC. The tolerance ellipse in A represents the 95% boundary on the 2-dimensional scores plot as per Hotelling’s  $T^2$  distribution.

		Predicted Subtype	
		T 1/2	T 3/4
True Subtype	T 1/2	40	36
	T 3/4	118	131

Figure 6.14 – a confusion matrix of REIMS on LOPO CV of an LDA model for the differentiation of early (T1/2) or advanced (T3/4) tumours based on the TNM criteria.

### 6.3.2.2 Presence of nodal micrometastasis

The presence of cancerous cells in the lymph nodes is believed to reflect micrometastasis along the lymphatic pathways, with its presence associated with a 5 year survival that decreases from 57 to 7%<sup>347</sup>. The ability of REIMS to differentiate the presence or absence of nodal disease according to the TNM criteria was assessed using an OPLS-DA model (figure 6.15.A). This shows a moderately increased accuracy in comparison to tumour stage however this is still poor, with an  $R^2X$  of 0.363 and  $Q^2$  of 0.348. The cross validated model (figure 6.15.B) again shows a loss of clustering, with LOPO CV revealing an overall model accuracy of 62.3%, with a sensitivity of 66.0%, specificity of 60.4%, PPV of 45.5% and NPV of 78.0% (figure 6.16).

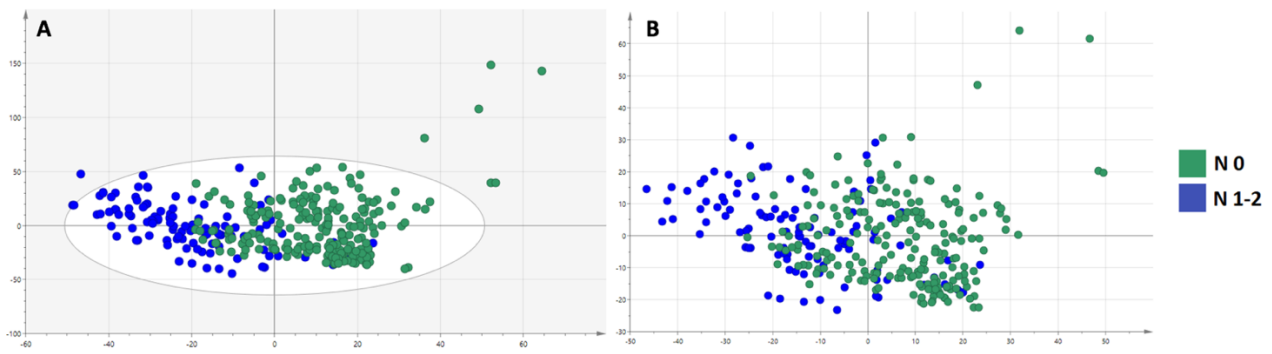


Figure 6.15 – an OPLS-DA plot with 1 orthogonal and 2 X-Y components (A) and a cross validated OPLS-DA plot (B) demonstrating the ability of REIMS to differentiate tumours with (N1-2) and without (N0) presence of nodal micrometastasis. The tolerance ellipse in A represents the 95% boundary on the 2-dimensional scores plot as per Hotelling’s  $T^2$  distribution.

		Predicted Subtype	
		N 0	N 1/2
True Subtype	N 0	128	84
	N 1/2	36	70

Figure 6.16 – a confusion matrix of REIMS on LOPO CV of an LDA model for the differentiation of tumours with (N 1/2) or without (N 0) nodal micrometastasis based on the TNM criteria.

### 6.3.2.3 AJCC stage

The AJCC stage is based on the values of each TNM constituent and is considered an improved approach to risk stratification given that it incorporates more data than the individual components alone<sup>348</sup>. However, the limited ability of REIMS in differentiating tumour and nodal stages appears to extend to the AJCC. Early (AJCC I/II) and advanced (AJCC III/IV) clusters moderately overlap on an OPLS-DA plot (figure 6.17.A), with an  $R^2X$  of 0.358 and  $Q^2$  of 0.326. The cross validated plot shows only a small number of AJCC III/IV spectra crossing the x value of 0 (figure 6.17.B), however LOPO CV shows poor predictive ability once again; with an accuracy of 60.9%, a sensitivity of 65.1%, specificity of 58.8%, PPV of 44.4% and NPV of 77.0% for advanced stage (figure 6.18).

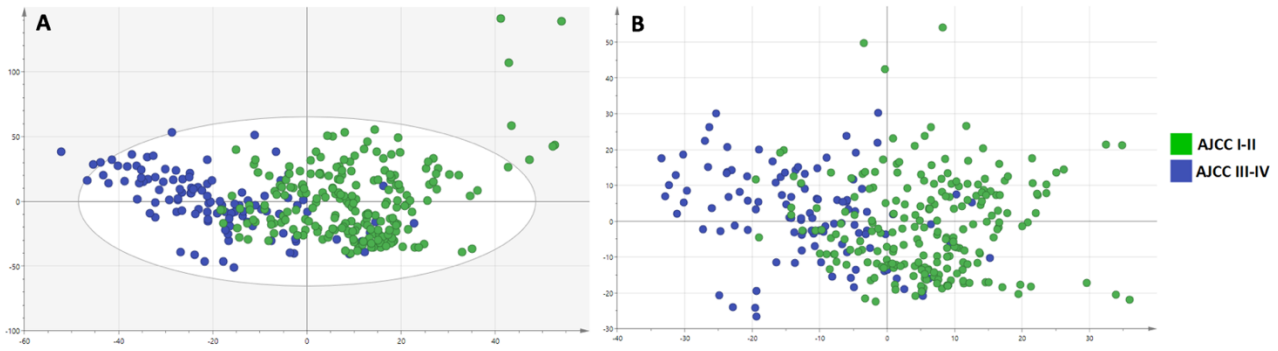


Figure 6.17 – an OPLS-DA plot with 1 orthogonal and 2 X-Y components (A) and a cross validated OPLS-DA plot (B) demonstrating the ability of REIMS to differentiate early (AJCC I/II) or advanced (AJCC III/IV) tumours. The tolerance ellipse in A represents the 95% boundary on the 2-dimensional scores plot as per Hotelling’s  $T^2$  distribution.

		Predicted Subtype	
		AJCC I/II	AJCC III/IV
True Subtype	AJCC I/II	127	89
	AJCC III/IV	38	71

Figure 6.18 – a confusion matrix of REIMS on LOPO CV of an LDA model for the differentiation of early (AJCC I/II) or advanced (AJCC III/IV) tumours.

#### 6.3.2.4 Presence of extramural venous invasion

Tumour cells exhibiting extramural venous invasion (EMVI) raises the concern for haematological spread of metastasis (particularly to the liver) and its absence is associated with increased metastasis free survival in rectal cancers (hazard ratio 0.5)<sup>349</sup>. REIMS had a poor level of accuracy in predicting which tumours had EMVI, which is evident on the OPLS-DA plots and on LOPO CV (figures 6.19 and 6.20). The overall accuracy was 53.8%, with no clear pattern to misclassifications.

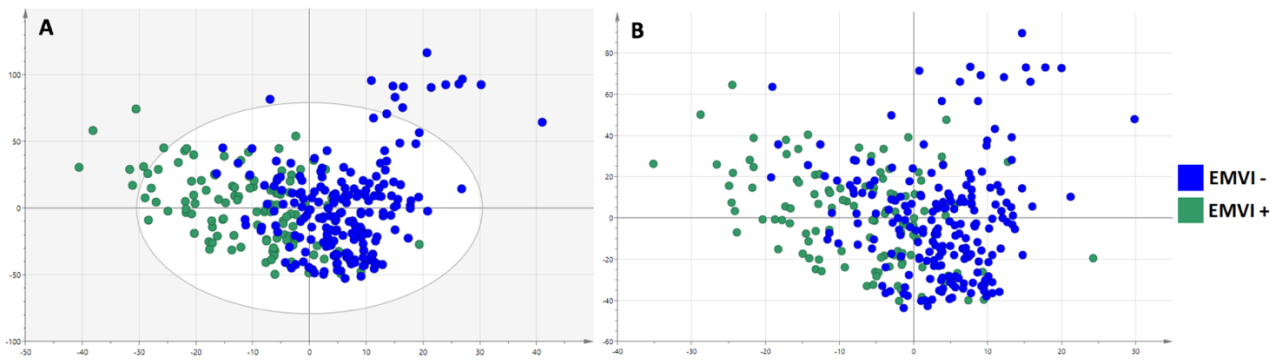


Figure 6.19 – an OPLS-DA plot with 1 orthogonal and 2 X-Y components, demonstrating an  $R^2X$  of 0.357 and  $Q^2$  of 0.285 (A) and a cross validated OPLS-DA plot (B) demonstrating the ability of REIMS to differentiate tumours with or without EMVI. The tolerance ellipse in A represents the 95% boundary on the 2-dimensional scores plot as per Hotelling's  $T^2$  distribution.

		Predicted Subtype	
		EMVI -	EMVI +
True Subtype	EMVI -	111	93
	EMVI +	54	60

Figure 6.20 – a confusion matrix of REIMS on LOPO CV of an LDA model for the differentiation of tumours with and without EMVI.

### 6.3.2.5 Presence of lymphovascular invasion

Lymphovascular invasion (LVI) is believed to be the precursor to lymph node micrometastasis and is associated with poor outcomes in many cancers including CRC<sup>350</sup>. It is of particular importance in stage I CRC, where the 5 year disease free survival (DFS) falls from 90.9 to 52.7% with the presence of LVI<sup>351</sup>. REIMS had a poor level of accuracy in predicting which tumours had LVI, which can be seen on an OPLS-DA plot and on LOPO CV (figures 6.21 and 6.22). The overall accuracy was 57.6%, with no clear pattern to misclassifications.

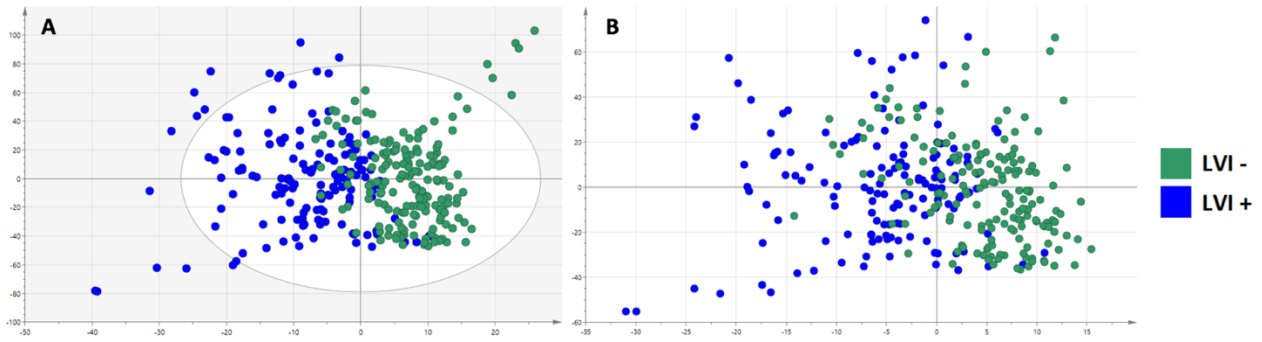


Figure 6.21 – an OPLS-DA plot with 1 orthogonal and 2 X-Y components, demonstrating an  $R^2X$  of 0.356 and  $Q^2$  of 0.389 (A) and a cross validated OPLS-DA plot (B) demonstrating the ability of REIMS to differentiate tumours with or without LVI. The tolerance ellipse in A represents the 95% boundary on the 2-dimensional scores plot as per Hotelling’s  $T^2$  distribution.

		Predicted Subtype	
		LVI -	LVI +
True Subtype	LVI -	104	70
	LVI +	65	79

Figure 6.22 – a confusion matrix of REIMS on LOPO CV of an LDA model for the differentiation of tumours with and without lymphovascular invasion (LVI).

### 6.3.2.6 Presence of tumour budding

Tumour budding refers to clusters of cells at the invasive edge of cancers, representing a transition from the epithelium into the stroma, and has been postulated to better stratify CRC patients than TNM<sup>352</sup>. REIMS was not able to accurately predict the presence of tumour budding in CRCs, with marked cluster overlap on both an OPLS-DA plot and a cross validated OPLS-DA plot (figure 6.23). LOPO CV results are presented in figure 6.24, showing an overall accuracy of 58.2%, with a notably low NPV of 38.2%.

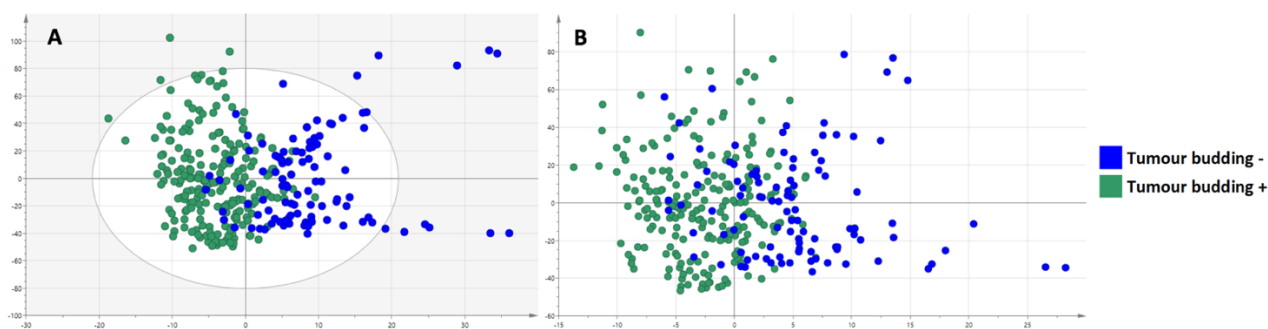


Figure 6.23 – an OPLS-DA plot with 1 orthogonal and 2 X-Y components, demonstrating an  $R^2X$  of 0.35 and  $Q^2$  of 0.354 (A) and a cross validated OPLS-DA plot (B) demonstrating the ability of REIMS to differentiate tumours with or without tumour budding. The tolerance ellipse in A represents the 95% boundary on the 2-dimensional scores plot as per Hotelling's  $T^2$  distribution.

		Predicted Subtype	
		Budding -	Budding +
True Subtype	Budding -	52	49
	Budding +	84	133

Figure 6.24 – a confusion matrix of REIMS on LOPO CV of an LDA model for the differentiation of tumours with and without tumour budding.

### 6.3.2.7 Mucinous subtype

The pools of mucin produced by mucinous tumours are largely composed of proteins and saccharides, and therefore it was anticipated that REIMS would not be sampling the mucin itself but rather the lipidomic changes of the tumour cells<sup>353</sup>. Having such a mucinous phenotype is associated with advanced stage at diagnosis and poor response to chemotherapy compared to non-mucinous adenocarcinoma<sup>354</sup>. An OPLS-DA model was built to assess the accuracy of REIMS in differentiating mucinous and non-mucinous CRC, with mucin-producing tumours categorised as mucinous for this purpose. The OPLS-DA plots in figure 6.25 are difficult to interpret due to the discrepancy in group sizes (156 vs 62 spectra), however the large intra-group compared to intra-

group variance is evident. This is reflected on LOPO CV, where there is an accuracy of 49.7%, a sensitivity of 48.4%, specificity of 50.0%, PPV of 19.0% and NPV of 80.0% (figure 6.26).

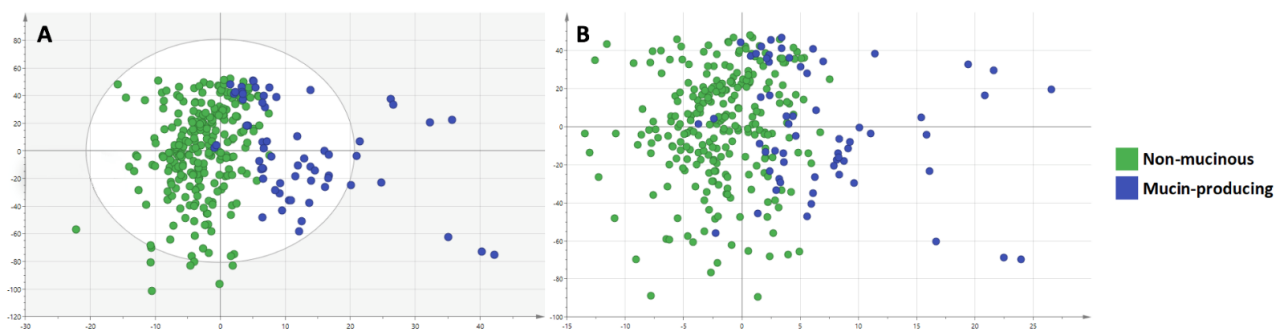


Figure 6.25 – an OPLS-DA plot with 1 orthogonal and 2 X-Y components, demonstrating an  $R^2X$  of 0.347 and  $Q^2$  of 0.368 (A) and a cross validated OPLS-DA plot (B) demonstrating the ability of REIMS to differentiate tumours that produce mucin from those that do not. The tolerance ellipse in A represents the 95% boundary on the 2-dimensional scores plot as per Hotelling’s  $T^2$  distribution.

		Predicted Subtype	
		Non-mucinous	Mucin-producing
True Subtype	Non-mucinous	128	128
	Mucin-producing	32	30

Figure 6.26 – a confusion matrix of REIMS on LOPO CV of an LDA model for the differentiation of tumours that produce mucin from those that do not.

### 6.3.3 REIMS in risk stratification of colorectal adenomas

The most clinically relevant question in the risk-stratification of colorectal adenomas is whether the dysplasia present is high-grade (HGD) or low-grade (LGD), with the former representing the last stage before invasive cancer and a diagnosis which requires a more aggressive management strategy<sup>12</sup>. The ability of REIMS to assess this was conducted in two ways. First, models were

created to predict the degree of dysplasia in the validation section of all included adenomas (as shown in figure 6.27), with any focus of HGD sufficient for this classification to be given. The OPLS-DA plots for this are shown in figure 6.28, showing some degree of cluster separation between the groups and little movement when this plot is cross validated (figure 6.28.B). The relatively high  $Q^2$  of 0.544 is reflected on LOPO CV, which demonstrates an overall accuracy of 89.9%, a sensitivity of 58.1%, specificity of 94.4%, PPV of 60% and NPV of 94.0% for HGD (figure 6.29.A). A more clinically relevant question is whether there was HGD (or invasive cancer) anywhere in the polyp on formal histopathology, even if the piece sampled contained only LGD. This definition increased the number of spectra classified as HGD from 31 to 73 (which includes a T1 and a T2 polyp cancer for this model), with the OPLS-DA plots presented in figure 6.30. These demonstrate a high intra-group variance particularly for the new HGD group, resulting in marked cluster overlaps when the plot is cross validated (figure 6.30.B). LOPO CV reflects this with a reduction in the predictive ability of REIMS, with an accuracy of 65.9%, 34.2% sensitivity, 79.2% specificity, 41.0% PPV and 74.1% NPV for HGD (figure 6.29.B).

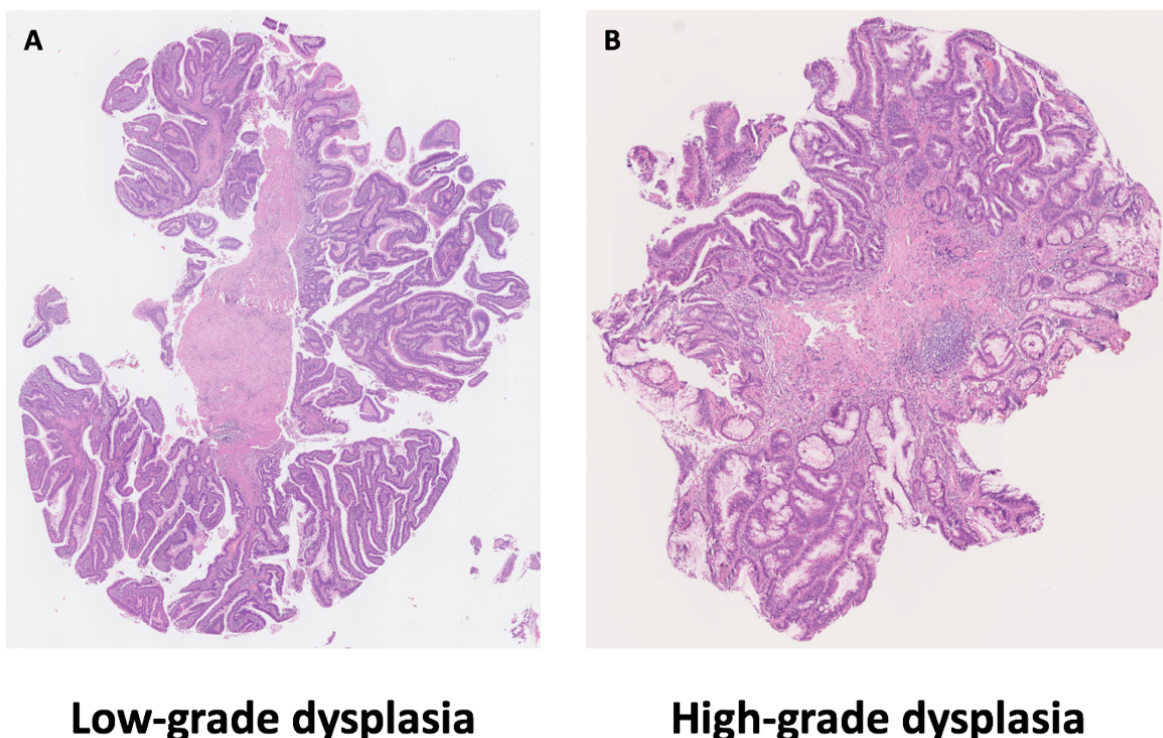


Figure 6.27 – photos of validation polyp validation sections showing low-grade (A) and high-grade (B) dysplasia.

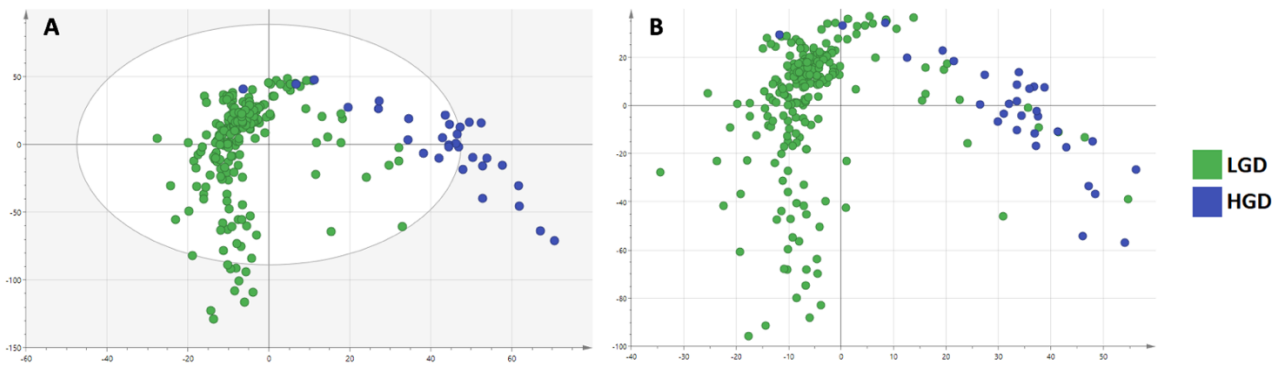


Figure 6.28 – an OPLS-DA plot with 1 orthogonal and 2 X-Y components, demonstrating an  $R^2X$  of 0.473 and  $Q^2$  of 0.544 (A) and a cross validated OPLS-DA plot (B) demonstrating the ability of REIMS to differentiate adenomas with low-grade from high-grade dysplasia. The tolerance ellipse in A represents the 95% boundary on the 2-dimensional scores plot as per Hotelling's  $T^2$  distribution.

A		Predicted Subtype of Validation Section		B		Predicted Subtype Anywhere in Polyp	
		LGD	HGD			LGD	HGD
True Subtype	LGD	203	12	True Subtype	LGD	137	36
	HGD	13	18		HGD	48	25

Figure 6.29 – confusion matrices of REIMS on LOPO CV of an LDA model for the prediction of adenomas that have HGD present in the validation section (A) or anywhere in the polyp on formal histopathology (B).

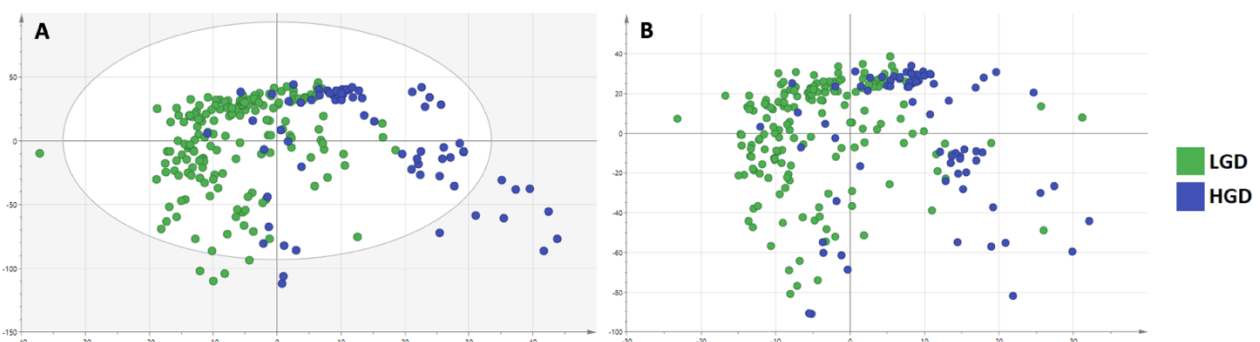


Figure 6.30 – an OPLS-DA plot with 1 orthogonal and 2 X-Y components, demonstrating an  $R^2X$  of 0.503 and  $Q^2$  of 0.333 (A) and a cross validated OPLS-DA plot (B) demonstrating the ability of REIMS to predict the highest grade of dysplasia within a sampled adenoma. The tolerance ellipse in A represents the 95% boundary on the 2-dimensional scores plot as per Hotelling's  $T^2$  distribution.

A further approach to risk stratification of adenomas is determining the histological subtype, such as the degree of villous component. This is a continuum, where tubular adenomas have less than 25% villous features, tubulovillous adenomas have 25-75% and villous adenomas show greater than 75%<sup>355</sup>. The potential subjectivity of this classification is such that REIMS was assessed in its ability to differentiate tubular (TA; 38 spectra) from villous adenomas (VA; 79 spectra), whilst excluding the middle tubulovillous (TVA) group. The OPLS-DA models are shown in figure 6.31, demonstrating a moderate level of clustering which is largely preserved when the plot is cross validated, with small clusters of spectra appearing to drive the misclassifications rather than large cluster overlaps. For example, the three TAs appearing in the VA group in figure 6.31.A all come from one patient sample, where the metadata was re-checked and found to be correct. LOPO CV presents an accuracy of 72.6%, 77.2% sensitivity, 63.2% specificity, 81.3% PPV and 57.1% NPV for VA (figure 6.32).

Other features suggested by the British Society of Gastroenterology for the definition of an advanced colorectal polyp include adenomas greater than 10mm, the presence of serrated features with dysplasia or without dysplasia if greater than 10mm<sup>12</sup>. It was not possible to assess the ability of REIMS to predict these features due to imbalances in the composition of the polyps sampled for research. For example, only 6 (11%) of the sampled adenomas were less than 10mm and only 3 (6%) were serrated.

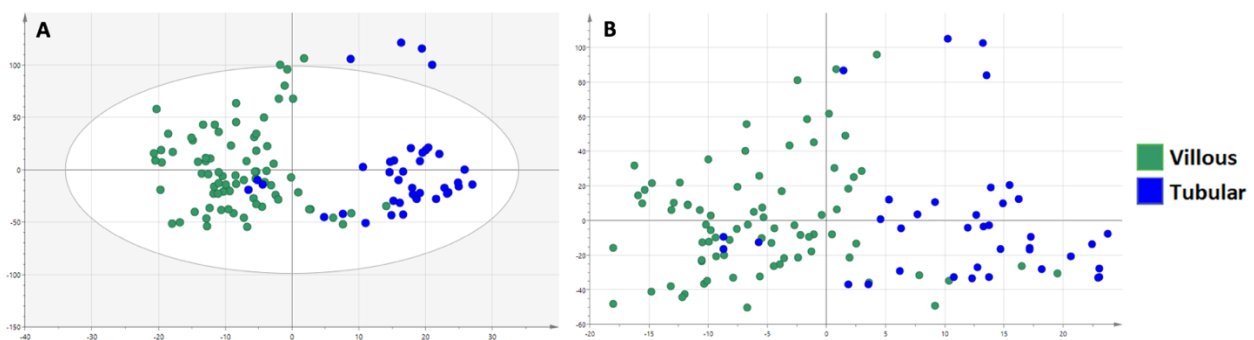


Figure 6.31 – an OPLS-DA plot with 1 orthogonal and 2 X-Y components, demonstrating an  $R^2X$  of 0.529 and  $Q^2$  of 0.513 (A) and a cross validated OPLS-DA plot (B) demonstrating the ability of REIMS to differentiate villous and tubular adenomas. The tolerance ellipse in A represents the 95% boundary on the 2-dimensional scores plot as per Hotelling's  $T^2$  distribution.

		Predicted Subtype	
		TA	VA
True Subtype	TA	24	14
	VA	18	61

Figure 6.32 – confusion matrix of REIMS on LOPO CV of an LDA model for the differentiation of villous adenomas (VA) and tubular adenomas (TA).

#### 6.3.4 Identification of lipid metabolites which differentiate colorectal tissue types

Univariate and multivariate methods were used to explore which metabolites were responsible for the differences in normal, adenoma and tumour colorectal tissues. This was approached by conducting three binary comparisons, with 84 bins of interest revealed by sampling VIP plots and through performing univariate ANOVA. The VIP plots (figure 6.33) revealed that a small proportion of the total bins appeared to be driving the differentiation apparent in the models, aiding selection of the m/z values.

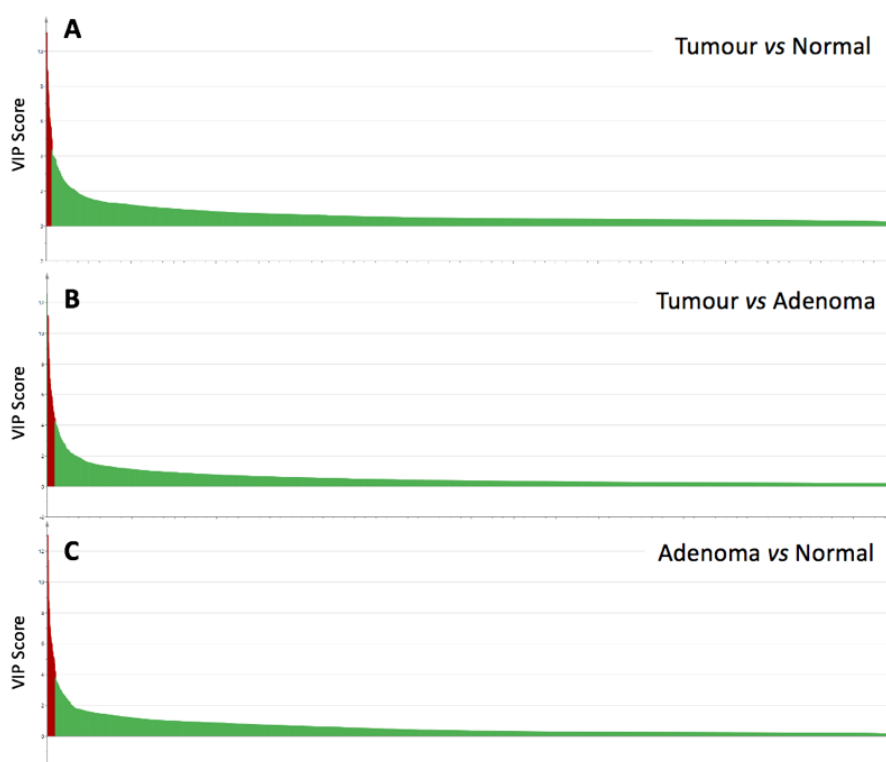


Figure 6.33 – VIP score plots from OPLS-DA models of tumour vs normal (A), tumour vs adenoma (B) and adenoma vs normal (C). The bins are ordered by descending score on the x axis, with those highlighted in red selected for MS/MS.

Identifying the metabolites within these 84 bins was attempted using MS/MS analysis in negative mode of 60 tissue samples from the same cohort of patients, most of which were also included in the primary modelling. This generated 410 spectra, with the structure of 61 metabolites identified to level 2 across 40 bins (table 6.5). This demonstrated a range of lipid metabolites across the glycerophospholipids (PE, PA, PG, PCh and PI), glycerolipids (DG) and sphingolipids (sphingomyelin, ceramide-1-phosphate and ceramide PE), with generally low errors when comparing the experimental and theoretical masses.

The patterns of ionisation and fragmentation showed consistency by lipid species or structural component. Lipids with an ethanolamine group (PE and PE\_Cer) were ionized by deprotonation, however, were mostly seen with the additional loss of ammonia (NH<sub>3</sub>) and the characteristic fragment at 123m/z representing ethanolamine phosphate – NH<sub>3</sub> (figure 6.34 for PE\_Cer and 6.35 for PE). The [M-NH<sub>3</sub>-H]<sup>-</sup> ions of PE and PE\_Cer can be distinguished in an MS/MS spectrum by detecting fragments representing deprotonated fatty acid ions as [CH<sub>3</sub>(CH<sub>2</sub>)<sub>n</sub>COO]<sup>-</sup> (such as 16:0 at 255.23m/z), which are not seen in sphingolipids due to the presence of amino alcohols and the nitrogen linkage of the fatty acyl to the sphingosine backbone. Minor fragments were seen from PE\_Cer where the acyl chain fragmented as a ketene (figure 6.34). PEs were one of the most abundant lipid species in the analysis, commonly seen with multiple combinations of acyl chains within the same bin. Lipids with a phosphocholine headgroup (PCh and SM) were ionized by demethylation, revealing a characteristic fragment at 168m/z representing the phosphocholine – CH<sub>3</sub> ion (figure 6.36). Similarly to PE\_Cer, SMs are not capable of neutral loss of fatty acids, which can be used to distinguish them from PChs. The remaining GPLs were seen to ionize through deprotonation, with occasional examples of Cl<sup>-</sup> adducts (as seen in [PA(20:4/18:0)+Cl]<sup>-</sup> in the bin 759.45). Lyso-lipids were commonly seen where a single fatty acyl chain had been fragmented off either neutrally or as a ketene. DGs were only seen to ionize through Cl<sup>-</sup> adducts and demonstrated characteristic fatty acid ion fragments (figure 6.37).

Bin	Ion Identity	Theoretical Mass (m/z)	Observed Mass (m/z)	Error (ppm)
616.45	CerP(d18:1/16:0)-H	616.471	616.470	1.95
642.45	PE_Cer(d18:1/16:0)-NH <sub>3</sub> -H	642.486	642.485	1.56
645.45	PE(16:0/14:0)-NH <sub>3</sub> -H	645.450	645.450	0
657.55	DG(18:1/18:0)+Cl	657.523	657.518	7.60
659.45	SM(d18:0/14:1)-CH <sub>3</sub>	659.513	659.515	2.43
671.45	PE(16:1/16:0)-NH <sub>3</sub> -H	671.465	671.465	0.30
	PE(18:1/14:0)-NH <sub>3</sub> -H	671.465	671.465	0.30
673.45	PA(18:1/16:0)-H	673.48	673.481	2.08
674.45	<sup>13</sup> C isotope of PA(18:1/16:0)-H	674.484	674.483	1.48
678.45	PE_Cer(36:5,O3)-NH <sub>3</sub> -H	678.450	678.457	10.3
690.55	PCh(16:0/14:0)-CH <sub>3</sub>	690.508	690.510	3.04
695.45	PA(20:4/16:0)-H	695.466	695.465	1.01
	PA(18:2/18:2)-H	695.466	695.465	1.01
696.45	<sup>13</sup> C isotope of PA(20:4/16:0)-H	696.469	696.468	0.72
697.45	PA(18:2/18:1)-H	697.481	697.483	2.87
	PA(20:3/16:0)-H	697.481	697.483	2.87
698.45	<sup>13</sup> C isotope of PA(18:2/18:1)-H	698.484	698.487	4.30
	<sup>13</sup> C isotope of PA(20:3/16:0)-H	698.484	698.487	4.30
699.45	PE(18:1/16:0)-NH <sub>3</sub> -H	699.496	699.497	1.43
700.45	<sup>13</sup> C isotope of PE(18:1/16:0)-NH <sub>3</sub> -H	700.500	700.502	2.86
701.55	PA(18:1/18:0)-H	701.513	701.510	4.28
	PA(20:1/16:0)-H	701.513	701.510	4.28
703.55	PE(18:0/16:0)-NH <sub>3</sub> -H	701.513	701.510	4.28
	x2 <sup>13</sup> C isotope of PA(18:1/18:0)-H	703.519	703.515	5.69
	x2 <sup>13</sup> C isotope of PA(20:1/16:0)-H	703.519	703.515	5.69
709.45	SM(34:1,O3)-CH <sub>3</sub>	703.535	703.530	6.54
	DG(20:3/18:2,O2)+Cl	709.481	709.480	1.41
716.55	DG(20:4/18:1,O2)+Cl	709.481	709.480	1.41
	PE(18:1/16:0)-H	716.524	716.520	5.02
721.45	PCh(16:1/16:0)-CH <sub>3</sub>	716.524	716.520	5.02
	PA(20:4/18:1)-H	721.481	721.480	1.39
723.45	PE(18:2/18:2)-NH <sub>3</sub> -H	721.481	721.480	1.39
	PA(20:4/18:0)-H	723.497	723.498	1.38
725.55	PE(20:3/16:0)-NH <sub>3</sub> -H	723.497	723.498	1.38
	PE(18:2/18:1)-NH <sub>3</sub> -H	723.497	723.498	1.38
726.55	PE(18:2/18:0)-NH <sub>3</sub> -H	725.513	725.512	1.38
	PE(18:1/18:1)-NH <sub>3</sub> -H	725.513	725.512	1.38
727.55	<sup>13</sup> C isotope of PE(18:2/18:0)-NH <sub>3</sub> -H	726.516	726.517	2.06
	<sup>13</sup> C isotope of PE(18:1/18:1)-NH <sub>3</sub> -H	726.516	726.517	2.06
728.55	PE(20:1/16:0)-NH <sub>3</sub> -H	727.528	727.527	1.37
	PE(18:1/18:0)-NH <sub>3</sub> -H	727.528	727.527	1.37
742.55	<sup>13</sup> C isotope of PE(18:1/18:0)-NH <sub>3</sub> -H	728.531	728.530	1.37
743.55	PCh(18:2/16:0)-CH <sub>3</sub>	742.539	742.538	1.35
	PCh(18:1/16:1)-CH <sub>3</sub>	742.539	742.538	1.35
744.55	<sup>13</sup> C isotope of PCh(18:2/16:0)-CH <sub>3</sub>	743.542	743.538	5.38
	<sup>13</sup> C isotope of PCh(18:1/16:1)-CH <sub>3</sub>	743.542	743.538	5.38
747.45	PCh(18:1/16:0)-CH <sub>3</sub>	744.555	744.553	2.55
	SM(34:3.O6)-CH <sub>3</sub>	747.493	747.496	4.01

747.55	PG(16:0/18:1)-H	747.518	747.512	8.29
759.45	PE(18:2/18:1)-NH <sub>3</sub> +Cl	759.473	759.472	1.32
	PA(20:4/18:0)+Cl	759.473	759.472	1.32
770.55	PCh(18:1/18:1)-CH <sub>3</sub>	770.571	770.570	0.65
	PCh(18:2/18:0)-CH <sub>3</sub>	770.571	770.570	0.65
771.55	<sup>13</sup> C isotope of PCh(18:1/18:1)-CH <sub>3</sub>	771.573	771.575	2.20
	<sup>13</sup> C isotope of PCh(18:2/18:0)-CH <sub>3</sub>	771.573	771.575	2.20
772.55	PCh(18:1/18:0)-CH <sub>3</sub>	772.586	772.585	1.29
773.55	PG(18:1/18:1)-H	773.534	773.534	0.26
775.55	PG(18:1/18:0)-H	775.550	775.547	3.22
797.65	SM(d16:0/26:2)-CH <sub>3</sub>	797.654	797.652	2.51
798.65	<sup>13</sup> C isotope of SM(d16:0/26:2)-CH <sub>3</sub>	798.660	798.657	3.76
887.55	PI(20:3/18:0)-H	887.566	887.570	4.51

Table 6.5 – The structural identity of 61 metabolites across 40 m/z bins determined by analysis of fragments during MS/MS in negative ion mode.

ppm – parts per million; CerP – ceramide-1-phosphate; PE\_Cer – ceramide phosphatidylethanolamine; PE – phosphatidylethanolamine; DG – diacylglycerol; SM – sphingomyelin; PA – phosphatidic acid; PCh – phosphatidylcholine; PG – phosphatidylglycerol; PI – phosphatidylinositol.

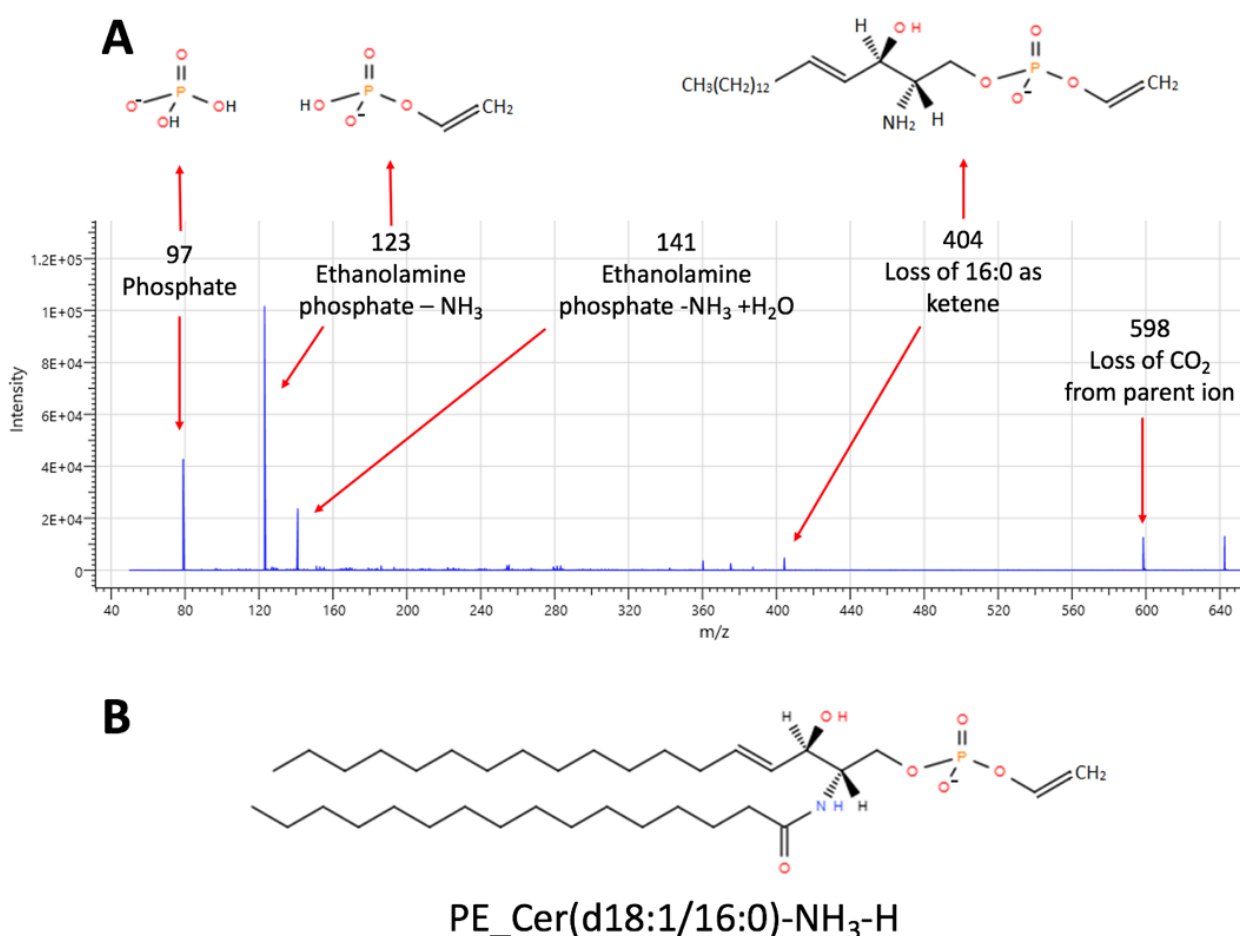


Figure 6.34 – MS/MS spectrum of PE\_Cer(d18:1/16:0)-NH<sub>3</sub>-H in bin 642.45m/z, with structural annotations of the fragments (A) and the parent ion (B).

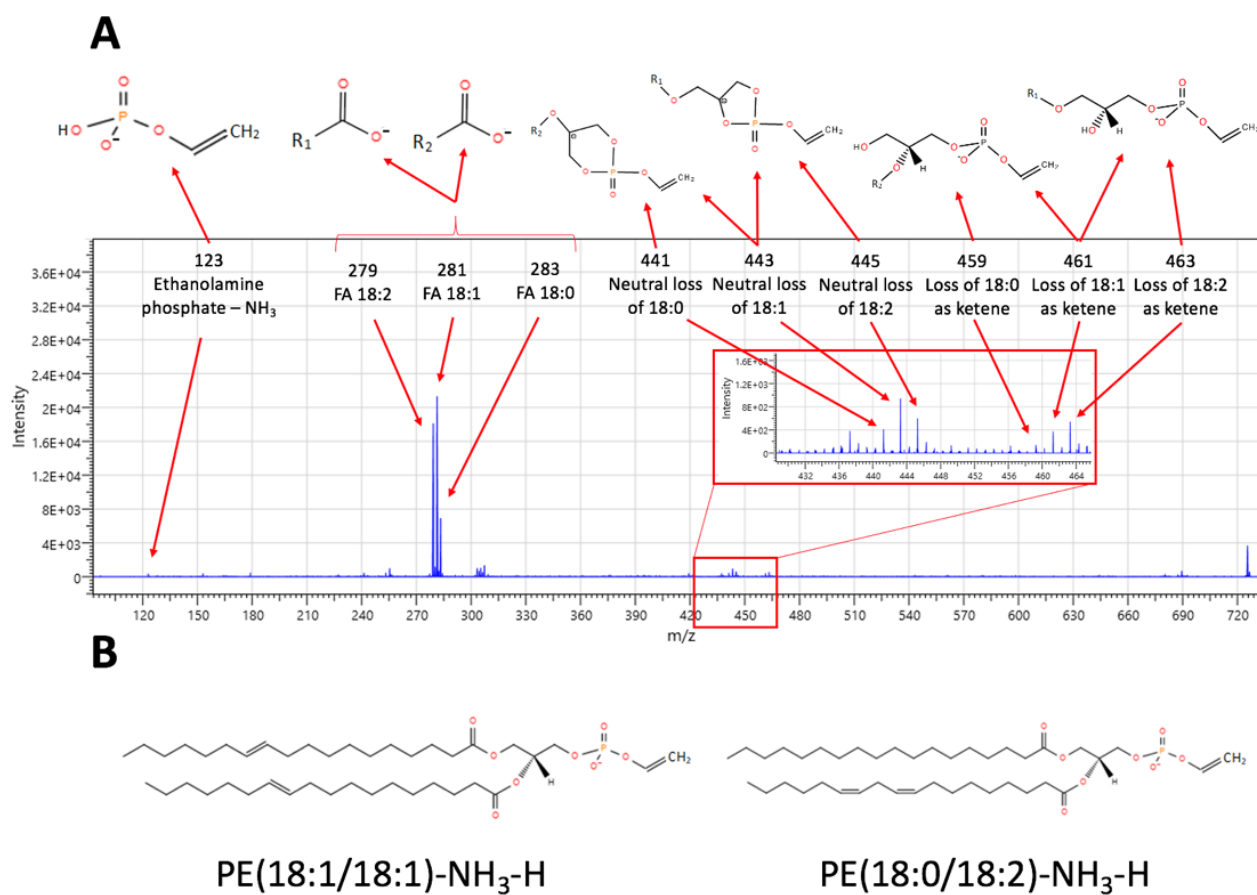


Figure 6.35 – MS/MS spectrum of PE(18:1/18:1)-NH<sub>3</sub>-H and PE(18:0/18:2)-NH<sub>3</sub>-H in bin 725.55m/z, with structural annotations of the fragments (A) and the parent ion (B).

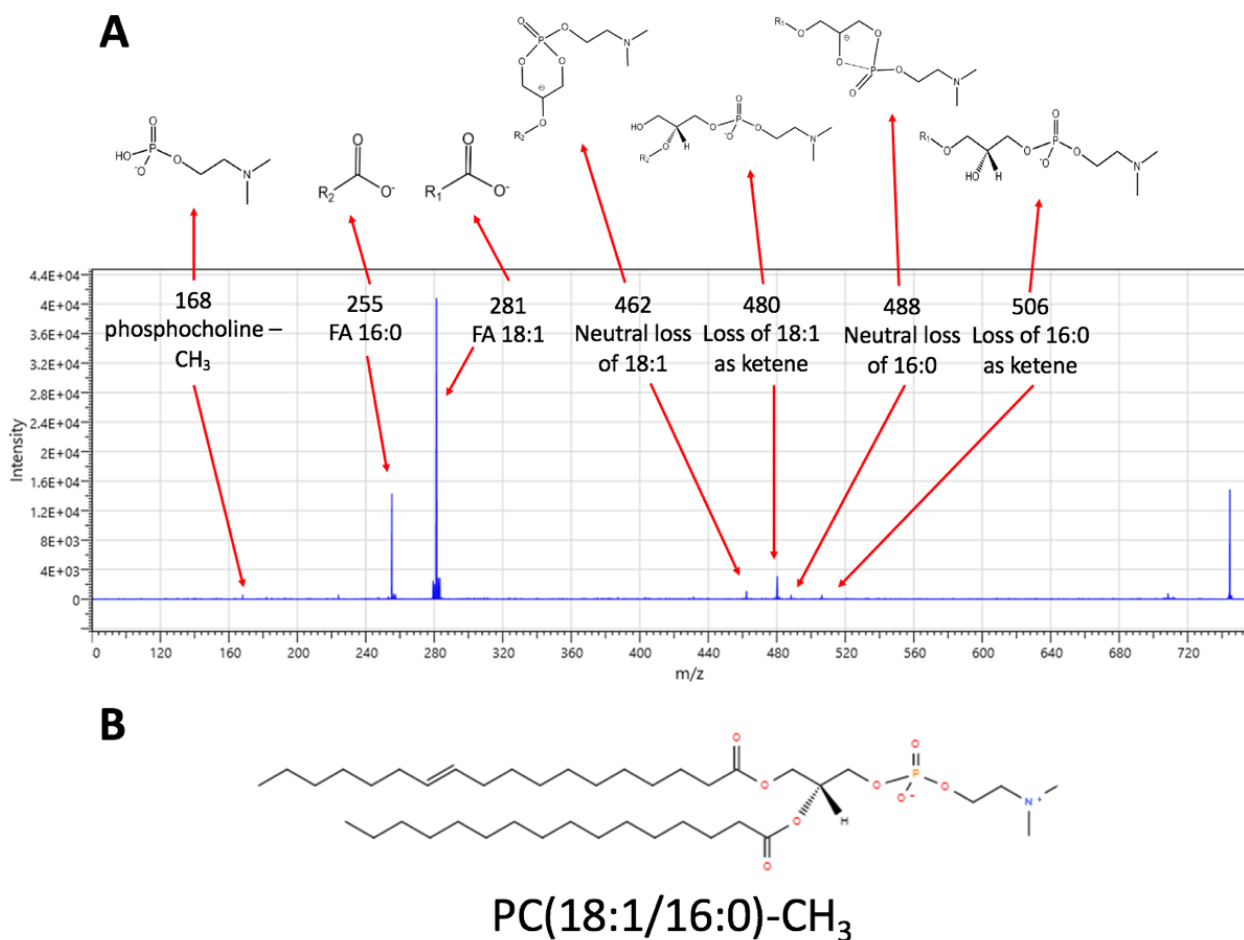


Figure 6.36 – MS/MS spectrum of PCh(18:1/16:0)-CH<sub>3</sub> in bin 744.55m/z, with structural annotations of the fragments (A) and the parent ion (B).

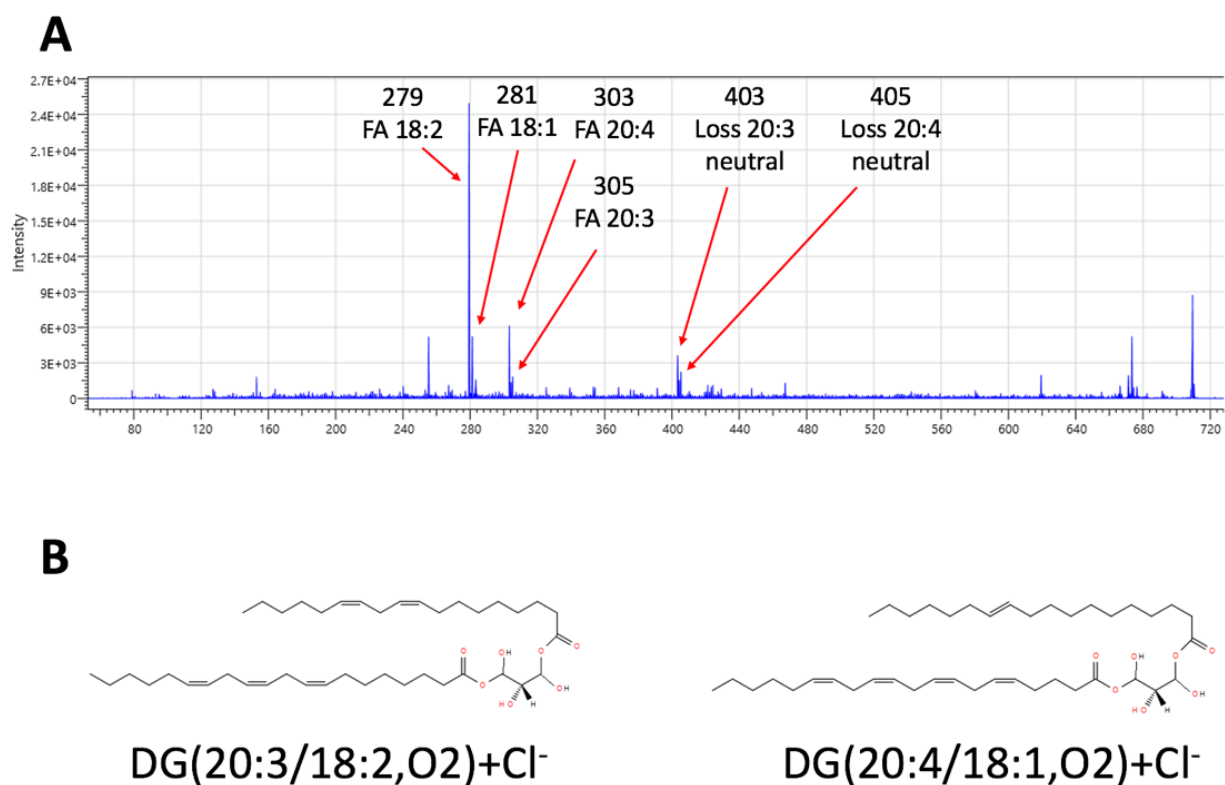


Figure 6.37 – MS/MS spectrum of DG(20:3/18:2,O<sub>2</sub>)+Cl and DG(20:4/18:1,O<sub>2</sub>)+Cl in bin 709.45m/z, with annotations of the fragments (A) and the parent ion structure presented(B).

Table 6.6 shows the results of multivariate and univariate measures of importance for the 61 metabolites identified by MS/MS in the differentiation of colorectal tissue types, with selected boxplots shown in figure 6.38. It is apparent that there is a general agreement between VIP scores and ANOVA in highlighting the metabolic differences between tissue types, however there are notable examples where this is not the case. [PA(18:2/18:1)-H]<sup>-</sup> and [PA(20:3/16:0)-H]<sup>-</sup> in the bin 697.45m/z have a VIP score of 6.3 for differentiating tumour and normal tissue (where greater than one shows importance within an OPLS-DA model), however, there is no statistical difference in their relative intensities. Conversely, [PCh(16:0/14:0)-CH<sub>3</sub>]<sup>-</sup> in bin 690.55 has a modest VIP score of 1.6 whilst demonstrating a 30% lower relative abundance in normal tissue compared to tumour, with a high level of statistical significance ( $p = 2.9e^{-8}$ ). When comparing metabolites across the normal-adenoma-carcinoma sequence, it is apparent that there is an association between carcinogenesis and an increase in relative abundance of identified metabolites. When a difference is statistically significant, 94% of metabolites show a relative increase in tumour compared to normal tissue, with 79% increasing for adenoma compared to normal tissue. It is apparent that the mean signal of adenoma and tumour tissues across the 600-1000m/z range is significantly higher

than normal tissue ( $2.3e^7$ ,  $5.4 e^7$  and  $3.0e^7$  for normal, adenoma and tumour respectively; both with  $p < 0.001$ ). This is also reflected in an increased signal-noise ratio for tumour and adenoma tissues (mean of 4652, 9516 and 8390 for normal, adenoma and tumour respectively), with many low intensity noise peaks in normal spectra contributing to a decrease in metabolite signal when included in the normalisation step. It not possible to determine from these data if the differences are intrinsic to the tissue type or to specific metabolic pathways which have become dysregulated.

Bin	Metabolite Ion Identity	Tumour vs Normal				Tumour vs Adenoma				Adenoma vs Normal			
		VIP Score	Change in Normal	Fold Change	<i>p</i> value*	VIP Score	Change in Adenoma	Fold Change	<i>p</i> value*	VIP Score	Change in Normal	Fold Change	<i>p</i> value*
616.45	CerP(d18:1/16:0)-H	2.0	Decrease	0.76	2.5e <sup>-25</sup>	1.5	Increase	1.20	1.7e <sup>-8</sup>	2.7	Decrease	0.63	7.8e <sup>-55</sup>
642.45	PE_Cer(d18:1/16:0)-NH <sub>3</sub> -H	8.9	Decrease	0.55	9.8e <sup>-37</sup>	4.6	Increase	1.12	NS	8.6	Decrease	0.49	4.6e <sup>-54</sup>
645.45	PE(16:0/14:0)-NH <sub>3</sub> -H	5.4	Decrease	0.50	1.0e <sup>-80</sup>	1.9	Decrease	0.87	NS	3.2	Decrease	0.57	7.2e <sup>-56</sup>
657.55	DG(18:1/18:0)+Cl	3.8	Increase	1.18	NS	4.5	Increase	1.38	2.5e <sup>-9</sup>	3.0	Decrease	0.85	NS
659.45	SM(d18:0/14:1)-CH <sub>3</sub>	6.0	Decrease	0.44	6.6e <sup>-107</sup>	2.1	Decrease	0.85	2.4e <sup>-3</sup>	3.9	Decrease	0.52	3.1e <sup>-79</sup>
671.45	PE(16:1/16:0)-NH <sub>3</sub> -H	9.1	Decrease	0.49	7.7e <sup>-72</sup>	3.5	Decrease	0.98	NS	7.1	Decrease	0.50	1.7e <sup>-75</sup>
	PE(18:1/14:0)-NH <sub>3</sub> -H	9.1	Decrease	0.49	7.7e <sup>-72</sup>	3.5	Decrease	0.98	NS	7.1	Decrease	0.50	1.7e <sup>-75</sup>
673.45	PA(18:1/16:0)-H	8.9	Decrease	0.59	1.0e <sup>-49</sup>	4.4	Increase	1.11	NS	8.9	Decrease	0.53	1.5e <sup>-65</sup>
674.45	<sup>13</sup> C isotope of PA(18:1/16:0)-H	4.9	Decrease	0.58	2.5e <sup>-44</sup>	2.5	Increase	1.14	NS	5.1	Decrease	0.51	1.2e <sup>-69</sup>
678.45	PE_Cer(36:5,O3)-NH <sub>3</sub> -H	2.8	Decrease	0.72	5.1e <sup>-3</sup>	6.3	Increase	2.38	7.6e <sup>-31</sup>	6.1	Decrease	0.30	3.4e <sup>-55</sup>
690.55	PCh(16:0/14:0)-CH <sub>3</sub>	1.6	Decrease	0.70	2.9e <sup>-8</sup>	2.1	Decrease	0.53	7.7e <sup>-18</sup>	1.2	Increase	1.33	4.3e <sup>-3</sup>
695.45	PA(20:4/16:0)-H	1.8	Decrease	0.95	NS	4.5	Increase	1.76	7.7e <sup>-47</sup>	4.3	Decrease	0.54	6.5e <sup>-56</sup>
	PA(18:2/18:2)-H	1.8	Decrease	0.95	NS	4.5	Increase	1.76	7.7e <sup>-47</sup>	4.3	Decrease	0.54	6.5e <sup>-56</sup>
696.45	<sup>13</sup> C isotope of PA(20:4/16:0)-H	1.0	Increase	1.03	NS	2.9	Increase	2.10	9.3e <sup>-49</sup>	2.6	Decrease	0.49	3.3e <sup>-47</sup>
697.45	PA(18:2/18:1)-H	6.3	Increase	1.00	NS	12.6	Increase	1.69	2.4e <sup>-31</sup>	11.5	Decrease	0.59	8.4e <sup>-31</sup>
	PA(20:3/16:0)-H	6.3	Increase	1.00	NS	12.6	Increase	1.69	2.4e <sup>-31</sup>	11.5	Decrease	0.59	8.4e <sup>-31</sup>
698.45	<sup>13</sup> C isotope of PA(18:2/18:1)-H	3.9	Increase	1.01	NS	8.0	Increase	1.73	6.2e <sup>-34</sup>	7.3	Decrease	0.58	2.4e <sup>-33</sup>
	<sup>13</sup> C isotope of PA(20:3/16:0)-H	3.9	Increase	1.01	NS	8.0	Increase	1.73	6.2e <sup>-34</sup>	7.3	Decrease	0.58	2.4e <sup>-33</sup>
699.45	PE(18:1/16:0)-NH <sub>3</sub> -H	11.1	Decrease	0.72	4.0e <sup>-13</sup>	9.5	Increase	1.21	2.5e <sup>-3</sup>	13.1	Decrease	0.59	3.1e <sup>-34</sup>
700.45	<sup>13</sup> C isotope of PE(18:1/16:0)-NH <sub>3</sub> -H	8.3	Decrease	0.77	1.4e <sup>-8</sup>	4.5	Increase	1.19	6.0e <sup>-3</sup>	6.1	Decrease	0.65	5.6e <sup>-28</sup>
701.55	PA(18:1/18:0)-H	6.3	Decrease	0.77	9.7e <sup>-16</sup>	4.4	Increase	1.05	NS	6.5	Decrease	0.73	7.6e <sup>-21</sup>
	PA(20:1/16:0)-H	6.3	Decrease	0.77	9.7e <sup>-16</sup>	4.4	Increase	1.05	NS	6.5	Decrease	0.73	7.6e <sup>-21</sup>
	PE(18:0/16:0)-NH <sub>3</sub> -H	6.3	Decrease	0.77	9.7e <sup>-16</sup>	4.4	Increase	1.05	NS	6.5	Decrease	0.73	7.6e <sup>-21</sup>
703.55	x2 <sup>13</sup> C isotope of PA(18:1/18:0)-H	2.3	Decrease	0.73	3.9e <sup>-27</sup>	1.9	Decrease	0.77	5.6e <sup>-15</sup>	1.1	Decrease	0.95	NS
	x2 <sup>13</sup> C isotope of PA(20:1/16:0)-H	2.3	Decrease	0.73	3.9e <sup>-27</sup>	1.9	Decrease	0.77	5.6e <sup>-15</sup>	1.1	Decrease	0.95	NS
	SM(34:1,O3)-CH <sub>3</sub>	2.3	Decrease	0.73	3.9e <sup>-27</sup>	1.9	Decrease	0.77	5.6e <sup>-15</sup>	1.1	Decrease	0.95	NS
709.45	DG(20:3/18:2,O2)+Cl	2.2	Decrease	0.90	NS	5.1	Increase	1.58	6.6e <sup>-39</sup>	5.1	Decrease	0.57	3.3e <sup>-58</sup>
	DG(20:4/18:1,O2)+Cl	2.2	Decrease	0.90	NS	5.1	Increase	1.58	6.6e <sup>-39</sup>	5.1	Decrease	0.57	3.3e <sup>-58</sup>
716.55	PE(18:1/16:0)-H	7.5	Decrease	0.62	3.8e <sup>-43</sup>	7.1	Decrease	0.58	2.9e <sup>-34</sup>	3.0	Increase	1.06	NS
	PCh(16:1/16:0)-CH <sub>3</sub>	7.5	Decrease	0.62	3.8e <sup>-43</sup>	7.1	Decrease	0.58	2.9e <sup>-34</sup>	3.0	Increase	1.06	NS
721.45	PA(20:4/18:1)-H	3.3	Decrease	0.92	NS	5.3	Increase	1.58	4.4e <sup>-16</sup>	5.7	Decrease	0.58	4.2e <sup>-25</sup>
	PE(18:2/18:2)-NH <sub>3</sub> -H	3.3	Decrease	0.92	NS	5.3	Increase	1.58	4.4e <sup>-16</sup>	5.7	Decrease	0.58	4.2e <sup>-25</sup>

723.45	PA(20:4/18:0)-H	3.5	Increase	1.04	NS	6.0	Increase	1.50	7.6e <sup>-24</sup>	5.5	Decrease	0.70	9.4e <sup>-18</sup>
	PE(20:3/16:0)-NH <sub>3</sub> -H	3.5	Increase	1.04	NS	6.0	Increase	1.50	7.6e <sup>-24</sup>	5.5	Decrease	0.70	9.4e <sup>-18</sup>
	PE(18:2/18:1)-NH <sub>3</sub> -H	3.5	Increase	1.04	NS	6.0	Increase	1.50	7.6e <sup>-24</sup>	5.5	Decrease	0.70	9.4e <sup>-18</sup>
725.55	PE(18:2/18:0)-NH <sub>3</sub> -H	6.8	Decrease	0.81	1.0e <sup>-2</sup>	7.6	Increase	1.31	5.9e <sup>-7</sup>	8.6	Decrease	0.62	2.0e <sup>-22</sup>
	PE(18:1/18:1)-NH <sub>3</sub> -H	6.8	Decrease	0.81	1.0e <sup>-2</sup>	7.6	Increase	1.31	5.9e <sup>-7</sup>	8.6	Decrease	0.62	2.0e <sup>-22</sup>
726.55	<sup>13</sup> C isotope of PE(18:2/18:0)-NH <sub>3</sub> -H	4.4	Decrease	0.96	NS	4.2	Increase	1.07	NS	5.1	Decrease	0.90	NS
	<sup>13</sup> C isotope of PE(18:1/18:1)-NH <sub>3</sub> -H	4.4	Decrease	0.96	NS	4.2	Increase	1.07	NS	5.1	Decrease	0.90	NS
727.55	PE(20:1/16:0)-NH <sub>3</sub> -H	6.2	Decrease	0.75	1.0e <sup>-12</sup>	4.2	Increase	1.02	NS	5.6	Decrease	0.73	1.3e <sup>-12</sup>
	PE(18:1/18:0)-NH <sub>3</sub> -H	6.2	Decrease	0.75	1.0e <sup>-12</sup>	4.2	Increase	1.02	NS	5.6	Decrease	0.73	1.3e <sup>-12</sup>
728.55	<sup>13</sup> C isotope of PE(18:1/18:0)-NH <sub>3</sub> -H	3.5	Decrease	0.90	NS	3.8	Decrease	0.86	4.6e <sup>-2</sup>	3.5	Increase	1.04	NS
742.55	PCh(18:2/16:0)-CH <sub>3</sub>	5.8	Decrease	0.96	NS	6.4	Decrease	0.81	6.8e <sup>-6</sup>	6.9	Increase	1.18	2.0e <sup>-2</sup>
	PCh(18:1/16:1)-CH <sub>3</sub>	5.8	Decrease	0.96	NS	6.4	Decrease	0.81	6.8e <sup>-6</sup>	6.9	Increase	1.18	2.0e <sup>-2</sup>
743.55	<sup>13</sup> C isotope of PCh(18:2/16:0)-CH <sub>3</sub>	5.0	Decrease	0.92	NS	6.7	Decrease	0.73	4.0e <sup>-13</sup>	6.0	Increase	1.26	8.5e <sup>-7</sup>
	<sup>13</sup> C isotope of PCh(18:1/16:1)-CH <sub>3</sub>	5.0	Decrease	0.92	NS	6.7	Decrease	0.73	4.0e <sup>-13</sup>	6.0	Increase	1.26	8.5e <sup>-7</sup>
744.55	PCh(18:1/16:0)-CH <sub>3</sub>	8.9	Decrease	0.83	4.7e <sup>-5</sup>	11.2	Decrease	0.68	1.5e <sup>-22</sup>	8.3	Increase	1.21	7.3e <sup>-5</sup>
747.45	SM(34:3.06)-CH <sub>3</sub>	1.8	Decrease	0.82	4.1e <sup>-4</sup>	1.6	Increase	1.49	NS	2.5	Decrease	0.72	6.3e <sup>-18</sup>
747.55	PG(16:0/18:1)-H	4.4	Decrease	0.66	2.7e <sup>-27</sup>	2.5	Decrease	0.87	NS	3.5	Decrease	0.75	7.0e <sup>-12</sup>
759.45	PE(18:2/18:1)-NH <sub>3</sub> +Cl	3.4	Increase	1.41	4.4e <sup>-9</sup>	6.2	Increase	2.2	3.4e <sup>-54</sup>	4.2	Decrease	0.64	3.1e <sup>-21</sup>
	PA(20:4/18:0)+Cl	3.4	Increase	1.41	4.4e <sup>-9</sup>	6.2	Increase	2.2	3.4e <sup>-54</sup>	4.2	Decrease	0.64	3.1e <sup>-21</sup>
770.55	PCh(18:1/18:1)-CH <sub>3</sub>	4.3	Increase	1.01	NS	5.8	Decrease	0.77	2.8e <sup>-13</sup>	6.5	Increase	1.31	4.8e <sup>-11</sup>
	PCh(18:2/18:0)-CH <sub>3</sub>	4.3	Increase	1.01	NS	5.8	Decrease	0.77	2.8e <sup>-13</sup>	6.5	Increase	1.31	4.8e <sup>-11</sup>
771.55	<sup>13</sup> C isotope of PCh(18:1/18:1)-CH <sub>3</sub>	4.0	Decrease	0.85	7.9e <sup>-6</sup>	4.9	Decrease	0.76	1.0e <sup>-16</sup>	3.7	Increase	1.13	NS
	<sup>13</sup> C isotope of PCh(18:2/18:0)-CH <sub>3</sub>	4.0	Decrease	0.85	7.9e <sup>-6</sup>	4.9	Decrease	0.76	1.0e <sup>-16</sup>	3.7	Increase	1.13	NS
772.55	PCh(18:1/18:0)-CH <sub>3</sub>	4.3	Decrease	0.76	8.1e <sup>-20</sup>	5.2	Decrease	0.67	9.8e <sup>-30</sup>	3.0	Increase	1.13	NS
773.55	PG(18:1/18:1)-H	5.7	Decrease	0.59	4.9e <sup>-45</sup>	5.7	Decrease	0.55	1.8e <sup>-38</sup>	1.4	Increase	1.07	NS
775.55	PG(18:1/18:0)-H	4.2	Decrease	0.48	6.6e <sup>-59</sup>	3.1	Decrease	0.61	3.0e <sup>-19</sup>	1.4	Decrease	0.78	1.4e <sup>-4</sup>
797.65	SM(d16:0/26:2)-CH <sub>3</sub>	2.6	Increase	1.26	NS	2.8	Decrease	0.54	1.5e <sup>-19</sup>	2.4	Increase	2.35	2.1e <sup>-10</sup>
798.65	<sup>13</sup> C isotope of SM(d16:0/26:2)-CH <sub>3</sub>	1.6	Increase	1.06	NS	2.6	Decrease	0.53	3.3e <sup>-34</sup>	1.8	Increase	2.0	2.6e <sup>-13</sup>
887.55	PI(20:3/18:0)-H	4.1	Decrease	0.46	1.4e <sup>-43</sup>	0.9	Decrease	0.93	NS	2.8	Decrease	0.50	2.0e <sup>-62</sup>

Table 6.6 – the VIP score, change in relative intensity, fold change and corrected *p* value of the 61 identified lipid metabolites when performing binary comparisons between colorectal tumour, adenoma and normal tissue.

VIP – variable importance in projection; CerP – ceramide-1-phosphate; PE\_Cer – ceramide phosphatidylethanolamine; PE – phosphatidylethanolamine; DG – diacylglycerol; SM – sphingomyelin; PA – phosphatidic acid; PCh – phosphatidylcholine; PG – phosphatidylglycerol; PI – phosphatidylinositol; NS – not significant

\**p* value calculated using ANOVA and then corrected using the Bonferroni procedure

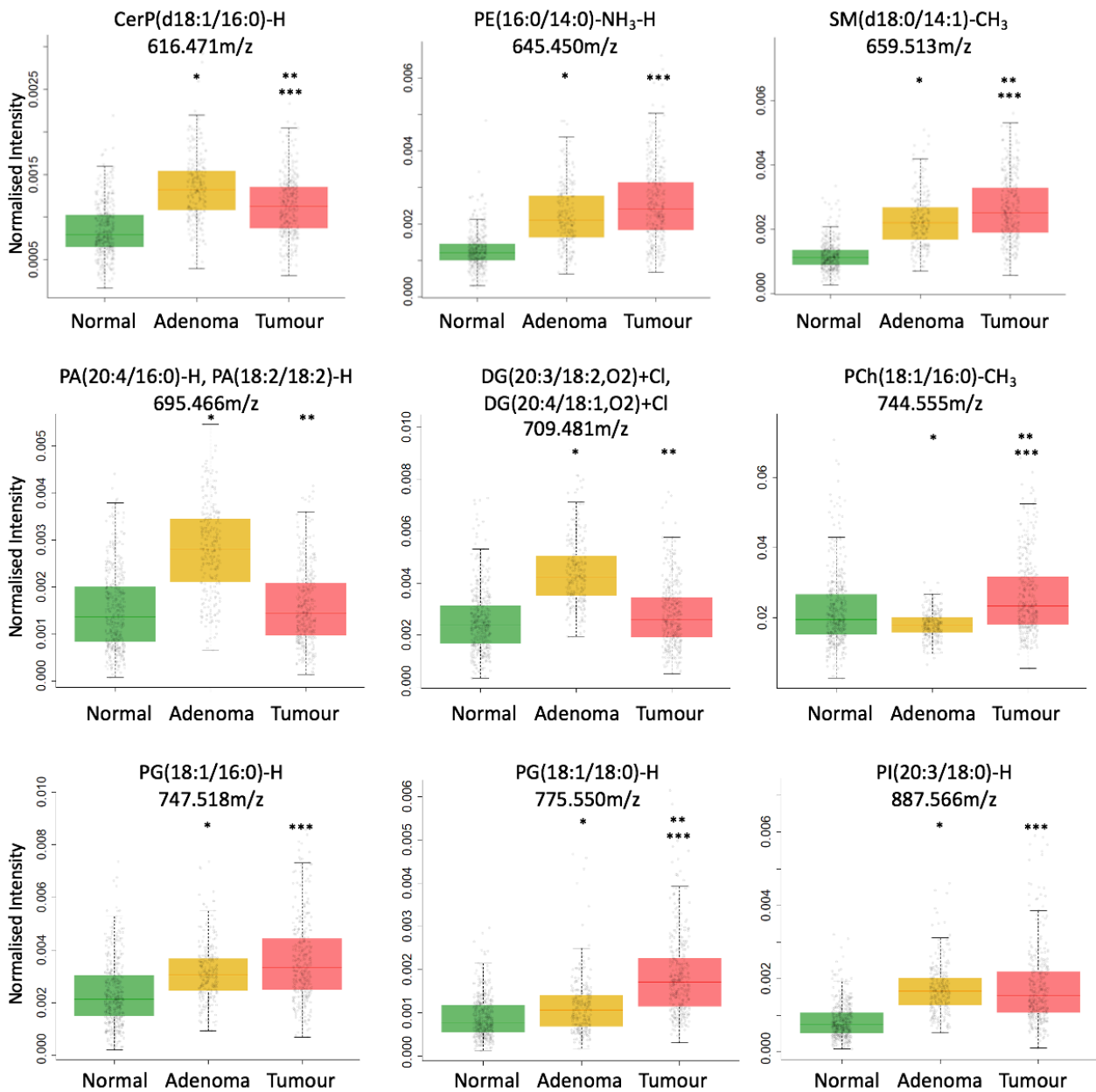


Figure 6.38 – box and whisker plots of the relative abundance of 9 metabolites across colorectal normal, adenoma and tumour tissue; with the exact mass and identity from MS/MS shown. The box reflects the 25-75<sup>th</sup> percentiles with a median line and the whiskers are 1.5 x interquartile range without extending beyond a datapoint. A jitter plot of the raw data is presented (grey). CerP – ceramide-1-phosphate; PE – phosphatidylethanolamine; SM – sphingomyelin; PA – phosphatidic acid; DG – diacylglycerol; PCh – phosphatidylcholine; PG – phosphatidylglycerol; PI – phosphatidylinositol.

\* reflects a statistically significant difference in adenoma compared to normal tissue.

\*\* reflects a statistically significant difference in tumour compared to adenoma tissue.

\*\*\* reflects a statistically significant difference in tumour compared to normal tissue.

The metabolites that were identified by MS/MS were categorised by lipid subclass and if three or more metabolites were included, the relative intensities across each spectrum were summed and then plotted by tissue type (figure 6.39). This revealed that the abundance of PGs appears to

progressively and statistically significantly increase throughout carcinogenesis, with a similar pattern seen with SMs (however the increase from normal to adenoma tissue was not statistically significant). A heat map with a dendrogram presenting unsupervised clustering demonstrates that the relative abundance of lipid classes appears to change independently of each other and that those with similar biosynthetic pathways (for example, ceramides and sphingomyelins) show little similarity in their changes (figure 6.40). It was then decided to assess if the acyl chain composition of GPLs was associated with colorectal tissue type. A heatmap comparing the relative abundance of GPLs containing at least one monounsaturated fatty acid (MUFA) and those with at least one polyunsaturated fatty acid (PUFA) can be seen in figure 6.41.A. Using this classification, the dendrogram clusters adenoma and tumour tissues together, which was not the case when lipid classes were used (where tumour was clustered with normal). GPLs containing MUFAs are seen to statistically significantly increase throughout the normal-adenoma-carcinoma sequence (figure 6.41.C), which is not the case for PUFAs (where there is no change between normal and tumour tissue, figure 6.41.B).

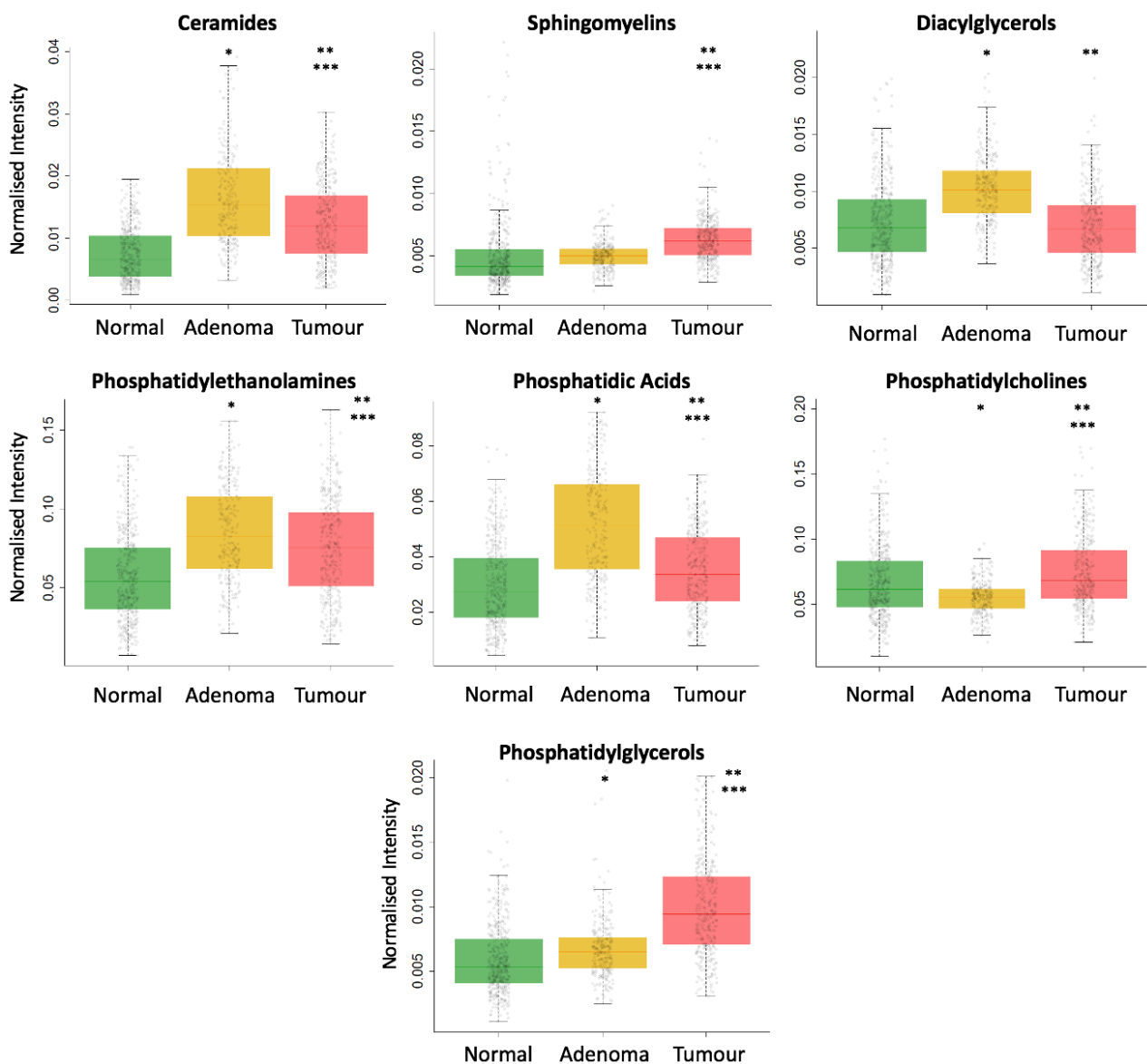


Figure 6.39 – box and whisker plots of the total relative abundance of 7 lipid classes across normal, adenoma and tumour tissue. The box reflects the 25-75<sup>th</sup> percentiles with a median line and the whiskers are 1.5 x interquartile range without extending beyond a datapoint. A jitter plot of the raw data is presented (grey).

\* reflects a statistically significant difference in adenoma compared to normal tissue.

\*\* reflects a statistically significant difference in tumour compared to adenoma tissue.

\*\*\* reflects a statistically significant difference in tumour compared to normal tissue.

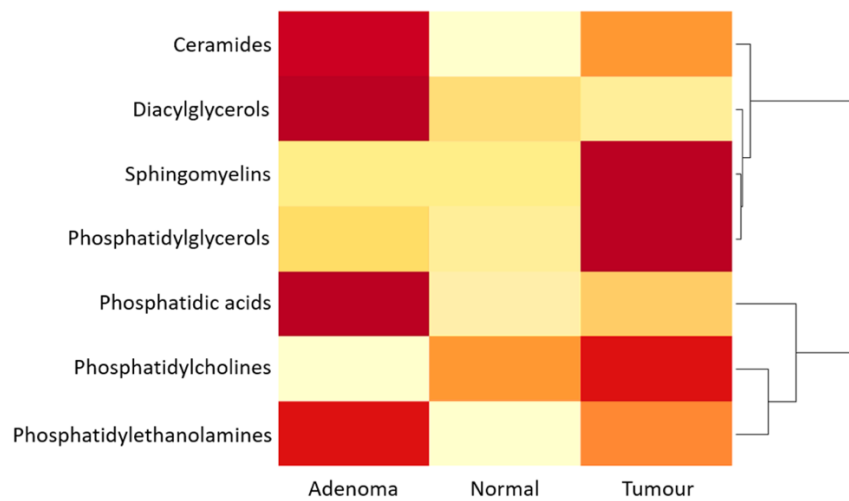


Figure 6.40 – heatmap of how the relative abundance of different lipid subtypes is associated with colorectal tissue type, with unsupervised clustering represented with a dendrogram.

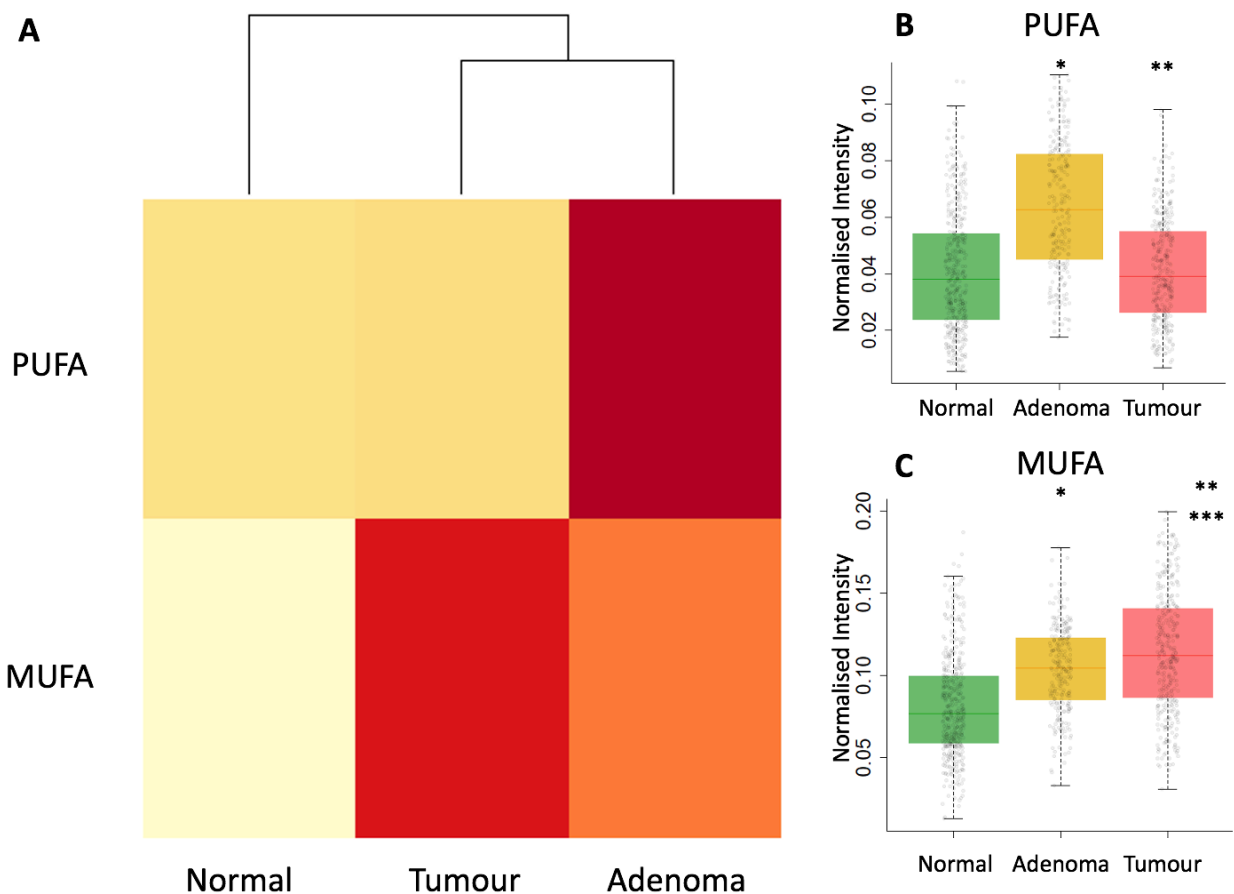


Figure 6.41 – heatmap of how the relative abundance of PUFAs and MUFAs within glycerophospholipids is associated with colorectal tissue type (A) and visualised in a box as whiskers plot with jitter (B and C respectively).

PUFA – polyunsaturated fatty acid; MUFA – monounsaturated fatty acid.

\* reflects a statistically significant difference in adenoma compared to normal tissue.

\*\* reflects a statistically significant difference in tumour compared to adenoma tissue.

\*\*\* reflects a statistically significant difference in tumour compared to normal tissue.

A further analysis was conducted to explore the differential abundance of lipid classes between colorectal tissues when adenomas were distinguished based on their grade of dysplasia. Section 6.3.1.2 revealed that adenomas with high grade dysplasia were commonly being misclassified as tumours when cross validating an LDA model, with the similarity in metabolite abundance between tumours and HGD adenomas also evident across multiple lipid classes (figure 6.42). As adenomas progress from LGD, through HGD and to tumour; PChs and PGs significantly increase in relative abundance. The metabolic similarities between HGD adenomas and tumour continue when studying the acyl chain composition (figure 6.43). PUFA chains in GPLs significantly reduce as an adenoma progresses from LGD to HGD and then remains unchanged for the transition to tumour, however it is noteworthy that the abundance in these high-risk subtypes is no different to in normal tissue (figure 6.43.B). When assessing the abundance of free PUFAs in the tissues (figure 6.44.A), this pattern appears to reverse, where the abundance of the free metabolite increases in tumour tissue. Furthermore, whilst PUFA chains in GPLs are a clear distinguishing feature differentiating LGD and HGD adenomas, the free metabolite levels in the tissues are no different. There is a greater correlation between MUFAs that are free in the tissue and those within the acyl chains of GPLs, where they both demonstrate the highest relative abundance in tumour tissue, with a significant increase from HGD adenomas to tumour (figure 6.43.C and figure 6.44.B). The association of MUFAs and dysplasia grade is unclear given that the abundance in GPLs decreases from LGD to HGD, however their free abundance in the tissue is unchanged.

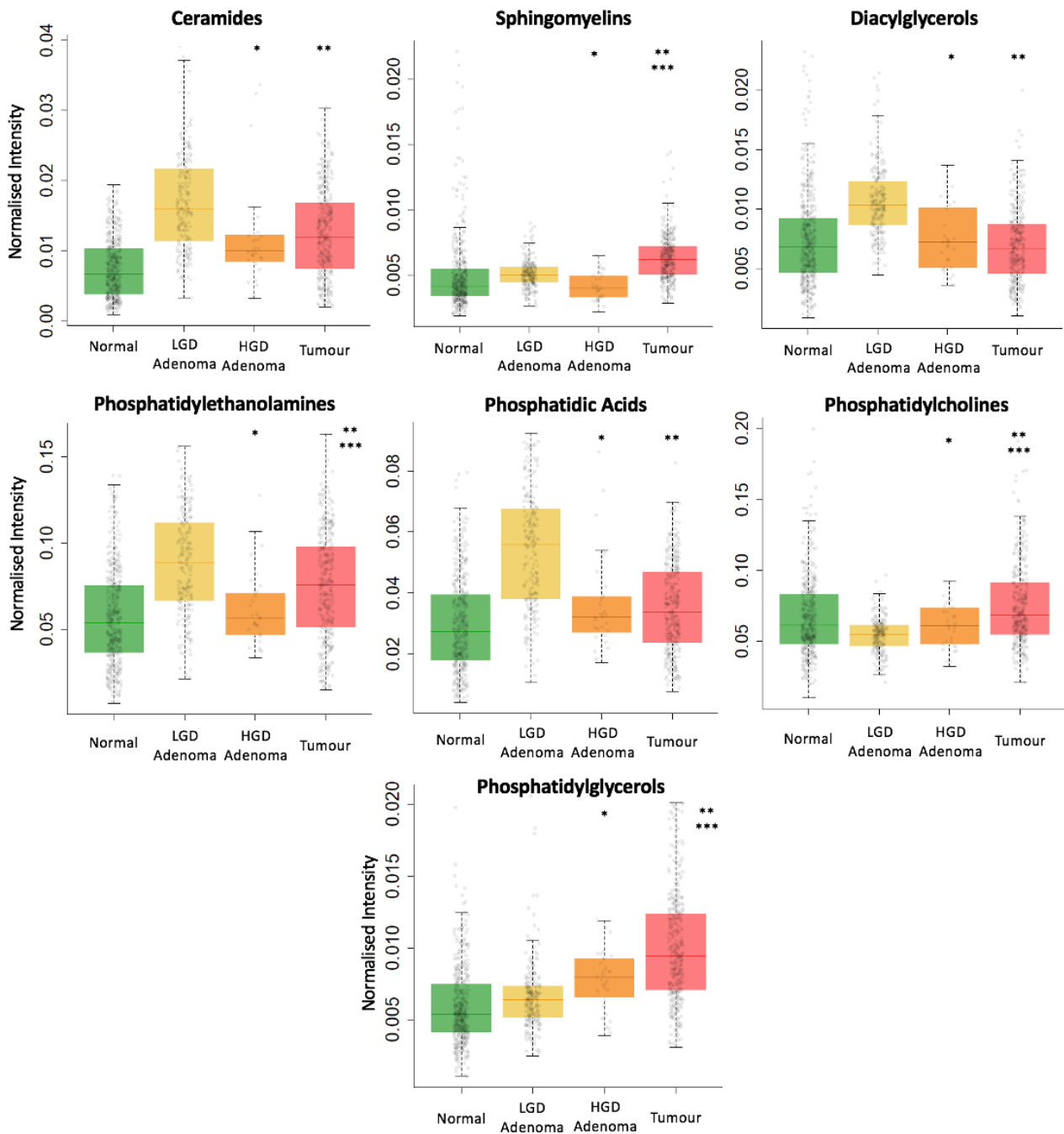


Figure 6.42 – box and whisker plots of the total relative abundance of seven lipid classes across normal, low-grade dysplastic adenomas, high-grade dysplastic adenomas and tumour tissue. LGD – low grade dysplasia; HGD – high grade dysplasia.

\* reflects a statistically significant difference between low- and high-grade dysplastic adenomas.

\*\* reflects a statistically significant difference between low grade dysplastic adenoma and tumour.

\*\*\* reflects a statistically significant difference between high grade dysplastic adenoma and tumour.

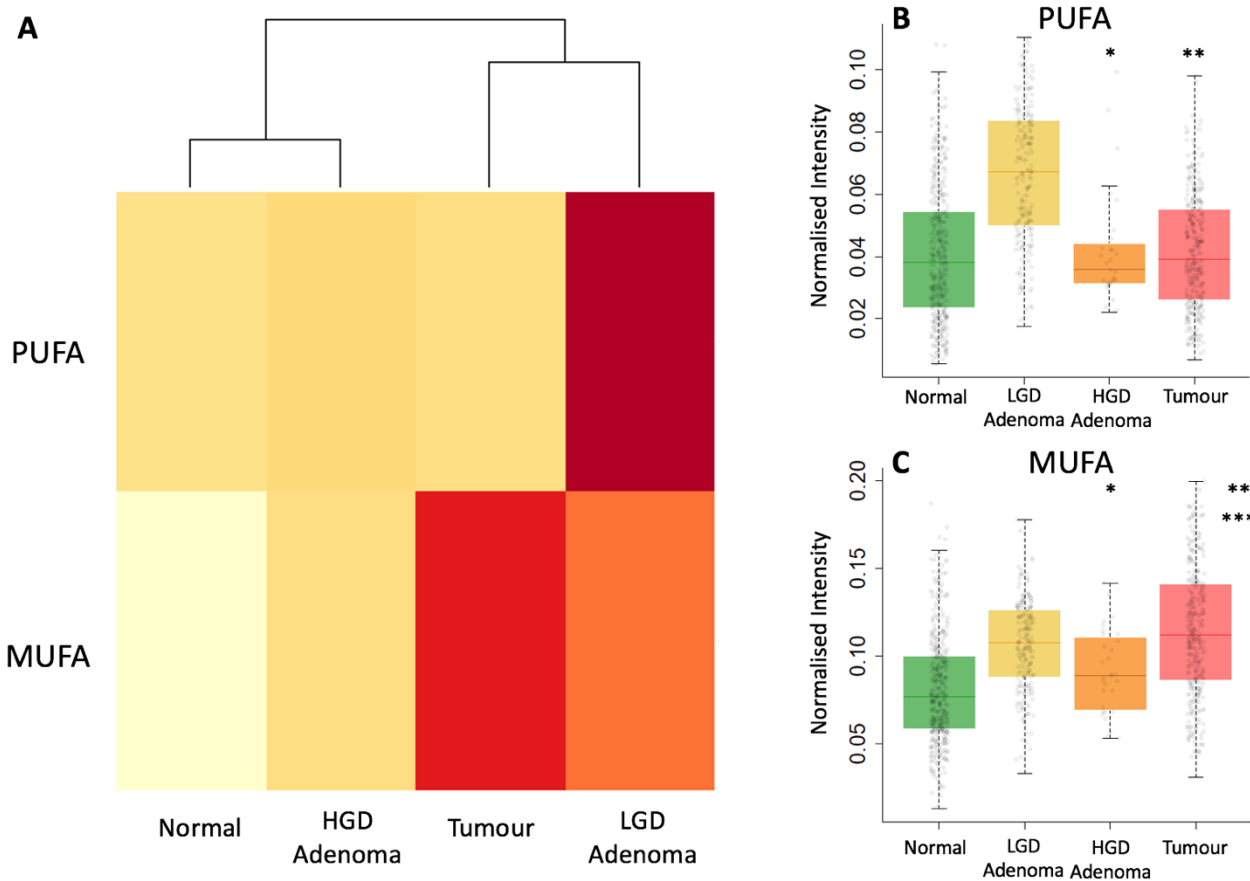


Figure 6.43 – heatmap of how the relative abundance of PUFAs and MUFAs within glycerophospholipids is associated with colorectal tissue type with adenomas separated into those with high- and low-grade dysplasia (**A**) and visualised in a box as whiskers plot with jitter (**B** and **C** respectively).

PUFA – polyunsaturated fatty acid; MUFA – monounsaturated fatty acid; HGD – high grade dysplasia; LGD dysplasia.

\* reflects a statistically significant difference between LGD adenoma and HGD adenoma.

\*\* reflects a statistically significant difference between LGD adenoma and tumour.

\*\*\* reflects a statistically significant difference between HGD and tumour.

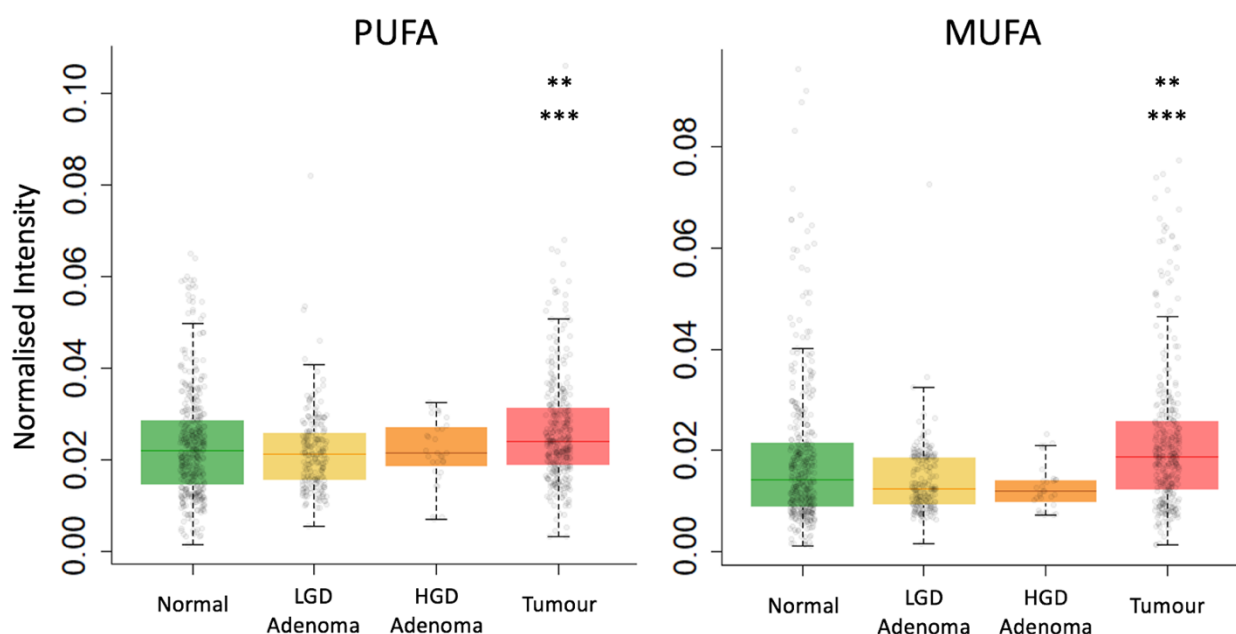


Figure 6.44 – boxplots of the relative abundance of free PUFAs (A) and MUFAs (B) across colorectal tissue types with adenomas separated into those with high- and low-grade dysplasia. PUFA – polyunsaturated fatty acid; MUFA – monounsaturated fatty acid; HGD – high grade dysplasia; LGD dysplasia. \*\* reflects a statistically significant difference between LGD adenoma and tumour. \*\*\* reflects a statistically significant difference between HGD and tumour.

## 6.4 Discussion

This chapter has explored the ability of REIMS to differentiate colorectal tissue types *ex vivo* through the creation of a validated and clinically annotated spectral database, application of chemometric functions and extraction of unique lipidomic features. It has revealed that the composition of cellular lipid metabolites can be used to accurately differentiate colorectal tumour, adenoma and normal mucosa; in addition to the risk stratification of adenomas. The accurate differentiation of colorectal tissue types by REIMS has revealed unique lipidomic fingerprints for the stages of colorectal carcinogenesis, with clear associations presented between clinical phenotype and metabolic profile.

### 6.4.1 Clinical impact of REIMS accuracy for tissue recognition and risk-stratification

Accurate real-time tissue recognition has the potential to transform the delivery of healthcare for patients with colorectal disease, by coupling REIMS to surgical devices that are used during routine

clinical care. This can be applied for two principal purposes, first as a diagnostic system upon which to make management decisions and two, as a platform to improve the quality of a therapeutic intervention. The diagnostic potential of these findings is best considered with colonoscopy and the management of colorectal polyps. It is promising to see that REIMS appears to have a diagnostic accuracy that is superior to its competitor endoscopic technologies appraised in chapter 2 (whilst recognising the differences in the study designs and tissue types analysed), with REIMS at a much earlier phase of its development. Diagnosing the luminal portion of colorectal polyps that are encountered clinically using a snare tip will be able to support the use of the '*diagnose and leave*' and '*resect and discard*' strategies, resulting in a reduction in unnecessary polypectomies, procedure time and histology processing costs<sup>184,186</sup>. REIMS may also be able to support therapeutic interventions in the endoscopic setting. A feedback model can now be created to inform clinicians performing an EMR if there appears to be adenoma in the dissection plane, in which case a further resection could be performed to reduce recurrence risk. REIMS used for the detection of tumour-involved margins can also be applied to TAMIS, which is the subject of chapter 7. A significant amount of further testing and validation is required, for example, to confirm the initial data quality that was captured in pilot studies of endoscopic REIMS<sup>85</sup> and to determine how the diagnostic accuracy can be applied in a prospective setting. The future pathway for REIMS tissue recognition and required steps in the development will be discussed later in the thesis.

When considering the misclassifications made by REIMS, one of the greatest concerns with its clinical application is the prevalence and impact of false negative predictions of disease; as this has a great potential adverse clinical implication (hence why NPV is such a valuable metric when assessing these technologies). Whilst a minimum 90% NPV for adenoma has been suggested for endoscopic technologies assessing polyps, it is likely that such a threshold in any clinical scenario is still too low for widespread acceptance by patients and clinicians<sup>185,316</sup>. The 91.8% NPV for disease shown by REIMS is promising, however it is recommended that there is patient involvement in the development process for clinical machine learning technologies in order to determine acceptability thresholds<sup>356</sup>. The greatest source of misclassifications in tissue recognition was adenomas predicted to be tumours, where a metabolic similarity (particularly between HGD adenoma and tumour) is biologically plausible given similarities between them on a genomic, transcriptomic and proteomic level<sup>357-360</sup>. From a genomic perspective, the normal-adenoma-carcinoma sequence is largely considered a progression of multiple steps<sup>361</sup>, however, the

diagnosis of cancer is a distinct and binary outcome. Dysplastic cells may have all the necessary dysregulation for invasion but have yet to extend through the muscularis mucosae to be defined as a cancer, making it very challenging to metabolically define the moment the lesion becomes neoplastic.

This phenomenon may also be a driving factor behind why REIMS performs so poorly at risk-stratifying CRCs and adenomas (with the exception of dysplasia grade in adenomas), where again, there are attempts to map complex metabolic shifts into somewhat arbitrary ordinal categories. The exact definition of the categories (for example, exactly what constitutes T1-T4; and the interpretation of which classes are 'early' or 'advanced' cancers) may be a source of error, where the relevant metabolic changes are not contemporaneous with the morphology described pathologically. An example of pathological definitions being incongruous with clinical findings is the vast array of oncological outcomes for patients with N2 disease (with 5 year DFS ranging from 62% for T1-2, to 30% for T4), despite them being all being categorised together in the AJCC criteria<sup>362</sup>. Additionally, the TNM is generally a poor predictor of DFS and does not feature in multifactorial risk models<sup>363</sup>.

It may also be the case that it is not possible to use the abundance of complex lipid metabolites to risk stratify CRCs based on histological features of poor prognosis. Other unmeasured factors may be of greater importance (such as small metabolites, time since lesion inception or mucosal microbiome<sup>364</sup>), which would also explain the paucity of literature exploring tissue metabolomics with the histological features described here. A further possibility is an imbalance in the number of spectra in each risk strata, as shown by tumour stage, where there were 76 spectra from T1/2 and 249 from T3/4. The relatively small number of patients constituting one of the groups may represent a lack of power (where the true lipidomic fingerprint of the phenotype cannot be distinguished from other sources of variation such as host genome), however even in groups which were relatively balanced, REIMS still had a poor accuracy in risk-stratification of CRCs. The limitations arising from the role of sampling location within the context of intra-tumour heterogeneity and subjectivity in histopathological assessment are addressed in section 6.4.3.4. Based on the data presented, REIMS is currently insufficiently accurate for the clinical risk-stratification of CRCs. Its use to this end would be invaluable in specific clinical scenarios, such as the staging of early rectal cancers. In order to reduce local recurrence and ensure any mesorectal lymph node metastasis is excised, rectal cancers with features such as greater than SM2 invasion,

LVI, poor differentiation and tumour budding should undergo radical resection rather than local excision<sup>365</sup>. It is not possible to fully assess these features pre-operatively using imaging or biopsy<sup>366</sup>, with an unmet need for a staging technology such as REIMS to aid in the decision making process.

#### 6.4.2 Lipidomic features of colorectal carcinogenesis

When exploring how the predictive models were able to differentiate colorectal tissue types, the primary finding of this work is that there does not appear to be a single metabolite which acts as a biomarker of carcinogenesis; the abundance of which can be used to make predictions of where a tissue is on the normal-adenoma-carcinoma sequence. Instead, the relative abundance of a large number of complex lipids varies in a way which can be closely associated with tissue phenotype; similar to findings from many other organs including breast<sup>367,368</sup>, lymphoma<sup>369</sup>, prostate<sup>370</sup>, lung<sup>371</sup>, colorectal<sup>57,85</sup>, liver<sup>137</sup> and several more<sup>372</sup>. In fact, the relative changes may be even more subtle in colorectal tissues given the similarity in lipid composition between normal and tumour tissues, unlike breast where there is a predominance of TGs in normal tissue and GPLs in tumour<sup>167</sup>. This prompted the significant efforts in this chapter to identify the structure of a large quantity of these metabolites using MS/MS; with the results presented in section 6.3.4 representing the most comprehensive level 2 metabolite identification of colorectal tissues using REIMS in the literature.

The changes in metabolite relative abundance between colorectal tumour, adenoma and normal tissue did follow some patterns when assessed by lipid class and GPL acyl chain composition. PChs were found to significantly increase in relative abundance between LGD adenoma, HGD adenoma and tumour tissue; a finding that has been previously described in colorectal and other cancers. The increase in colorectal tissues has been attributed to an over-expression of choline kinase starting at the adenoma stage<sup>83,373</sup>, however, this dataset noted a fall in PCh abundance when normal tissue first becomes adenomatous. This is consistent with increased phospholipase D activity (which hydrolyses PCh into a PA and choline)<sup>374</sup>, with a PCh decrease and PA increase seen with adenoma formation. Overexpression of LPCAT has also been demonstrated in CRC<sup>87,375</sup>, which is responsible for re-acylating lyso-PCh into PCh. It appears that these PCh species are more than simply structural components, as reducing their abundance (such as with siRNA for LPCAT)

reduces cell growth and induces apoptosis *in vitro*<sup>87</sup>. PChs are intrinsically related to SMs, which are even more clearly increased in abundance throughout carcinogenesis and where their shared headgroup is transferred from a PCh to a ceramide by SM synthase<sup>375</sup>. Sphingosine kinase is overexpressed in CRC (driven by FASN), with its inhibition resulting in decreased cell proliferation and migration *in vitro*; likely due to its role as a signalling molecule within the plasma membrane<sup>376</sup>. SM hydrolysis and the formation of ceramide with SMase is considered to be anti-tumourigenic, however, the activity of SMase is seen to fall in sporadic colorectal adenomas and cancers<sup>377</sup>. It therefore appears that REIMS is able to sample the complex and inter-twined dysregulation of PCh and SM metabolism during carcinogenesis, where the relative abundance of these lipids can be directly associated with cellular phenotype. However, determining and validating the exact metabolic processes responsible for these findings is beyond the scope of this thesis.

PGs showed a significant increase in relative abundance as tissues progressed from normal, to LGD adenomas, HGD adenoma and finally, to tumour; with the three identified by MS/MS representing the most abundant in human colorectal tissues<sup>86</sup>. The reasoning behind this increase in relative abundance is unclear, as PGs constitute only 1-2mol% of cellular phospholipids and their functions are mostly described in relation to the mitochondria and endoplasmic reticulum<sup>378,379</sup>. PGs (particularly PG(18:1/18:1) and PG(18:1/16:0)) have been demonstrated to selectively activate nuclear protein kinase C  $\beta$ II during the G2 phase of the cell cycle, which is required for mitosis<sup>380</sup>; and is therefore a potential mechanism upon which they are tumourigenic. There is a potential role for PGs in mucinous CRCs, however that is also unclear. An increased abundance of PGs has also been associated given their role as surfactants<sup>381</sup>, however in this dataset the relative abundance of PGs actually fell with mucinous phenotype. Whilst the  $\epsilon$  subtype of protein kinase C is responsible for colonic mucin secretion<sup>382</sup>, there is no clear evidence that this subtype of protein kinase C can be activated by PGs.

It was generally found that lipid class was associated with tissue type only in selected cases (as described above), however the acyl chain composition of GPLs has also been found to play a significant role. This work has identified that GPLs containing MUFAs significantly increase in relative abundance as carcinogenesis progresses. Previous research has largely focused on the study of free fatty acids in the serum of CRC or adenoma patients, or for free MUFAs in tissues; with both approaches showing similar findings to this work<sup>77,383-385</sup>. Shim *et al.* have described the

abundance of fatty acids within GPLs in CRC, adenoma and normal tissues in a total of 83 patients, demonstrating the same progressive increases for 16:1 and 18:1 FAs, however 20:1 abundance appears to decrease<sup>386</sup>. The analysis presented in this chapter was unable to consistently separate the abundances of GPLs based on the exact MUFAs present due to mixtures within bins (a consequence of a lack of chromatography) and therefore cannot address whether increasing MUFA length impacts the relationship with carcinogenesis. Despite this, the finding presented may give insight into which components of the biosynthetic pathway have been dysregulated in CRC. Palmitic acid (16:0) is the product of *de novo* fatty acid synthesis, which is then desaturated using Delta-9 desaturase (SCD-1) prior to or after elongation to C18<sup>387</sup>. Over-expression of SCD-1 during carcinogenesis would be consistent with the lipidomic findings here and this has been shown to be the case in colorectal and many other cancer types<sup>57</sup>. Furthermore, SCD-1 activity is correlated with proliferation of cancer cells, poorer outcomes from CRC and has been made a target of anti-cancer therapies<sup>57,388-390</sup>. The relative abundance of MUFAs may therefore be used as a biomarker of disease response in anti-SCD treatments, with the potential to determine this in real-time using REIMS if desired. When distinguishing the MUFA abundance between the dysplasia grade of adenomas, an unexpected decrease was witnessed between LGD and HGD, before the increase to tumour. The cause for this is unclear and may represent a non-linear relationship between MUFA abundance and progressive carcinogenesis, or this may simply be an underpowered comparison due to the relatively low numbers of HGD adenomas.

The PUFA content of mucosal GPLs appears to have a more significant role in the initial stages of carcinogenesis progression, where the relative abundance was found to be significantly increased only in LGD adenomas. To my knowledge, this is the first time this association has been described, with a previous group only demonstrating free tissue eicosapentaenoic acid (EPA; FA 20:5) increased in LGD compared to HGD and tumour<sup>385</sup>. There are conflicting views in the existing literature as to the general relationship between tissue PUFA abundance and the presence of colorectal tumour cells. Whilst it is not contested that tumour cells preferentially uptake free PUFAs to aid in their proliferation *in vitro* (compared to normal tissue)<sup>391</sup> and that supra-physiological supplementation of cancer cell line supernatant with EPA causes an increased incorporation of this into GPL acyl chains<sup>392</sup>; this association has not been replicated when analysing human samples. When clinical biopsies were assayed, the composition of PUFAs in GPLs varies markedly between tissues types by carbon chain length and saturation status<sup>385,386</sup>. EPA for example, appears to decrease in abundance both free in the tissue and as an acyl chain of a GPL,

which may be explained by an apparent preference for PUFA incorporation into TGs rather than polar lipids<sup>393</sup>. This could not be explored in detail in this thesis given that TGs were of low relative abundance and were not responsible for differentiating colorectal tissue types on the multivariate models. It may therefore be the case that PUFA-containing GPLs are best used by REIMS to differentiate low- from high-grade dysplasia in adenomatous lesions. Further insight could be sought if it was possible to distinguish how the abundance of each PUFA is impacted, however, mixtures of metabolites in bins limited the ability to achieve this.

### 6.4.3 Limitations

#### 6.4.3.1 Exclusions due to insufficient spectral quality

There are several limitations to this work that need to be explored, the first of which is that 554 REIMS spectra (35.4% of the total collected) were deemed of insufficient quality for inclusion in the statistical modelling. If this high percentage was to continue as the technology was translated *in vivo*, it would be a significant threat to the feasibility of REIMS during clinical applications. However, when examining the causes of the poor quality, it is evident that a large proportion are unique to the research process (and would not apply in a clinical setting) or are where analytical processes have been adapted to mitigate against their recurrence. The most common cause of poor quality was the technical batch effect due to mass drift in 116 spectra collected on a specific instrument between March and June 2015, where appraisal of the instrument logs revealed a lack of calibration check prior to analysis (discussed in detail in section 5.2.3.2). Following this, a process change was initiated where calibration with sodium formate (and a subsequent check for mass drift) must be conducted prior to every analytical session; resulting in no further instances of batch effects from mass drift in the remaining samples. It is therefore considered that this is of very low risk of occurring again in future analyses. 160 spectra were affected by the sampling of non-mucosal tissue, most commonly where there was excessing sampling of the submucosa (recognised by its high TG levels) or where no mucosa at all was found in the validation sections. This failure is a function of the process by which tissue is sampled and then analysed *ex vivo* with REIMS, where a piece is dissected from the surgical specimen, often cut into sufficiently small pieces, placed in an Eppendorf tube for storage and then analysed at a later date. This causes the

orientation of the tissue piece to be lost, which is often exacerbated by cutting research samples again prior to analysis; increasing the chance of insufficiently analysing the mucosa. This would not be a risk during trans-luminal application of REIMS for gastrointestinal disease, as the energy device being used would have to be applied to the mucosa by virtue of its position as the inner lining of the bowel wall. 20 spectra were excluded from the analysis because they were not conducted with cut monopolar diathermy (and instead largely with coagulation diathermy), which, as discussed in section 5.3.3.2, causes markedly different spectra from the same tissue piece. This limitation is most relevant when considering that in a clinical setting, the clinician will employ the energy device most suited to the task and therefore may wish not to use purely cut diathermy. Whether it is during a TAMIS where coagulation mode may be preferred, or during an EMR where a blended (combination coagulation and cut) are used; it is currently unclear how that change will impact the diagnostic accuracy when performing tissue recognition. This dataset could not address this question given 99.9% of spectra were collected with *cut* diathermy, however this will be discussed in chapter 7 during *in vivo* translation of the technology. 171 spectra (11% of the total) had an insufficient signal:noise ratio which resulted in their exclusion from modelling. As explored in section 5.2.4, noise in spectrometry can have many causes, including biological; which appears to be present here given the tissue-specific signal:noise ratios witnessed and its negative impact on tumour misclassifications. It has been beyond the scope of this section to define the causes of poor signal:noise ratio in any more depth and it is likely that it is a continued risk for REIMS spectra collected in the future. However, this risk is likely to be relatively limited. It is reassuring that 79.8% of the failures due to signal:noise ratio were in the first half of the analyses and it is likely they were impacted by differences in the analytical process such as instrument cleaning regime and IPA flow rate. Only 4.1% of spectra analysed since March 2017 have had a signal:noise ratio <1000, which is not likely to be a significant hurdle to translation of the technology *in vivo*. It has therefore been shown that despite an initial impression of a high rate of REIMS spectra being excluded from modelling due to quality concerns, in fact, it is apparent that these factors are much less significant with optimised analytical procedures and an understanding of how the technology is used in a clinical setting. It is anticipated that approximately 5% of REIMS spectra will have to be excluded in future analyses for not meeting the minimum quality standards, which when considering the speed of acquisition and ease of repeated analysis, is not expected to cause a significant obstacle to clinical use.

#### 6.4.3.2 Using histopathology as a reference standard

Using histopathological validation of tissue pieces analysed by REIMS for determining the tissue subtype presented challenges both from the perspective of the research process and when considering how the technology could be translated intraoperatively. A pathological section is a 5µm snapshot of a piece of tissue, which is often small and with distorted architecture after analysis with REIMS. This meant that there was a possibility of the validation section not truly representing the overall composition of the tissue piece as it may only be presenting a portion of it. This is likely to have had a limited impact due to the progressive use of smaller tissue pieces to mitigate against this and there was a very high correlation between the raw spectra and validation section report (for example, a noisy spectrum would be seen when only muscle is present in the tissue sample). It was also not possible to say with high levels of accuracy the exact tissue subtype at the site of the diathermy burn when smaller tissue pieces were used and instead, the validation would have to be from the section as a whole. This may have contributed to false negatives, where REIMS analysed normal tissue immediately adjacent to tumour in the same tissue piece, however, without being able to identify every burn, it was not possible to mitigate against this. Furthermore, it is recognised that there is inter-observer variability between histopathologists when making diagnoses of colorectal tissues. van Putten *et al.* demonstrated that there was disagreement in 4% of polyp sections regarding the presence of adenoma or non-adenoma tissue, which increased to 17% when asked to differentiate advanced from non-advanced adenomas<sup>319</sup>. This is exacerbated by applying diathermy to the tissue, where the thermal energy causes morphological distortion and risks 'up-staging' the section (anecdotal report from collaborating histopathologist). These limitations in the validation process make it difficult to fairly assess the accuracy of REIMS and optimise it as close to 100% accuracy as possible, particularly with comparisons such as LGD vs HGD in adenomas. This can be mitigated by using two pathologists to review sections and blinded repeat reviews (which were employed for the majority of the samples here), however, the innate limitations of histopathology are still likely to impact the more subtle analyses.

#### 6.4.3.3 Sampling selection bias

The processes by which colorectal tissues were sampled for research presents a selection bias which is evident when observing the histological subtypes of tissues collected. A priority when sampling tissue from a resected specimen is not to compromise the clinical diagnosis, which means that certain regions of the lesion cannot be dissected for research. For cancers, this is most importantly the invasive margins, where formal assessment is required to determine factors such as invasion depth or distance to resection margin, however, this is mitigated by the fact that these are often large lesions and therefore can be sampled from elsewhere. The issue becomes much more significant for this thesis when considering colorectal polyps, as both the size and the shape of the lesions impacts the ability to sample tissue for research. It is vitally important in a polyp that the mucosa/submucosa border is preserved for clinical diagnosis, as this is the region where an invasive cancer is diagnosed. In small polyps (which make up the majority, given that 81% are less than 10mm in diameter<sup>394</sup>) it is very challenging to macroscopically sample polyp mucosa *ex vivo* whilst ensuring that the submucosal layer remains intact, a fact exacerbated by polyp tissue naturally contracting following excision. As such, histopathologists are very reluctant to sample such small polyps and this was reflected by the mean polyp size in this chapter of 33mm. This is worsened in flat sessile lesions, where the distance between the luminal aspect and submucosa can be millimetres and consequently very few were sampled in this dataset. Furthermore, a colorectal polyp is categorised as having high-grade dysplasia if a single focus is present anywhere in the lesion (as per the Vienna criteria<sup>191</sup>), meaning that histopathologists are keen to cut sections through a large majority of a polyp to assess for this. The lack of small polyps sampled for the *ex vivo* REIMS analysis has had a marked impact on the tissue subtypes collected in addition to how the findings can be contextualized to a clinical setting. No hyperplastic polyps were included in this dataset due to their tendency to be smaller than adenomas (67% are less than 5mm in diameter), which is concerning given their high prevalence at 27% of all polyps<sup>394</sup>. Therefore, it is unclear if hyperplastic polyps have a lipidomic signature unique from normal mucosa and whether REIMS would be capable of supporting clinical decision making based on tissue recognition from this dataset. Similarly, this chapter risk-stratified adenomas by the presence of HGD, however the British Society of Gastroenterology also risk-stratify them based on a combination of size and subtype; where an adenoma greater than 9mm in diameter is considered an advanced lesion, as is a serrated lesion with dysplasia over 9mm<sup>12</sup>. Due to the relative lack of small adenomas in the

sample set (for example, the smallest serrated lesion was 32mm diameter), it is unclear if the accuracy of REIMS in recognizing these tissues is preserved when analysing non-advanced lesions.

The selection bias that is evident in this dataset from the sampling methodology is difficult to overcome considering the strict and appropriate requirements to protect the clinical diagnostics. It was not possible to use excess tissue after the formal histopathological diagnosis was made as by that point, it had been formalin-fixed, and xylene had been used to remove the paraffin (and the lipid metabolites with it). One could argue that synchronous diminutive polyps in patients who have undergone a surgical resection for a CRC could be sampled for research whole (considering their formal diagnosis would not impact patient management in the context of having a cancer), however the histopathology department collaborating with this work required formal diagnosis of all lesions. Another solution is training REIMS spectral databases on analyses of polyps *in vivo* or immediately *ex vivo* on the surgical specimen. This would not require any dissection of the lesion for research, however, histopathological validation of the burns may become difficult and it would require an operational instrument prepared at all times in case a specimen was retrieved clinically. Future work on REIMS analysis of polyps requires these obstacles to be overcome in order to develop a sample set most reflective of clinical practice and consequently, be able to answer the pertinent clinical questions to allow improved clinical decision making in real-time.

A further issue with tissue selection in this dataset was that it was cross-sectional. The most valuable insights would be sought from longitudinally sampling a single patient as their tissue transforms from normal, through the grades of dysplastic adenoma to tumour. This would be able to reveal the lipidomic signatures associated with colorectal carcinogenesis whilst removing the variation between patients. Unfortunately, a longitudinal sampling methodology is not feasible for this work given the clinical requirements to remove lesions as soon as they are identified, and an animal model may be the only option.

#### 6.4.3.4 Intra-lesion heterogeneity

When a lesion encountered clinically is analysed using REIMS, this analysis will occur at a specific location over a volume of 1-2mm<sup>3</sup>; however, the lipid composition of the cells in that region may not be representative of the lesion as a whole. Intra-tumour heterogeneity has been well

documented in CRC, referring to spatial variation in cancer cells due to factors such as clonal populations, microenvironmental influences and epigenetic plasticity<sup>395,396</sup>. This variation can have a dramatic influence on the clinical phenotype of cancer cells, impacting factors such as sensitivity to chemotherapy and rate of metastasis<sup>397</sup>. In fact, the cancer stem cell theory supports this by describing how a small proportion of the total cells with advantageous cellular functions are believed to be the cause of proliferation and metastasis<sup>398,399</sup>. As a consequence, using REIMS analysis of a limited tumour region to make predictions based on the lipidomic data relevant only to that exact location creates a source of inaccuracy. For example, there may be a single clonal population within a tumour which has a predisposition to metastasise to lymph nodes and this population may have a unique lipidomic signature that is associated with this. However, it is most likely that REIMS does not sample this exact clonal population (due to the large numbers that are present) and therefore, is unable to make the association between the unique lipidomic profile and the clinically relevant pathological status. The same phenomenon has been described using a genomic approach, where the mutational burden in a single biopsy of a tumour cannot be considered representative of the whole lesion and therefore tumour evolution cannot be fully understood based on this limited information<sup>400</sup>. MS imaging techniques such as DESI and MALDI have the potential to spatially resolve metabolites to explore intra-tumour heterogeneity<sup>381,401</sup> however, these are not suitable tools for intraoperative translation.

A similar issue arises when exploring heterogeneity within polyps, where there can be single focusses of HGD or invasive cancer, but the LGD portion has been sampled. This appeared to be an issue in this dataset, where the diagnostic accuracy of REIMS dramatically fell when predicting the histological subtype for the whole polyp rather than simply at the exact location analysed. Field effects refer to biological changes that can extend beyond the physical borders of a lesion and into the adjacent 'normal' mucosa, having been described in colorectal cancer for genetic abnormalities (such as methylation status, copy number variation and loss of heterozygosity) and differential gene expression<sup>402-404</sup>. This phenomenon appears to impact the metabolome of these surrounding tissues, where the abundance of both lipid and non-lipid metabolites is impacted by field effects as measured using NMR spectroscopy and MALDI<sup>405,406</sup>. Given this, it may be that there is a lipidomic signature for tumour-adjacent normal, which is distinct to truly normal mucosa. Similarly, there may be a lipidomic signature for LGD mucosa immediately adjacent to HGD, which is distinct from when there is only LGD in the polyp. It is beyond the scope of this thesis to explore if this is the case due to the stringent sampling and analytical documentation that

would be required to reliably conduct this experiment, in addition to the fact that the immediate field of lesions was rarely sampled due to concerns that one may be dissecting the invasive edge.

#### 6.4.3.5 Minimum composition of tumour and adenoma for inclusion of REIMS spectra

For inclusion in the modelling presented here, the validation section of tumour and adenoma spectra required at least a 15% composition of the index tissue. As revealed in section 5.2.3.1, this threshold increases the diagnostic accuracy of REIMS by reducing the misclassification of tumour as normal, however this would not be suitable for clinical use (given the oncological outcomes associated with this involved margin). REIMS is still in development and the use of this threshold has allowed the lipidomic features of colorectal tissue types to be identified *ex vivo*, the sensitivity of which would have been threatened if spectra were overwhelmingly of a different tissue type to that which it is annotated with. However, clinical use for margin detection would require reconsideration of this threshold in order to increase the likelihood of detecting involved margins. The potential impact of this on *in vivo* accuracy and how definitions of involved tumour margin are relevant to REIMS are explored later in chapter 7.

#### 6.4.3.6 Over-fitting of data

The spectral dataset presented in this chapter contained 1013 observations (the spectra) of 4000 variables (the bins within each spectrum), which therefore raises the possibility that the predictive models were over-fit and that they used data-specific information to make classifications<sup>160,407</sup>. It is challenging to evaluate the degree to which models are over-fit, as there is no single way to assess this, with LOPO CV, CV plots and  $Q^2$  metrics used here. LOPO CV was the principal method applied, which would show a drop in diagnostic accuracy if data is over-fit and reassuringly, this did not appear to be the case for the differentiation of tumour, adenoma and normal tissue. When OPLS-DA models were built and  $Q^2$  was calculated (such as in the risk-stratification of CRCs), a minimal number of components were used to build the models as a mitigation strategy (most commonly 1 orthogonal and 2 X-Y) and the CV scores plots were created. Using additional numbers of components would have increased  $R^2$  (and the immediate appearance of accuracy), however this would not necessarily be accompanied by an increase in  $Q^2$  (as shown with the EMVI classification, where an additional X-Y component decreased the  $Q^2$  from 0.285 to 0.281). I

therefore have cautious confidence that the results presented here are not over-fit and that the diagnostic accuracies are representative of the ability of REIMS.

The most appropriate method for assessing true ability of REIMS in tissue recognition is to apply it to a completely independent dataset, where the predictive model can be fixed in advance and the diagnostic accuracy assessed prospectively<sup>408</sup>. This approach would also help assess the external validity of the results. The colorectal tissues included in this chapter were all collected from three London hospitals and from a patient cohort where the majority were Caucasian. Analysing an external validation dataset would help explore whether the findings presented here are specific or somehow associated with the selected population and whether they can be applied across geographical regions and ethnicities. It was beyond the scope of this thesis to perform this work; however, it is vitally important in the development of the technology.

#### *6.4.3.7 The impact of tissue storage and handling*

The metabolic processes in cells do not suddenly halt when tissues are resected from a patient and in fact, are likely to change due to the shift towards anaerobic metabolism and a reduction in ATP availability. As a consequence, the metabolic profile detected by REIMS may markedly change with an increased warm ischaemia time. A previous study revealed that over the first two hours following resection, the abundance of a wide range of metabolite types significantly changes, however this was largely focused on metabolites with smaller masses (such as lactate, glycine, myoinositol and glutamine)<sup>409</sup>. The study did show that the abundance of PChs was unchanged after 90 minutes, implying that the complex (and particularly structural) lipids studied in these analyses may be better conserved during ischaemia. It was not possible to explore the impact of warm ischaemia time on REIMS spectra given the lack of documentation regarding this for the samples collected. It is also difficult to estimate the duration of time between first ischaemic insult and freezing, given that during segmental colonic resections, the vascular tree is ligated prior to plane dissection (which may require a further hour to be completed). Once the specimen has been resected, the journey to collect it, attend the pathology department, sample it and then transport the research specimens to the laboratory can often take in the region of 30 minutes. In future REIMS research, it would be ideal to sample the surgical specimen immediately *ex vivo* and snap freeze it with liquid nitrogen, reducing this potential impact, however this

requires the presence of a trained pathology technician. It is an important consideration that predictive models are being built on these pieces of tissue which have potentially undergone a prolonged ischaemic time, with an aim to translate the findings *in vivo* into living tissues. The impact of delayed freezing on complex lipid abundance in metabolomic studies needs to be addressed in future work.

#### 6.4.3.8 Incomplete coverage of relevant metabolites

The experimental design of this chapter was such that compromises had to be made regarding the potential metabolites that were analysed and used for tissue recognition, in order to have a system which can be applied to real-time *in vivo* sampling. This work focusses on the complex lipids, where a large proportion are prone to deprotonation and are therefore readily seen in negative ion mode, however, this is not the case for lipids such as TGs. TGs show a much lower signal in negative ion mode due to their preponderance to form  $[M+NH_4]^+$  ions<sup>410</sup> and therefore lipids with these electrochemical properties are likely to be under-sampled. Given the need for continuous acquisition when sampling *in vivo*, one charge mode had to be selected and the negative ions were chosen as they generate a higher TIC. The 600-1000m/z threshold was used to improve tissue recognition, however it excludes many smaller lipid and non-lipid metabolites which are intrinsically related to cellular metabolism, carcinogenesis and signalling; including arachidonic acid, Krebs's cycle products, amino acids and prostaglandins<sup>411,412</sup>. The ability to gather data using other '-omics' approaches such as genomics, transcriptomics and proteomics would certainly assist when defining the features of colorectal carcinogenesis<sup>104,413-416</sup>, however, it is not possible to incorporate them into a real-time REIMS workflow. Whilst MS can be used for proteomics, the use of energy devices at the point of sampling causes thermal denaturing of proteins and therefore they cannot be sampled. It is not possible to estimate the impact of the lost biological data by sampling a relatively narrow portion of the spectrum, however many of these limitations were an unavoidable consequence of using a clinically translatable REIMS technology. Future work should focus on complementary analyses of these other biological components to integrate the findings with those of the complex lipids found by REIMS. This should also assess the drivers of the metabolic changes being demonstrated, as this thesis has been unable to explore how genomic, transcriptomic and proteomic factors are responsible for the differences in lipid metabolism.

With regards to the complex lipid metabolites in the 600-1000m/z range, it was not possible to identify the structure of all metabolites within bins found to differentiate tissue types. Due to the lack of a chromatography step, bins in REIMS spectra regularly contain many metabolites with a similar or exactly the same m/z, but very different chemical structures and electrochemical properties (such as polarity). These mixtures cannot always be determined using techniques such as identification of characteristic fragments due to some lipids lacking these (such as PAs) and the presence of structural isomers. The metabolites identified did account for 29% of the signal above background, which is a significant proportion considering attempts to identify lipids was focused only on those that differentiated the models. However, it is likely that there are additional patterns in the relationship between lipid metabolite and tissue phenotype that could not be described here due to a lack of complete identification. Future work may consider using a complementary technique such as LC-MS/MS to better identify the composition of mixtures.

## 6.5 Chapter conclusion

This chapter has generated, curated, analysed and explored a substantial high-quality dataset of REIMS analysis of colorectal tissues, constituting by far the largest example of its kind. It has demonstrated that there are unique lipid metabolic fingerprints that exist for colorectal tissues, which can be used by REIMS to accurately differentiate tumour, adenoma and normal mucosa; in addition to risk-stratifying adenomas. This has two principal benefits. First, it is a strength of the technique that it has been possible to start to interrogate the biological differences in the lipid metabolites between groups of interest, with novel descriptions of how lipid classes and saturation status of fatty acid chains in GPLs are associated with colorectal carcinogenesis.

A further benefit is that the spectral reference database and multivariate models constructed as part of this chapter can be used as the basis for *in vivo* tissue characterisation in real-time. I am confident that the accomplishments demonstrated here and the stringent methodological processes that were used will give the best possible chances of success during the next phase of study. Whilst the diagnostic accuracy of REIMS has been demonstrated to be high in a laboratory setting, one of the main values of the technology is translating it into clinical practice where the logistics of its use and 'real world' accuracies can be assessed. Chapter 7 will explore the first-in-

man use of MS-coupled TAMIS as an exemplar case of where real-time colorectal tissue recognition by REIMS has the potential to support clinical decision making during oncologic surgery.

## Chapter 7 – WP3: *In vivo* application of REIMS during TAMIS

### 7.1 Chapter Rationale, Aims and Objectives

This chapter is the final instalment in a journey from understanding what quality is for REIMS spectra and how it can be impacted (chapter 5), how an *ex vivo* reference database of REIMS spectra can be created and appraised to assess factors such as colorectal tissue recognition accuracy (chapter 6) and now finally; to explore how the REIMS technology can be translated from the laboratory into a clinical space for real-time colorectal tissue recognition *in vivo*.

In order to assess this clinical translation, an exemplar case study needed to be selected, where there was an unmet need for real-time tissue recognition during colorectal oncologic surgery. After discussion between the clinical members of the research group, TAMIS for advanced rectal polyps and early rectal cancers was selected. The rationale for this is that when local excision is technically feasible, oncologic outcome at TAMIS is directly related to resection of the lesion *en bloc*, with no cancer-involved margins<sup>417</sup>. However, neoplastic disease can be microscopic, such that the surgeon is unable to identify it through visual or haptic feedback, leading to a 16% positive margin rate<sup>418</sup>. It is therefore straightforward to appreciate how the ability to differentiate between normal, adenoma and tumour tissue in real-time during TAMIS has the potential to improve patient outcomes. Furthermore, TAMIS has a rate of intra-peritoneal perforation of up to 10%<sup>419</sup>, with no tools currently able to guide the surgeon in the correct and safe plane of dissection.

The aim of this chapter is to determine the feasibility of coupling REIMS to TAMIS instruments *in vivo* during human colorectal surgery. This will be addressed through the following objectives:

1. To optimise logistical, technical and analytical factors for MS-TAMIS in the operating theatre
2. To appraise the spectra generated during MS-TAMIS
3. To assess the accuracy of REIMS in differentiating colorectal tumour, adenoma and normal tissue during TAMIS dissection
4. To assess the ability of REIMS in differentiating bowel wall layers

## 7.2 Methods

This chapter is a feasibility study of the *in vivo* application of REIMS coupled to TAMIS. Full details of the methodologies used in this chapter regarding patient recruitment, MS analysis and statistical processes can be found in chapter 4; with specific features to this study stated below.

### 7.2.1 Patient recruitment

Between August 2018 and November 2020, all patients with advanced rectal polyps or early rectal cancer at St Mary's or Charing Cross hospitals were reviewed in the multidisciplinary team meeting. If they were subsequently scheduled for a TAMIS, the patient was recruited for this project.

### 7.2.2 MS analysis and specifications

As described in detail in chapter 4, the specifications of the MS were designed to remain as unchanged as possible between the *ex vivo* components of the work and this *in vivo* translation. At the start of the case, the PTFE aspiration tubing was taped alongside the primary dissection instrument in a sterile fashion as shown in figure 7.1. Surgical aerosols were continually aspirated throughout the TAMIS, with spectral data collected whenever the monopolar diathermy was applied (most commonly at 20-25W and at the discretion of the surgeon). In addition to the usual application of diathermy for excision, the surgeon performed diagnostic analyses of the luminal component of the lesion for 1s if its diameter was over 20mm.



Figure 7.1 – PTFE tubing taped alongside the TAMIS dissection instrument to allow aerosol aspiration intraoperatively.

### 7.2.3 Statistical analyses

An LDA model was created using a subset of the reference spectral database in chapter 6 to include only tissues that were sampled from the rectum (considering this was the only tissue type which could be encountered during TAMIS). This model was uploaded to the AMX Recognition software in order to appraise the accuracy of REIMS for tissue recognition *in vivo*. Due to the accuracy not yet being fully assessed, no live tissue feedback data was given to the surgeon during the case.

## 7.3 Results

Seven patients were recruited for this study, with five suffering from an early rectal cancer and two from advanced adenomas. Six patients successfully underwent MS-TAMIS, representing the first-in-man use. The focus of each case evolved throughout the data collection period, with the initial phases largely concentrating on optimisation and then later, tissue recognition. The video recording for patient six (JLA 635) stopped prematurely due to the storage capacity of the Storz system reaching maximum capacity and therefore no tissue recognition analyses could be performed. Table 7.1 describes the patient demographics, lesion characteristics, analytical notes and focus of data analysis for the seven patients.

Study ID	Age/Gender	Lesion Type <sup>a</sup>	Lesion Size	Lesion Location <sup>b</sup>	Case Outcome	Focus of Case
JLA 572	63/M	T2 NO cancer	3cm	10cm	R0 resection with no recurrence at follow-up	Optimisation
JLA 575	68/M	T1 NO cancer	3cm	11cm	R1 resection (<1mm deep margin, cancer at lateral margin). Subsequent anterior resection showed no cancer	Optimisation
JLA 581	67/F	Serrated adenoma with HGD	5.1cm	3cm	LGD portion included in lateral margin but no polyp recurrence at 1 year	Optimisation
JLA 594	64/M	T2 NO cancer	1.2cm	5cm	R1 resection (0.8mm deep margin) with subsequent biopsy and MRI negative	Optimisation
JLA 623	68/M	T2 NO cancer	1.5cm	5cm	R1 resection (<1mm deep margin, cancer at distal margin). No recurrence following neoadjuvant chemoradiation	Tissue recognition
JLA 635	65/F	TVA with LGD	2.8cm	4cm	Complete excision with no recurrence at follow-up.	Nil due to video recording failure
JLA 717	76/M	T2 NO cancer	3.8cm	Rectosigmoid junction	TAMIS abandoned due to surgical challenges with lesion location	Nil

Table 7.1 – the demographics, lesion characteristics and case outcome for the seven recruited patients scheduled to undergo TAMIS.

<sup>a</sup>as per TNM v7; <sup>b</sup>distance from the anal verge

### 7.3.1 LDA model for rectal tissue recognition

A subset of the reference spectral database for rectal samples was used to power the *in vivo* tissue recognition software containing 345 spectra from 48 patients (114 tumour, 99 adenoma, 132 normal). Considering that adenoma and tumour tissues are managed the same during TAMIS (they require excision), models were built to assess its ability to differentiate diseased (tumour or adenoma) from normal rectal mucosa (figure 7.2.A). An LDA model on LOPO-CV demonstrated an 87.3% accuracy, 84.5% sensitivity, 91.7% specificity, 94.2% PPV and 78.6% NPV for disease (figure

7.2.B); lower than the 93.5% accuracy reported for all colorectal analyses in section 6.3.1.2.

Despite this, this model was used for the *in vivo* rectal tissue recognition.

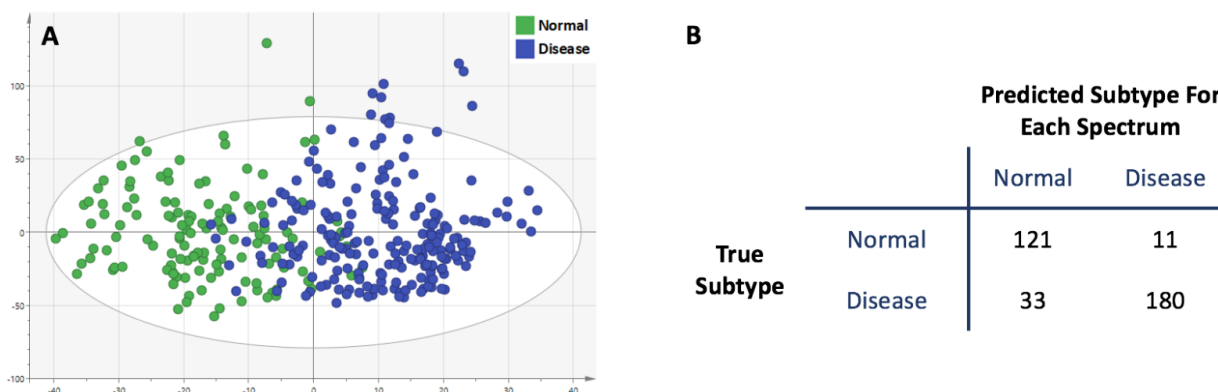


Figure 7.2 – OPLS-DA plot with 1 orthogonal and 2 X-Y components, demonstrating an  $R^2X$  of 0.424 and  $Q^2$  of 0.538 differentiating spectra from rectal normal, adenoma and tumour tissues (A) and a confusion matrix of the diagnostic accuracy on LOPO CV from an LDA model (B).

### 7.3.2 Optimising MS-TAMIS

#### 7.3.2.1 Signal enhancement

There were many factors identified which had the potential to reduce the signal detected during MS-TAMIS, which was considered one of the greatest risks to the successful implementation of the technology. These included the need for a high extractor fan speed to increase aerosol transfer speeds, variable distance between the analysis site and end of the aspiration tube as the instrument may be moving during sampling, use of tubing connectors which reduce the internal diameter, short time of diathermy application and long total length of aspiration tube (as demonstrated in section 5.3.3.3). Representative spectra were plotted comparing the *ex vivo* analysis of normal mucosa (patient JLA 335 from chapter 6) and *in vivo* analysis during the second MS-TAMIS case (patient JLA 575), which is shown in figure 7.3. In addition, technical metrics for the spectra were calculated and presented in table 7.2. In order to make these comparable, the *in vivo* spectra show the mean intensity from four burns over three scans each; all taken from the beginning of the case when the dissection margins are being marked and only normal mucosa is being analysed.

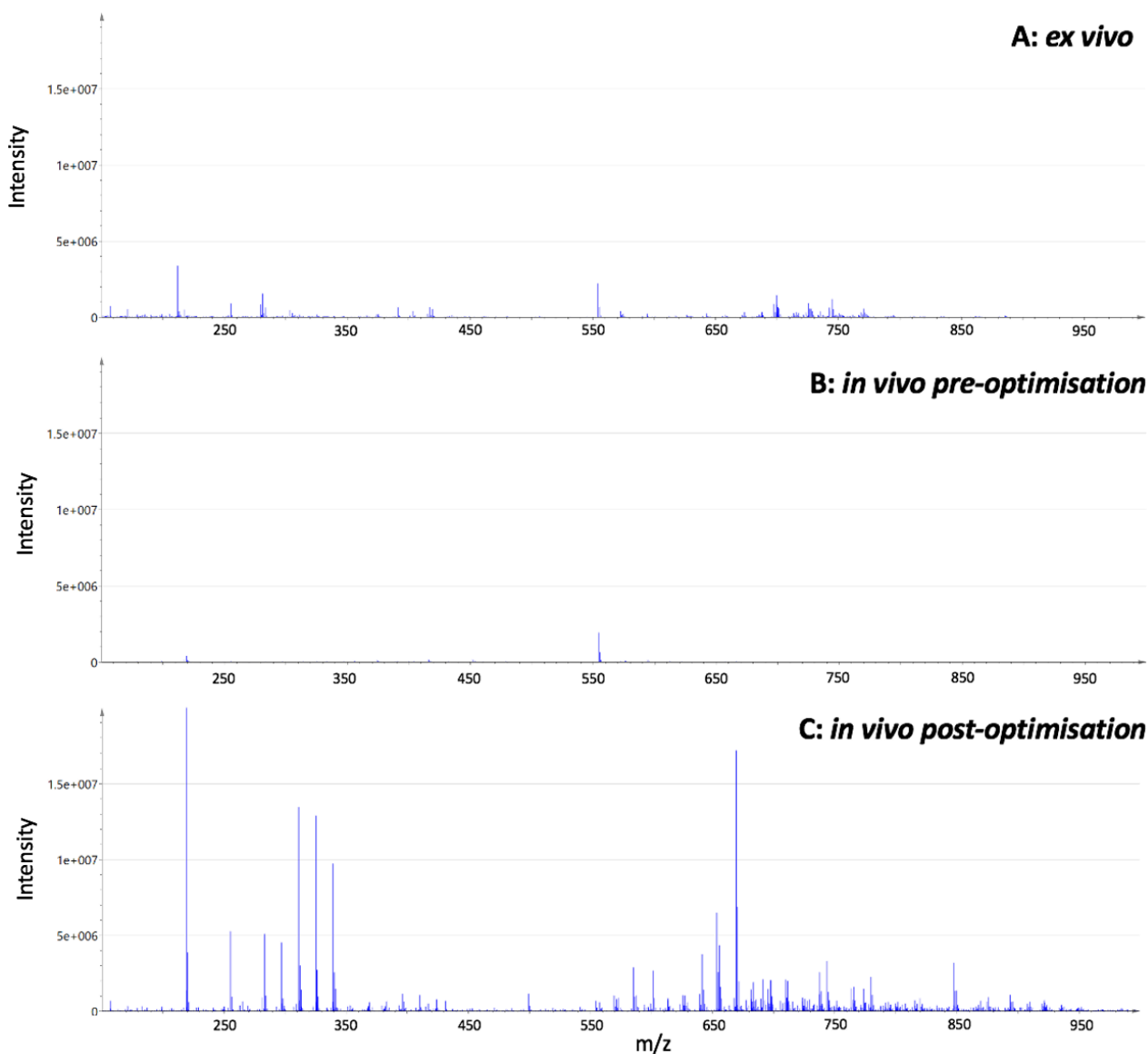


Figure 7.3 – representative spectra over the 150-1000m/z range for the analysis of normal mucosa *ex vivo* (A), *in vivo* prior to the optimisation of the analytical system (B) and *in vivo* collection following optimisation (C). All spectra have the same y axis scale to allow comparison.

Time Sampled	150-1000m/z		600-1000m/z	
	Signal ( $\times 10^7$ )	Signal:noise ( $\times 10^3$ )	Signal ( $\times 10^7$ )	Signal:noise ( $\times 10^3$ )
<i>ex vivo</i>	8.0	33.9	3.6	28.4
Early <i>in vivo</i>	2.2	6.7	0.79	7.6
Late <i>in vivo</i>	41	55.7	23	52.2

Table 7.2 – Technical factors for the representative spectra from analysis of normal mucosa *ex vivo*, the second MS-TAMIS case and the penultimate one.

It is evident that the initial MS-TAMIS analyses had poor signal compared to *ex vivo* analysis over the whole mass range (73% drop), with a simultaneous 80% fall in signal:noise ratio. Similar findings were evident when limiting the mass range to 600-1000m/z, over which the tissue recognition functions were due to be applied. Visually appraising the spectra presented (figure 7.3), where the scales are fixed to aid comparison, there was almost no GPL or TG signal visible.

Once the drop in signal during MS-TAMIS had been recognised, four interventions were made to attempt improve it. First, there appeared to be an optimum position for the aspiration tube taped onto the TAMIS dissector. Whilst the distal opening needed to be as close to the main electrode as possible, the first priority was that it would not obscure the view of the surgeon (as demonstrated in figure 7.4.B). However, that resulted in it often being positioned at the 5-6 O'clock location which is also where the lesion is placed (for technical reasons); resulting in a tendency for adjacent mucosa to occlude the tube's opening (reducing aerosol sampling) and aspirating contamination such as blood (figure 7.4.A). Once this was identified, the tubing was firmly secured to the upper and lateral most part of the dissector for the remaining cases, which resolved these issues (figure 7.4.C).



Figure 7.4 – still photographs from MS-TAMIS cases showing the impact of tubing position on the dissector – with a tubing that is prone to aspirate blood from the dissection (A), obscuring the view of the surgeon (B) and optimally positioned (C).

It was also identified that a potential source of aerosol limitation was both the length of the aspiration tubing and the types of connectors used between tubing segments. The resistance of a gas through a tube is inversely proportional to the 4<sup>th</sup> power of the diameter and proportional to the length. For the initial cases, the connectors used to adjoin segments of aspiration tubing were placed inside the tube and were dramatically reducing the internal diameter, from 3mm to

approximately 1.5mm (figure 7.5). This theoretically increased the aerosol resistance by a factor of 16 over two short segments. The second intervention was to address this, where connectors were used which had an internal diameter of 2.5mm; which should have had a much-reduced impact on the aerosol transfer rate (however, this was not directly measured considering the *in vivo* setting). The third intervention was made to the length of the aspiration tubing. The tubing segments come in 1.5m length and given the positioning of the MS and patient in the operating theatre, a length of at least 3.5m tended to be required. For the first four MS-TAMIS cases, three tubing segments were used in their entirety even though this resulted in redundant tubing. Section 5.3.3.3 demonstrates that whilst using a longer aspiration tube does not appear to impact signal:noise ratio, it can impact TIC. To address this, once the patient positioning had been completed in the final three MS-TAMIS cases, the minimum feasible tubing length was determined, and the tubing cut as a result (with an approximate reduction in length of 50-100cm).



Figure 7.5 – The internal connector used to adjoin two lengths of PTFE tubing, reducing the internal diameter from 3mm to approximately 1.5mm

The final intervention was in controlling the speed of the exhaust fan connected to the Venturi interface. The RapidVac™ system has five fan speeds and this was routinely placed on the highest setting to increase the transfer speed of the aerosol from the point of analysis to the MS. The consequence of this is that a smaller proportion of the aerosol enters the perpendicular inlet capillary. For the final three MS-TAMIS cases, the fan speed was reduced to medium (the 3<sup>rd</sup> setting) aiming to increase the aerosol volume reaching the MS, with no clear reduction in transfer time noted (this was not formally measured).

The impact of the four interventions to increase the signal intensity were evident when comparing the spectra from before and after the changes were made. Table 7.2 demonstrates that over the whole  $m/z$  range, the signal increased by a factor of 18.6 and was greater than that seen on average *ex vivo*, with concomitant increase in the signal:noise ratio to  $56 \times 10^3$ . Similar findings were also apparent when focusing only on the lipid region of 600-1000 $m/z$ , which is used by the chemometric functions for tissue recognition. These differences are reflected in the raw data as seen in figure 7.3, where a much greater biological richness appears to have been sampled in the post-optimisation spectra. These optimisation steps to increase the signal intensity as described over the first MS-TAMIS cases generated data that was deemed sufficient to allow exploratory statistical analyses to be conducted, as presented below.

#### *7.3.2.2 Avoiding contamination of aspiration tube*

The surgical field during TAMIS contains many different potential contaminants, including mucus, faecal matter, saline wash and the most prevalent, blood. Droplets of contamination were found to regularly enter the aspiration tubing alongside the instrument due to the constant negative pressure, which impacted the ability to transfer the surgical aerosol but also risked the integrity of the MS. Having droplets of contamination such as blood enter the REIMS source appeared to cause spikes in background which interfere with measurement of the biological ions present, cause contamination to the internal components such as the StepWave and over time, reduce the TOF vacuum.

This issue was combatted using two techniques. First, if a droplet was identified in the tubing, that section was quickly replaced, however this did mean that intraoperative data could not be collected for those 5-10 seconds. A second approach was to manually kink the aspiration tube when the surgeon was not dissecting and there was contamination present, causing a loss of the negative pressure at the tube opening and therefore decreasing unwanted aspiration. This was an effective technique however did require constant attention from the MS operator and does not resolve the issue of contamination being aspirated whilst also collecting biologically relevant surgical aerosol. As such these two approaches were used in combination for the final three MS-TAMIS cases.

### 7.3.3 Tissue recognition during MS-TAMIS

For the 5<sup>th</sup> MS-TAMIS case, it was possible to co-register the raw mass spectra generated at each burn site with the histological diagnosis of the tissue being analysed. REIMS was able to detect the rectal wall layer being dissected based on the relative abundance of GPLs and TGs sampled, considering that these are of greatest abundance in the mucosa and submucosa respectively (figure 7.6). When diathermy was applied to the muscularis layer, there was an almost complete absence of the lipid signal in the 600-1000m/z range, with a marked increase in signal background. This was such that there was no characteristic spectrum for the muscularis and therefore a recognition system could not be created for this wall layer.

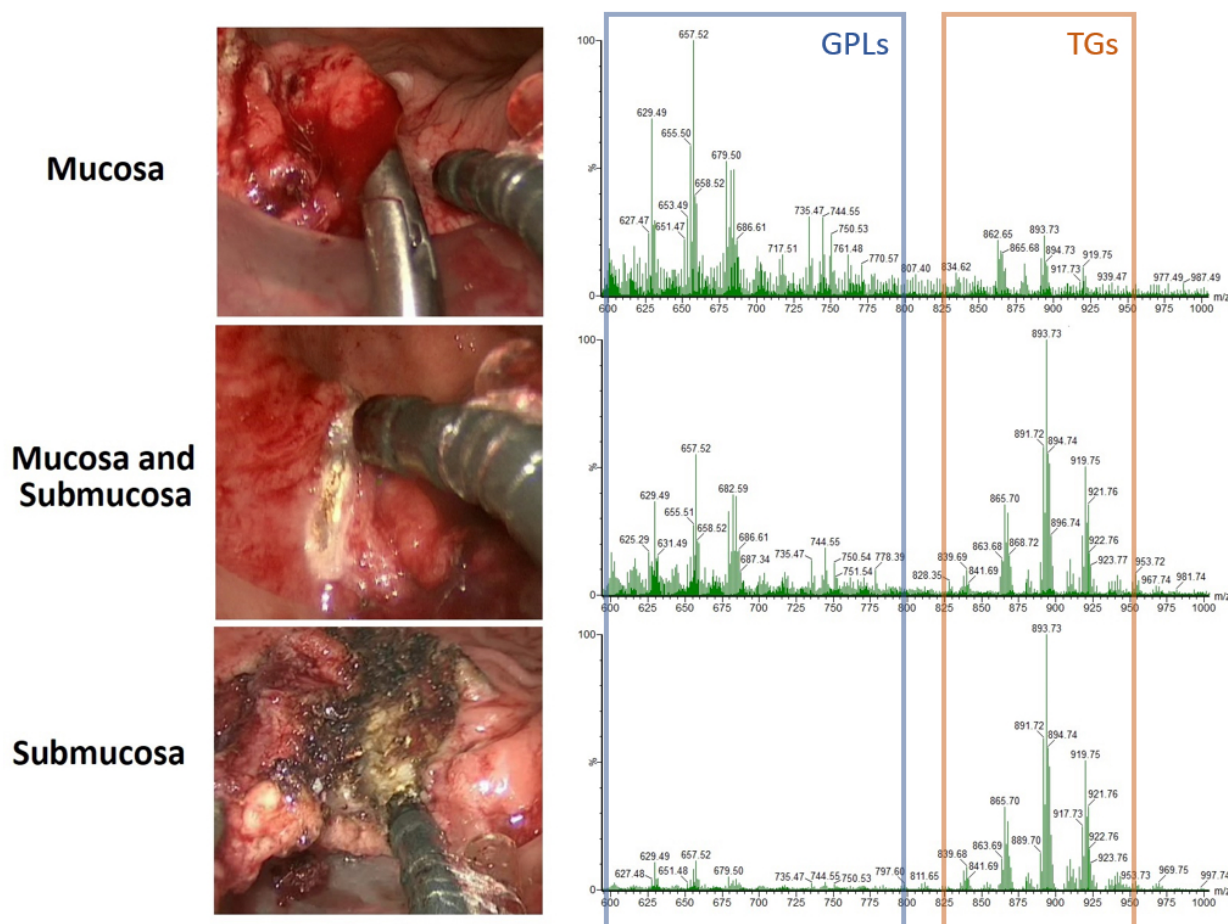


Figure 7.6 – the raw spectra collected *in vivo* during MS-TAMIS from rectal mucosa, submucosa and a mixture of the two. The ratio between the glycerophospholipids (GPLs, blue box) and triglycerides (TG, orange box) can be used to differentiate the layers. Reused with permission from Mason *et al.*<sup>420</sup>

The ability of REIMS to differentiate disease (carcinoma or adenoma) from normal rectal mucosa was assessed across the 100 discrete burns in the 5<sup>th</sup> MS-TAMIS case (patient JLA623), using the LDA model generated in section 7.3.1. The confusion matrix can be seen in figure 7.7, demonstrating an 83.0% accuracy, 95.7% sensitivity, 79.2% specificity, 57.9% PPV and 98.4% NPV for disease. The first 3 applications of diathermy were to the luminal component of the lesion, with all three being recognised as disease. The low false negative rate was such that REIMS was able to detect both the deep and lateral cancer-involved margins, which were not visually perceptible to the surgeon. The main source of misclassifications were false positives, where normal mucosa was predicted to be disease. These misclassifications were focused on the proximal margin where a mixture of mucosa and submucosa were being analysed, with significant distance from the lesion. Considering that these data were not fed back to the surgeon in real-time, it is not possible to assess how the REIMS predictions would have impacted the surgical procedure or whether they could have reduced the R1 resection rate.

		Predicted Subtype	
		Normal	Disease
True Subtype	Normal	61	16
	Disease	1	22

Figure 7.7 – confusion matrix of ability of REIMS to differentiate rectal disease from normal mucosa during MS-TAMIS in patient JLA 623.

#### 7.4 Discussion

This chapter explores the translation of the REIMS technology into the operating theatre, where it was coupled with monopolar diathermy for a case series describing first-in-man MS-TAMIS. The novel nature of this work was such a large focus was optimisation of the technique to improve critical factors such as signal intensity, however; it was also possible to collect data of sufficient quality for basic tissue recognition to be performed, showing early promise of REIMS for MS-TAMIS.

#### 7.4.1 Optimisation of REIMS for MS-TAMIS

The optimisation phase of this work was conducted in the operating theatre during *in vivo* sampling, which has many advantages and disadvantages over a laboratory-based process. Following the first two cases, it was quickly realised that a significant challenge to the successful translation was the ability to collect data with sufficiently high signal and signal:noise ratio; with the *ex vivo* collection protocols requiring some adaptation for translation to the theatre. Achieving these spectral parameters is necessary to ensure the biological variation in the tissue is being sampled and analysed adequately, reducing the risk of misclassifications when using recognition software based on a high-quality spectral database collected *ex vivo* (as shown in chapter 5). Whilst the four interventions designed to increase the signal intensity and signal:noise ratio could be considered a success given their dramatic increases; it was not possible to determine the impact of each of these individually given the methodological process used. This could have been achieved in a laboratory setting, where standardised analyses could be conducted on an animal model of rectal disease, however, the scarcity of human TAMIS cases were such that an *in vivo* optimisation process was pragmatically chosen. It is likely that specific interventions had a much greater impact on the signal intensity and future laboratory analyses should be conducted to validate these findings and assess for negative impacts of these changes. For example, the reduction in extractor fan speed at the Venturi is likely to have slowed the aerosol flow rate; however, the exact impact on the timing cannot be defined here and it should be confirmed that this would not cause sufficient delays to impact the real-time nature of the sampling. Whilst the changes described here have been incorporated into the standard operating procedures for future analyses, the learning-curve for how to optimise the system during this novel application of the technology has not plateaued and is an ongoing process. Use of gas/liquid separators may be useful to remove droplets from the aspiration tubing prior to the Venturi interface and will be assessed in future cases. The PTFE aspiration tubing itself is prone to inadvertent kinking and can be compressed by staff members standing on it. A tubing material which is resistant to these would be optimal. I anticipate that there will continue to be refinement to the materials and analytical processes used as our understanding deepens.

#### 7.4.2 Challenges translating REIMS technology *in vivo*

It was apparent from the work in this chapter that there are many obstacles to overcome when translating a laboratory-grade piece of analytical equipment into the complex and ever-changing clinical setting. Some of these difficulties could be overcome with design changes to the MS itself, whereas others will be more challenging to address. Successful translation of a diagnostic technology requires clinical staff with little training to set-up and control it, which means that large portions of the calibration and operation would require automation in future systems (including a problem-solving process). Currently, skilled and attentive technicians are required to ensure the machine is functioning as expected throughout a clinical case, using delicate and cumbersome equipment at the interface such as syringe pumps. There were many occasions during this case series where active troubleshooting was required, such as to correct calibration failures by excluding low mass peaks, re-starting the electronics due to abnormal signal background or to resolve peak splitting by changing the attenuator. If clinical processes were transformed around the use of intraoperative REIMS, then a malfunctioning instrument would present a concern for the safe and effective delivery of patient care. Furthermore, the MS in its current form is large and its fan creates a significant amount of noise. This may be necessary given that this research is still in the discovery phase (with largely untargeted analyses), however in the future, it may be possible to manufacture small and unobtrusive MS instruments which are designed to target specific metabolic features without the need for high sensitivity or mass accuracy. This may not even use a TOF mass analyser, as many different MS designs have been presented for 'fieldable' instruments<sup>421</sup>. The design of future instruments will be integral to the acceptability by staff members, which has been an issue that was studied during the implementation of robotic-assisted surgery<sup>422</sup>. Barriers such as 'perceived ease of use and complexity' and 'perceived usefulness' were identified, which are also likely to apply to the translation of MS technologies; however, it was beyond the scope of this thesis to explore this.

#### 7.4.3 Clinical impact of MS-TAMIS

A further consideration with the intraoperative translation of REIMS is how it can be used to augment clinical decision-making to improve patient outcome. Once data collection had been optimised, it was possible to preliminarily assess its ability for real-time tissue recognition, where

meaningful data can be generated for both the bowel wall layer and the histological tissue subtype. Considering TAMIS has an intraperitoneal perforation rate of up to 10%<sup>419</sup> (which would most likely require repair with or without a diverting stoma), it would be ideal if a technology could give a perforation warning based on the layer of the bowel wall being dissected. This would allow the surgeon to inspect closely if perforation was a risk and prophylactically repair it if necessary. The muscularis layer would be the best candidate for this warning point as it has the most strength of the rectal wall and does not need to be dissected in adenomatous and the majority of T1 disease. Unfortunately, this muscle layer does not appear to have the lipid-rich phenotype of the mucosa and submucosa and therefore such a recognition system is not currently possible. The other clinical application is in margin detection, where adenomatous or cancerous tissue is being included in the dissection plane and therefore increases the risk of lesion recurrence<sup>423,424</sup>. MS-TAMIS showed an *in vivo* accuracy that was only slightly diminished in differentiating diseased and non-diseased rectal tissue compared to the *ex vivo* model and more promisingly, a NPV of 98%. The fact that two cancer involved margins were identified is an exciting finding because the surgeon was not able to recognise the margins macroscopically and real-time feedback at those points would have allowed additional tissue dissection to occur and potentially a reduced risk of an R1 resection. Such surgical precision does not exist with any other technique. This finding is complicated by the 16% false positive predictions of disease, where if implemented with the current accuracy characteristics; the recognition system may cause the surgeon to increase the dissection area unnecessarily on frequent occasions. It may be possible that the rectal-specific *ex vivo* spectral database underpinning the recognition software was underpowered and collecting more data would improve the *in vivo* accuracies. This is supported by assessing the impact of adding the most recent 10 patients to the model, which increased the accuracy by 5%. One of the benefits of using a machine learning approach is that this spectral dataset should only continue to improve in accuracy as it is exposed to more data. In addition, creating a margin-detection device for TAMIS is a challenge when considering what it means to have an R1 resection. The broadly accepted definition of an R1 resection is having microscopic tumour within 1mm of the cut margin<sup>425,426</sup>, which means for REIMS to be able to identify this as a positive margin, it would need to be able to do this by detecting the tumour field (which is histologically normal). This is quite a challenge as the spectral database upon which the recognition software is built has not collected data from such specific tissue, as explained in section 6.4.3.4.

The accuracy of MS-TAMIS for margin detection will need to be assessed in a much larger patient cohort following this proof-of-principle work, with particular focus on how the R1 definition impacts accuracy. Ultimately, clinical implementation would require a specific research study to demonstrate clinical benefit. An example would be a multicentred randomised controlled trial, where in one arm the surgeon is given real-time tissue feedback during MS-TAMIS (at which point they can make any clinical decisions they wish) and in the other arm, care is delivered as normal. The primary outcome should be the R1 resection rate, with secondary outcomes assessing the logistics of MS-TAMIS (including set-up time), staff acceptability and a cost-effectiveness analysis. Such an implementation study would be able to account for variability between instruments, surgeons and patients. It would also stimulate important discussions regarding how best to deal with scenarios such as tissue recognition from a contaminated surface and how exactly to change the dissection plane when a positive margin has been potentially identified. Such a study is likely to require a large number of participants, with a power calculation suggesting 199 are needed in each arm if  $\alpha = 0.05$ ,  $\beta = 0.8$  and the intervention is expected to reduce the incidence of R1 resection from 20% to 10%.

#### 7.4.4 Limitations of histological validation

In order to assess the accuracy of REIMS for tissue recognition during MS-TAMIS *in vivo*, it was necessary to co-register the raw spectra with the histological diagnosis of the tissue being analysed. This was done using high-definition videos however, the histological validation was only possible with reference to the formal report of the orientated specimen. Unfortunately, this could not give the granularity of an exact diagnosis at each analytical point. This meant that in the case of an involved deep margin, all burns at the margin were annotated as tumour, despite it being likely that some were in fact in normal tissue. It is unlikely that this had a marked impact on this dataset given the low rates of false negatives for disease, however this is a methodological challenge which will be present in subsequent analyses. Similarly, creating a model to differentiate adenoma from carcinoma *in vivo* will suffer from the same issue. One option is to take a distinct biopsy for validation whenever REIMS predicts an involved margin however this would interfere with the flow of a procedure, add time and the additional biopsies may cause bleeding.

## 7.5 Chapter conclusion

This chapter explores the first-in-man experience of translating the REIMS technology intraoperatively for TAMIS of advanced rectal adenomas and early cancers. The focus has largely been the optimisation of the methodological processes for this novel technique, which were successful in generating high quality and clinically meaningful preliminary data. Despite this, there is still much development that is required to combat challenges with the technology, analytical processes and in understanding the clinical application. The potential ability of MS-TAMIS for *in vivo* real-time tissue recognition has now been realised, with this proof-of-principle work providing a basis upon which the REIMS technology can continue to be developed both within and beyond colorectal diseases.

## Chapter 8 – Thesis conclusions and future work

### 8.1 Conclusions

The hypothesis of this thesis was that colorectal lipid metabolism and cellular lipid composition are associated with the phenotype of colorectal adenomas and carcinomas, and that this can be leveraged using REIMS for accurate real-time recognition of colorectal tissues. This was addressed across three primary data chapters with each laying a foundation of new knowledge upon which the subsequent ones were built.

This journey started by developing a better understanding of colorectal REIMS data, by systematically defining seven minimum thresholds of spectral quality and exploring the impact of technical and environmental factors. This was to provide a framework for determining which spectral characteristics were necessary for robust statistical analyses and therefore, to reduce the risk of misclassifications. Next, this was used to build a powerful, high-quality, clinically annotated and histologically validated spectral reference database from the *ex vivo* analysis of colorectal carcinoma, adenoma and normal tissues. The relative abundance of complex lipid metabolites was interrogated using a variety of chemometric functions to explore how this relates to tissue phenotype, both in the form of tissue recognition and lesion risk-stratification. The ‘white box’ nature of the REIMS technology was such that the metabolic differences could be more deeply defined on a molecular level, by describing the structural composition of lipids whose abundance differed between groups. Finally, the REIMS technology was deployed into the operating theatre using the exemplar case of TAMIS and coupling it to the monopolar diathermy. This first-in-man case series focused on the challenges and optimisation that were required when translating such a technology into a complex clinical space, whilst exploring the clinical utility that would come from real-time tissue recognition.

When considering the findings of the work, my first impression is amazement at the power of the metabolomic tissue profiling that can be achieved using REIMS. Unique lipid metabolic fingerprints could be defined in a matter of seconds, with a flexibility that allows deployment in any environment with a coupled energy device and with no sample preparation. It was certainly a challenge as a clinician with no chemistry background to develop an understanding of this

technique and in particular the raw data it generates and how this relates to the biochemistry on a molecular level. The work in chapter 5 exploring the characteristics of spectral data and how these can impact tissue recognition was vital for both my understanding of the topic but should also directly inform the future research of both ours and wider groups. My approach to systematically defining spectral quality has addressed the need for a method of post-sampling quality control for REIMS that is objective and can be automatically applied prospectively, increasing the likelihood of statistical analyses having the necessary power to elucidate biological differences of interest. No such pipeline has yet to be described in the literature.

Chapter 6 builds a strong case that the hypothesis of this thesis can be confirmed to be true, with a large volume of evidence directly linking cellular lipid composition of colorectal tissues with clinically relevant phenotypes such as pathological tissue type or grade of dysplasia in adenomas. The inability to risk-stratify carcinomas does imply that changes in the relative abundance of lipid metabolites are insufficient to define all phenotypes that may be of interest; however, the key finding of high accuracy in differentiating colorectal cancer, adenoma and normal tissue will have marked impact. Not only is there the possible clinical utility that can come from a real-time tissue recognition device (as explored with promise in chapter 7), but this work gives insights into the metabolic transitions that accompany colorectal carcinogenesis. I hope that the findings described here are a small piece of the puzzle in the efforts to better understand cancer biology.

The work in chapter 7 translating REIMS as a tissue recognition device for use in TAMIS, whilst successful as a proof-of-principle; presented a ream of obstacles related to both the REMIS technology itself and understanding how it can be effectively applied clinically. Despite this, MS-TAMIS has shown early promise for *in vivo* tissue recognition and its role in margin detection, which would be a much-needed technological advancement to promote the use of local excision techniques for the management of advanced rectal adenomas and early rectal cancers. Technologies for precision-surgical local excision of rectal lesions, if successfully translated, would promote organ preservation, reduce patient morbidity, improve oncological outcomes, reduce long-term functional sequelae of radical surgery and reduce healthcare costs.

## 8.2 Future work

This thesis has been able to address pressing research questions but as is expected in the research process, a variety of new questions have arisen that should be tackled in future work. I have approached these in the discussion sections of data chapters, however, will provide a summary here across four domains – validation of the current findings, identifying the biological drivers of metabolic dysregulation, need for technological development and better understanding the clinical applications of REIMS.

### 8.2.1 Validation of *ex vivo* findings

This thesis presents many analyses describing the lipidomic changes associated with colorectal carcinogenesis, including down to a molecular level; however, it must be considered that this is a single dataset. As such, identified or unidentified biases may have been unintentionally incorporated which could invalidate the findings when attempting to apply them more generally. An example is selection bias considering this dataset is generated from three academic London hospitals, where the geographical location of this patient cohort may render them intrinsically different from the wider population based on factors such as environmental exposures (particularly diet and lifestyle), gender, ethnicity, co-morbidities or age. A further bias can relate to the statistical techniques used to analyse the REIMS spectra, with many decisions required for how to pre-process the data and which chemometric functions were to be used in multivariate modelling (and with what parameters). Small changes in such decisions can potentially have a great impact on the findings of metabolomic datasets. This may have caused type I errors to emerge (particularly through over-fitting) or type II errors where true biological effects were not detected. Additionally, these decisions may have been subconsciously impacted by a confirmation bias, where I made choices based on the differences I expected or wished to see.

These issues can be resolved by externally validating the findings of this thesis. This should most likely take the form of a truly independent cohort of colorectal tissue, which has been collected and stored in the same fashion as those used in this thesis. The data processing methodology and tissue recognition model should be set and then the accuracy of REIMS can be prospectively assessed. In advance, efforts should be taken to ensure this patient cohort is representative of the

wider population. Whilst research such as this is based in the UK and therefore has a largely Caucasian population, the impact of factors such as ethnicity needs to be considered in this validation cohort to understand how the technology could be applicable worldwide. It is not possible to perform a power calculation to determine how many tissue samples should constitute this dataset however if it is to be able to assess factors such as ethnicity, it is likely to be in excess of 200.

### 8.2.2 Identifying biological drivers of metabolic dysregulation

The relationship between the unique lipidomic fingerprints and tissue phenotypes described in this thesis can only be considered associative, as it is beyond the scope of this work to start to identify biological drivers and causative factors. For example, PGs appear to increase in relative abundance as colorectal carcinogenesis progresses, however, it is unknown if this required for the progression or is simply a consequence of it. Correlating the metabolic dysregulation seen with data from complementary -omics technologies (such as genomics, transcriptomics and proteomics) would give further insight into the biological changes during carcinogenesis. For example, the increased abundance of PGs may be due to chromosomal copy number duplication or increased transcription of the phosphatidylglycerophosphatase gene (assessed with DNA and RNA sequencing respectively<sup>427,428</sup>) or changes in enzyme activity through post-translational modifications (detected using techniques such as proteomic mass spectrometry and activity assays<sup>429,430</sup>). Quantitative MS techniques should also be used to measure the absolute abundance of precursors in the biosynthesis pathway, comparing products and substrates either side of key enzymatic steps. Being able to describe how alterations to metabolic processes lead to differences in metabolite abundance seen by REIMS is a further validation step, as it demonstrates that differences in abundance were not related to analytical errors or confounding factors. Targeted extraction of RNA and DNA has already been performed on 108 colorectal tissue samples included in this REIMS dataset.

Complementary metabolomic techniques should also be used in these colorectal tissues, having the advantage of exploring other areas of cellular biology that were not analysed by REIMS. LC-MS for example, can be optimised for the sensitive detection of key molecules involved in cellular metabolism such as Krebs cycle components<sup>431</sup>, saacharides<sup>432</sup>, peptides<sup>433</sup> and amino acids<sup>434</sup>.

The work in this thesis was biased by being semi-targeted to negatively charged metabolites in the 600-1000m/z range (largely lipids), however analysis of these other components of cellular metabolism will reveal further insights. Techniques such as LC-MS/MS can also be used to help identify the molecular structure of the lipid metabolites where that was not possible using REIMS MS/MS. The microbiome appears to be intrinsically linked to colorectal carcinogenesis and is commonly described within a 'driver passenger model'<sup>435</sup>. 16S rRNA gene sequencing should be performed on the mucosal microbiome of the tissue samples analysed here by REIMS, to correlate how the presence of pathobionts such as *Fusobacterium nucleatum* impact the metabolic profile of tissues and how this relates to tissue phenotype. We have sequenced DNA from 300 colorectal tissue samples and are currently performing exploratory statistical analyses to this end.

### 8.2.3 Technological development

The REIMS source and TOF MS used in this thesis is an adaptation of a piece of laboratory analytical equipment for the purposes of *in vivo* sampling, with many challenges arising as a result of this (as described in detail previously). If the future trajectory of REIMS in powering a commercial clinical device is to be recognised, it will require a significant amount of technological and device design development. The first priority would be to make a device which can collect high-quality data more reliably and easily, without the need for extensive troubleshooting from experienced technicians. Clinical staff who would operate such an instrument would have no technical expertise and little training, such that an instrument would need to be operational shortly after being powered on without requiring any complex pattern of inputs from the operator. The calibration step would therefore need to be automated from an internally stored standard solution, with mass correction performed as necessary. The surgical instrument used would need integrated aerosol aspiration solutions which can be easily and reliably connected to the device. Overall, use of the instrument would require a low technical 'failure' rate to gain the confidence of the staff to integrate it into the routine clinical pathways. Cleaning of internal components would also need to be automated to avoid contaminants carrying over to future patients, as disassembling and reassembling an MS for cleaning would require dedicated training and equipment that would be an additional burden on clinical staff.

The next priority would be to develop an instrument which is less cumbersome to work with in a clinical environment. If the exact metabolic features which require detection could be defined, a targeted MS could be developed which is significantly smaller than the Xevo G2S, with a reduction in sensitivity and mass accuracy that is acceptable within a targeted analysis. The current system generates significant noise which (anecdotally) is tiresome for the theatre staff, with acceptability of a new system contingent on factors such as quiet operation. Medical devices are regularly moved in and out of the operating room as required and this process is most convenient if they are on wheels and can safely be moved and positioned by a single person. These design requirements appear somewhat limiting but future work needs to focus on such things if they are to be well tolerated by staff.

The technological and design development that has been described above will require a multidisciplinary approach, likely to include an MS manufacturer, engineers, scientists and members of the clinical team.

#### 8.2.4 Clinical applications in colorectal disease

The successful clinical application of REIMS technology requires a significant amount of work to identify exact clinical situations where there may be utility, but also how outputs from the technology should be presented and utilised. The MS-TAMIS presented in chapter 7 used REIMS for tissue recognition, however it does not approach subjects such as how best to inform the surgeon of tissue types being analysed; such as through audio or integrated visual cues. Furthermore, work needs to be done to understand how the surgeon should change their dissection based on REIMS predicting the presence of an involved margin, considering the possibility for false positives and whether simply taking a slightly wider dissection path is sufficient. Ultimately, for margin detection applications such as TAMIS, research will need to demonstrate an oncological advantage by using the technology (such as reduced R1 resection rate or local recurrence); with an example RCT study design proposed in section 7.4.3.

As described in chapter 2, the unmet clinical need for real-time colorectal tissue recognition also extends to polyps seen endoscopically, where decision-making depends on the pathological subtype. As part of an NIHR invention for innovation grant, the group are building on the previous

proof-of-principle work demonstrating endoscopic REIMS (coined the iEndoscope)<sup>85</sup>. A clinical study is scheduled to start, where 72 polypectomies will be conducted using the iEndoscope, with a primary outcome of detecting the presence of dysplasia in colorectal polyps powered by the data collected in this thesis. If this can be determined accurately, it would allow the consideration of management strategies such as 'resect and discard' or 'diagnose and leave'. Unfortunately, due to the COVID-19 pandemic and the loss of many non-emergency services, this study has been delayed but will commence in 2021.

## Bibliography

1. Arnold M, Sierra MS, Laversanne M, Soerjomataram I, Jemal A, Bray F. Global patterns and trends in colorectal cancer incidence and mortality. *Gut*. 2017;66(4):683-691.
2. Araghi M, Soerjomataram I, Bardot A, et al. Changes in colorectal cancer incidence in seven high-income countries: a population-based study. *Lancet Gastroenterol Hepatol*. 2019;4(7):511-518.
3. Cancer Research UK. Bowel cancer statistics. <https://www.cancerresearchuk.org/health-professional/cancer-statistics/statistics-by-cancer-type/bowel-cancer#heading-Zero>. Published 2020. Accessed 19/08/2020.
4. Malvezzi M, Carioli G, Bertuccio P, et al. European cancer mortality predictions for the year 2018 with focus on colorectal cancer. *Ann Oncol*. 2018;29(4):1016-1022.
5. Ibanez-Sanz G, Diez-Villanueva A, Alonso MH, et al. Risk Model for Colorectal Cancer in Spanish Population Using Environmental and Genetic Factors: Results from the MCC-Spain study. *Sci Rep*. 2017;7:43263.
6. Jeon J, Du M, Schoen RE, et al. Determining Risk of Colorectal Cancer and Starting Age of Screening Based on Lifestyle, Environmental, and Genetic Factors. *Gastroenterology*. 2018;154(8):2152-2164 e2119.
7. Usher-Smith JA, Walter FM, Emery JD, Win AK, Griffin SJ. Risk Prediction Models for Colorectal Cancer: A Systematic Review. *Cancer Prev Res (Phila)*. 2016;9(1):13-26.
8. Johnson CM, Wei C, Ensor JE, et al. Meta-analyses of colorectal cancer risk factors. *Cancer Causes Control*. 2013;24(6):1207-1222.
9. Bradbury KE, Murphy N, Key TJ. Diet and colorectal cancer in UK Biobank: a prospective study. *Int J Epidemiol*. 2020;49(1):246-258.
10. Aune D, Chan DS, Lau R, et al. Dietary fibre, whole grains, and risk of colorectal cancer: systematic review and dose-response meta-analysis of prospective studies. *BMJ*. 2011;343:d6617.
11. Monahan KJ, Bradshaw N, Dolwani S, et al. Guidelines for the management of hereditary colorectal cancer from the British Society of Gastroenterology (BSG)/Association of Coloproctology of Great Britain and Ireland (ACPGBI)/United Kingdom Cancer Genetics Group (UKCGG). *Gut*. 2020;69(3):411-444.
12. Rutter MD, East J, Rees CJ, et al. British Society of Gastroenterology/Association of Coloproctology of Great Britain and Ireland/Public Health England post-polypectomy and post-colorectal cancer resection surveillance guidelines. *Gut*. 2020;69(2):201-223.
13. Koo S, Neilson LJ, Von Wagner C, Rees CJ. The NHS Bowel Cancer Screening Program: current perspectives on strategies for improvement. *Risk Manag Healthc Policy*. 2017;10:177-187.
14. National Institute of Health and Care Excellence. Suspected cancer: recognition and referral. <https://www.nice.org.uk/guidance/ng12>. Published 2017. Accessed 01/09/2020, 2020.
15. Rees CJ, Thomas Gibson S, Rutter MD, et al. UK key performance indicators and quality assurance standards for colonoscopy. *Gut*. 2016;65(12):1923-1929.
16. Pickhardt PJ, Hassan C, Halligan S, Marmo R. Colorectal cancer: CT colonography and colonoscopy for detection--systematic review and meta-analysis. *Radiology*. 2011;259(2):393-405.
17. Nguyen HT, Duong HQ. The molecular characteristics of colorectal cancer: Implications for diagnosis and therapy. *Oncol Lett*. 2018;16(1):9-18.
18. Humphries A, Wright NA. Colonic crypt organization and tumorigenesis. *Nat Rev Cancer*. 2008;8(6):415-424.

19. Barker N, Ridgway RA, van Es JH, et al. Crypt stem cells as the cells-of-origin of intestinal cancer. *Nature*. 2009;457(7229):608-611.
20. Armaghany T, Wilson JD, Chu Q, Mills G. Genetic alterations in colorectal cancer. *Gastrointest Cancer Res*. 2012;5(1):19-27.
21. Lee-Six H, Olafsson S, Ellis P, et al. The landscape of somatic mutation in normal colorectal epithelial cells. *Nature*. 2019;574(7779):532-537.
22. Leslie A, Carey FA, Pratt NR, Steele RJ. The colorectal adenoma-carcinoma sequence. *Br J Surg*. 2002;89(7):845-860.
23. Chen CD, Yen MF, Wang WM, Wong JM, Chen TH. A case-cohort study for the disease natural history of adenoma-carcinoma and de novo carcinoma and surveillance of colon and rectum after polypectomy: implication for efficacy of colonoscopy. *Br J Cancer*. 2003;88(12):1866-1873.
24. Walther A, Johnstone E, Swanton C, Midgley R, Tomlinson I, Kerr D. Genetic prognostic and predictive markers in colorectal cancer. *Nat Rev Cancer*. 2009;9(7):489-499.
25. Stewart SL, Wike JM, Kato I, Lewis DR, Michaud F. A population-based study of colorectal cancer histology in the United States, 1998-2001. *Cancer*. 2006;107(5 Suppl):1128-1141.
26. Nagtegaal ID, Odze RD, Klimstra D, et al. The 2019 WHO classification of tumours of the digestive system. *Histopathology*. 2020;76(2):182-188.
27. Roseweir AK, McMillan DC, Horgan PG, Edwards J. Colorectal cancer subtypes: Translation to routine clinical pathology. *Cancer Treat Rev*. 2017;57:1-7.
28. Guinney J, Dienstmann R, Wang X, et al. The consensus molecular subtypes of colorectal cancer. *Nat Med*. 2015;21(11):1350-1356.
29. Roepman P, Schlicker A, Tabernero J, et al. Colorectal cancer intrinsic subtypes predict chemotherapy benefit, deficient mismatch repair and epithelial-to-mesenchymal transition. *Int J Cancer*. 2014;134(3):552-562.
30. Foss FA, Milkins S, McGregor AH. Inter-observer variability in the histological assessment of colorectal polyps detected through the NHS Bowel Cancer Screening Programme. *Histopathology*. 2012;61(1):47-52.
31. Edge SB, Byrd DR, Compton CC, Fritz AG, Greene FL, Trotti A. *AJCC cancer staging manual*. 7th ed. New York: Springer-Verlag; 2010.
32. Turnbull RB, Jr., Kyle K, Watson FR, Spratt J. Cancer of the colon: the influence of the no-touch isolation technic on survival rates. *Ann Surg*. 1967;166(3):420-427.
33. Dukes CE. The classification of cancer of the rectum. *The Journal of Pathology and Bacteriology*. 1932;35:10.
34. O'Connell JB, Maggard MA, Ko CY. Colon cancer survival rates with the new American Joint Committee on Cancer sixth edition staging. *J Natl Cancer Inst*. 2004;96(19):1420-1425.
35. Quirke P, Williams GT, Ectors N, Ensari A, Piard F, Nagtegaal I. The future of the TNM staging system in colorectal cancer: time for a debate? *Lancet Oncol*. 2007;8(7):651-657.
36. Shia J, Klimstra DS, Bagci P, Basturk O, Adsay NV. TNM staging of colorectal carcinoma: issues and caveats. *Semin Diagn Pathol*. 2012;29(3):142-153.
37. Lee TJ, Rutter MD, Blanks RG, et al. Colonoscopy quality measures: experience from the NHS Bowel Cancer Screening Programme. *Gut*. 2012;61(7):1050-1057.
38. Zauber AG, Winawer SJ, O'Brien MJ, et al. Colonoscopic polypectomy and long-term prevention of colorectal-cancer deaths. *N Engl J Med*. 2012;366(8):687-696.
39. Horiuchi A, Ikuse T, Tanaka N. Cold snare polypectomy: Indications, devices, techniques, outcomes and future. *Dig Endosc*. 2019;31(4):372-377.
40. Draganov PV. Endoscopic Mucosal Resection Vs Endoscopic Submucosal Dissection for Colon Polyps. *Gastroenterol Hepatol (N Y)*. 2018;14(1):50-52.

41. Ferlitsch M, Moss A, Hassan C, et al. Colorectal polypectomy and endoscopic mucosal resection (EMR): European Society of Gastrointestinal Endoscopy (ESGE) Clinical Guideline. *Endoscopy*. 2017;49(3):270-297.
42. Saito Y, Sakamoto T, Fukunaga S, Nakajima T, Kiriya S, Matsuda T. Endoscopic submucosal dissection (ESD) for colorectal tumors. *Dig Endosc*. 2009;21 Suppl 1:S7-12.
43. Chang AJ, Nahas CS, Araujo SE, et al. Early rectal cancer: local excision or radical surgery? *J Surg Educ*. 2008;65(1):67-72.
44. Landmann RG, Wong WD, Hoepfl J, et al. Limitations of early rectal cancer nodal staging may explain failure after local excision. *Dis Colon Rectum*. 2007;50(10):1520-1525.
45. Buess G, Mentges B, Manncke K, Starlinger M, Becker HD. Technique and results of transanal endoscopic microsurgery in early rectal cancer. *Am J Surg*. 1992;163(1):63-69; discussion 69-70.
46. Christoforidis D, Cho HM, Dixon MR, Mellgren AF, Madoff RD, Finne CO. Transanal endoscopic microsurgery versus conventional transanal excision for patients with early rectal cancer. *Ann Surg*. 2009;249(5):776-782.
47. Atallah S, Albert M, Larach S. Transanal minimally invasive surgery: a giant leap forward. *Surg Endosc*. 2010;24(9):2200-2205.
48. Winde G, Nottberg H, Keller R, Schmid KW, Bunte H. Surgical cure for early rectal carcinomas (T1). Transanal endoscopic microsurgery vs. anterior resection. *Dis Colon Rectum*. 1996;39(9):969-976.
49. Clermonts S, van Loon YT, Wasowicz DK, Langenhoff BS, Zimmerman DDE. Comparative Quality of Life in Patients Following Transanal Minimally Invasive Surgery and Healthy Control Subjects. *J Gastrointest Surg*. 2018;22(6):1089-1097.
50. You YN, Baxter NN, Stewart A, Nelson H. Is the increasing rate of local excision for stage I rectal cancer in the United States justified?: a nationwide cohort study from the National Cancer Database. *Ann Surg*. 2007;245(5):726-733.
51. Nash GM, Weiser MR, Guillem JG, et al. Long-term survival after transanal excision of T1 rectal cancer. *Dis Colon Rectum*. 2009;52(4):577-582.
52. Rasheed S, Bowley DM, Aziz O, et al. Can depth of tumour invasion predict lymph node positivity in patients undergoing resection for early rectal cancer? A comparative study between T1 and T2 cancers. *Colorectal Dis*. 2008;10(3):231-238.
53. Kobayashi H, Mochizuki H, Kato T, et al. Is total mesorectal excision always necessary for T1-T2 lower rectal cancer? *Ann Surg Oncol*. 2010;17(4):973-980.
54. Kidane B, Chadi SA, Kanters S, Colquhoun PH, Ott MC. Local resection compared with radical resection in the treatment of T1N0M0 rectal adenocarcinoma: a systematic review and meta-analysis. *Dis Colon Rectum*. 2015;58(1):122-140.
55. Massarweh NN, Cosgriff N, Slakey DP. Electrosurgery: history, principles, and current and future uses. *J Am Coll Surg*. 2006;202(3):520-530.
56. IUPAC. *Compendium of Chemical Terminology*. 2nd ed. Oxford: Blackwell Scientific Publications; 1995.
57. Pakiet A, Kobiela J, Stepnowski P, Sledzinski T, Mika A. Changes in lipids composition and metabolism in colorectal cancer: a review. *Lipids Health Dis*. 2019;18(1):29.
58. Blanco A, Blanco G. Chapter 5 - Lipids. In: Blanco A, Blanco G, eds. *Medical Biochemistry*. Academic Press; 2017:99-119.
59. Han X, Gross RW. Shotgun lipidomics: electrospray ionization mass spectrometric analysis and quantitation of cellular lipidomes directly from crude extracts of biological samples. *Mass Spectrom Rev*. 2005;24(3):367-412.
60. Simons K, Vaz WL. Model systems, lipid rafts, and cell membranes. *Annu Rev Biophys Biomol Struct*. 2004;33:269-295.

61. Magee T, Pirinen N, Adler J, Pagakis SN, Parmryd I. Lipid rafts: cell surface platforms for T cell signaling. *Biol Res.* 2002;35(2):127-131.
62. Lodhi IJ, Semenkovich CF. Peroxisomes: a nexus for lipid metabolism and cellular signaling. *Cell Metab.* 2014;19(3):380-392.
63. Guillou H, Zadavec D, Martin PG, Jacobsson A. The key roles of elongases and desaturases in mammalian fatty acid metabolism: Insights from transgenic mice. *Prog Lipid Res.* 2010;49(2):186-199.
64. Ma XY, Qiang J, He J, Gabriel NN, Xu P. Changes in the physiological parameters, fatty acid metabolism, and SCD activity and expression in juvenile GIFT tilapia (*Oreochromis niloticus*) reared at three different temperatures. *Fish Physiol Biochem.* 2015;41(4):937-950.
65. Hsu PP, Sabatini DM. Cancer cell metabolism: Warburg and beyond. *Cell.* 2008;134(5):703-707.
66. Warburg O. On respiratory impairment in cancer cells. *Science.* 1956;124(3215):269-270.
67. Santos CR, Schulze A. Lipid metabolism in cancer. *FEBS J.* 2012;279(15):2610-2623.
68. Menendez JA, Lupu R. Fatty acid synthase and the lipogenic phenotype in cancer pathogenesis. *Nat Rev Cancer.* 2007;7(10):763-777.
69. Pyne NJ, Pyne S. Sphingosine 1-phosphate and cancer. *Nat Rev Cancer.* 2010;10(7):489-503.
70. Szlasa W, Zendran I, Zalesinska A, Tarek M, Kulbacka J. Lipid composition of the cancer cell membrane. *J Bioenerg Biomembr.* 2020.
71. Yousefnia S, Momenzadeh S, Seyed Forootan F, Ghaedi K, Nasr Esfahani MH. The influence of peroxisome proliferator-activated receptor gamma (PPARgamma) ligands on cancer cell tumorigenicity. *Gene.* 2018;649:14-22.
72. Cruz-Gil S, Sanchez-Martinez R, Gomez de Cedron M, et al. Targeting the lipid metabolic axis ACSL/SCD in colorectal cancer progression by therapeutic miRNAs: miR-19b-1 role. *J Lipid Res.* 2018;59(1):14-24.
73. Luo X, Cheng C, Tan Z, et al. Emerging roles of lipid metabolism in cancer metastasis. *Mol Cancer.* 2017;16(1):76.
74. Wu H, Han Y, Rodriguez Sillke Y, et al. Lipid droplet-dependent fatty acid metabolism controls the immune suppressive phenotype of tumor-associated macrophages. *EMBO Mol Med.* 2019;11(11):e10698.
75. Lochner M, Berod L, Sparwasser T. Fatty acid metabolism in the regulation of T cell function. *Trends Immunol.* 2015;36(2):81-91.
76. Mika A, Pakiet A, Czumaj A, et al. Decreased Triacylglycerol Content and Elevated Contents of Cell Membrane Lipids in Colorectal Cancer Tissue: A Lipidomic Study. *J Clin Med.* 2020;9(4).
77. Mika A, Kobiela J, Czumaj A, Chmielewski M, Stepnowski P, Sledzinski T. Hyper-Elongation in Colorectal Cancer Tissue - Cerotic Acid is a Potential Novel Serum Metabolic Marker of Colorectal Malignancies. *Cell Physiol Biochem.* 2017;41(2):722-730.
78. Qiu Y, Cai G, Zhou B, et al. A distinct metabolic signature of human colorectal cancer with prognostic potential. *Clin Cancer Res.* 2014;20(8):2136-2146.
79. Tian Y, Xu T, Huang J, et al. Tissue Metabonomic Phenotyping for Diagnosis and Prognosis of Human Colorectal Cancer. *Sci Rep.* 2016;6:20790.
80. Li F, Qin X, Chen H, et al. Lipid profiling for early diagnosis and progression of colorectal cancer using direct-infusion electrospray ionization Fourier transform ion cyclotron resonance mass spectrometry. *Rapid Commun Mass Spectrom.* 2013;27(1):24-34.
81. Zhang J, Zhang L, Ye X, et al. Characteristics of fatty acid distribution is associated with colorectal cancer prognosis. *Prostaglandins Leukot Essent Fatty Acids.* 2013;88(5):355-360.

82. Yang K, Li H, Dong J, Dong Y, Wang CZ. Expression profile of polyunsaturated fatty acids in colorectal cancer. *World J Gastroenterol*. 2015;21(8):2405-2412.
83. Guo S, Wang Y, Zhou D, Li Z. Significantly increased monounsaturated lipids relative to polyunsaturated lipids in six types of cancer microenvironment are observed by mass spectrometry imaging. *Scientific Reports*. 2014;4(1):5959.
84. Chen L, Chen H, Li Y, Li L, Qiu Y, Ren J. Endocannabinoid and ceramide levels are altered in patients with colorectal cancer. *Oncol Rep*. 2015;34(1):447-454.
85. Alexander J, Gildea L, Balog J, et al. A novel methodology for in vivo endoscopic phenotyping of colorectal cancer based on real-time analysis of the mucosal lipidome: a prospective observational study of the iKnife. *Surg Endosc*. 2017;31(3):1361-1370.
86. Wang Y, Hinz S, Uckermann O, et al. Shotgun lipidomics-based characterization of the landscape of lipid metabolism in colorectal cancer. *Biochim Biophys Acta Mol Cell Biol Lipids*. 2020;1865(3):158579.
87. Kurabe N, Hayasaka T, Ogawa M, et al. Accumulated phosphatidylcholine (16:0/16:1) in human colorectal cancer; possible involvement of LPCAT4. *Cancer Sci*. 2013;104(10):1295-1302.
88. Shen S, Yang L, Li L, Bai Y, Cai C, Liu H. A plasma lipidomics strategy reveals perturbed lipid metabolic pathways and potential lipid biomarkers of human colorectal cancer. *J Chromatogr B Analyt Technol Biomed Life Sci*. 2017;1068-1069:41-48.
89. Pradas I, Huynh K, Cabre R, et al. Lipidomics Reveals a Tissue-Specific Fingerprint. *Front Physiol*. 2018;9:1165.
90. Murphy SA, Nicolaou A. Lipidomics applications in health, disease and nutrition research. *Mol Nutr Food Res*. 2013;57(8):1336-1346.
91. Gode D, Volmer DA. Lipid imaging by mass spectrometry - a review. *Analyst*. 2013;138(5):1289-1315.
92. Peng W, Tan S, Xu Y, et al. LCMS/MS metabolome analysis detects the changes in the lipid metabolic profiles of dMMR and pMMR cells. *Oncol Rep*. 2018;40(2):1026-1034.
93. Dettmer K, Aronov PA, Hammock BD. Mass spectrometry-based metabolomics. *Mass Spectrom Rev*. 2007;26(1):51-78.
94. Fiehn O. Metabolomics--the link between genotypes and phenotypes. *Plant Mol Biol*. 2002;48(1-2):155-171.
95. Sender R, Fuchs S, Milo R. Revised Estimates for the Number of Human and Bacteria Cells in the Body. *PLoS Biol*. 2016;14(8):e1002533.
96. Garza DR, van Verk MC, Huynen MA, Dutilh BE. Towards predicting the environmental metabolome from metagenomics with a mechanistic model. *Nat Microbiol*. 2018;3(4):456-460.
97. Deng P, Li X, Petriello MC, Wang C, Morris AJ, Hennig B. Application of metabolomics to characterize environmental pollutant toxicity and disease risks. *Rev Environ Health*. 2019;34(3):251-259.
98. Jones DP, Park Y, Ziegler TR. Nutritional metabolomics: progress in addressing complexity in diet and health. *Annu Rev Nutr*. 2012;32:183-202.
99. Huo T, Canepa R, Sura A, Modave F, Gong Y. Colorectal cancer stages transcriptome analysis. *PLoS One*. 2017;12(11):e0188697.
100. Uhlen M, Zhang C, Lee S, et al. A pathology atlas of the human cancer transcriptome. *Science*. 2017;357(6352).
101. Kim ST, Sohn I, Do IG, et al. Transcriptome analysis of CD133-positive stem cells and prognostic value of survivin in colorectal cancer. *Cancer Genomics Proteomics*. 2014;11(5):259-266.

102. Eberhart CE, Coffey RJ, Radhika A, Giardiello FM, Ferrenbach S, DuBois RN. Up-regulation of cyclooxygenase 2 gene expression in human colorectal adenomas and adenocarcinomas. *Gastroenterology*. 1994;107(4):1183-1188.
103. Tariq K, Ghias K. Colorectal cancer carcinogenesis: a review of mechanisms. *Cancer Biol Med*. 2016;13(1):120-135.
104. Grady WM, Carethers JM. Genomic and epigenetic instability in colorectal cancer pathogenesis. *Gastroenterology*. 2008;135(4):1079-1099.
105. Zanke BW, Greenwood CM, Rangrej J, et al. Genome-wide association scan identifies a colorectal cancer susceptibility locus on chromosome 8q24. *Nat Genet*. 2007;39(8):989-994.
106. Habermann JK, Paulsen U, Roblick UJ, et al. Stage-specific alterations of the genome, transcriptome, and proteome during colorectal carcinogenesis. *Genes Chromosomes Cancer*. 2007;46(1):10-26.
107. Goodacre R, Vaidyanathan S, Dunn WB, Harrigan GG, Kell DB. Metabolomics by numbers: acquiring and understanding global metabolite data. *Trends Biotechnol*. 2004;22(5):245-252.
108. Patti GJ, Yanes O, Siuzdak G. Innovation: Metabolomics: the apogee of the omics trilogy. *Nat Rev Mol Cell Biol*. 2012;13(4):263-269.
109. Johnson CH, Ivanisevic J, Siuzdak G. Metabolomics: beyond biomarkers and towards mechanisms. *Nat Rev Mol Cell Biol*. 2016;17(7):451-459.
110. Koen N, Du Preez I, Loots du T. Metabolomics and Personalized Medicine. *Adv Protein Chem Struct Biol*. 2016;102:53-78.
111. Fuhrer T, Zamboni N. High-throughput discovery metabolomics. *Curr Opin Biotechnol*. 2015;31:73-78.
112. Dunn WB, Bailey NJ, Johnson HE. Measuring the metabolome: current analytical technologies. *Analyst*. 2005;130(5):606-625.
113. Marshall DD, Powers R. Beyond the paradigm: Combining mass spectrometry and nuclear magnetic resonance for metabolomics. *Prog Nucl Magn Reson Spectrosc*. 2017;100:1-16.
114. Ren J-L, Zhang A-H, Kong L, Wang X-J. Advances in mass spectrometry-based metabolomics for investigation of metabolites. *RSC Advances*. 2018;8:16.
115. Emwas AH, Roy R, McKay RT, et al. NMR Spectroscopy for Metabolomics Research. *Metabolites*. 2019;9(7).
116. Alonso A, Marsal S, Julia A. Analytical methods in untargeted metabolomics: state of the art in 2015. *Front Bioeng Biotechnol*. 2015;3:23.
117. Ho CS, Lam CW, Chan MH, et al. Electrospray ionisation mass spectrometry: principles and clinical applications. *Clin Biochem Rev*. 2003;24(1):3-12.
118. Bahr U, Karas M, Hillenkamp F. Analysis of biopolymers by matrix-assisted laser desorption/ionization (MALDI) mass spectrometry. *Fresenius' Journal of Analytical Chemistry volume 1994*;348:9.
119. Cole RB. *Electrospray and MALDI Mass Spectrometry: Fundamentals, Instrumentation, Practicalities, and Biological Applications*. 2 ed: John Wiley & Sons; 2011.
120. Takats Z, Wiseman JM, Cooks RG. Ambient mass spectrometry using desorption electrospray ionization (DESI): instrumentation, mechanisms and applications in forensics, chemistry, and biology. *J Mass Spectrom*. 2005;40(10):1261-1275.
121. Siuzdak G. An Introduction to Mass Spectrometry Ionization: An Excerpt from The Expanding Role of Mass Spectrometry in Biotechnology, 2nd ed.; MCC Press: San Diego, 2005. *JALA: Journal of the Association for Laboratory Automation*. 2004;9(2):14.
122. Brunnee C. The ideal mass analyzer: Fact or fiction? *International Journal of Mass Spectrometry and Ion Processes*. 1987;76(2):113.

123. Dunn WB. Mass spectrometry in systems biology an introduction. *Methods Enzymol.* 2011;500:15-35.
124. Medhe S. Mass Spectrometry: Detectors Review. *Chemical and Biomolecular Engineering.* 2018;3(4):8.
125. Annesley TM. Ion suppression in mass spectrometry. *Clin Chem.* 2003;49(7):1041-1044.
126. Metz TO, Zhang Q, Page JS, et al. The future of liquid chromatography-mass spectrometry (LC-MS) in metabolic profiling and metabolomic studies for biomarker discovery. *Biomark Med.* 2007;1(1):159-185.
127. Ogiso H, Suzuki T, Taguchi R. Development of a reverse-phase liquid chromatography electrospray ionization mass spectrometry method for lipidomics, improving detection of phosphatidic acid and phosphatidylserine. *Anal Biochem.* 2008;375(1):124-131.
128. Simon R, Enjalbert Q, Biarc J, Lemoine J, Salvador A. Evaluation of hydrophilic interaction chromatography (HILIC) versus C(1)(8) reversed-phase chromatography for targeted quantification of peptides by mass spectrometry. *J Chromatogr A.* 2012;1264:31-39.
129. Pham TH, Zaeem M, Fillier TA, et al. Targeting Modified Lipids during Routine Lipidomics Analysis using HILIC and C30 Reverse Phase Liquid Chromatography coupled to Mass Spectrometry. *Sci Rep.* 2019;9(1):5048.
130. Binkley J, Libarondi M. Comparing the Capabilities of Time-of-Flight and Quadrupole Mass Spectrometers. *Current Trends in Mass Spectrometry.* 2010;8(3):6.
131. Diaz JA, Giese CF, Gentry WR. Sub-miniature ExB sector-field mass spectrometer. *J Am Soc Mass Spectrom.* 2001;12(6):619-632.
132. Zubarev RA, Makarov A. Orbitrap mass spectrometry. *Anal Chem.* 2013;85(11):5288-5296.
133. Balog J, Szaniszló T, Schaefer KC, et al. Identification of biological tissues by rapid evaporative ionization mass spectrometry. *Anal Chem.* 2010;82(17):7343-7350.
134. Schaefer KC, Denes J, Albrecht K, et al. In vivo, in situ tissue analysis using rapid evaporative ionization mass spectrometry. *Angew Chem Int Ed Engl.* 2009;48(44):8240-8242.
135. Genangeli M, Heeren RMA, Porta Siegel T. Tissue classification by rapid evaporative ionization mass spectrometry (REIMS): comparison between a diathermic knife and CO<sub>2</sub> laser sampling on classification performance. *Anal Bioanal Chem.* 2019;411(30):7943-7955.
136. Cameron SJ, Bolt F, Perdonés-Montero A, et al. Rapid Evaporative Ionisation Mass Spectrometry (REIMS) Provides Accurate Direct from Culture Species Identification within the Genus *Candida*. *Sci Rep.* 2016;6:36788.
137. Balog J, Sasi-Szabo L, Kinross J, et al. Intraoperative tissue identification using rapid evaporative ionization mass spectrometry. *Sci Transl Med.* 2013;5(194):194ra193.
138. Black C, Chevallier OP, Haughey SA, et al. A real time metabolomic profiling approach to detecting fish fraud using rapid evaporative ionisation mass spectrometry. *Metabolomics.* 2017;13(12):153.
139. Hinz KP, Gelhausen E, Schaefer KC, Takats Z, Spengler B. Characterization of surgical aerosols by the compact single-particle mass spectrometer LAMPAS 3. *Anal Bioanal Chem.* 2011;401(10):3165-3172.
140. Guenther S, Schaefer KC, Balog J, et al. Electrospray post-ionization mass spectrometry of electrosurgical aerosols. *J Am Soc Mass Spectrom.* 2011;22(11):2082-2089.
141. Jones EA, Simon D, Karancsi T, Balog J, Pringle SD, Takats Z. Matrix Assisted Rapid Evaporative Ionization Mass Spectrometry. *Anal Chem.* 2019;91(15):9784-9791.
142. Giles K, Pringle SD, Worthington KR, Little D, Wildgoose JL, Bateman RH. Applications of a travelling wave-based radio-frequency-only stacked ring ion guide. *Rapid Commun Mass Spectrom.* 2004;18(20):2401-2414.
143. Kind T, Liu KH, Lee DY, DeFelice B, Meissen JK, Fiehn O. LipidBlast in silico tandem mass spectrometry database for lipid identification. *Nat Methods.* 2013;10(8):755-758.

144. Sumner LW, Amberg A, Barrett D, et al. Proposed minimum reporting standards for chemical analysis Chemical Analysis Working Group (CAWG) Metabolomics Standards Initiative (MSI). *Metabolomics*. 2007;3(3):211-221.
145. Tautenhahn R, Cho K, Uritboonthai W, Zhu Z, Patti GJ, Siuzdak G. An accelerated workflow for untargeted metabolomics using the METLIN database. *Nat Biotechnol*. 2012;30(9):826-828.
146. Fahy E, Subramaniam S, Murphy RC, et al. Update of the LIPID MAPS comprehensive classification system for lipids. *J Lipid Res*. 2009;50 Suppl:S9-14.
147. Jeck V, Korf A, Vosse C, Hayen H. Localization of double-bond positions in lipids by tandem mass spectrometry succeeding high-performance liquid chromatography with post-column derivatization. *Rapid Commun Mass Spectrom*. 2019;33 Suppl 1:86-94.
148. Bowman AP, Abzalimov RR, Shvartsburg AA. Broad Separation of Isomeric Lipids by High-Resolution Differential Ion Mobility Spectrometry with Tandem Mass Spectrometry. *J Am Soc Mass Spectrom*. 2017;28(8):1552-1561.
149. Schrimpe-Rutledge AC, Codreanu SG, Sherrod SD, McLean JA. Untargeted Metabolomics Strategies-Challenges and Emerging Directions. *J Am Soc Mass Spectrom*. 2016;27(12):1897-1905.
150. Worley B, Powers R. Multivariate Analysis in Metabolomics. *Curr Metabolomics*. 2013;1(1):92-107.
151. Blasco H, Blaszczyński J, Billaut JC, et al. Comparative analysis of targeted metabolomics: dominance-based rough set approach versus orthogonal partial least square-discriminant analysis. *J Biomed Inform*. 2015;53:291-299.
152. Bartel J, Krumsiek J, Theis FJ. Statistical methods for the analysis of high-throughput metabolomics data. *Comput Struct Biotechnol J*. 2013;4:e201301009.
153. Antonelli J, Claggett BL, Henglin M, et al. Statistical Workflow for Feature Selection in Human Metabolomics Data. *Metabolites*. 2019;9(7).
154. Eriksson L, Byrne T, Johansson E, Trygg J, Vikström C. *Multi- and Megavariate Data Analysis Basic Principles and Applications, version 1*. Umetrics Academy; 2013.
155. Fonville JM, Richards SE, Barton RH, et al. The evolution of partial least squares models and related chemometric approaches in metabolomics and metabolic phenotyping. *Journal of Chemometrics*. 2010;24(11-12):636-649.
156. Gromski PS, Muhamadali H, Ellis DI, et al. A tutorial review: Metabolomics and partial least squares-discriminant analysis--a marriage of convenience or a shotgun wedding. *Anal Chim Acta*. 2015;879:10-23.
157. Khan A, Farooq H. Principal Component Analysis-Linear Discriminant Analysis Feature Extractor for Pattern Recognition. *International Journal of Computer Science Issues*. 2011;8(6):4.
158. Dixon SJ, Brereton RG. Comparison of performance of five common classifiers represented as boundary methods: Euclidean Distance to Centroids, Linear Discriminant Analysis, Quadratic Discriminant Analysis, Learning Vector Quantization and Support Vector Machines, as dependent on data structure. *Chemometrics and Intelligent Laboratory Systems*. 2009;95(1):1-17.
159. Acuna E, Rodriguez C. *A meta analysis study of outlier detection methods in classification*. 2004.
160. Xi B, Gu H, Baniasadi H, Raftery D. Statistical analysis and modeling of mass spectrometry-based metabolomics data. *Methods Mol Biol*. 2014;1198:333-353.
161. Triba MN, Le Moyec L, Amathieu R, et al. PLS/OPLS models in metabolomics: the impact of permutation of dataset rows on the K-fold cross-validation quality parameters. *Mol Biosyst*. 2015;11(1):13-19.

162. Petersen D, Naveed P, Ragheb A, et al. Raman fiber-optical method for colon cancer detection: Cross-validation and outlier identification approach. *Spectrochim Acta A Mol Biomol Spectrosc.* 2017;181:270-275.
163. Jiang G, Wang W. Error estimation based on variance analysis of k-fold cross-validation. *Pattern Recognition.* 2017;69:94-106.
164. Simundic AM. Measures of Diagnostic Accuracy: Basic Definitions. *EJIFCC.* 2009;19(4):203-211.
165. Platt RW. ANOVA, t tests, and linear regression. *Inj Prev.* 1998;4(1):52-53.
166. Gordon A, Glazko G, Qiu X, Yakovlev A. Control of the mean number of false discoveries, Bonferroni and stability of multiple testing. *Ann Appl Stat.* 2007;1(1):179-190.
167. St John ER, Balog J, McKenzie JS, et al. Rapid evaporative ionisation mass spectrometry of electrosurgical vapours for the identification of breast pathology: towards an intelligent knife for breast cancer surgery. *Breast Cancer Res.* 2017;19(1):59.
168. Phelps DL, Balog J, Gildea LF, et al. The surgical intelligent knife distinguishes normal, borderline and malignant gynaecological tissues using rapid evaporative ionisation mass spectrometry (REIMS). *Br J Cancer.* 2018;118(10):1349-1358.
169. Balog J, Kumar S, Alexander J, et al. In vivo endoscopic tissue identification by rapid evaporative ionization mass spectrometry (REIMS). *Angew Chem Int Ed Engl.* 2015;54(38):11059-11062.
170. Takats Z, Strittmatter N, McKenzie JS. Ambient Mass Spectrometry in Cancer Research. *Adv Cancer Res.* 2017;134:231-256.
171. Hanel L, Kwiatkowski M, Heikaus L, Schluter H. Mass spectrometry-based intraoperative tumor diagnostics. *Future Sci OA.* 2019;5(3):FSO373.
172. Chen CH, Lin Z, Garimella S, et al. Development of a mass spectrometry sampling probe for chemical analysis in surgical and endoscopic procedures. *Anal Chem.* 2013;85(24):11843-11850.
173. Zhang J, Rector J, Lin JQ, et al. Nondestructive tissue analysis for ex vivo and in vivo cancer diagnosis using a handheld mass spectrometry system. *Sci Transl Med.* 2017;9(406).
174. Sans M, Zhang J, Lin JQ, et al. Performance of the MasSpec Pen for Rapid Diagnosis of Ovarian Cancer. *Clin Chem.* 2019;65(5):674-683.
175. Sachfer KC, Szaniszló T, Gunther S, et al. In situ, real-time identification of biological tissues by ultraviolet and infrared laser desorption ionization mass spectrometry. *Anal Chem.* 2011;83(5):1632-1640.
176. Hiraoka K, Nishidate K, Mori K, Asakawa D, Suzuki S. Development of probe electrospray using a solid needle. *Rapid Communications in Mass Spectrometry.* 2007;21(18):3139-3144.
177. Mandal M, Saha S, Yoshimura K, et al. Biomolecular analysis and cancer diagnostics by negative mode probe electrospray ionization. *The Analyst.* 2013;138:7.
178. Yoshimura K, Chen LC, Mandal MK, et al. Analysis of Renal Cell Carcinoma as a First Step for Developing Mass Spectrometry-Based Diagnostics. *Journal of The American Society for Mass Spectrometry.* 2012;23(10):1741-1749.
179. Ashizawa K, Yoshimura K, Johno H, et al. Construction of mass spectra database and diagnosis algorithm for head and neck squamous cell carcinoma. *Oral Oncol.* 2017;75:111-119.
180. Fatou B, Saudemont P, Leblanc E, et al. In vivo Real-Time Mass Spectrometry for Guided Surgery Application. *Sci Rep.* 2016;6:25919.
181. Saudemont P, Quanicco J, Robin Y-M, et al. Real-Time Molecular Diagnosis of Tumors Using Water-Assisted Laser Desorption/Ionization Mass Spectrometry Technology. *Cancer Cell.* 2018;34(5):840-851.e844.

182. Schafer KC, Balog J, Szaniszló T, et al. Real time analysis of brain tissue by direct combination of ultrasonic surgical aspiration and sonic spray mass spectrometry. *Anal Chem*. 2011;83(20):7729-7735.
183. Qumseya BJ, Coe S, Wallace MB. The effect of polyp location and patient gender on the presence of dysplasia in colonic polyps. *Clin Transl Gastroenterol*. 2012;3:e20.
184. Fujiya M, Tanaka K, Dokoshi T, et al. Efficacy and adverse events of EMR and endoscopic submucosal dissection for the treatment of colon neoplasms: a meta-analysis of studies comparing EMR and endoscopic submucosal dissection. *Gastrointest Endosc*. 2015;81(3):583-595.
185. Committee AT, Abu Dayyeh BK, Thosani N, et al. ASGE Technology Committee systematic review and meta-analysis assessing the ASGE PIVI thresholds for adopting real-time endoscopic assessment of the histology of diminutive colorectal polyps. *Gastrointest Endosc*. 2015;81(3):502 e501-502 e516.
186. Kessler WR, Imperiale TF, Klein RW, Wielage RC, Rex DK. A quantitative assessment of the risks and cost savings of forgoing histologic examination of diminutive polyps. *Endoscopy*. 2011;43(8):683-691.
187. Aisenberg J. Optical biopsy for colorectal polyps: moving along the S-shaped curve. *Gastrointest Endosc*. 2014;79(3):399-401.
188. Wanders LK, East JE, Uitentuis SE, Leeflang MM, Dekker E. Diagnostic performance of narrowed spectrum endoscopy, autofluorescence imaging, and confocal laser endomicroscopy for optical diagnosis of colonic polyps: a meta-analysis. *Lancet Oncol*. 2013;14(13):1337-1347.
189. McGill SK, Evangelou E, Ioannidis JP, Soetikno RM, Kaltenbach T. Narrow band imaging to differentiate neoplastic and non-neoplastic colorectal polyps in real time: a meta-analysis of diagnostic operating characteristics. *Gut*. 2013;62(12):1704-1713.
190. McInnes MDF, Moher D, Thombs BD, et al. Preferred Reporting Items for a Systematic Review and Meta-analysis of Diagnostic Test Accuracy Studies: The PRISMA-DTA Statement. *JAMA*. 2018;319(4):388-396.
191. Schlemper RJ, Riddell RH, Kato Y, et al. The Vienna classification of gastrointestinal epithelial neoplasia. *Gut*. 2000;47(2):251-255.
192. Whiting PF, Rutjes AW, Westwood ME, et al. QUADAS-2: a revised tool for the quality assessment of diagnostic accuracy studies. *Ann Intern Med*. 2011;155(8):529-536.
193. Guo J, Riebler A. meta4diag: Bayesian Bivariate Meta-Analysis of Diagnostic Test Studies for Routine Practice. *Journal of Statistical Software*. 2018;83(1):31.
194. Mason SE, Poynter L, Takats Z, Darzi A, Kinross JM. Optical Technologies for Endoscopic Real-Time Histologic Assessment of Colorectal Polyps: A Meta-Analysis. *Am J Gastroenterol*. 2019;114(8):1219-1230.
195. Systems OM. Narrow Band Imaging (NBI). A New Wave of Diagnostic Possibilities. 2018.
196. van den Broek FJ, Fockens P, Van Eeden S, et al. Clinical evaluation of endoscopic trimodal imaging for the detection and differentiation of colonic polyps. *Clin Gastroenterol Hepatol*. 2009;7(3):288-295.
197. Buchner AM, Shahid MW, Heckman MG, et al. Comparison of probe-based confocal laser endomicroscopy with virtual chromoendoscopy for classification of colon polyps. *Gastroenterology*. 2010;138(3):834-842.
198. Dai J, Shen YF, Sano Y, et al. Evaluation of narrow-band imaging in the diagnosis of colorectal lesions: is a learning curve involved? *Dig Endosc*. 2013;25(2):180-188.
199. East JE, Suzuki N, Bassett P, et al. Narrow band imaging with magnification for the characterization of small and diminutive colonic polyps: pit pattern and vascular pattern intensity. *Endoscopy*. 2008;40(10):811-817.

200. Hewett DG, Huffman ME, Rex DK. Leaving distal colorectal hyperplastic polyps in place can be achieved with high accuracy by using narrow-band imaging: an observational study. *Gastrointest Endosc.* 2012;76(2):374-380.
201. Kuiper T, Marsman WA, Jansen JM, et al. Accuracy for optical diagnosis of small colorectal polyps in nonacademic settings. *Clin Gastroenterol Hepatol.* 2012;10(9):1016-1020; quiz e1079.
202. Kuiper T, van den Broek FJ, Naber AH, et al. Endoscopic trimodal imaging detects colonic neoplasia as well as standard video endoscopy. *Gastroenterology.* 2011;140(7):1887-1894.
203. Ladabaum U, Fioritto A, Mitani A, et al. Real-time optical biopsy of colon polyps with narrow band imaging in community practice does not yet meet key thresholds for clinical decisions. *Gastroenterology.* 2013;144(1):81-91.
204. Lee CK, Lee SH, Hwangbo Y. Narrow-band imaging versus I-Scan for the real-time histological prediction of diminutive colonic polyps: a prospective comparative study by using the simple unified endoscopic classification. *Gastrointest Endosc.* 2011;74(3):603-609.
205. Machida H, Sano Y, Hamamoto Y, et al. Narrow-band imaging in the diagnosis of colorectal mucosal lesions: a pilot study. *Endoscopy.* 2004;36(12):1094-1098.
206. Paggi S, Rondonotti E, Amato A, et al. Resect and discard strategy in clinical practice: A prospective cohort study. *Endoscopy.* 2012;44(10):889-904.
207. Shahid MW, Buchner AM, Heckman MG, et al. Diagnostic accuracy of probe-based confocal laser endomicroscopy and narrow band imaging for small colorectal polyps: a feasibility study. *Am J Gastroenterol.* 2012;107(2):231-239.
208. Sakamoto T, Matsuda T, Aoki T, Nakajima T, Saito Y. Time saving with narrow-band imaging for distinguishing between neoplastic and non-neoplastic small colorectal lesions. *J Gastroenterol Hepatol.* 2012;27(2):351-355.
209. Rastogi A, Early DS, Gupta N, et al. Randomized, controlled trial of standard-definition white-light, high-definition white-light, and narrow-band imaging colonoscopy for the detection of colon polyps and prediction of polyp histology. *Gastrointest Endosc.* 2011;74(3):593-602.
210. Rex DK. Narrow-band imaging without optical magnification for histologic analysis of colorectal polyps. *Gastroenterology.* 2009;136(4):1174-1181.
211. Rogart JN, Jain D, Siddiqui UD, et al. Narrow-band imaging without high magnification to differentiate polyps during real-time colonoscopy: improvement with experience. *Gastrointest Endosc.* 2008;68(6):1136-1145.
212. Rotondano G, Bianco MA, Sansone S, et al. Trimodal endoscopic imaging for the detection and differentiation of colorectal adenomas: a prospective single-centre clinical evaluation. *Int J Colorectal Dis.* 2012;27(3):331-336.
213. Sano Y, Ikematsu H, Fu KI, et al. Meshed capillary vessels by use of narrow-band imaging for differential diagnosis of small colorectal polyps. *Gastrointest Endosc.* 2009;69(2):278-283.
214. Singh R, Nordeen N, Mei SL, Kaffes A, Tam W, Saito Y. West meets East: preliminary results of narrow band imaging with optical magnification in the diagnosis of colorectal lesions: a multicenter Australian study using the modified Sano's classification. *Dig Endosc.* 2011;23 Suppl 1:126-130.
215. Yoo HY, Lee MS, Ko BM, et al. Correlation of narrow band imaging with magnifying colonoscopy and histology in colorectal tumors. *Clin Endosc.* 2011;44(1):44-50.
216. Zhou QJ, Yang JM, Fei BY, Xu QS, Wu WQ, Ruan HJ. Narrow-band imaging endoscopy with and without magnification in diagnosis of colorectal neoplasia. *World J Gastroenterol.* 2011;17(5):666-670.

217. Rogart JN, Aslanian HR, Siddiqui UD. Narrow band imaging to detect residual or recurrent neoplastic tissue during surveillance endoscopy. *Dig Dis Sci.* 2011;56(2):472-478.
218. Ikematsu H, Matsuda T, Osera S, et al. Usefulness of narrow-band imaging with dual-focus magnification for differential diagnosis of small colorectal polyps. *Surg Endosc.* 2015;29(4):844-850.
219. Iwatate M, Sano Y, Hattori S, et al. The addition of high magnifying endoscopy improves rates of high confidence optical diagnosis of colorectal polyps. *Endosc Int Open.* 2015;3(2):E140-145.
220. Sano W, Sano Y, Iwatate M, et al. Prospective evaluation of the proportion of sessile serrated adenoma/polyps in endoscopically diagnosed colorectal polyps with hyperplastic features. *Endosc Int Open.* 2015;3(4):E354-358.
221. Sola-Vera J, Cuesta R, Uceda F, et al. Accuracy for optical diagnosis of colorectal polyps in clinical practice. *Rev Esp Enferm Dig.* 2015;107(5):255-261.
222. Chandran S, Parker F, Lontos S, Vaughan R, Efthymiou M. Can we ease the financial burden of colonoscopy? Using real-time endoscopic assessment of polyp histology to predict surveillance intervals. *Intern Med J.* 2015;45(12):1293-1299.
223. Paggi S, Rondonotti E, Amato A, et al. Narrow-band imaging in the prediction of surveillance intervals after polypectomy in community practice. *Endoscopy.* 2015;47(9):808-814.
224. Kuruvilla N, Paramsothy R, Gill R, Selby WS, Remedios ML, Kaffes AJ. A prospective dual-center proof-of-principle study evaluating the incremental benefit of narrow-band imaging with a fixed zoom function in real-time prediction of polyp histology. Can we resect and discard? *Gastrointest Endosc.* 2015;82(2):362-369.
225. Kaltenbach T, Rastogi A, Rouse RV, et al. Real-time optical diagnosis for diminutive colorectal polyps using narrow-band imaging: the VALID randomised clinical trial. *Gut.* 2015;64(10):1569-1577.
226. Seref Koksak A, Yildiz H, Taskiran I, et al. Low magnification narrow band imaging by inexperienced endoscopists has a high accuracy in differentiation of colon polyp histology. *Clin Res Hepatol Gastroenterol.* 2014;38(6):763-769.
227. Wallace MB, Crook JE, Coe S, et al. Accuracy of in vivo colorectal polyp discrimination by using dual-focus high-definition narrow-band imaging colonoscopy. *Gastrointest Endosc.* 2014;80(6):1072-1087.
228. Takeuchi Y, Hanafusa M, Kanzaki H, Ohta T, Hanaoka N. Proposal of a new 'resect and discard' strategy using magnifying narrow band imaging: pilot study of diagnostic accuracy. *Dig Endosc.* 2014;26 Suppl 2:90-97.
229. Singh R, Jayanna M, Navadgi S, Ruszkiewicz A, Saito Y, Uedo N. Narrow-band imaging with dual focus magnification in differentiating colorectal neoplasia. *Dig Endosc.* 2013;25 Suppl 2:16-20.
230. Repici A, Hassan C, Radaelli F, et al. Accuracy of narrow-band imaging in predicting colonoscopy surveillance intervals and histology of distal diminutive polyps: results from a multicenter, prospective trial. *Gastrointest Endosc.* 2013;78(1):106-114.
231. Takeuchi Y, Hanafusa M, Kanzaki H, et al. An alternative option for "resect and discard" strategy, using magnifying narrow-band imaging: a prospective "proof-of-principle" study. *J Gastroenterol.* 2015;50(10):1017-1026.
232. Kang HY, Kim YS, Kang SJ, et al. Comparison of Narrow Band Imaging and Fujinon Intelligent Color Enhancement in Predicting Small Colorectal Polyp Histology. *Dig Dis Sci.* 2015;60(9):2777-2784.
233. Pohl H, Bensen S, Toor A, et al. Quality of optical diagnosis of diminutive polyps and associated factors. *Endoscopy.* 2016;48(9):817-822.

234. Ashktorab H, Etaati F, Rezaeean F, et al. Can optical diagnosis of small colon polyps be accurate? Comparing standard scope without narrow banding to high definition scope with narrow banding. *World J Gastroenterol.* 2016;22(28):6339-6456.
235. Klare P, Haller B, Wormbt S, et al. Narrow-band imaging vshigh definition white light for optical diagnosis of small colorectal polyps: A randomized multicenter trial. *Endoscopy.* 2016;48(10):909-915.
236. Rees CJ, Rajasekhar PT, Wilson A, et al. Narrow band imaging optical diagnosis of small colorectal polyps in routine clinical practice: the Detect Inspect Characterise Resect and Discard 2 (DISCARD 2) study. *Gut.* 2017;66(5):887-895.
237. Szura M, Pasternak A, Bucki K, Urbanczyk K, Matyja A. Two-stage optical system for colorectal polyp assessments. *Surg Endosc Interv Tech Journal Translated Name Surgical Endoscopy and Other Interventional Techniques.* 2016;30(1):204-214.
238. Ren J, Jiang XL. Narrow-band imaging of meshed capillary vessels for differential diagnosis of colorectal lesions. *World Chin J Dig.* 2012;20(6):473-478.
239. Belderbos TDG, van Oijen MGH, Moons LMG, Siersema PD. Implementation of real-time probe-based confocal laser endomicroscopy (pCLE) for differentiation of colorectal polyps during routine colonoscopy. *Endosc Int Open.* 2017;5(11):E1104-E1110.
240. Okamoto Y, Watanabe H, Tominaga K, et al. Evaluation of microvessels in colorectal tumors by narrow band imaging magnification: including comparison with magnifying chromoendoscopy. *Dig Dis Sci.* 2011;56(2):532-538.
241. Hewett DG, Kaltenbach T, Sano Y, et al. Validation of a simple classification system for endoscopic diagnosis of small colorectal polyps using narrow-band imaging. *Gastroenterology.* 2012;143(3):599-607 e591.
242. Canales Sevilla O, Miyagui Maeda J, Takano Moron J, Poquioma Rojas E. [NBI utility and optical magnification in the differential diagnosis of neoplastic and non-neoplastic colorectal lesions in Peru]. *Rev Gastroenterol Peru.* 2010;30(4):277-283.
243. Salazar Muelle F, Barreda Costa C, Barriga Briceno JA. [Utility of the capilar pattern in the NBI diagnosis of superficial lesions of the colon: prospective validation in a private endoscopic center Lima, Peru]. *Rev Gastroenterol Peru.* 2012;32(3):281-289.
244. Kudo S, Rubio CA, Teixeira CR, Kashida H, Kogure E. Pit pattern in colorectal neoplasia: endoscopic magnifying view. *Endoscopy.* 2001;33(4):367-373.
245. Sano Y, Horimatsu T, Fu K, Katagiri A, Muto M, Ishikawa H. Magnifying observations of microvascular architecture of colorectal lesions using a narrow-band imaging system. *Digestive Endoscopy.* 2006;18(Suppl. 1):8.
246. Goto N, Kusaka T, Tomita Y, et al. Magnifying narrow-band imaging with acetic acid to diagnose early colorectal cancer. *World J Gastroenterol.* 2014;20(43):16306-16310.
247. Yamashina T, Takeuchi Y, Uedo N, et al. Diagnostic features of sessile serrated adenoma/polyps on magnifying narrow band imaging: a prospective study of diagnostic accuracy. *J Gastroenterol Hepatol.* 2015;30(1):117-123.
248. Katagiri A, Fu KI, Sano Y, et al. Narrow band imaging with magnifying colonoscopy as diagnostic tool for predicting histology of early colorectal neoplasia. *Aliment Pharmacol Ther.* 2008;27(12):1269-1274.
249. Tate DJ, Jayanna M, Awadie H, et al. A standardized imaging protocol for the endoscopic prediction of dysplasia within sessile serrated polyps (with video). *Gastrointest Endosc.* 2018;87(1):222-231 e222.
250. Liu H, Wu J, Liu XC, et al. Correlation between microvascular characteristics and the expression of MVD, IGF-1 and STAT3 in the development of colonic polyps carcinogenesis. *Exp Ther Med Journal Translated Name Experimental and Therapeutic Medicine.* 2017;13(1):49-54.

251. Fujinon. FICE. Fuji Intelligent Chromo Endoscopy. 2005:6.
252. Liu YX, Huang LY, Bian XP, Cui J, Xu N, Wu CR. Fuji Intelligent Chromo Endoscopy and staining technique for the diagnosis of colon tumor. *Chin Med J*. 2008;121(11):977-982.
253. Togashi K, Osawa H, Koinuma K, et al. A comparison of conventional endoscopy, chromoendoscopy, and the optimal-band imaging system for the differentiation of neoplastic and non-neoplastic colonic polyps. *Gastrointest Endosc*. 2009;69(3 Pt 2):734-741.
254. Pohl J, Lotterer E, Balzer C, et al. Computed virtual chromoendoscopy versus standard colonoscopy with targeted indigocarmine chromoscopy: a randomised multicentre trial. *Gut*. 2009;58(1):73-78.
255. dos Santos CE, Lima JC, Lopes CV, et al. Computerized virtual chromoendoscopy versus indigo carmine chromoendoscopy combined with magnification for diagnosis of small colorectal lesions: a randomized and prospective study. *Eur J Gastroenterol Hepatol*. 2010;22(11):1364-1371.
256. Longcroft-Wheaton GR, Higgins B, Bhandari P. Flexible spectral imaging color enhancement and indigo carmine in neoplasia diagnosis during colonoscopy: a large prospective UK series. *Eur J Gastroenterol Hepatol*. 2011;23(10):903-911.
257. Kim YS, Kim D, Chung SJ, et al. Differentiating small polyp histologies using real-time screening colonoscopy with Fuji Intelligent Color Enhancement. *Clin Gastroenterol Hepatol*. 2011;9(9):744-749 e741.
258. Dos Santos CE, Malaman D, Lopes CV, Pereira-Lima JC, Parada AA. Digital chromoendoscopy for diagnosis of diminutive colorectal lesions. *Diagn Ther Endosc*. 2012;2012:7.
259. Longcroft-Wheaton G, Brown J, Cowlshaw D, Higgins B, Bhandari P. High-definition vs. standard-definition colonoscopy in the characterization of small colonic polyps: results from a randomized trial. *Endoscopy*. 2012;44(10):905-910.
260. Dos Santos C, Moreira H, Pereira-Lima J, et al. Hyoscine butylbromide for colorectal polyp detection: prospective, randomized, placebo-controlled trial. *Clinics (Sao Paulo)*. 2017;72(7):395-399.
261. Santos CE, Pereira-Lima JC, Lopes CV, Malaman D, Parada AA, Salomao AD. [Comparative study between MBI (FICE) and magnification chromoendoscopy with indigo carmine in the differential diagnosis of neoplastic and non-neoplastic lesions of the colorectum]. *Arq Gastroenterol*. 2009;46(2):111-115.
262. Hoffman A, Sar F, Goetz M, et al. High definition colonoscopy combined with i-Scan is superior in the detection of colorectal neoplasias compared with standard video colonoscopy: A prospective randomized controlled trial. *Endoscopy*. 2010;42(10):827-833.
263. Chan J, Lin L, Feiler M, Wolf A, Cardona D, Gellad Z. Comparative effectiveness of i-SCAN™ and high-definition white light characterizing small colonic polyps. *World J Gastroenterol*. 2012;18(41):5905-5911.
264. Hong S, Choe W, Lee J, et al. Prospective, randomized, back-to-back trial evaluating the usefulness of i-SCAN in screening colonoscopy. *Gastrointest Endosc*. 2012;75(5):1011-1021 e1012.
265. Pigo F, Bertani H, Manno M, et al. i-Scan high-definition white light endoscopy and colorectal polyps: prediction of histology, interobserver and intraobserver agreement. *Int J Colorectal Dis*. 2013;28(3):399-406.
266. Schachschal G, Mayr M, Treszl A, et al. Endoscopic versus histological characterisation of polyps during screening colonoscopy. *Gut*. 2014;63(3):458-465.

267. Basford PJ, Longcroft-Wheaton G, Higgins B, Bhandari P. High-definition endoscopy with i-Scan for evaluation of small colon polyps: the HiSCOPE study. *Gastrointest Endosc.* 2014;79(1):111-118.
268. Rath T, Tontini GE, Nagel A, et al. High-definition endoscopy with digital chromoendoscopy for histologic prediction of distal colorectal polyps. *BMC Gastroenterol.* 2015;15:145.
269. Hoffman A, Kagel C, Goetz M, et al. Recognition and characterization of small colonic neoplasia with high-definition colonoscopy using i-Scan is as precise as chromoendoscopy. *Dig Liver Dis.* 2010;42(1):45-50.
270. Resende RH, Ribeiro IB, de Moura DTH, et al. Surveillance in inflammatory bowel disease: is chromoendoscopy the only way to go? A systematic review and meta-analysis of randomized clinical trials. *Endosc Int Open.* 2020;8(5):E578-E590.
271. Kohut M, Liszka L, Boldys H, Rymarczyk G, Pajak J. Pit pattern analysis using acetic-acid magnification chromoendoscopy in predicting histopathology of small colorectal polyps. The diagnostic yield and intra-/inter-observer reproducibility. *Przegląd Gastroenterologiczny.* 2009;4(6):6.
272. Ljubicic N, Kujundzic M, Banic M, Roic G. The role of standard videochromocolonoscopy in distinguishing adenomatous from nonadenomatous diminutive colorectal polyps. *Acta Clin Croat.* 2001;40(3):197-201.
273. Bianco MA, Rotondano G, Marmo R, et al. Predictive value of magnification chromoendoscopy for diagnosing invasive neoplasia in nonpolypoid colorectal lesions and stratifying patients for endoscopic resection or surgery. *Endoscopy.* 2006;38(5):470-476.
274. De Palma GD, Rega M, Masone S, et al. Conventional colonoscopy and magnified chromoendoscopy for the endoscopic histological prediction of diminutive colorectal polyps: a single operator study. *World J Gastroenterol.* 2006;12(15):2402-2405.
275. Apel D, Jakobs R, Schilling D, et al. Accuracy of high-resolution chromoendoscopy in prediction of histologic findings in diminutive lesions of the rectosigmoid. *Gastrointest Endosc.* 2006;63(6):824-828.
276. Togashi K, Hewett DG, Whitaker DA, Hume GE, Francis L, Appleyard MN. The use of acetic acid in magnification chromocolonoscopy for pit pattern analysis of small polyps. *Endoscopy.* 2006;38(6):613-616.
277. Kato S, Fu KI, Sano Y, et al. Magnifying colonoscopy as a non-biopsy technique for differential diagnosis of non-neoplastic and neoplastic lesions. *World J Gastroenterol.* 2006;12(9):1416-1420.
278. Fu KI, Sano Y, Kato S, et al. Chromoendoscopy using indigo carmine dye spraying with magnifying observation is the most reliable method for differential diagnosis between non-neoplastic and neoplastic colorectal lesions: a prospective study. *Endoscopy.* 2004;36(12):1089-1093.
279. Hurlstone DP, Cross SS, Adam I, et al. Efficacy of high magnification chromoscopic colonoscopy for the diagnosis of neoplasia in flat and depressed lesions of the colorectum: a prospective analysis. *Gut.* 2004;53(2):284-290.
280. Liu HH, Kudo SE, Juch JP. Pit pattern analysis by magnifying chromoendoscopy for the diagnosis of colorectal polyps. *J Formos Med Assoc.* 2003;102(3):178-182.
281. Eisen GM, Kim CY, Fleischer DE, et al. High-resolution chromoendoscopy for classifying colonic polyps: a multicenter study. *Gastrointest Endosc.* 2002;55(6):687-694.
282. Kiesslich R, von Bergh M, Hahn M, Hermann G, Jung M. Chromoendoscopy with indigocarmine improves the detection of adenomatous and nonadenomatous lesions in the colon. *Endoscopy.* 2001;33(12):1001-1006.

283. Axelrad AM, Fleischer DE, Geller AJ, et al. High-resolution chromoendoscopy for the diagnosis of diminutive colon polyps: implications for colon cancer screening. *Gastroenterology*. 1996;110(4):1253-1258.
284. Longcroft-Wheaton G, Brown J, Cowlshaw D, Higgins B, Bhandari P. High-definition vs. standard-definition endoscopy with indigo carmine for the in vivo diagnosis of colonic polyps. *United European Gastroenterol J*. 2013;1(6):425-429.
285. Ince AT, Bolukbas C, Peker O, Bolukbas F, Ovunc O. Pit pattern type analyses of colon polyps with high-resolution colonoscope. *Hepatogastroenterology*. 2007;54(73):67-70.
286. Konishi K, Kaneko K, Kurahashi T, et al. A comparison of magnifying and nonmagnifying colonoscopy for diagnosis of colorectal polyps: A prospective study. *Gastrointest Endosc*. 2003;57(1):48-53.
287. Togashi K, Konishi F, Ishizuka T, Sato T, Senba S, Kanazawa K. Efficacy of magnifying endoscopy in the differential diagnosis of neoplastic and non-neoplastic polyps of the large bowel. *Dis Colon Rectum*. 1999;42(12):1602-1608.
288. Tung SY, Wu CS, Su MY. Magnifying colonoscopy in differentiating neoplastic from nonneoplastic colorectal lesions. *Am J Gastroenterol*. 2001;96(9 SUPPL.):2628-2632.
289. Urban O, Fojtik P, Liberda M, Kliment M. Magnifying chromocolonoscopy - Beginner's diagnostic accuracy. *Endoskopie*. 2005;14(1):3.
290. Averbach M, Zanoni EC, Correa PA, et al. [High resolution chromoendoscopy in the differential diagnosis of neoplastic and non-neoplastic polyps]. *Arq Gastroenterol*. 2003;40(2):99-103.
291. Prosst RL, Gahlen J. Fluorescence diagnosis of colorectal neoplasms: a review of clinical applications. *Int J Colorectal Dis*. 2002;17(1):1-10.
292. Aihara H, Saito S, Inomata H, et al. Computer-aided diagnosis of neoplastic colorectal lesions using 'real-time' numerical color analysis during autofluorescence endoscopy. *Eur J Gastroenterol Hepatol*. 2013;25(4):488-494.
293. Keller R, Winde G, Terpe HJ, Foerster EC, Domschke W. Fluorescence endoscopy using a fluorescein-labeled monoclonal antibody against carcinoembryonic antigen in patients with colorectal carcinoma and adenoma. *Endoscopy*. 2002;34(10):801-807.
294. Ussui VM, Wallace MB. Confocal endomicroscopy of colorectal polyps. *Gastroenterol Res Pract*. 2012;2012:545679.
295. Kiesslich R, Burg J, Vieth M, et al. Confocal laser endoscopy for diagnosing intraepithelial neoplasias and colorectal cancer in vivo. *Gastroenterology*. 2004;127(3):706-713.
296. Wallace M, Lauwers GY, Chen Y, et al. Miami classification for probe-based confocal laser endomicroscopy. *Endoscopy*. 2011;43(10):882-891.
297. Xie XJ, Li CQ, Zuo XL, et al. Differentiation of colonic polyps by confocal laser endomicroscopy. *Endoscopy*. 2011;43(2):87-93.
298. Sanduleanu S, Driessen A, Gomez-Garcia E, Hameeteman W, de Bruine A, Masclee A. In vivo diagnosis and classification of colorectal neoplasia by chromoendoscopy-guided confocal laser endomicroscopy. *Clin Gastroenterol Hepatol*. 2010;8(4):371-378.
299. Shahid M, Buchner A, Raimondo M, Woodward T, Krishna M, Wallace M. Accuracy of real-time vs. blinded offline diagnosis of neoplastic colorectal polyps using probe-based confocal laser endomicroscopy: A pilot study. *Endoscopy*. 2012;44(4):6.
300. Kudo SE, Misawa M, Wada Y, et al. Endocytoscopic microvasculature evaluation is a reliable new diagnostic method for colorectal lesions (with video). *Gastrointest Endosc*. 2015;82(5):912-923.
301. Sasajima K, Kudo SE, Inoue H, et al. Real-time in vivo virtual histology of colorectal lesions when using the endocytoscopy system. *Gastrointest Endosc*. 2006;63(7):1010-1017.

302. Rotondano G, Bianco MA, Salerno R, et al. Endocytoscopic classification of preneoplastic lesions in the colorectum. *Int J Colorectal Dis.* 2010;25(9):1111-1116.
303. Mori Y, Kudo S, Ikehara N, et al. Comprehensive diagnostic ability of endocytoscopy compared with biopsy for colorectal neoplasms: a prospective randomized noninferiority trial. *Endoscopy.* 2013;45(2):98-105.
304. Rath T, Tontini G, Vieth M, Nagel A, Neurath M, Neumann H. In vivo real-time assessment of colorectal polyp histology using an optical biopsy forceps system based on laser-induced fluorescence spectroscopy. *Endoscopy.* 2016;48(6):557-562.
305. Kuiper T, Alderlieste YA, Tytgat KM, et al. Automatic optical diagnosis of small colorectal lesions by laser-induced autofluorescence. *Endoscopy.* 2015;47(1):56-62.
306. Kominami Y, Yoshida S, Tanaka S, et al. Computer-aided diagnosis of colorectal polyp histology by using a real-time image recognition system and narrow-band imaging magnifying colonoscopy. *Gastrointest Endosc.* 2016;83(3):643-649.
307. Rex DK, Kahi C, O'Brien M, et al. The American Society for Gastrointestinal Endoscopy PIVI (Preservation and Incorporation of Valuable Endoscopic Innovations) on real-time endoscopic assessment of the histology of diminutive colorectal polyps. *Gastrointest Endosc.* 2011;73(3):419-422.
308. Ignjatovic A, East JE, Suzuki N, Vance M, Guenther T, Saunders BP. Optical diagnosis of small colorectal polyps at routine colonoscopy (Detect InSpect ChAracterise Resect and Discard; DISCARD trial): a prospective cohort study. *Lancet Oncol.* 2009;10(12):1171-1178.
309. Hogan RB, 3rd, Brill JV, Littenberg G, Demarco DC. Predict, resect, and discard ... really? *Gastrointest Endosc.* 2012;75(3):503-505.
310. East JE, Vleugels JL, Roelandt P, et al. Advanced endoscopic imaging: European Society of Gastrointestinal Endoscopy (ESGE) Technology Review. *Endoscopy.* 2016;48(11):1029-1045.
311. Kobayashi Y, Hayashino Y, Jackson JL, Takagaki N, Hinotsu S, Kawakami K. Diagnostic performance of chromoendoscopy and narrow band imaging for colonic neoplasms: a meta-analysis. *Colorectal Dis.* 2012;14(1):18-28.
312. Ravi D, Wong C, Deligianni F, et al. Deep Learning for Health Informatics. *IEEE J Biomed Health Inform.* 2017;21(1):4-21.
313. Mori Y, Kudo SE, Misawa M, et al. Real-Time Use of Artificial Intelligence in Identification of Diminutive Polyps During Colonoscopy: A Prospective Study. *Ann Intern Med.* 2018;169(6):357-366.
314. Rex DK, Ahnen DJ, Baron JA, et al. Serrated lesions of the colorectum: review and recommendations from an expert panel. *Am J Gastroenterol.* 2012;107(9):1315-1329; quiz 1314, 1330.
315. Willems P, Djinbachian R, Ditisheim S, et al. Uptake and barriers for implementation of the resect and discard strategy: an international survey. *Endosc Int Open.* 2020;8(5):E684-E692.
316. Sakata S, Lee AHS, Kheir AO, et al. Patient acceptance of the optical diagnosis and misdiagnosis of diminutive colorectal polyps. *Gastrointest Endosc.* 2017;86(2):372-375 e372.
317. Dimitriou N, Arandjelovic O, Harrison DJ, Caie PD. A principled machine learning framework improves accuracy of stage II colorectal cancer prognosis. *NPJ Digit Med.* 2018;1:52.
318. Maguire A, Sheahan K. Controversies in the pathological assessment of colorectal cancer. *World J Gastroenterol.* 2014;20(29):9850-9861.
319. van Putten PG, Hol L, van Dekken H, et al. Inter-observer variation in the histological diagnosis of polyps in colorectal cancer screening. *Histopathology.* 2011;58(6):974-981.
320. Wickham H, Averick M, Bryan J, et al. Welcome to the Tidyverse. *Journal of Open Source Software.* 2019;4:1686.

321. Kocher T, Pichler P, Swart R, Mechtler K. Quality control in LC-MS/MS. *Proteomics*. 2011;11(6):1026-1030.
322. Union E. Regulation (EU) 2017/746 of the European Parliament and of the Council of 5 April 2017 on in vitro diagnostic medical devices and repealing Directive 98/79/EC and Commission Decision 2010/227/EU. *Official Journal of the European Union*. 2017.
323. Hong H, Dragan Y, Epstein J, et al. Quality control and quality assessment of data from surface-enhanced laser desorption/ionization (SELDI) time-of flight (TOF) mass spectrometry (MS). *BMC Bioinformatics*. 2005;6 Suppl 2:S5.
324. Kirwan JA, Weber RJ, Broadhurst DI, Viant MR. Direct infusion mass spectrometry metabolomics dataset: a benchmark for data processing and quality control. *Sci Data*. 2014;1:140012.
325. Cuklina J, Pedrioli PGA, Aebersold R. Review of Batch Effects Prevention, Diagnostics, and Correction Approaches. *Methods Mol Biol*. 2020;2051:373-387.
326. Sánchez-Illana Á, Pérez-Guaita D, Cuesta-García D, et al. Model selection for within-batch effect correction in UPLC-MS metabolomics using quality control - Support vector regression. *Analytica Chimica Acta*. 2018;1026:62-68.
327. Kuligowski J, Perez-Guaita D, Lliso I, et al. Detection of batch effects in liquid chromatography-mass spectrometry metabolomic data using guided principal component analysis. *Talanta*. 2014;130:442-448.
328. Sánchez-Illana Á, Piñeiro-Ramos JD, Sanjuan-Herráez JD, Vento M, Quintás G, Kuligowski J. Evaluation of batch effect elimination using quality control replicates in LC-MS metabolite profiling. *Analytica Chimica Acta*. 2018;1019:38-48.
329. Limbach PA, Grosshans PB, Marshall AG. Experimental determination of the number of trapped ions, detection limit, and dynamic range in Fourier transform ion cyclotron resonance mass spectrometry. *Analytical Chemistry*. 1993;65(2):135-140.
330. Xue AY, Szymczak LC, Mrksich M, Bagheri N. Machine Learning on Signal-to-Noise Ratios Improves Peptide Array Design in SAMDI Mass Spectrometry. *Analytical chemistry*. 2017;89(17):9039-9047.
331. Paraskevaïdi M, Cameron SJS, Whelan E, et al. Laser-assisted rapid evaporative ionisation mass spectrometry (LA-REIMS) as a metabolomics platform in cervical cancer screening. *EBioMedicine*. 2020;60:103017.
332. Swayze GA, Clark RN, Goetz AFH, Chrien TG, Gorelick NS. Effects of spectrometer band pass, sampling, and signal-to-noise ratio on spectral identification using the Tetracorder algorithm. *Journal of Geophysical Research: Planets*. 2003;108(E9).
333. Alkemade CTJ, Snelleman W, Boutilier GD, et al. A review and tutorial discussion of noise and signal-to-noise ratios in analytical spectrometry—I. Fundamental principles of signal-to-noise ratios. *Spectrochimica Acta Part B: Atomic Spectroscopy*. 1978;33(8):383-399.
334. Neubauer KR, Johnston MV, Wexler AS. Humidity effects on the mass spectra of single aerosol particles. *Atmospheric Environment*. 1998;32(14):2521-2529.
335. Sudhindra TV, Joseph A, Hacking CJ, Haray PN. Are surgeons aware of the dangers of diathermy? *Ann R Coll Surg Engl*. 2000;82(1):31-32.
336. van Meer G. Cellular lipidomics. *EMBO J*. 2005;24(18):3159-3165.
337. Singh N, Harrison M, Rex DK. A survey of colonoscopic polypectomy practices among clinical gastroenterologists. *Gastrointest Endosc*. 2004;60(3):414-418.
338. Fincher JA, Korte AR, Reschke B, Morris NJ, Powell MJ, Vertes A. Enhanced sensitivity and metabolite coverage with remote laser ablation electrospray ionization-mass spectrometry aided by coaxial plume and gas dynamics. *Analyst*. 2017;142(17):3157-3164.
339. Garimella S, Xu W, Huang G, Harper JD, Cooks RG, Ouyang Z. Gas-flow assisted ion transfer for mass spectrometry. *J Mass Spectrom*. 2012;47(2):201-207.

340. Cotte-Rodriguez I, Cooks RG. Non-proximate detection of explosives and chemical warfare agent simulants by desorption electrospray ionization mass spectrometry. *Chem Commun (Camb)*. 2006(28):2968-2970.
341. Han X, Gross RW. Shotgun lipidomics: Electrospray ionization mass spectrometric analysis and quantitation of cellular lipidomes directly from crude extracts of biological samples. *Mass Spectrometry Reviews*. 2005;24(3):367-412.
342. Hsu F-F, Bohrer A, Turk J. Formation of lithiated adducts of glycerophosphocholine lipids facilitates their identification by electrospray ionization tandem mass spectrometry. *Journal of the American Society for Mass Spectrometry*. 1998;9(5):516-526.
343. Duffin KL, Henion JD, Shieh JJ. Electrospray and tandem mass spectrometric characterization of acylglycerol mixtures that are dissolved in nonpolar solvents. *Anal Chem*. 1991;63(17):1781-1788.
344. Han X, Gross RW. Electrospray ionization mass spectroscopic analysis of human erythrocyte plasma membrane phospholipids. *Proc Natl Acad Sci U S A*. 1994;91(22):10635-10639.
345. Mohandas N, Gallagher PG. Red cell membrane: past, present, and future. *Blood*. 2008;112(10):3939-3948.
346. Patel D, Witt SN. Ethanolamine and Phosphatidylethanolamine: Partners in Health and Disease. *Oxid Med Cell Longev*. 2017;2017:4829180.
347. Mehrkhani F, Nasiri S, Donboli K, Meysamie A, Hedayat A. Prognostic factors in survival of colorectal cancer patients after surgery. *Colorectal Dis*. 2009;11(2):157-161.
348. Edge SB, Compton CC. The American Joint Committee on Cancer: the 7th edition of the AJCC cancer staging manual and the future of TNM. *Ann Surg Oncol*. 2010;17(6):1471-1474.
349. Zhang XY, Wang S, Li XT, et al. MRI of Extramural Venous Invasion in Locally Advanced Rectal Cancer: Relationship to Tumor Recurrence and Overall Survival. *Radiology*. 2018;289(3):677-685.
350. Zhong JW, Yang SX, Chen RP, et al. Prognostic Value of Lymphovascular Invasion in Patients with Stage III Colorectal Cancer: A Retrospective Study. *Med Sci Monit*. 2019;25:6043-6050.
351. Chang S-C, Lin C-C, Wang H-S, et al. Lymphovascular invasion determines the outcome of stage I colorectal cancer patients. *Formosan Journal of Surgery*. 2012;45(5):141-145.
352. Mitrovic B, Schaeffer DF, Riddell RH, Kirsch R. Tumor budding in colorectal carcinoma: time to take notice. *Mod Pathol*. 2012;25(10):1315-1325.
353. Rao CV, Janakiram NB, Mohammed A. Molecular Pathways: Mucins and Drug Delivery in Cancer. *Clin Cancer Res*. 2017;23(6):1373-1378.
354. Luo C, Cen S, Ding G, Wu W. Mucinous colorectal adenocarcinoma: clinical pathology and treatment options. *Cancer Commun (Lond)*. 2019;39(1):13.
355. Myers DJ, Arora K. Villous Adenoma. In: *StatPearls*. Treasure Island (FL)2020.
356. Vollmer S, Mateen BA, Bohner G, et al. Machine learning and artificial intelligence research for patient benefit: 20 critical questions on transparency, replicability, ethics, and effectiveness. *BMJ*. 2020;368:l6927.
357. Takayama T, Miyanishi K, Hayashi T, Sato Y, Niitsu Y. Colorectal cancer: genetics of development and metastasis. *J Gastroenterol*. 2006;41(3):185-192.
358. Nissan A, Stojadinovic A, Mitrani-Rosenbaum S, et al. Colon cancer associated transcript-1: a novel RNA expressed in malignant and pre-malignant human tissues. *Int J Cancer*. 2012;130(7):1598-1606.
359. Yang Y, Junjie P, Sanjun C, Ma Y. Long non-coding RNAs in Colorectal Cancer: Progression and Future Directions. *J Cancer*. 2017;8(16):3212-3225.
360. Roblick UJ, Hirschberg D, Habermann JK, et al. Sequential proteome alterations during genesis and progression of colon cancer. *Cell Mol Life Sci*. 2004;61(10):1246-1255.

361. Fearon ER, Vogelstein B. A genetic model for colorectal tumorigenesis. *Cell*. 1990;61(5):759-767.
362. Gunderson LL, Callister M, Marschke R, Young-Fadok T, Heppell J, Efron J. Stratification of rectal cancer stage for selection of postoperative chemoradiotherapy: current status. *Gastrointest Cancer Res*. 2008;2(1):25-33.
363. Mlecnik B, Tosolini M, Kirilovsky A, et al. Histopathologic-based prognostic factors of colorectal cancers are associated with the state of the local immune reaction. *J Clin Oncol*. 2011;29(6):610-618.
364. Nakatsu G, Li X, Zhou H, et al. Gut mucosal microbiome across stages of colorectal carcinogenesis. *Nat Commun*. 2015;6:8727.
365. Williams JG, Pullan RD, Hill J, et al. Management of the malignant colorectal polyp: ACPGBI position statement. *Colorectal Dis*. 2013;15 Suppl 2:1-38.
366. Morino M, Risio M, Bach S, et al. Early rectal cancer: the European Association for Endoscopic Surgery (EAES) clinical consensus conference. *Surg Endosc*. 2015;29(4):755-773.
367. Guenther S, Muirhead LJ, Speller AV, et al. Spatially resolved metabolic phenotyping of breast cancer by desorption electrospray ionization mass spectrometry. *Cancer Res*. 2015;75(9):1828-1837.
368. Hilvo M, Denkert C, Lehtinen L, et al. Novel theranostic opportunities offered by characterization of altered membrane lipid metabolism in breast cancer progression. *Cancer Res*. 2011;71(9):3236-3245.
369. Eberlin LS, Gabay M, Fan AC, et al. Alteration of the lipid profile in lymphomas induced by MYC overexpression. *Proc Natl Acad Sci U S A*. 2014;111(29):10450-10455.
370. Wang X, Han J, Hardie DB, Yang J, Pan J, Borchers CH. Metabolomic profiling of prostate cancer by matrix assisted laser desorption/ionization-Fourier transform ion cyclotron resonance mass spectrometry imaging using Matrix Coating Assisted by an Electric Field (MCAEF). *Biochim Biophys Acta Proteins Proteom*. 2017;1865(7):755-767.
371. Lee GK, Lee HS, Park YS, et al. Lipid MALDI profile classifies non-small cell lung cancers according to the histologic type. *Lung Cancer*. 2012;76(2):197-203.
372. Ifa DR, Eberlin LS. Ambient Ionization Mass Spectrometry for Cancer Diagnosis and Surgical Margin Evaluation. *Clin Chem*. 2016;62(1):111-123.
373. Nakagami K, Uchida T, Ohwada S, et al. Increased choline kinase activity and elevated phosphocholine levels in human colon cancer. *Jpn J Cancer Res*. 1999;90(4):419-424.
374. Baan B, Dihal AA, Hoff E, et al. 5-Aminosalicylic acid inhibits cell cycle progression in a phospholipase D dependent manner in colorectal cancer. *Gut*. 2012;61(12):1708-1715.
375. Mansilla F, da Costa KA, Wang S, et al. Lysophosphatidylcholine acyltransferase 1 (LPCAT1) overexpression in human colorectal cancer. *J Mol Med (Berl)*. 2009;87(1):85-97.
376. Jafari N, Drury J, Morris AJ, et al. De Novo Fatty Acid Synthesis-Driven Sphingolipid Metabolism Promotes Metastatic Potential of Colorectal Cancer. *Mol Cancer Res*. 2019;17(1):140-152.
377. Duan RD. Anticancer compounds and sphingolipid metabolism in the colon. *In Vivo*. 2005;19(1):293-300.
378. Uphoff A, Hermansson M, Haimi P, Somerharju P. Chapter 11 - Analysis of complex lipidomes. In: Vékey K, Telekes A, Vertes A, eds. *Medical Applications of Mass Spectrometry*. Amsterdam: Elsevier; 2008:223-249.
379. Morita SY, Terada T. Enzymatic measurement of phosphatidylglycerol and cardiolipin in cultured cells and mitochondria. *Sci Rep*. 2015;5:11737.
380. Murray NR, Fields AP. Phosphatidylglycerol is a physiologic activator of nuclear protein kinase C. *J Biol Chem*. 1998;273(19):11514-11520.

381. Inglese P, McKenzie JS, Mroz A, et al. Deep learning and 3D-DESI imaging reveal the hidden metabolic heterogeneity of cancer. *Chem Sci*. 2017;8(5):3500-3511.
382. Hong DH, Forstner JF, Forstner GG. Protein kinase C-epsilon is the likely mediator of mucin exocytosis in human colonic cell lines. *Am J Physiol*. 1997;272(1 Pt 1):G31-37.
383. Kondo Y, Nishiumi S, Shinohara M, et al. Serum fatty acid profiling of colorectal cancer by gas chromatography/mass spectrometry. *Biomark Med*. 2011;5(4):451-460.
384. Pickens CA, Lane-Elliott A, Comstock SS, Fenton JI. Altered Saturated and Monounsaturated Plasma Phospholipid Fatty Acid Profiles in Adult Males with Colon Adenomas. *Cancer Epidemiol Biomarkers Prev*. 2016;25(3):498-506.
385. Fernandez-Banares F, Esteve M, Navarro E, et al. Changes of the mucosal n3 and n6 fatty acid status occur early in the colorectal adenoma-carcinoma sequence. *Gut*. 1996;38(2):254-259.
386. Shim YJ, Choi KY, Lee WC, Kim MK, Lee SY, Lee-Kim YC. Phospholipid fatty acid patterns in the mucosa of human colorectal adenomas and carcinomas. *Nutrition Research*. 2005;25(3):261-269.
387. Green CD, Ozguden-Akkoc CG, Wang Y, Jump DB, Olson LK. Role of fatty acid elongases in determination of de novo synthesized monounsaturated fatty acid species. *J Lipid Res*. 2010;51(7):1871-1877.
388. Xu X, Ding Y, Yao J, et al. miR-215 Inhibits Colorectal Cancer Cell Migration and Invasion via Targeting Stearoyl-CoA Desaturase. *Comput Math Methods Med*. 2020;2020:5807836.
389. Liao C, Li M, Li X, et al. Trichothecin inhibits invasion and metastasis of colon carcinoma associating with SCD-1-mediated metabolite alteration. *Biochim Biophys Acta Mol Cell Biol Lipids*. 2020;1865(2):158540.
390. Vargas T, Moreno-Rubio J, Herranz J, et al. ColoLipidGene: signature of lipid metabolism-related genes to predict prognosis in stage-II colon cancer patients. *Oncotarget*. 2015;6(9):7348-7363.
391. Mika A, Kobiela J, Pakiet A, et al. Preferential uptake of polyunsaturated fatty acids by colorectal cancer cells. *Sci Rep*. 2020;10(1):1954.
392. Zhao S, Jia L, Gao P, et al. Study on the effect of eicosapentaenoic acid on phospholipids composition in membrane microdomains of tight junctions of epithelial cells by liquid chromatography/electrospray mass spectrometry. *J Pharm Biomed Anal*. 2008;47(2):343-350.
393. Hofmanova J, Ciganek M, Slavik J, et al. Lipid alterations in human colon epithelial cells induced to differentiation and/or apoptosis by butyrate and polyunsaturated fatty acids. *J Nutr Biochem*. 2012;23(6):539-548.
394. Turner K, Genta R, Sonnenberg A. Lesions of All Types Exist in Colon Polyps of All Sizes. *The American Journal of Gastroenterology*. 2017;113.
395. Prasetyanti PR, Medema JP. Intra-tumor heterogeneity from a cancer stem cell perspective. *Mol Cancer*. 2017;16(1):41.
396. Marusyk A, Polyak K. Tumor heterogeneity: causes and consequences. *Biochim Biophys Acta*. 2010;1805(1):105-117.
397. Molinari C, Marisi G, Passardi A, Matteucci L, De Maio G, Ulivi P. Heterogeneity in Colorectal Cancer: A Challenge for Personalized Medicine? *Int J Mol Sci*. 2018;19(12).
398. Buczacki SJ, Davies RJ. The confounding effects of tumour heterogeneity and cellular plasticity on personalized surgical management of colorectal cancer. *Colorectal Dis*. 2014;16(5):329-331.
399. Li F, Tiede B, Massague J, Kang Y. Beyond tumorigenesis: cancer stem cells in metastasis. *Cell Res*. 2007;17(1):3-14.

400. Gerlinger M, Rowan AJ, Horswell S, et al. Intratumor heterogeneity and branched evolution revealed by multiregion sequencing. *N Engl J Med*. 2012;366(10):883-892.
401. Balluff B, Frese CK, Maier SK, et al. De novo discovery of phenotypic intratumour heterogeneity using imaging mass spectrometry. *J Pathol*. 2015;235(1):3-13.
402. Okugawa Y, Grady WM, Goel A. Epigenetic Alterations in Colorectal Cancer: Emerging Biomarkers. *Gastroenterology*. 2015;149(5):1204-1225 e1212.
403. Hawthorn L, Lan L, Mojica W. Evidence for field effect cancerization in colorectal cancer. *Genomics*. 2014;103(2-3):211-221.
404. Giovannucci E, Oginio S. DNA methylation, field effects, and colorectal cancer. *J Natl Cancer Inst*. 2005;97(18):1317-1319.
405. Mirnezami R, Spagou K, Vorkas PA, et al. Chemical mapping of the colorectal cancer microenvironment via MALDI imaging mass spectrometry (MALDI-MSI) reveals novel cancer-associated field effects. *Mol Oncol*. 2014;8(1):39-49.
406. Jimenez B, Mirnezami R, Kinross J, et al. 1H HR-MAS NMR spectroscopy of tumor-induced local metabolic "field-effects" enables colorectal cancer staging and prognostication. *J Proteome Res*. 2013;12(2):959-968.
407. Barding GA, Jr., Salditos R, Larive CK. Quantitative NMR for bioanalysis and metabolomics. *Anal Bioanal Chem*. 2012;404(4):1165-1179.
408. Tzoulaki I, Ebbels TM, Valdes A, Elliott P, Ioannidis JP. Design and analysis of metabolomics studies in epidemiologic research: a primer on -omic technologies. *Am J Epidemiol*. 2014;180(2):129-139.
409. Haukaas TH, Moestue SA, Vettukattil R, et al. Impact of Freezing Delay Time on Tissue Samples for Metabolomic Studies. *Front Oncol*. 2016;6:17.
410. Gerbig S, Takats Z. Analysis of triglycerides in food items by desorption electrospray ionization mass spectrometry. *Rapid Commun Mass Spectrom*. 2010;24(15):2186-2192.
411. Koundouros N, Karali E, Tripp A, et al. Metabolic Fingerprinting Links Oncogenic PIK3CA with Enhanced Arachidonic Acid-Derived Eicosanoids. *Cell*. 2020;181(7):1596-1611 e1527.
412. Williams MD, Zhang X, Belton AS, et al. HMGA1 drives metabolic reprogramming of intestinal epithelium during hyperproliferation, polyposis, and colorectal carcinogenesis. *J Proteome Res*. 2015;14(3):1420-1431.
413. Bi X, Lin Q, Foo TW, et al. Proteomic analysis of colorectal cancer reveals alterations in metabolic pathways: mechanism of tumorigenesis. *Mol Cell Proteomics*. 2006;5(6):1119-1130.
414. Pei H, Zhu H, Zeng S, et al. Proteome analysis and tissue microarray for profiling protein markers associated with lymph node metastasis in colorectal cancer. *J Proteome Res*. 2007;6(7):2495-2501.
415. Shaath H, Toor SM, Nair VS, Elkord E, Alajez NM. Transcriptomic Analyses Revealed Systemic Alterations in Gene Expression in Circulation and Tumor Microenvironment of Colorectal Cancer Patients. *Cancers (Basel)*. 2019;11(12).
416. Woolston A, Khan K, Spain G, et al. Genomic and Transcriptomic Determinants of Therapy Resistance and Immune Landscape Evolution during Anti-EGFR Treatment in Colorectal Cancer. *Cancer Cell*. 2019;36(1):35-50 e39.
417. Martin-Perez B, Andrade-Ribeiro GD, Hunter L, Atallah S. A systematic review of transanal minimally invasive surgery (TAMIS) from 2010 to 2013. *Tech Coloproctol*. 2014;18(9):775-788.
418. Caycedo-Marulanda A, Jiang HY, Kohtakangas EL. Transanal minimally invasive surgery for benign large rectal polyps and early malignant rectal cancers: experience and outcomes from the first Canadian centre to adopt the technique. *Can J Surg*. 2017;60(6):416-423.

419. Rega D, Pace U, Niglio A, Scala D, Sassaroli C, Delrio P. TAMIS for rectal tumors: advancements of a new approach. *Updates Surg.* 2016;68(1):93-97.
420. Mason S, Manoli E, Poynter L, et al. Mass spectrometry transanal minimally invasive surgery (MS-TAMIS) to promote organ preservation in rectal cancer. *Surg Endosc.* 2020;34(8):3618-3625.
421. Snyder DT, Pulliam CJ, Ouyang Z, Cooks RG. Miniature and Fieldable Mass Spectrometers: Recent Advances. *Anal Chem.* 2016;88(1):2-29.
422. Benmessaoud C, Kharrazi H, MacDorman KF. Facilitators and barriers to adopting robotic-assisted surgery: contextualizing the unified theory of acceptance and use of technology. *PLoS One.* 2011;6(1):e16395.
423. Khan MA, Hakeem AR, Scott N, Saunders RN. Significance of R1 resection margin in colon cancer resections in the modern era. *Colorectal Dis.* 2015;17(11):943-953.
424. Bhangu A, Ali SM, Darzi A, Brown G, Tekkis P. Meta-analysis of survival based on resection margin status following surgery for recurrent rectal cancer. *Colorectal Dis.* 2012;14(12):1457-1466.
425. Schmoll HJ, Van Cutsem E, Stein A, et al. ESMO Consensus Guidelines for management of patients with colon and rectal cancer. a personalized approach to clinical decision making. *Ann Oncol.* 2012;23(10):2479-2516.
426. Wittekind C, Compton C, Quirke P, et al. A uniform residual tumor (R) classification: integration of the R classification and the circumferential margin status. *Cancer.* 2009;115(15):3483-3488.
427. Wang H, Liang L, Fang JY, Xu J. Somatic gene copy number alterations in colorectal cancer: new quest for cancer drivers and biomarkers. *Oncogene.* 2016;35(16):2011-2019.
428. Griffith M, Griffith OL, Mwenifumbo J, et al. Alternative expression analysis by RNA sequencing. *Nat Methods.* 2010;7(10):843-847.
429. Larsen MR, Trelle MB, Thingholm TE, Jensen ON. Analysis of posttranslational modifications of proteins by tandem mass spectrometry. *Biotechniques.* 2006;40(6):790-798.
430. Ou Y, Wilson RE, Weber SG. Methods of Measuring Enzyme Activity Ex Vivo and In Vivo. *Annu Rev Anal Chem (Palo Alto Calif).* 2018;11(1):509-533.
431. Sulkowski PL, Sundaram RK, Oeck S, et al. Krebs-cycle-deficient hereditary cancer syndromes are defined by defects in homologous-recombination DNA repair. *Nat Genet.* 2018;50(8):1086-1092.
432. Staples GO, Bowman MJ, Costello CE, et al. A chip-based amide-HILIC LC/MS platform for glycosaminoglycan glycomics profiling. *Proteomics.* 2009;9(3):686-695.
433. Gustafsson JOR, Eddes JS, Meding S, et al. Internal calibrants allow high accuracy peptide matching between MALDI imaging MS and LC-MS/MS. *J Proteomics.* 2012;75(16):5093-5105.
434. Liu Z, Tu MJ, Zhang C, Jilek JL, Zhang QY, Yu AM. A reliable LC-MS/MS method for the quantification of natural amino acids in mouse plasma: Method validation and application to a study on amino acid dynamics during hepatocellular carcinoma progression. *J Chromatogr B Analyt Technol Biomed Life Sci.* 2019;1124:72-81.
435. Kinross J, Mirnezami R, Alexander J, et al. A prospective analysis of mucosal microbiome-metabonome interactions in colorectal cancer using a combined MAS 1H NMR and metataxonomic strategy. *Sci Rep.* 2017;7(1):8979.

## Appendix

### Appendix 1 – TNM version 7 classification for colorectal cancers

	Stage	Description
<b>Primary Tumour</b>	Tx	Primary tumour cannot be assessed
	Tis	Tumour <i>in-situ</i> , where it is confined to the mucosa or the lamina propria
	T1	Tumour invading into submucosa
	T2	Tumour invading into muscularis propria
	T3	Tumour invades through muscularis propria into peri-colorectal tissues
	T4a	Tumour penetrates to the surface of the visceral peritoneum
	T4b	Tumour invades or is adherent to a local structure
<b>Nodes</b>	Nx	Regional lymph nodes cannot be assessed
	N0	No regional lymph node involvement
	N1a	Metastasis in 1 regional lymph node
	N1b	Metastasis in 2-3 regional lymph nodes
	N1c	Tumour deposit in the subserosa, mesentery or non-peritonealised peri-colorectal tissues without regional nodal metastasis
	N2a	4-6 regional lymph nodes containing metastasis
	N2b	7+ regional lymph nodes containing metastasis
<b>Metastasis</b>	M0	No evidence of distant metastasis
	M1a	Distant metastasis present in one organ or site
	M1b	Distant metastasis present in more than one organ or site or the peritoneum

This summary table was adapted from the AJCC cancer staging manual v7<sup>31</sup>.

Appendix 2 – AJCC and Duke’s staging for colorectal cancers

<b>AJCC Stage</b>	<b>T</b>	<b>N</b>	<b>M</b>	<b>Dukes Stage</b>
<b>0</b>	Tis	0	0	-
<b>I</b>	1	0	0	A
	2	0	0	B
<b>IIa</b>	3	0	0	B
<b>IIb</b>	4a	0	0	B
<b>IIc</b>	4b	0	0	B
<b>IIIa</b>	1-2	1	0	C
	1	2a	0	C
	3-4a	1	0	C
<b>IIIb</b>	2-3	2a	0	C
	1-2	2b	0	C
	4a	2a	0	C
<b>IIIc</b>	3-4a	2b	0	C
	4b	1-2	0	C
<b>IVa</b>	Any	Any	1a	D
<b>IVb</b>	Any	Any	1b	D

This summary table was adapted from AJCC cancer staging manual v7 and the modified Dukes criteria<sup>31-33</sup>.

Appendix 3 – search strategy for meta-analysis on real-time optical technologies for histological assessment of colorectal polyps

1. Exp Intestine, Large/
2. C?ecum.ti,ab
3. Colon\*.ti,ab
4. Rect\*.ti,ab
5. Colorectal.ti,ab
6. OR/1-5
7. Dysplas\*.ti,ab
8. Adenoma\*.ti,ab
9. Polyp\*.ti,ab
10. Adenomatous polyps/
11. Pseudopolyp\*.ti,ab
12. Neoplas\*.ti,ab
13. Lesion\*.ti,ab
14. OR/7-13
15. 6 AND 14
16. exp Colonic Neoplasms/
17. exp Colonic Polyps/
18. exp Rectal Neoplasms/
19. OR/15-18
20. exp Colonoscopy/
21. Colonoscop\*.ti,ab
22. Endoscop\*.ti,ab
23. Sigmoidoscop\*.ti,ab
24. OR/20-23
25. (Real adj time).ti,ab
26. (In adj vivo).ti,ab
27. Spectroscop\*.ti,ab
28. Endomicroscop\*.ti,ab
29. Chrom?endoscop\*.ti,ab
30. FI?orosc\*.ti,ab
31. (Narrow adj band).ti,ab
32. Optical.ti,ab
33. (i adj scan).ti,ab
34. (colo?r AND enhancement)/ti,ab
35. FICE.ti,ab
36. OR/25-35
37. Diagnos\*.ti,ab
38. Detect\*.ti,ab
39. Classif\*.ti,ab
40. Histolog\*.ti,ab
41. Assessment.ti,ab
42. Analysis.ti,ab
43. Characteri\*.ti,ab
44. OR/37-43
45. 19 AND 24 AND 36 AND 44
46. limit 45 to human

Appendix 4 – QUADAS-2 scores for digital chromoendoscopy studies

	Risk of Bias				Applicability			Reason for <i>Unclear</i> or <i>High</i> Score
	Patient Selection	Index Test	Reference Standard	Flow and Timing	Patient Selection	Index Test	Reference Standard	
Ashktorab 2016								Unclear endoscopist experience with NBI technology prior to study
Ashktorab 2016								Unclear endoscopist experience with NBI technology prior to study
Basford 2014								-
Belderbos 2017								Unclear if consecutive patients were eligible, limited sampling of rectal hyperplastic polyps reduces adenoma
Buchner 2010								Unclear if consecutive patients were eligible, some lesions known to be adenomas prior to index test
Buchner 2010								Unclear if consecutive patients were eligible, some lesions known to be adenomas prior to index test
Canales-Sevilla 2010								Unclear if consecutive patients were eligible for study. Unclear endoscopist experience with NBI technology prior to study
Chan 2012								-
Chandran 2015								-
Dai 2013								-
dos Santos 2009								Unclear if consecutive patients were eligible
dos Santos 2010								-
dos Santos 2012								-
dos Santos 2017								-
dos Santos 2017								-
East 2008								-

Hewett 2012	?	+	+	+	+	+	+	Unclear if consecutive patients were eligible for study
Hewett 2012	?	+	+	+	+	+	+	Unclear if consecutive patients were eligible for study
Hoffman 2010	+	+	+	+	+	+	+	-
Hoffman 2010	+	+	+	+	+	+	+	-
Hong 2012	+	+	+	+	+	+	+	-
Hong 2012	+	+	+	+	+	+	+	-
Ikematsu 2015	+	+	+	+	+	+	+	-
Iwatate 2015	+	?	+	+	+	+	+	Unclear if all endoscopists had sufficient experience with NBI prior to study
Iwatate 2015	+	?	+	+	+	+	+	Unclear if all endoscopists had sufficient experience with NBI prior to study
Kaltenbach 2015	+	+	+	+	+	+	+	-
Kaltenbach 2015	+	+	+	+	+	+	+	-
Kang 2015	+	+	+	+	+	+	+	-
Kang 2015	+	+	+	+	+	+	+	-
Kim 2011	+	+	+	+	+	+	+	-
Klare 2016	+	+	+	+	+	+	+	-
Kuiper 2011	+	-	+	+	+	+	+	Lesions also assessed with AFI, likely biasing interpretation of the NBI
Kuiper 2012	+	+	+	+	+	+	+	-
Kuruvilla 2015	+	+	+	+	?	+	+	High incidence of SSAs (17%) unrepresentative of routine clinical practice
Ladabaum 2013	?	+	+	+	+	+	+	Unclear if consecutive patients were eligible for study
Lee 2011	+	+	+	+	+	+	+	-
Lee 2011	+	+	+	+	+	+	+	-
Liu 2008	?	+	+	+	+	+	+	Unclear how patients were selected and if consecutive patients were eligible for study

Longcroft-Wheaton 2011								-
Longcroft-Wheaton 2012								-
Longcroft-Wheaton 2012								-
Machida 2004								Unclear how patients were selected and if consecutive patients were eligible for study
Okamoto 2011								Unclear how patients were selected and if consecutive patients were eligible for study. High incidence of adenomas (95%) not representative of practice
Paggi 2012								-
Paggi 2015								-
Pigo 2013								Unclear if all endoscopists had sufficient experience with iSCAN prior to study
Pohl 2009								Endoscopists were often inexperienced with FICE prior to the study starting
Pohl 2016								-
Pohl 2016								-
Rastogi 2011								-
Rath 2015								Unclear if endoscopists had sufficient experience with iSCAN prior to study
Rees 2017								-
Ren 2012								Unclear if endoscopists had sufficient experience with NBI prior to study
Repici 2013								-
Rex 2009								-
Rogart 2008								-
Rogart 2011								-
Rogart 2011								-
Rotondano 2012								High incidence of adenomas (90%) not representative of clinical practice

Sakamoto 2012								Half of the lesions had just been assessed by dye chromoendoscopy, likely biasing the interpretation of NBI. High incidence of adenomas (89%) not representative of practice
Salazar Muentel 2012								Unclear if consecutive patients were eligible for study
Sano 2009								-
Sano 2015								Unclear if consecutive patients were eligible for study. IC dye was used for detection and may have biased NBI
Schachschal 2014								-
Seref Koksak 2014								Endoscopists had no experience using NBI prior to the study starting
Shahid 2012								Unclear how patients selected and if consecutive patients were eligible for the study
Singh 2011								Unclear how patients were selected, likely not consecutive. Unlikely sufficient endoscopist experience with NBI
Singh 2013								Unlikely sufficient endoscopist experience with NBI
Sola-Vera 2015								-
Szura 2016								Unclear how patients were selected, likely not consecutive. Unlikely sufficient endoscopist experience with NBI
Takeuchi 2014								-
Takeuchi 2015								-
Takeuchi 2015								-
Togashi 2009								Unclear how patients were selected, likely not consecutive
Van den Broek 2009								Unlikely sufficient endoscopist experience with NBI prior to study start. Some lesions previously assessed with AFI, likely biasing interpretation
Wallace 2014								-
Wallace 2014								-
Yoo 2011								Unclear how patients were selected. High incidence of adenomas (93%) not representative of clinical practice

Appendix 5 – QUADAS-2 scores for dye chromoendoscopy studies

	Risk of Bias				Applicability			Reason for <i>Unclear</i> or <i>High</i> Score
	Patient Selection	Index Test	Reference Standard	Flow and Timing	Patient Selection	Index Test	Reference Standard	
Apel 2006	+	?	-	+	+	+	+	Unclear endoscopist experience with chromoendoscopy. Pathologists were not blinded to intra-operative prediction
Averbach 2003	+	+	+	+	+	+	+	-
Axelrad 1996	+	+	+	+	+	+	+	-
Bianco 2006	?	+	+	+	+	+	+	Unclear endoscopist experience with chromoendoscopy prior to study start
de Palma 2006	?	+	+	+	+	+	+	Unclear how patients were selected, likely not consecutive
dos Santos 2009	+	+	+	+	+	+	+	-
dos Santos 2010	+	+	+	+	+	+	+	-
dos Santos 2012	+	+	+	+	+	+	+	-
Eisen 2002	-	?	+	+	+	+	+	Some patients only had sigmoidoscopy, changing the prevalence of lesion histological subtypes. Unclear endoscopist experience with chromoendoscopy
Fu 2004	+	+	+	+	+	+	+	-
Hurlstone 2004	?	?	+	+	+	+	+	Unclear if consecutive patients eligible. Unclear if sufficient endoscopist experience with chromoendoscopy
Ince 2007	?	+	+	+	+	+	+	Unclear how patients were selected, likely not consecutive
Kato 2006	?	+	+	+	?	+	+	Unclear how patients were selected. High incidence of adenomas (88%) not representative of clinical practice
Kiesslich 2001	+	?	+	+	+	+	+	Unclear endoscopist experience with chromoendoscopy prior to study start
Konishi 2003	+	+	+	+	+	+	+	-
Konishi 2003	+	+	+	+	+	+	+	-
Liu 2003	?	?	+	+	+	+	+	Unclear indications for colonoscopy. Unclear endoscopist experience with chromoendoscopy prior to study start
Liu 2008	?	-	+	+	+	+	+	Unclear how patients were selected, likely not consecutive. Lesion chromoendoscopy interpretation was biased by just having performed FICE. Unclear endoscopist experience
Ljubcic 2001	?	?	+	+	+	+	+	Unclear if consecutive patients eligible. Unclear if sufficient endoscopist experience with chromoendoscopy

Longcroft-Wheaton 2011								Chromoendoscopy interpretation was biased by just performing FICE
Longcroft-Wheaton 2013								-
Longcroft-Wheaton 2013								-
Machida 2004								Unclear if consecutive patients eligible. Chromoendoscopy interpretation was biased by just performing NBI
Pohl 2009								Unclear endoscopist experience with chromoendoscopy prior to study start
Sakamoto 2012								Chromoendoscopy interpretation was biased by just having been analysed by NBI. High incidence of adenomas (89%) not representative of practice
Togashi 1999								Unclear endoscopist experience with chromoendoscopy prior to study start
Togashi 2006								Unclear endoscopist experience with chromoendoscopy prior to study start
Togashi 2009								Unclear if consecutive patients were eligible. Lesion chromoendoscopy interpretation was biased by just having performed FICE
Tung 2001								-
Urban 2005								-

## Appendix 6 – QUADAS-2 scores for fluorescence studies

	Risk of Bias				Applicability			Reason for <i>Unclear</i> or <i>High</i> Score
	Patient Selection	Index Test	Reference Standard	Flow and Timing	Patient Selection	Index Test	Reference Standard	
Aihara 2013								-
Kuiper 2011								Lesions also assessed with NBI, likely biasing interpretation of the AFI
van den Broek 2009								Lesions also assessed with NBI, likely biasing interpretation of the AFI

## Appendix 7 – QUADAS-2 scores for microscopic imaging studies

	Risk of Bias				Applicability			Reason for <i>Unclear</i> or <i>High</i> Score
	Patient Selection	Index Test	Reference Standard	Flow and Timing	Patient Selection	Index Test	Reference Standard	
Kiesslich 2004	?	?	+	+	+	+	+	Unclear how patients were selected, likely not consecutive. Unlikely sufficient endoscopist experience with technology
Sanduleanu 2010	+	+	+	+	+	+	+	-
Shahid 2012	?	?	+	+	+	+	+	Unclear how patients were selected, likely not consecutive. Unlikely sufficient endoscopist experience with technology
Xie 2011	+	+	+	+	+	+	+	-

## Appendix 8 – QUADAS-2 scores for computer-aided recognition studies

	Risk of Bias				Applicability			Reason for <i>Unclear</i> or <i>High</i> Score
	Patient Selection	Index Test	Reference Standard	Flow and Timing	Patient Selection	Index Test	Reference Standard	
Kominami 2016	?	+	+	+	+	+	+	Unclear if consecutive patients were eligible for inclusion
Kuiper 2015	+	?	+	+	+	+	+	Unclear endoscopist experience with the technology prior to the study start
Rath 2016	+	+	+	+	+	+	+	-

## Appendix 9 – Permissions from publishers for the use of figures

### License Details

This Agreement between Imperial College London -- Sam Mason ("You") and John Wiley and Sons ("John Wiley and Sons") consists of your license details and the terms and conditions provided by John Wiley and Sons and Copyright Clearance Center.

License Number	4971910460529
License date	Dec 18, 2020
Licensed Content Publisher	John Wiley and Sons
Licensed Content Publication	FEBS Journal
Licensed Content Title	Lipid metabolism in cancer
Licensed Content Author	Almut Schulze, Claudio R. Santos
Licensed Content Date	Jul 3, 2012
Licensed Content Volume	279
Licensed Content Issue	15
Licensed Content Pages	14
Type of Use	Dissertation/Thesis
Requestor type	University/Academic
Format	Electronic
Portion	Figure/table
Number of figures/tables	1
Will you be translating?	No
Title	Examining lipid metabolism of colorectal adenomas and carcinomas using Rapid Evaporative Ionisation Mass Spectrometry (REIMS)
Institution name	Imperial College London
Expected presentation date	Mar 2021
Portions	Figure 1
Requestor Location	Imperial College London 10th Floor, QEQM Building St Mary's Hospital  London, W2 1NY United Kingdom Attn: Imperial College London
Publisher Tax ID	EU826007151
Total	<b>0.00 GBP</b>

### License Details

This Agreement between Imperial College London -- Sam Mason ("You") and Springer Nature ("Springer Nature") consists of your license details and the terms and conditions provided by Springer Nature and Copyright Clearance Center.

License Number	4971910665214
License date	Dec 18, 2020
Licensed Content Publisher	Springer Nature
Licensed Content Publication	Nature Reviews Cancer
Licensed Content Title	Genetic prognostic and predictive markers in colorectal cancer

Licensed Content Author	Axel Walther et al
Licensed Content Date	Jun 18, 2009
Type of Use	Thesis/Dissertation
Requestor type	academic/university or research institute
Format	print and electronic
Portion	figures/tables/illustrations
Number of figures/tables/illustrations	1
High-res required	no
Will you be translating?	no
Circulation/distribution	1 - 29
Author of this Springer Nature content	no
Title	Examining lipid metabolism of colorectal adenomas and carcinomas using Rapid Evaporative Ionisation Mass Spectrometry (REIMS)
Institution name	Imperial College London
Expected presentation date	Mar 2021
Portions	Figure 1
Requestor Location	Imperial College London 10th Floor, QEQM Building St Mary's Hospital  London, W2 1NY United Kingdom Attn: Imperial College London
Total	<b>0.00 USD</b>

## License Details

This Agreement between Imperial College London -- Sam Mason ("You") and Wolters Kluwer Health, Inc. ("Wolters Kluwer Health, Inc.") consists of your license details and the terms and conditions provided by Wolters Kluwer Health, Inc. and Copyright Clearance Center.

License Number	4971990804324
License date	Dec 18, 2020
Licensed Content Publisher	Wolters Kluwer Health, Inc.
Licensed Content Publication	American Journal of Gastroenterology
Licensed Content Title	Optical Technologies for Endoscopic Real-Time Histologic Assessment of Colorectal Polyps: A Meta-Analysis
Licensed Content Author	Sam E. Mason, Liam Poynter, Zoltan Takats, et al
Licensed Content Date	Feb 26, 2019
Licensed Content Volume	114
Licensed Content Issue	8
Type of Use	Dissertation/Thesis
Requestor type	University/College
Sponsorship	No Sponsorship
Format	Print and electronic
Will this be posted online?	Yes, on an unrestricted website
Portion	Figures/tables/illustrations

Number of figures/tables/illustrations	6
Author of this Wolters Kluwer article	Yes
Will you be translating?	No
Intend to modify/change the content	No
Title	Examining lipid metabolism of colorectal adenomas and carcinomas using Rapid Evaporative Ionisation Mass Spectrometry (REIMS)
Institution name	Imperial College London
Expected presentation date	Mar 2021
Portions	Figure 1-4 and Tables 1-2
Requestor Location	Imperial College London 10th Floor, QEQM Building St Mary's Hospital  London, W2 1NY United Kingdom Attn: Imperial College London
Publisher Tax ID	EU826013006
Billing Type	Invoice
Billing address	Imperial College London 10th Floor, QEQM Building St Mary's Hospital  London, United Kingdom W2 1NY Attn: Imperial College London
Total	<b>0.00 USD</b>